

---

# Molecular interactions and their impact on life sciences

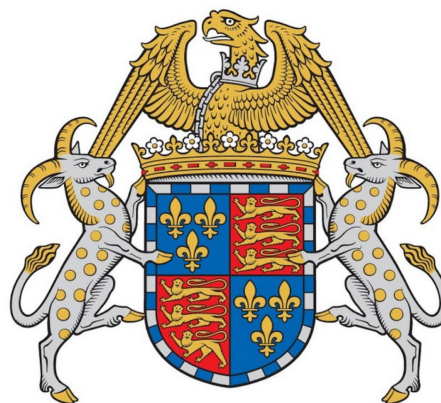
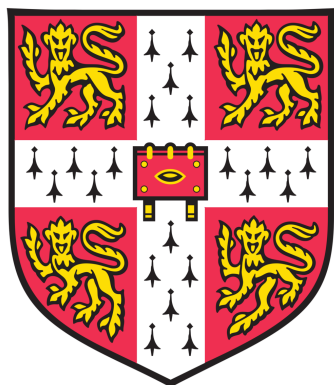
---

Tom Scheidt

St. John's College

University of Cambridge

Department of Chemistry



This dissertation is submitted for the degree of *Doctor of Philosophy*

September 2019

Supervisor: Prof. Tuomas P. J. Knowles



*"No amount of experimentation can ever prove me right; a single experiment can prove me wrong."*

*Albert Einstein*



# Declaration of Authorship

I, Tom Scheidt, declare that this thesis titled, 'Molecular interactions and its impact on life sciences' and the work presented in it are my own. I confirm that:

- This thesis is the result of my own work and includes nothing which is the outcome of work done in collaboration except as declared in the Preface and specified in the text.
- It is not substantially the same as any that I have submitted, or, is being concurrently submitted for a degree or diploma or other qualification at the University of Cambridge or any other University or similar institution except as declared in the Preface and specified in the text. I further state that no substantial part of my dissertation has already been submitted, or, is being concurrently submitted for any such degree, diploma or other qualification at the University of Cambridge or any other University or similar institution except as declared in the Preface and specified in the text.
- It does not exceed the prescribed word limit for the relevant Degree Committee.
- Where I have consulted the published work of others, this is always clearly attributed.
- Where I have quoted from the work of others, the source is always given. With the exception of such quotations, this thesis is entirely my own work.

Signed:

---

Date:

---

# Abstract

## Molecular interactions and their impact on life sciences

Tom Scheidt

The behaviour and function of biomolecules represent a fundamental aspect in modulating the activity of micro and macro-scale complexes evolved in cells and tissues. The network of interactions of such biomolecules allow for the formation and regulation of the basic machinery of life, yet is commonly studied under non-physiological conditions. In order to characterise the behaviour and function of such biomolecules, they have to be analysed under relevant conditions, ideally in biofluids, cells or artificial systems which mainly imitate these properties. Recent microfluidic applications present an orthogonal approach for determining the interactions between a wide range of biomolecules, thus allow the study of molecular binding in the condensed phase with no need for extensive dilution, sample immobilisation or changes to the molecular environment from the liquid to the gas phase.

As part of my PhD, I capitalised on microfluidic diffusion approaches, developed in the Knowles lab to systematically study the binding and thermodynamics of small heat shock proteins, such as clusterin,  $\alpha$ B-crystallin and the Brichos chaperone domain, to aggregated forms of amyloid-beta and  $\alpha$ -synuclein, protein aggregates that are associated with a wide range of neurodegenerative diseases. The three chaperones are crucial components of the cellular proteostasis network and characteristically overexpressed during cell stress. Each chaperone type shows distinct binding behaviour to protein aggregates, which can be related to its inhibitory function. While  $\alpha$ B-crystallin binding to  $\alpha$ -synuclein is entropically driven by conformational rearrangement, the binding of Brichos to amyloid-beta fibrils is shown to be enthalpically driven as it inhibits specifically secondary nucleation processes. In contrast to the specific secondary nucleation inhibition by Brichos, clusterin inhibits specifically fibril elongation of amyloid-beta.

I could show that these two specific aggregation processes are affected by the two chaperones, Brichos and clusterin, in a non-cooperative manner.

These molecular details are particularly relevant in the context of the rational design of drug molecules that could, potentially in combination, target multiple specific aggregation steps in a selective manner. Therefore, I further screened the binding of a wide range of monoclonal antibodies to either amyloid-beta monomers or fibrils, which are currently at different stages of clinical phase trials for Alzheimer's therapy. I thus show that the obtained stoichiometry and affinity information of the drug correlates with the distinct inhibition mechanisms and consequently provides mechanistic and structural information.

In contrast to studying disease related model systems *in vitro* under homogeneous conditions, measurements in complex body fluids are key in medical applied science, e.g. cancer treatment or immunological characterisation. In my research, I have undertaken the challenge of extending the platform developed above to characterise the binding of a wide range of molecules under complex solution conditions. Preliminary data obtained during my PhD underlines the extraordinary capability of the diffusion-based microfluidics to being applicable for investigating the binding parameters of molecules involved in alloimmunisation in human serum.

Along with my main focus on measuring protein interactions with diffusion-based microfluidics, I further developed a technique using selective separation properties, such as particle charge, hydrophobicity, size or immunoaffinity and coupled it with a series of microfluidic devices for an instantaneous and full biophysical characterisation of heterogeneous solutions. This new technique can be used to explore the formation of protein oligomers or protein complexation, characterisation and identification of complex mixtures in the context of amyloid formation and protein homeostasis.

# Acknowledgements

First and foremost, I would like to thank Kerstin, my girlfriend, for the support for all the many years of my PhD, her love and kindness in those difficult years. Furthermore, I want to thank my parents for the support, trust and motivation over the years.

This report concludes the work which was done at the Centre for Misfolding Diseases at the Department of Chemistry, the Department of Surgery at the Addenbrooks Hospital, part of the University of Cambridge and at the Lund University in Sweden from October 2015 till September 2019.

I would like to thank Tuomas Knowles, who gave me the opportunity to come to Cambridge to do my Ph.D. in his group independently and for the support and encouragement he gave me. Furthermore, I also got a great financial and organisational support from the European Research Council and I want to thank Tuomas for organising my funding. I want to thank the entire CMD for the support in everyday laboratory work. In particular, I want to thank Tadas, Aviad, Georg, Gordon, Thomas and Therese not only for their help and advice but also for the friendship they offered. Besides them, I would like to thank my companions Janet, Tuuli, Zenon, Magda, Itzel, Yufan, Will, Matthias, Manuela, Marc, Challa, Simon, Dominik, Ula, Francesco and Patrick for the fruitful and joyful discussions and that they endured my crazy input. Last but not least, I would like to thank Fluidic Analytics Inc. for their encouraging ideas and help, especially Sean and Maren. Likewise, I want to thank my collaborators and especially Paolo, Sara and Vasilis for their hospitality and trust in our work.

---

# Contents

---

<b>Contents</b>	<b>ix</b>
<b>List of Figures</b>	<b>xiii</b>
<b>Abbreviations &amp; Symbols</b>	<b>xv</b>
<b>1 An introduction to protein interactions</b>	<b>1</b>
1.1 Protein interactions . . . . .	1
1.1.1 Intramolecular interactions - the driving force of protein folding and misfolding . . . . .	2
1.1.2 Intermolecular protein interactions . . . . .	3
1.1.2.1 Functional protein assembly . . . . .	4
1.1.2.2 Protein aggregation and related diseases . . . . .	5
1.1.2.3 Molecular chaperones as counterparts to protein aggregation . . . . .	7
1.2 Microfluidic applications for the investigation of protein interactions under native conditions . . . . .	8
1.2.1 Diffusional sizing of heterogeneous protein solutions . . . . .	8
<b>2 The binding of chaperones and therapeutic antibodies to amyloid fibrils</b>	<b>13</b>
2.1 Introduction: Chaperones - natural inhibitors of protein aggregation . . .	14
2.1.1 The small heat shock protein $\alpha$ B-crystallin . . . . .	15
2.1.2 The Brichos chaperone domain . . . . .	17
2.1.3 The extracellular chaperone clusterin . . . . .	18
2.1.4 Antibody and small molecule strategies as potential therapeutics targeting $A\beta(42)$ aggregation . . . . .	20
2.2 How the interaction of the small heat-shock protein $\alpha$ B-crystallin to $\alpha$ -synuclein fibrils is driven by entropic forces and what that means for the binding mechanism . . . . .	21
2.2.1 Microfluidic measurements of protein interactions in the condensed phase . . . . .	21
2.2.2 Experiments under native conditions reveal a nanomolar affinity for $\alpha$ B-crystallin binding to $\alpha$ -syn fibrils . . . . .	23
2.2.3 The binding of $\alpha$ B-crystallin to $\alpha$ -syn fibrils exhibits strong entropy/enthalpy compensation . . . . .	26

2.2.4	Analysis of thermodynamic contributions to the activated state . .	28
2.2.5	Discussion . . . . .	29
2.3	Brichos and clusterin - a model system that shows how secondary nucleation and elongation occurs at distinct sites along amyloid fibrils . . . . .	30
2.3.1	Clusterin suppresses specifically the elongation step of A $\beta$ (M1-42) aggregation . . . . .	30
2.3.2	Quantification of interactions between clusterin and A $\beta$ (M1-42) fibrils by microfluidic diffusional sizing . . . . .	33
2.3.3	Modulation of A $\beta$ (M1-42) aggregation by Brichos reveals that the reactive sites of secondary nucleation and elongation are distinct . . . . .	38
2.3.4	Discussion . . . . .	39
2.4	Thermodynamic evaluation of the enthalpic Brichos binding reveals very limited catalytic sites along amyloid-beta fibrils . . . . .	41
2.4.1	Binding affinity determination . . . . .	44
2.4.2	Thermodynamic parameters of Brichos binding to A $\beta$ (M1-42) fibrils . . . . .	45
2.4.3	Brichos binding kinetics indicate a limitation of secondary nucleation sites . . . . .	48
2.4.4	Discussion . . . . .	48
2.5	How the binding characteristics of therapeutic antibodies control their inhibitory capabilities . . . . .	49
2.5.1	Kinetic and mechanistic analysis of potential Alzheimer's therapeutics . . . . .	49
2.5.1.1	Aducanumab . . . . .	49
2.5.1.2	Bapineuzumab . . . . .	51
2.5.1.3	Gantenerumab . . . . .	51
2.5.1.4	Solanezumab . . . . .	52
2.5.2	Discussion . . . . .	52
2.6	Conclusion . . . . .	53
<b>A</b>	<b>Methods and Analysis</b>	<b>55</b>
A.1	Proteins . . . . .	55
A.1.1	$\alpha$ B-crystallin . . . . .	55
A.1.2	$\alpha$ -Synuclein . . . . .	55
A.1.3	Amyloid- $\beta$ (M1-42) . . . . .	56
A.1.4	Amyloid- $\beta$ (1-42) . . . . .	56
A.1.5	proSP-C Brichos . . . . .	57
A.1.6	Clusterin . . . . .	57
A.1.7	Generation and purification of anti-A $\beta$ antibodies . . . . .	58
A.1.8	Alexa-647 labelling of A $\beta$ peptides and antibodies . . . . .	58
A.2	Fabrication and use of microfluidic diffusion devices . . . . .	58
A.3	Aggregation kinetics . . . . .	59
A.3.1	$\alpha$ -synuclein . . . . .	59
A.3.2	Clusterin and proSP-C Brichos . . . . .	59
A.3.3	Anti-Amyloid- $\beta$ antibodies . . . . .	60
A.3.4	Kinetic analysis and simulations . . . . .	60

---

A.4	Sample preparation for binding experiments . . . . .	62
A.4.1	$\alpha$ -Synuclein . . . . .	62
A.4.2	Clusterin and proSP-C Brichos . . . . .	62
A.4.3	proSP-C Brichos only . . . . .	63
A.4.4	Anti-Amyloid- $\beta$ antibodies . . . . .	63
A.5	Diffusion image analysis and fitting . . . . .	64
A.6	Native mass spectrometry . . . . .	66
A.7	Equilibrium and kinetic curve fitting . . . . .	66
A.8	Determination of Binding parameters . . . . .	68
A.8.1	Curve fitting to obtain thermodynamic and kinetic parameters of $\alpha$ -synuclein . . . . .	68
A.8.2	Thermodynamic equilibrium analysis of proSP-C Brichos . . . . .	69
A.8.3	Binding constant determination for anti-Amyloid- $\beta$ antibodies . . . . .	70
A.9	Immunogold-labelling Transmission Electron Microscopy (TEM) . . . . .	71
A.10	SDS-PAGE analysis . . . . .	72
<b>B</b>	<b>Supplementary information</b>	<b>73</b>
<b>3</b>	<b>Using microfluidic diffusional sizing for immunological screening</b>	<b>91</b>
3.1	Clinical relevance of diffusional binding measurements for alloimmunisation detection . . . . .	91
3.2	Binding measurements of human leukocyte antigens and related antibodies in buffer . . . . .	93
3.3	Investigation of graft rejection factors in human serum . . . . .	95
3.4	Discussion . . . . .	99
<b>C</b>	<b>Methods and Analysis</b>	<b>101</b>
C.1	Sample preparation . . . . .	101
C.1.1	Biotinylated HLA together with mAB in PBS or human serum . . . . .	101
C.2	Labelling of non-biotinylated HLA with Alexa Fluor 647 fluorophore . . . . .	101
C.3	Fabrication and use of microfluidic diffusion devices . . . . .	102
C.4	Native-PAGE analysis . . . . .	102
C.5	Binding analysis . . . . .	102
C.5.1	Derivation of non-linear binding equation . . . . .	102
C.5.2	Binding equation with background subtraction . . . . .	104
<b>D</b>	<b>Supplementary information</b>	<b>105</b>
<b>4</b>	<b>Multidimensional characterisation of complex mixtures by microfluidic coupled size-exclusion chromatography</b>	<b>111</b>
4.1	Introduction . . . . .	111
4.2	Results and Discussion . . . . .	115
4.2.1	Label-free protein characterisation . . . . .	115
4.2.2	Heterogeneous labelled analyte separation and characterisation . . . . .	117
4.3	Conclusion . . . . .	120
<b>E</b>	<b>Methods and Analysis</b>	<b>123</b>
E.1	Analyte mixtures . . . . .	123

---

E.2	LC separation . . . . .	124
E.3	Microfluidic flow adapter . . . . .	124
E.4	Flow control . . . . .	125
E.5	Microfluidic chip design and operation . . . . .	125
E.6	Microfluidic chip fabrication . . . . .	126
E.7	Fluorescence microscope setups . . . . .	127
E.8	Time matching . . . . .	127
E.9	Electrophoresis device calibration and mobility analysis . . . . .	128
E.10	Size and charge calculations . . . . .	128
E.11	Isoelectric point and net charge prediction . . . . .	129
E.12	Second derivative analysis of chromatograms . . . . .	129
<b>F</b>	<b>Supplementary information</b>	<b>131</b>
<b>5</b>	<b>Concluding remarks</b>	<b>135</b>
	<b>Bibliography</b>	<b>139</b>

---

## List of Figures

---

1.1	Free-energy landscape of protein interactions . . . . .	2
1.2	Aggregation mechanisms of $A\beta_{40}$ and $A\beta_{42}$ . . . . .	6
1.3	Diffusion-based microfluidic device . . . . .	11
2.1	Oligomeric organisation of $\alpha$ B-crystallin . . . . .	16
2.2	X-ray diffraction structure of the proSP-C Brichos domain and its inhibition mechanism . . . . .	18
2.3	Diffusion profiles of $\alpha$ B-crystallin and $\alpha$ -synuclein fibril binding . . . . .	22
2.4	Binding kinetics of $\alpha$ B-crystallin and $\alpha$ -synuclein fibrils . . . . .	24
2.5	Thermodynamic analysis of $\alpha$ B-crystallin and $\alpha$ -synuclein fibril binding . . . . .	27
2.6	Potential binding models of $\alpha$ B-crystallin and $\alpha$ -synuclein fibrils . . . . .	28
2.8	TEM images of clusterin with $A\beta(M1-42)$ fibrils . . . . .	34
2.9	Microfluidic analysis of clusterin and $A\beta(M1-42)$ fibrils . . . . .	36
2.10	Binding curve of clusterin to $A\beta(M1-42)$ fibrils at 21 °C . . . . .	37
2.11	Modulated $A\beta(M1-42)$ aggregation by clusterin and/or Brichos . . . . .	38
2.12	Microfluidic analysis of Brichos and $A\beta(M1-42)$ fibrils . . . . .	42
2.13	Binding curve of Brichos to $A\beta(M1-42)$ fibrils at 21 °C . . . . .	44
2.14	Thermodynamic binding evaluation of Alexa-488 labelled Brichos with $A\beta(M1-42)$ fibrils . . . . .	46
2.15	Binding kinetics of Brichos to $A\beta(M1-42)$ fibrils measured by MDS . . . . .	47
2.16	Characteristic binding behaviour of selected therapeutic antibodies to $A\beta(M1-42)$ monomers and fibrils . . . . .	50
2.17	Summary of binding and inhibition characteristics of selected therapeutic antibodies to $A\beta(1-42)$ monomers and fibrils . . . . .	53
B.1	Kinetic comparison of GFP labelled and unlabelled $\alpha$ B-crystallin . . . . .	74
B.2	Microfluidic analysis and size distribution of $\alpha$ B-crystallin together with $\alpha$ -synuclein . . . . .	74
B.3	Size distribution analysis of $\alpha$ B-c by native mass spectrometry . . . . .	75
B.4	Equilibration binding curve of $\alpha$ B-crystallin with $\alpha$ -synuclein . . . . .	76
B.5	Dissociation kinetic of $\alpha$ B-crystallin from $\alpha$ -synuclein fibrils . . . . .	77
B.6	Representation of regulating fitting parameters for ideal $\alpha$ B-c diffusion analysis . . . . .	78
B.7	Aggregation kinetics of $A\beta(M1-42)$ in the presence and absence of clusterin at 37°C . . . . .	79

B.8	Aggregation kinetics of A $\beta$ (M1-42) in the presence and absence of clusterin at 21°C . . . . .	79
B.9	Seed experiments with A $\beta$ (M1-42) in the presence and absence of clusterin	80
B.10	TEM images of A $\beta$ (M1-42) fibrils formed in the presence of clusterin . . .	81
B.11	Example diffusion profiles of clusterin in the presence of A $\beta$ (M1-42) fibrils	82
B.12	Investigation of inhibition specificity of clusterin in A $\beta$ (M1-42) aggregation	83
B.13	Investigation of potential altering inhibition effects of clusterin labelling .	83
B.14	Modulated A $\beta$ (M1-42) aggregation by clusterin and/or Brichos . . . . .	84
B.15	Kinetic comparison of A $\beta$ (M1-42) aggregation in the presence of labelled and unlabelled Brichos . . . . .	84
B.16	Binding kinetics of Brichos to A $\beta$ (M1-42) fibrils measured by MDS . . . .	85
B.17	Example diffusion profiles of Brichos in the presence of A $\beta$ (M1-42) fibrils	86
B.18	SDS-PAGE of Brichos proving thermal stability . . . . .	87
B.19	Effects of the antibodies on the kinetics of aggregation of A $\beta$ (1-42) in the presence and absence of pre-formed fibrils . . . . .	88
B.20	Low concentrated seeding experiments of A $\beta$ (42) in the presence of selected therapeutic antibodies . . . . .	89
3.1	Principle of applying MDS for human serum . . . . .	92
3.2	Diffusion profiles of HLA in the absence/presence of monoclonal antibodies	94
3.3	Binding curve of WIM8E5 mAB to HLA A*01:01 . . . . .	95
3.4	Binding studies of HLA and antibodies in unpurified patient human serum	97
3.5	Binding studies of monovalent HLA and antibody infused serum in . . . .	98
D.1	Native-PAGE of Alexa-488 labelled HLA . . . . .	105
D.2	Chromatogram of tetrameric HLA . . . . .	106
D.3	Least-square fits of HLA A*01:01 + mAB WIM8E5 diffusion profiles . . .	107
D.4	Luminex measurements of human serum . . . . .	108
D.5	Least-square fits of HLA A*02:01 + human serum diffusion profiles . . .	109
D.6	Stoichiometric verification of monovalent HLA and antibody binding . . .	110
4.1	Schematic of the in-line microfluidic setup . . . . .	112
4.2	Microfluidic components in a single camera field of view with subsequent analytical processes . . . . .	113
4.3	Molecule compositions applied for the in-line diffusional sizing . . . . .	114
4.4	Label-free multidimensional characterisation . . . . .	116
4.5	Multidimensional characterisation of labelled molecules in a heterogeneous composition . . . . .	118
F.1	Scheme describing the details of the flow splitter . . . . .	131
F.2	Individual flow rate measurements for the individual devices . . . . .	132
F.3	Assignment of labelled molecule composition to SEC-chromatogram . . .	133
F.4	Representation of the electronic circuit used for multidimensional characterisation . . . . .	134
F.5	Image of microfluidic flow adapter . . . . .	134

---

## Abbreviations & Symbols

---

$\alpha$ B-c	$\alpha$ B-crystallin
$\alpha$ -syn	$\alpha$ -synuclein
aa	Amino acid
A $\beta$	Amyloid-beta
AD	Alzheimer's disease
APP	Amyloid precursor protein
ATP	Adenosine triphosphate
BSA	Bovine serum albumin
CSF	Cerebrospinal fluid
$\Delta G^\ominus$	Standard state free binding energy
$\Delta H^\ominus$	Standard binding enthalpy
$\Delta S^\ominus$	Standard binding entropy
DMSO	Dimethyl sulfoxide
DOL	Degree of labelling
$D_t$	Translational diffusion coefficient
DTT	Dithiothreitol
$\eta$	Viscosity
$E_A$	Activation energy
<i>E. coli</i>	<i>Escherichia coli</i>
EDTA	Ethylenediaminetetraacetic acid
ELISA	Enzyme-linked immunosorbent assay
FCS	Fetal calf serum

---

Fig.	Figure
h	Hour
HLA	Human leukocyte antigen
HLAab	Human leukocyte antigen antibodies
Hsp	Heat shock protein
IgG	Immunoglobulin G
IPA	Isopropyl alcohol
ITC	Isothermal titration calorimetry
kDa	Kilodalton
$K_D$	Dissociation constant
$K_{D,app}$	Apparent dissociation constant
$k_+$ , $k_n$ , $k_2$	rate constants for elongation, primary and secondary nucleation
$k_{on}$ , $k_{off}$	Dissociation rate constants
$\mu\text{M}$	Micromolar
$M$	Binding site concentration
mAB	Monoclonal antibody
MDS	Microfluidic diffusional sizing
MHC	Major histocompatibility complex
min	Minute
MW	Molecular weight
nm	Nanometer
nM	Nanomolar
NMR	Nuclear magnetic resonance spectroscopy
PAGE	Polyacrylamide gel electrophoresis
PBS	Phosphate-buffered saline
PDMS	Poly(dimethylsiloxane)
PGMEA	Propylene glycol methyl ether acetate
pM	Picomolar
RDS	Rate-determining step
$r_H$	Hydrodynamic radius
RNA	Ribonucleic acid
SDS	Sodium dodecyl sulfate
SEC	Size-exclusion chromatography

sHsp	Small heat shock protein
SPR	Surface Plasmon Resonance Spectroscopy
T	Temperature
t	Time
TEM	Transmission electron microscopy
ThT	Thioflavin T
WT	Wild type



# Chapter 1

---

## An introduction to protein interactions

---

### 1.1 Protein interactions

Proteins, the major structural material of animal tissues, are condensed polymers composed of amino acids and can adapt a wide range of morphologies, ranging from very extended fibrous structures to highly condensed spheres[205]. In order to shape a diverse set of structural elements and execute a multitude of functionalities, the structural flexibility and static/dynamic interactions are crucial attributes of living organisms. Therefore, it is not surprising that over 80% of proteins do not appear on their own but as part of complexes[22]. The assembly of proteins into macromolecules is a highly regulated process in organisms and often lethal if malfunctioning[62, 139]. The majority of protein interactions are transient, so called non-covalent interactions. In contrast, covalent bonds between molecules evolve from interactions involving electron sharing and lead to the formation of stable and discrete molecules or complexes. This is often found in protein modifications, such as ubiquitination, phosphorylation or glycosylation. Transient "non-covalent" interactions, on the other hand, with variations classified by their physical basis can be characterised as electrostatic forces involving point charges, dipole and induced dipole interactions, ion pairs and salt bridges, van der Waals and hydrophobic interactions or hydrogen bonds, resulting in a wide range of structurally discrete assemblies which in turn lead to different chemical and physical properties of

the formed complex. This interplay is not limit to intermolecular protein interactions, but also to intramolecular interactions where they enable correct protein folding.

### 1.1.1 Intramolecular interactions - the driving force of protein folding and misfolding

Following decades of research, the mechanism of protein folding is only partially understood. It is commonly accepted that protein folding is the stochastic search for accessible conformations which leads to the structure that is most thermodynamically or kinetically favoured[60, 64, 250]. The thermodynamic stability of a protein depends on the intrinsic properties of the amino acid sequence[3]. Usually, the most thermodynamically stable conformation under physiological conditions is the native state of proteins[64]. The stochastic search is often described as a trial and error process with

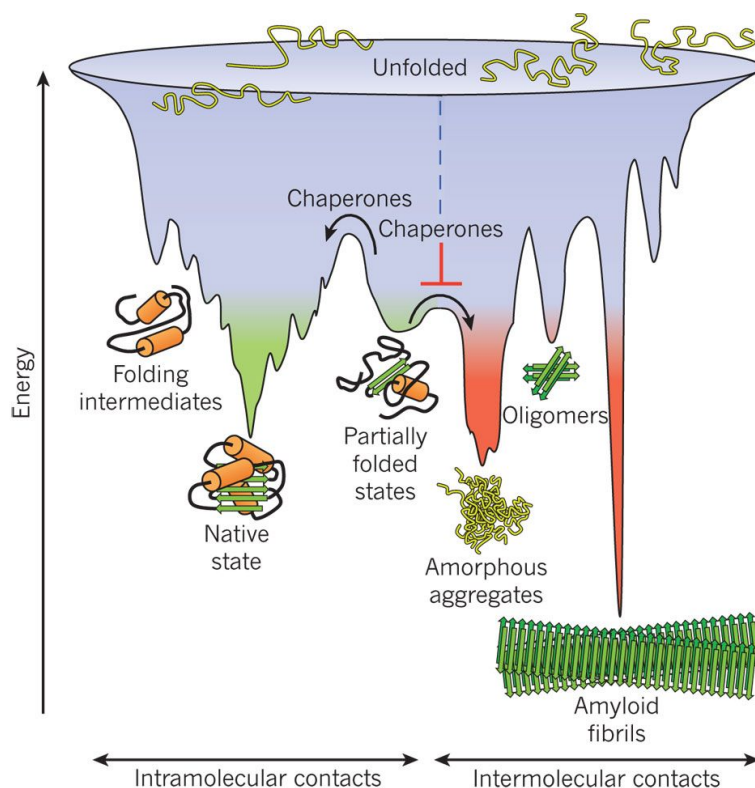


**Figure 1.1:** Funnel shaped free-energy landscape showing how intra- and intermolecular interactions lead to stable protein conformations which can be either the native protein structure or a wide range of aggregates. *In vivo* the process of protein folding, assembly and aggregation are controlled by chaperones, which can recover or prevent kinetically trapped conformations or deleterious intermolecular interactions. Reproduced with permission from ref. 92.

a downhill path through only a small number of possible conformations in a funnel-shaped potential energy surface (Fig. 1.1). Based on experimental results, a nucleation model of protein folding was proposed in which few amino acids form a nucleus followed by a step-wise restriction of the accessible conformations[75]. However, besides this postulated molten globule model different other folding mechanisms are possible *in vivo*. On the one hand, the co-translational protein folding exists with partial folding of the nascent-chain, whereas the complete protein is not yet fully synthesised by the ribosome[88]. On the other hand, many proteins are mainly folded after being released from the ribosome or even translocated into cellular compartments, such as the mitochondria or the endoplasmic reticulum[34, 93]. However, in the crowded cellular milieu, harsh conditions preventing efficient protein folding are represented. Despite the low concentration of proteins (6% plasma, 2% interstitial fluid, 30% cytosol) in the extracellular milieu, the conditions are even worse, where fluids are continuously subjected to shear stress and a more oxidising environment[212]. These harsh conditions can interfere with the formation of stabilising intramolecular interactions, such as disulfide bond or electrostatic bond formation, crucial for native secondary and tertiary structures. Incompletely folded proteins are prone to inappropriate interaction with other biomolecules. These interactions or the failure to fold correctly can lead to protein aggregation, amyloid synthesis or malfunction.

### 1.1.2 Intermolecular protein interactions

Intermolecular interactions all possess an electromagnetic nature. Nevertheless, they can be classified by the distance between the interacting moieties, according to the three ranges of interatomic separation[124]. The short range interactions are dominated by repulsion and electronic exchange, due to overlap of electron shells. In the intermediate range with the van der Waals minimum, those repulsive forces are in balance with attractive forces. Whereas, for the large distance interactions, essentially only attractive forces can be observed[124]. "Biological intermolecular interactions" are different from simple chemical reactions or physical changes of a system, as these include a complex set of different molecules in terms of type, size and properties under continuous non-equilibrated conditions[113]. The intermolecular interactions found in living organisms, thus, are dynamic yet tend to lead toward the equilibrium state or some local metastable low energy state[113]. More precisely, the cellular milieu represents a densely packed

body, filled with a diverse set of molecules, leading to constant collision of individual proteins, ions, membranes, nucleic acids and other biomolecules. Those interactions can vary in frequency, specificity and duration[152]. The variation of such intermolecular interactions is responsible on the one hand for the appearance of stable assemblies and on the other hand for short-lived interactions with no or little biological relevance promoted by intracellular crowding[152]. However, even interactions of very short duration can be of crucial functional importance, such as those found in cell signalling[181, 204]. Therefore, intermolecular interactions play a major role in all enzymatic processes, protein assembly and molecule recognition. Thus, formation of tertiary and quaternary protein structures is driven by intermolecular interactions. Those interactions lead usually to a stabilisation of the complex and increase the rigidity of the individual molecules[152].

### **1.1.2.1 Functional protein assembly**

Functional protein assembly and even protein polymerisation are crucial, highly regulated processes in living organisms, ranging from the formation of ribosomes, composed of 79-80 proteins and four RNAs in eukaryotes or the  $\sim 120$  MDa nuclear pore complex containing about 1000 protein subunits to continuously polymerising and depolymerising cytoskeleton protein complexes of actin and tubulin[55, 144]. The advantages of extended quaternary protein structures are the accumulation of different functions in close proximity and therefore being able to increase the efficiency and speed of biological processes. In this manner, a substrate can be bound/detected and get directly facilitated to an active site to initiate a wide range of enzymatic reactions. Furthermore, functional protein aggregation can be found e.g. in bacteria where it leads to the formation of extracellular biofilms. However, functional protein aggregation is highly regulated and fibril self-replication is prevented by several mechanisms such as controlling local monomer concentration and low elongation rates[2]. An increasing number of aggregated or even amyloid forms of proteins have been found in living organisms where they fulfil functional purposes[174]. Those functional amyloids work as structural components as seen for bacterial biofilms, storage units as found for peptide hormones in eukaryotes or as "immunological" barrier and signaling mechanism known for HET-s/S prion systems in fungi[174]. The crucial difference between functional and disease-related amyloids or other polymers is, that the macromolecules are not toxic,

coming from their distinct structure which is diverging from their disease-related counterparts. The aggregation/polymerisation of such biomolecules is highly regulated and depending on the homeostasis of different proteins together with the control of the physical-chemical environment and that there is no off-pathway being responsible for toxic oligomer formation[174]. The advantages of protein assembly is not limited to morphological and enzymatic purposes only, but are also energetically economical. It is simpler to assemble a large complex from multiple copies of smaller subunits rather than producing a much larger protein[51]. The reduction of genetic code and better quality control of proteins would be one advantage[152]. Another advantage can be a polydisperse distribution of large complexes or oligomeric proteins inside the cell providing regulatory abilities and extending the functionality of the subunits, as has been previously shown for small heat-shock proteins (sHsps)[113, 216].

### 1.1.2.2 Protein aggregation and related diseases

Currently, ~36 proteins have been identified in the context of mammalian amyloid diseases, yet *in vitro* experiments indicate that the ability to form ordered amyloid structures is not a rare phenomenon associated with a small number of diseases[61, 62, 211]. This has led to the hypothesis that physiological mechanisms have been evolved in nature as a protection against amyloid formation. The microscopic phenotype of amyloid related diseases is associated with the deposition of such aggregates in a variety of organs and tissues, e.g. brain, central nervous system (CNS), heart, liver, spleen, skeletal tissues and joints[244]. All of the disease-related amyloid deposits are found extracellular and just a few disease-related intracellular inclusions have been found to exhibit partial amyloid-like characteristics[211]. Despite the diversity in the characteristics of the soluble forms of the proteins and the progression of the related diseases, the structural, physical and chemical properties of the aggregates are similar. The amyloid external morphology (long, unbranched formation, typically 6-12 nm in diameter and typically consists of 2-6 protofilaments that are often twisted around each other to form supercoiled rope like structures) and internal structure (beta strands running perpendicular to the protofilament axis) are commonly found, contributing to a characteristic ‘cross- $\beta$ ’ X-ray fibre diffraction pattern and a specific optical behaviour upon bind of certain dyes e.g. thioflavin T (ThT) or Congo red[217]. Fibril formation is a nucleated polymerisation reaction presenting a sigmoidal-like growth curve, describing the conversion from

soluble proteins into ordered amyloid structures[130]. This aggregation phenomena is divided into several microscopic processes (Fig. 1.2). Primary nucleation describes the process of spontaneous nucleation of free monomers, whereas fibril elongation is specified as the addition of monomers to the fibrillar ends. Furthermore, several secondary processes are also involved in the aggregation process. One such secondary process is fragmentation, which doubles the number of growing fibril ends following each breakage[45]. Another secondary process is secondary nucleation, which is characterised as a monomer nucleation process with the fibril surface acting as a template for aggregation also known as prion-like behaviour[33, 130]. Such nucleation processes play a significant role in disease initiation and progression as they increase the amount of soluble oligomers, shown to be the primary toxic species in neurodegenerative diseases[90, 135, 147]. Whereas fibrillar aggregates or their deposits may be inert or even protective[66, 248]. It is known that the amyloid burden in neurodegenerative diseases, such as Alzheimer's, the most common neurodegenerative disease, can be quite low and its existence is poorly correlated with the local extent of neuronal death and synaptic loss, as well as with cognitive impairments[36, 84, 147, 232]. Suspected reasons for oligomer toxicity are e.g. disruption of membrane homeostasis caused by amphipathic oligomer insertion, complex

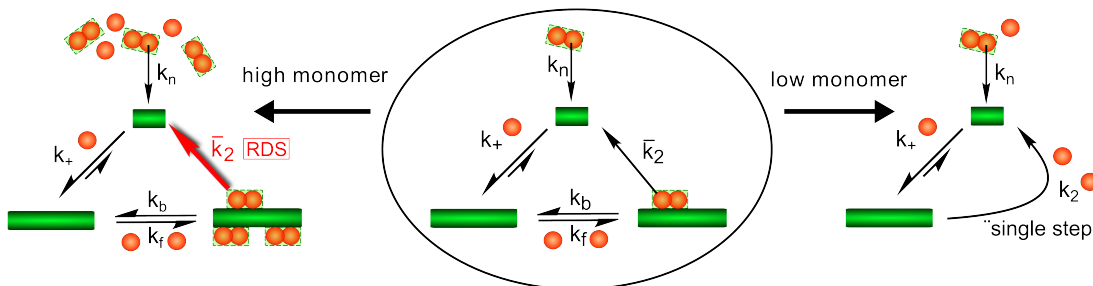


**Figure 1.2:** The Aggregation of proteins is divided into several mechanisms. The  $A\beta_{40}$  and  $A\beta_{42}$ -aggregation can be described by primary nucleation, fibril elongation and secondary nucleation, in which the primary nucleation describes the spontaneous nucleation of free monomers (orange spheres), elongation the addition of free monomers to the fibril ends (green stick) and secondary nucleation the nucleation process of free monomers on the fibril surface. The impact of each single mechanism depends on the  $A\beta$ -monomer concentration. Analysed, measured and simulated data indicate that the second step of secondary nucleation is the rate-determining step (RDS) under high monomer concentration, whereas under low monomer conditions, effectively only single-step secondary nucleation can be observed. Both conditions are relevant for  $A\beta_{40}$ , but for  $A\beta_{42}$ , only the low monomer behaviour could be observed[158].

formation with ions, induction of Fenton reactions and disruption of the electron transport chain in the mitochondria or activated apoptosis[198]. Amyloid related diseases such as Alzheimer's, Parkinson's and type 2 diabetes are strongly age-associated disorders that has emerged as the most costly, in terms of health care and social disruption with an increasing life expectancy in industrial and developed countries[177, 179]. Currently >26 million people are affected by Alzheimer's and it is predicted that by 2050 the amount will increase to ~106 million people[30]. Therefore, there is a high demand for therapies leading to the development of antibody and small molecule therapeutics with some being in clinical trial, yet without any success.

### 1.1.2.3 Molecular chaperones as counterparts to protein aggregation

Increasing evidence indicates that amyloid structures have a smaller free energy level than the proteins functional "native" state, which is separated by a high activation barrier from the metastable states[20]. *In vivo* mice studies have shown that chaperone deficiency or knock-out can lead to lethality[103], which underlines the necessity of chaperones for accurate folding in the presence of destabilising mutations and harsh environmental conditions. The aggregation process *in vivo* occurs in the presence of other proteins, membranes, metabolites and a wide range of more biomolecules, each of which may affect both its rate and equilibrium with free protein[52, 81]. Molecular chaperones are defined as an essential and ubiquitous group of proteins with a wide range of functionalities, which are mainly responsible for the stabilisation of unfolded proteins and facilitate their native folding, control protein assembly, cellular transport of proteins into subcellular compartments and guiding proteins to degradation[91]. The term 'molecular chaperone' was first used by Ron Laskey in 1978[138] and the concept of its general function was suggested by Hugh Pelham in 1986[178]. Since these pioneering works, many different classes of structurally unrelated chaperones have been identified to exist in the cell. Most of the molecular chaperones have been found to be upregulated under stress conditions, in which the concentration of aggregation-prone folding intermediates increases, and are therefore known as heat-shock proteins (Hsps). However, it should be noted that not all chaperones are Hsps and not all Hsps are chaperones. Chaperones are usually classified according to their molecular weight or their sequence/structural homology. Their interaction partners are typically identified by their hydrophobic amino acid side chains exposed by non-native proteins[92]. Chaperones are important for protein

quality control and essential for the maintenance of protein homeostasis. The ability to buffer mutations which disrupt the stable fold of a protein is crucial for the evolution of new protein functions and phenotypic traits[92]. Malfunctioning chaperones or their lack of function (chaperonopathy) has thus been implicated in several diseases such as the MitCHAP-60 disease[148], interstitial lung diseases, familial British and Danish dementia[202] and their involvement in others may be underestimated. Whereas many intracellular chaperones have been identified, only seven molecules are known to populate the extracellular environment: these are clusterin, haptoglobin,  $\alpha_2$ -macroglobulin, apolipoprotein E, serum amyloid P component,  $\alpha_E$ -fibrinogen and casein[114]. Intracellular chaperones such as Hsp70 and Hsp90 have been observed extracellular as well, but whether their existence is functional or whether they are released by necrosis or apoptosis is still unclear. The extracellular concentration of these primarily intracellular chaperones is very low (ng/ml) and the required ATP-concentration is a thousand times lower than inside the cell[72, 259, 260]. Currently, several other extracellular chaperones (EC) or chaperone-domains are being investigated due to their potential diverse function compared to intracellular chaperones. A better understanding of their basic functions can give necessary information in the context of disease evolution and provide starting points for future therapies.

## 1.2 Microfluidic applications for the investigation of protein interactions under native conditions

### 1.2.1 Diffusional sizing of heterogeneous protein solutions

Generally, microfluidics stand for fluid control in channels (often consisting of polydimethylsiloxane, polyimide, polycarbonate, glass or silicon) at the scale of microns. This leads to the reduction of gravity effects and inertial forces. On the other hand, viscosity forces come to the fore. In the case of a low Reynolds number of the fluid, a laminar flow behaviour occurs and the mixing between parallel streams of fluids happens only by translational diffusion. This process can be described by the Einstein-Smoluchowski equation:

$$\langle x^2 \rangle = 2D_t t \quad (1.1)$$

where the average mean square displacement  $\langle x^2 \rangle$  of a molecule in three dimensions is proportional to the time  $t$  and the translational diffusion coefficient  $D_t$ , which itself is inversely proportional to the hydrodynamic radius  $r_H$ .

In order to characterise the size distribution of a wide range of molecular species under native conditions, I have used a previous designed microfluidic system that allows molecular diffusion to be monitored directly in solution (Figure 1.3)[9, 164]. Within this microfluidic device, a beam of analyte is generated through flow focussing in the centre of a micron-sized channel between two streams of buffer. While advecting along the longitudinal direction  $y$ , the biomolecules diffuse laterally along the perpendicular directions  $x$  and  $z$ . At low Reynolds numbers, convective mixing is generated, leading to highly reproducible mass transport properties. The diffusion profiles, giving the mass-concentration of analyte molecules as a function of  $x$  at different times and at different positions along the channel, are then recorded directly within the device by fluorescence microscopy and fitted by model simulations based on advection-diffusion equations to provide the distribution of diffusivities, and therefore of the sizes, of the analytes[9, 164]. The flow velocity in the channel is set to have a dominance of convective flow along the longitudinal direction (Péclet number,  $P_{ex} \gg 1$ ) and of diffusive motion in the vertical direction (Péclet number,  $P_{ez} \ll 1$ ). The sample concentration is therefore uniform along the height of the channel. By contrast, it exhibits a spatial dependence along the horizontal direction, where the  $P_{ey} > 1$ . The diffusional sizing technique applied in this work monitors this spatial propagation along the horizontal direction at different diffusion times and different diffusion positions along the channel. The relation of the diffusion coefficient and the hydrodynamic radius is well described by the Stokes-Einstein equation:

$$r_H = \frac{k_B T}{6\pi\eta D_t} \quad (1.2)$$

where  $k_B$  is the Boltzmann constant and  $\eta$  the viscosity of the fluid at a given temperature  $T$ . This implicates that besides the diffusion profiles measured by the diffusion-based microfluidic device, the molecular size distribution can be determined based on accurate numerical calculations and least square fittings of simulated and measured diffusion profiles. For the simulation of the experimental fluorescence profiles, a combination of basis functions were used[164]

$$|D - \sum_{i=1}^n c_i B^i|^2 - \alpha \sum_{i=1}^n c_i \ln(c_i) \quad (1.3)$$

where  $D$  is the measured profile and  $B^i$  represents a kernel function for different molecules  $i$  at given measurement points. Their coefficients  $c_i$  regulate the amplitudes of each kernel and are fixed between 0 and 1 to give the amount of each molecule species and  $\alpha$  can be used as a control of the allowed maximum entropy term. The Kernel function is based on the Einstein-Smoluchowski and Langevin equation[164]

$$\nabla_{k+1} = \nabla_k + \sqrt{2D_t dt} \cdot \text{Random}\{-1, +1\} + v(x_k)dt \quad (1.4)$$

which calculates the position  $\nabla$  of a molecule at a given time point  $k$  for all three dimensions in respect to the channel's velocity profile  $v(x_k)dt$ , which is taken into account only in flow direction  $x$ . The advantage of using fluorescence-labels, such as the fusion-protein GFP or chemically attached Alexa or Atto dyes, is the ability to target and follow only specific proteins and their behaviour in heterogeneous solutions. However, intrinsic fluorescence generated by the aromatic amino acids tryptophan, tyrosin and phenylalanin can be exploited but only works for homogeneous samples.

As seen above, bound molecules can be distinguished from their unbound counterparts by their altered hydrodynamic radius and diffusion. The ability of the diffusion-based microfluidic device to handle polydisperse and heterogeneous mixtures and species, ranging from small molecules to large biological polymers, often hundreds of nanometers in diameter, makes this method ideal for high-throughput application for binding studies with protein aggregates[203]. The variably sized molecules are characterised by a significantly different diffusion coefficient. The interaction or non-interaction behaviour results in a difference in the intensity profiles by using fluorescence-label. Thus, a bimodal size distribution is expected under interacting conditions, where bound and unbound fractions are quantifiable by their given coefficients.

Based on this microfluidic approach, commercial applications have evolved such as the Fluidity One and the Fluidity One-W from Fluidic Analytics Ltd. based in Cambridge, UK. However, both commercial machines are based on a parallel stream with sample coming from one side and an auxiliary flow from the other (see Fig. 2.16A). At the end of the device, both streams are split and target quantity is acquired in a diffused and undiffused chamber. Therefore, this commercial system can only provide an average radius of the target molecules rather than a size distribution.

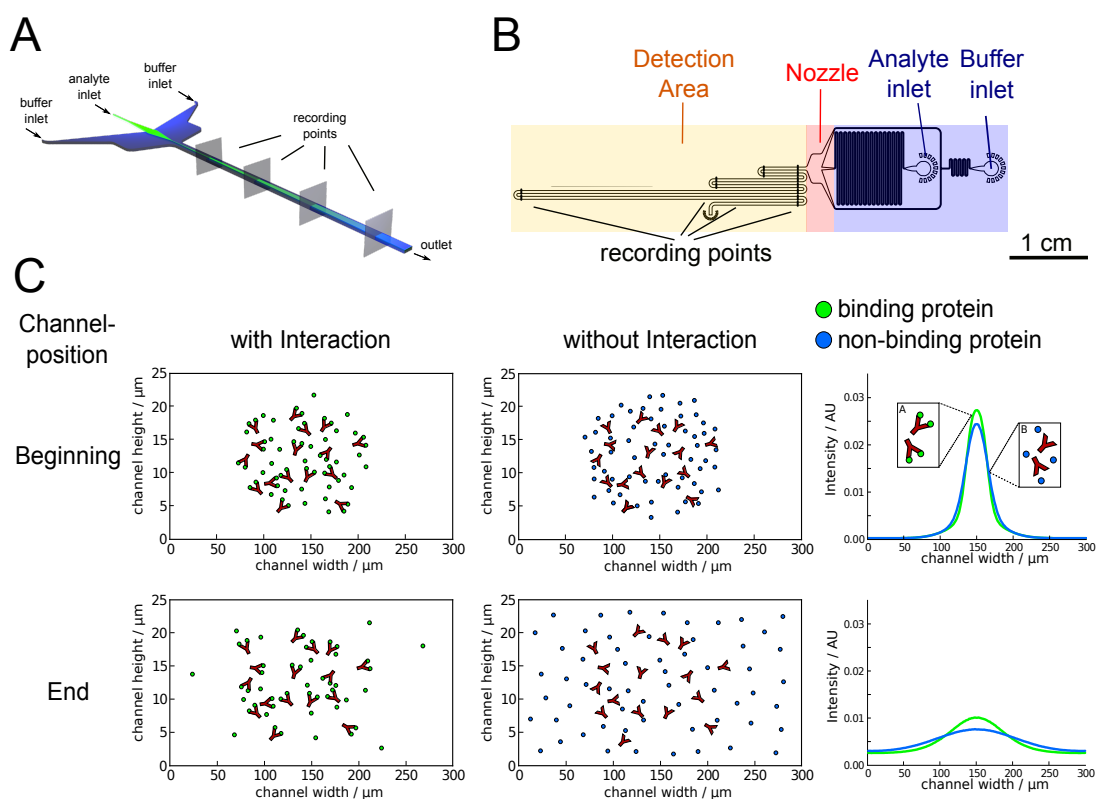


**Figure 1.3:** Description of the microfluidic platform used for binding measurements. (A-B) Scheme of the device and relevant components: the beam of the analyte sample is focused between two streams of the buffer in the nozzle area of the microfluidic device. The diffusion coefficient of the molecules is measured by recording the diffusion profiles at different positions along the channel length. (C) Representative scheme of the diffusion behaviour of a protein in the presence and absence of interacting antibodies; proteins interacting with antibodies (indicated in green colour) remain localised in the middle of the channel; in contrast, proteins, which do not interact with antibodies (indicated in blue colour), diffuse rapidly to the edges of the channel. This behaviour results in a difference in the fluorescence intensity profiles of the interacting (green profiles) and the non-interacting (blue profiles) molecules.

The investigation of protein-protein interactions is challenging as molecules can e.g. interfere unspecifically with surfaces or following individual and rare binding events in heterogeneous mixtures is hard to achieve. The clinical demand for quick and sufficient interaction studies is increasing for, e.g. determining the risk of alloimmunisation after transplantation[134], drug screening[169] and disease recognition[101]. Different methods have been established over the years to characterise the molecular (non-covalent) interactions between biomolecules, which are commonly described in terms of the dissociation constant ( $K_D$ ), the association and dissociation rate constants ( $k_{on}$  and  $k_{off}$ ), the standard binding enthalpy ( $\Delta H^\ominus$ ), the standard binding entropy ( $\Delta S^\ominus$ ) and the

standard state free energy ( $\Delta G^\ominus$ ). Techniques providing an experimental set-up for simultaneous measurements of all parameters are rare and often non-applicable for a wide variety of proteins. Such conventional approaches include calorimetry[185, 231], capillary electrophoresis[168, 199], equilibrium dialysis[15, 109], ultrafiltration[27, 254], affinity chromatography[246], nuclear magnetic resonance spectroscopy (NMR)[76, 141], mass spectrometry[40, 71, 187], fluorescence-/Raman-spectroscopy[140, 256], circular dichroism[82], bilayer interferometry[171], sedimentation assay[207] and surface plasmon resonance (SPR)[106]. All of these techniques have their advantages and disadvantages and suffer from a series of limitations. For instance, some approaches require high sample concentration (e.g. calorimetry and mass spectrometry)[115, 167], other techniques require special probes (e.g. isotopes, protein-tags or fluorescence labelling) while other methods often show non-specific binding and low signal to noise ratio (e.g. NMR, capillary electrophoresis, SPR)[18, 77, 218]. In particular, the accurate quantification of binding parameters is severely impaired by approaches which require surface immobilisation, such as SPR, where possible unspecific interactions with the chip surface often result in an overestimation of the binding affinity[171]. The usage of a diffusion-based microfluidic device (Fig. 1.3 A, B) for interaction measurements enables binding incidences to be examined directly in the condensed phase resembling physiological conditions. Compared to the conventional approaches described above, this method is tolerant to highly polydisperse and heterogeneous solutions, has no limitation in terms of size of protein/complexes and offers a series of advantages including demand for limited amount of sample and the absence of surface interactions. Furthermore, requiring small amounts of sample is often a key consideration when analysing clinical samples from a human source or proteins such as amyloid  $\beta$  and  $\alpha$ -synuclein, which are challenging to synthesise and therefore expensive to acquire.

One aim of my Ph.D. was to show that the diffusion-based microfluidic device is an accurate and sensitive technique for binding parameter quantification and thermodynamic measurements and represents an important step in the characterisation of chaperone function with respect to aggregation inhibition and binding. Furthermore, I wanted to show the practical and potential functionalities of the diffusional sizing approach for unpurified clinical samples on the one hand and on the other hand to expand its capabilities to characterise the biophysical properties of complex solutions in an instant multidimensional way.

## Chapter 2

---

# The binding of chaperones and therapeutic antibodies to amyloid fibrils

---

### List of publications

- **T Scheidt**, JA Carozza, CC Kolbe, FA Aprile, O Tkachenko, MMJ Bellaiche, G Meisl, Q Peter, TW Herling, S Ness, JLP Benesch, M Vendruscolo, CM Dobson, P Arosio and TPJ Knowles, The binding of the small heat-shock protein  $\alpha$ B-crystallin to fibrils of  $\alpha$ -synuclein is driven by entropic forces, in preparation.
- **T Scheidt**, U Łapińska, JR Kumita, DR Whiten, D Klenerman, MR Wilson, SIA Cohen, S Linse, M Vendruscolo, CM Dobson, TPJ Knowles, P Arosio, Secondary nucleation and elongation occur at different sites on Alzheimer's amyloid-beta aggregates, *Sci. Adv.*, **5**, 4, eaau3112 (2019).
- **T Scheidt**, TCT Michaels, T Müller, U Łapińska, Q Peter, M Andreassen, S Linse, M Vendruscolo, CM Dobson, P Arosio, TPJ Knowles, A Saric, Thermodynamic characterisation of the binding of a molecular chaperone to amyloid beta fibrils by microfluidic diffusion measurements, in preparation.
- S Linse, **T Scheidt**, K Bernfur, M Vendruscolo, CM Dobson, SIA Cohen, E Siliekis, M Lundquist, F Qian, T O'Malley, T Bussiere, PH Weinreb, CK Xu,

G Meisl, S Devenish, TPJ Knowles, O Hansson, Kinetic fingerprints differentiate anti-A $\beta$  therapies, in preparation.

## 2.1 Introduction: Chaperones - natural inhibitors of protein aggregation

Molecular chaperones are crucial components of the cellular proteostasis network and characteristically overexpressed during cell stress[69, 70, 92, 94]. Their roles involve the suppression of aberrant processes, including misfolding and aggregation of proteins, within the context of the complex flux of protein production and degradation. In addition to guiding nascent proteins towards their native structures following their biosynthesis by ribosomes, chaperones are increasingly recognised to also inhibit key steps in the aberrant conversion of normally soluble proteins into amyloid fibrils, protein aggregates that are associated with a wide range of neurodegenerative diseases[8, 13, 63, 203]. The overall process that leads to the formation of amyloid fibrils consists of a series of microscopic events, including primary and secondary nucleation and fibril elongation and fragmentation[44]. Recent analysis of the aggregation kinetics of several proteins has revealed that molecular chaperones can inhibit the process of amyloid formation through a variety of different mechanisms[10]. In some cases, molecular chaperones have been found to suppress a single specific microscopic step in the aggregation process. In other cases, they have been shown to affect more than one type of aggregation event[8, 41, 150, 203]. The modulation of the different molecular steps of protein aggregation is mediated by the binding of chaperones to misfolded protein monomers and various aggregated species[41, 207, 235]. In order to gain a comprehensive understanding of such inhibition processes, it is therefore crucial to elucidate the thermodynamic and kinetic determinants of chaperones binding to different species populated during amyloid formation. A large number of observations, including genetic and epidemiological studies, indicate that the aberrant aggregation of normally soluble peptides and proteins into insoluble amyloid fibrils is associated with the onset and the progression of a wide range of neurodegenerative disorders[39, 68, 89, 90, 125, 129]. Biophysical studies are currently revealing important molecular details underlying the formation of the fibrillar aggregates from initially supersaturated monomer solutions[74, 130, 221]. In addition, secondary nucleation in particular increases the rate of formation of low molecular weight

oligomers that accompany the formation of mature fibrils and are currently thought to represent the most toxic species produced during such processes[21, 41, 42, 90, 135]. Inhibition of such key aggregation processes therefore represents a potentially attractive therapeutic strategy to combat amyloid associated diseases[10].

Understanding the underlying molecular determinants of these different mechanistic processes is therefore of fundamental importance for the design of strategies that target specifically the reactions responsible for the formation of the most highly toxic species. Indeed, in the context of developing drugs to combat protein aggregation disorders, targeted interventions rather than nonspecific suppression of the aggregation process, are required[10]. The inhibition of different microscopic steps can lead to similar effects on the overall formation of amyloid fibrils, yet can have dramatic differences in the generation of toxic oligomeric species[5, 10, 85]. An intervention strategy targeting the specific microscopic steps that represent the major sources of the formation of such oligomers is, therefore, likely to be an optimal approach to suppress the most detrimental effects of protein aggregation.

By investigating a series of molecular chaperones that can inhibit selectively one or more specific steps in the aggregation process of different amyloidogenic proteins, I have shown that these molecules can influence aggregation processes through a variety of different microscopic events and have revealed the complex mechanism evolved by nature in order to maintain protein homeostasis[4, 8, 150]. With such information I can exploit molecular chaperones to perturb, in a selective way, a given aggregation network and thereby investigate the effects of individual steps in the reaction on the formation of key intermediate species.

### 2.1.1 The small heat shock protein $\alpha$ B-crystallin

A prevalent group of molecular chaperones that inhibit amyloid formation are the small heat-shock proteins (sHsps), including the vertebrate  $\alpha$ B-crystallin ( $\alpha$ B-c). The structure of  $\alpha$ B-c is a conserved  $\alpha$ -crystallin domain with a  $\beta$ -sheet structure, flanked by a hydrophobic N-terminal region and a polar C-terminal tail, both structurally flexible and heterogeneous[102]. Similar to other sHsps in solution,  $\alpha$ B-c exists in a polydisperse oligomeric state characterised by dynamic subunit exchange leading to the formation of oligomers with 10-50 subunits and molecular weights from 300 to 1000 kDa

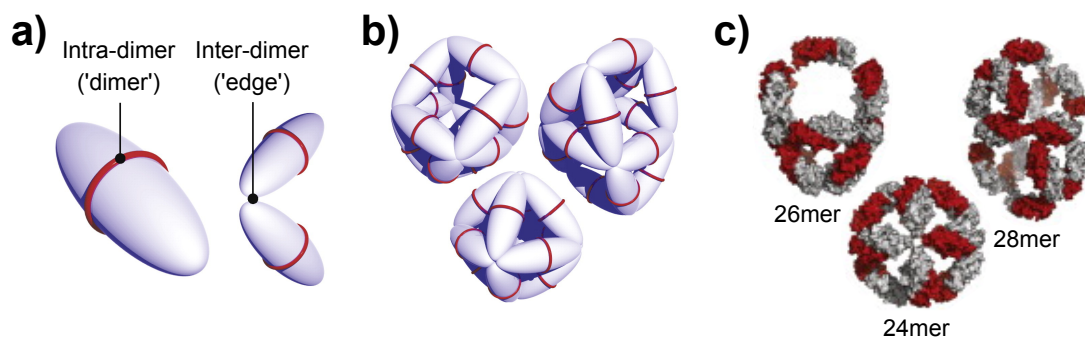


**Figure 2.1:** Oligomeric assembly of  $\alpha$ B-crystallin ( $\alpha$ B-c). a)  $\alpha$ B-c units interact *via* intra-dimer interfaces and assemble through inter-dimer interactions to higher order oligomers as commonly seen for sHsps. Dimeric subunits are shown here as ellipsoids. b) and c) Most dominant even-numbered oligomeric species are shown with different binding modes of polyhedral architecture as schematic (b) and at pseudo-atomic level (c). Reproduced with permission from ref. 104 and 14.

(Fig. 2.1)[104, 112].  $\alpha$ B-c has been shown to inhibit the overall amyloid formation process of  $\alpha$ -synuclein ( $\alpha$ -syn), a protein whose aggregation is closely associated with the onset and progression of Parkinson's disease[48]. The mechanism of inhibition has been shown to originate from interactions of the chaperone with aggregated forms of  $\alpha$ -syn, ranging from oligomers to mature amyloid fibrils, rather than with  $\alpha$ -syn monomers[192, 193]. In particular, it has been demonstrated that  $\alpha$ B-c binds to  $\alpha$ -syn fibrils and inhibits their elongation, thus suppressing the toxicity associated with  $\alpha$ -syn aggregation in cells[175, 235].

The mechanistic importance of the interactions of  $\alpha$ B-c with protein aggregates raises the key question of how such chaperones recognise misfolded and aggregated proteins amongst the diverse ensemble of native states. Elucidating the binding interactions between these protein species poses fundamental challenges that originate from the heterogeneity and dynamic nature of the system explored. Both the chaperone and aggregate populations are heterogeneous, and the large difference in size between relatively small chaperones and high molecular weight client protein aggregates make interactions between them difficult to access with conventional biophysical techniques designed to probe interactions between individual biomolecules under bulk conditions[105, 251]. I have addressed these limitations using a microfluidic platform to characterise the binding[9]. By exploiting the different diffusion coefficients of bound and unbound chaperones, I have shown that it is possible to quantify the thermodynamics and the kinetics of binding on the time scale of seconds, where the spatial variation in concentration along the device

has a negligible effect on the kinetics due to the short measurement times[9, 257]. In this thesis, I apply this approach to identify the intermolecular interactions underlying the recognition of  $\alpha$ -syn amyloid fibrils by  $\alpha$ B-c and characterise the energetic tradeoff during this binding process in a quantitative manner.

### 2.1.2 The Brichos chaperone domain

The Brichos domain was identified by Stefan D. Knight in 2013 as the first example of a chaperone-like domain with specificity for beta prone regions, amino acid sequences which are likely to form beta-sheet structures found in amyloids. The  $\sim 100$ aa-Brichos domain has been found in more than 300 proteins and more than 30 human genes[97, 128, 202]. Some of these proteins are associated with degenerative and proliferative diseases. Mutation in the Brichos domain triggers protein aggregation (e.g. in familial dementia and interstitial lung diseases) or cancer suppression (e.g. chondrosarcoma) [202]. The ability of the Brichos domain to interact with peptides which have a high beta-sheet propensity, its role as a trigger for protein aggregation of Bri23 (formerly proBri2) and lung surfactant protein C (formerly proSP-C), their expression together with APP and its further secretion into the extracellular space together with  $A\beta$ [153] makes it an ideal candidate in the context of Alzheimer's research, especially in combination with  $A\beta$  aggregation. It has been observed that the introduction of the Brichos domain blocks the aggregation of  $A\beta_{40}$ [127, 180, 242] and delays the aggregation of  $A\beta(M1-42)$ [99, 242] in a concentration dependent manner both *in vivo* and *in vitro*. An overexpression of Bri2, the secreted Brichos domain part of proBri2, in AD mice[126, 127, 156] and *Drosophila melanogaster*[99] models showed reduced AD pathology. This effect was suggested to be correlated to higher levels of unprocessed Bri2 in the hippocampus[56] and cerebrospinal fluid of AD patient which led to an introduction of Bri2 as a new AD-biomarker[162]. According to biophysical and chemical kinetic analysis, in the case of the  $A\beta(M1-42)$  peptide, the Brichos domain of proSP-C (Fig. 2.2 a) inhibits its aggregation by suppressing specifically the secondary nucleation reaction (Fig. 2.2 b-d) and by that the seeding effect is almost completely killed[41]. The specific inhibition of secondary nucleation suppresses effectively the amount of toxic oligomers, whose generation is mainly catalysed on the fibril surface. Brichos binding to the monomeric form of  $A\beta$  is not supported by the data, as there is no indication for inhibition of primary nucleation and inhibition of secondary nucleation is present far

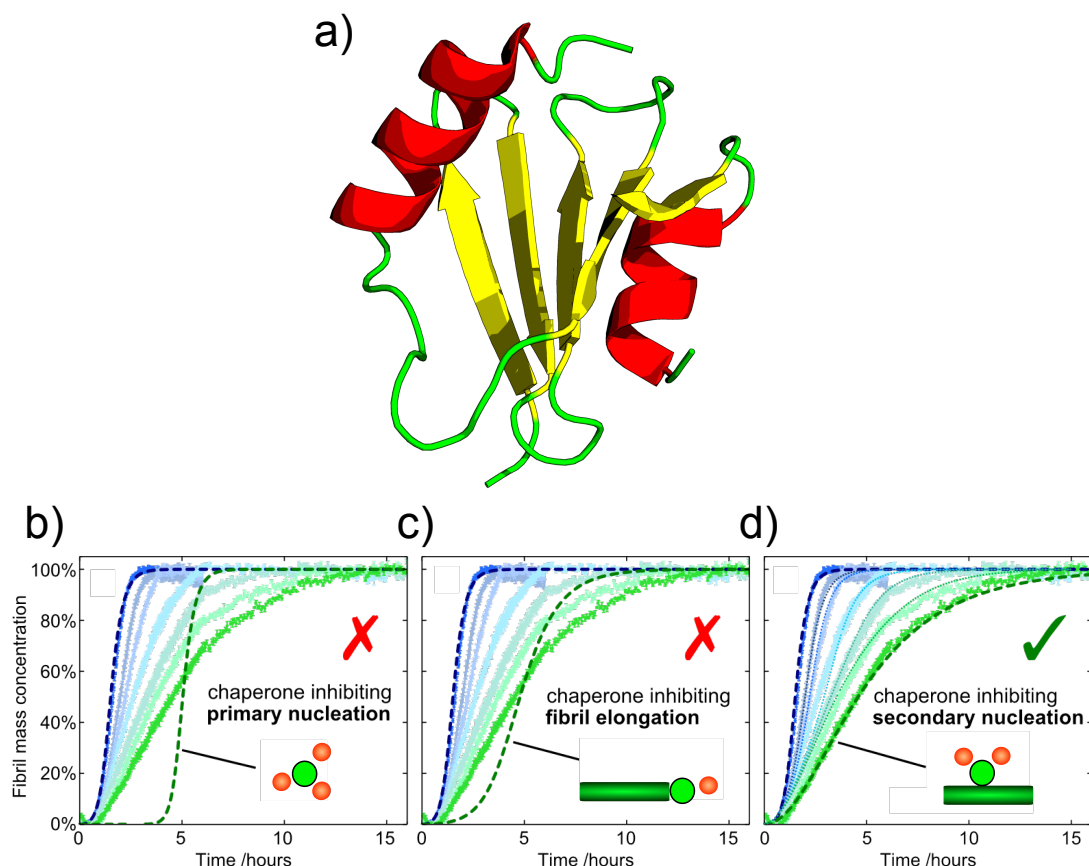


**Figure 2.2:** (a) The Brichos domain of SP-C shows a five stranded beta-sheet with alpha-helices on each side in the x-ray structure. The  $\beta$ -sheet faces are a likely binding site surface with many conserved hydrophobic residues[241]. (B-D) Previous studies by *Cohen et al.* could show that the Brichos domain specifically inhibits the secondary nucleation processes involved in  $A\beta(M1-42)$  aggregation. The data of ref. 41 were reproduced with permission and show the aggregation of  $A\beta(M1-42)$  (monomers shown as orange spheres, fibrils as green sticks) from left to right in the absence of Brichos and with 10%, 15%, 22%, 35%, 50% and 75%  $A\beta(M1-42)$  monomer equivalents of unlabelled Brichos (shown as green spheres). Three different scenarios of inhibition mechanisms were simulated and compared to the plotted data. The simulated inhibition of primary nucleation (b) and fibril elongation (c) showed no match with the data, whereas the model for inhibition of secondary nucleation indicates the best fit (d).

below of equimolar amounts with the chaperone. A binding of the Brichos domain along the fibril surface can be expected.

### 2.1.3 The extracellular chaperone clusterin

Clusterin (also known as apolipoprotein J (ApoJ), sulfated glycoprotein 2 and SP-40) was the first identified secreted protein and is an abundant extracellular chaperone[110].

The chaperone consists of an  $\alpha$ - and a  $\beta$ -subunit connected by two disulfide bonds and contains highly sulfated carbohydrates (23-30%). Structural information are still missing, but prediction of structural elements by sequence analysis show three amphipathic  $\alpha$ -helices[59] and two coiled-coil helices[145]. It has been suggested that the  $\alpha$ -helices form a molten globule-like binding pocket for a variety of ligands[12]. Due to its interaction with structurally diverse molecules, the exact biological role of clusterin is still controversial. Clusterin is classified as an ATP-independent holdase-type chaperone with similarities to sHsps and has the tendency to form oligomers[114]. Alternative hypothesised biological functions are a role in lipid transport[59], sperm maturation[100], complement regulation[117], membrane recycling[121] and apoptosis[35]. However, the fact that clusterin was found to be upregulated in AD tissues supports its regulatory role in protein aggregation as molecular chaperone. In general, clusterin is active in the presence of amorphous aggregates and inhibits the formation of amyloid fibrils from a large variety of proteins including PrP106-126, apolipoprotein C-II, disease-associated variants of lysozyme,  $\alpha$ -synuclein, calcitonin,  $\kappa$ -casein, SH3 and CC $\beta_W$  *in vivo* and *in vitro*. Furthermore, the uptake of clusterin-complexes with A $\beta$  by neural epithelial cells by megalin (LRP2)-mediated endocytosis and subsequent degradation could be observed *in vivo*[86]. It is suggested that the megalin-receptor binds specifically to the clusterin-A $\beta$  complex and initiates an internalisation where A $\beta$  is targeted for lysosomal degradation. Thus, not only targeting of aggregates, but also the aggregation process of A $\beta$  itself is influenced by clusterin.

Clusterin is an important member of a family of largely extracellular chaperones, which have been observed to interact with different aggregation states of amyloidogenic proteins, including oligomers, pre-fibrillar species and mature fibrils, and hence affect a wide range of events leading to the formation of amyloid fibrils[19, 133, 166, 253, 258, 259]. As part of my PhD, I examined the combined ability of clusterin and another type of molecular chaperone, a Brichos domain, to influence specific microscopic events in the aggregation process, and analyse the cooperative nature of the inhibition process, thus extracting information about the location of specific sites on the fibrils that are involved with secondary nucleation and with fibril elongation.

### 2.1.4 Antibody and small molecule strategies as potential therapeutics targeting A $\beta$ (42) aggregation

The significance of A $\beta$ (42) aggregation as major driving force for AD is seen critically, yet the formation of A $\beta$ (42) plaques remains the main target for various therapeutics in clinical trials or prior studies. However, evidence suggest that aggregation inhibitors derived without determining their underlying mechanism of action may not decrease the neurotoxicity of A $\beta$  aggregates. Even though the small A $\beta$  peptide aggregates to form macromolecular amyloid fibrils, the oligomers produced during the process of fibril formation have been uncovered as the dominant toxic species and have been shown to play a key role in the death of neurons[232]. The demand for Alzheimer's diagnostics and treatment is increasing with a rising trend of medical cases, going together with enormous suffering of affected individuals and resulting in expensive supervisions. Current treatment approaches focus on immunotherapy or the use of small molecules, which has been tested with varying success rates[28, 176, 201, 206]. The main focus of most therapies is the general delay of A $\beta$  assembly by inhibiting specific aggregation processes[87]. More specifically, along with the recruitment of microglia and subsequent cellular phagocytosis[28, 206], the prevention of plaque formation and/or the clearance of oligomers is the main goal. However, recent setbacks increased the reservation from the amyloid cascade hypothesis as clinical trials did not achieve much success. Reasons for these drugs to fail might be manifold, yet the current evolution of Alzheimer's therapies does not take into account the critical connections of A $\beta$  aggregation mechanisms and how the generation of toxic species is affected by individual microscopic steps and their dependence to each other[8, 41]. The inhibition of specific microscopic steps may limit the toxicity of A $\beta$ , whereas others might even amplify the damage. As such, specific inhibition of fibril elongation can shift the reaction flux towards an increase of secondary nucleation and therefore increase the content of toxic A $\beta$  species.

During my PhD, I had the opportunity to study the murine versions of the therapeutic antibodies gantenerumab (<sup>ch</sup>gantenerumab), bapineuzumab (3D6), aducanumab (<sup>ch</sup>aducanumab) and solanezumab (m266), as potential inhibitors for AD. The human-derived monoclonal antibody aducanumab has shown promising results in a previous phase 1b trial, with dose- and time-dependent reduction of brain amyloid burden, as

measured by PET imaging, accompanied by a slowing of cognitive deterioration in subjects with early AD[206]. However, Biogen Inc. halted the phase 3 trial in 2019 as the delay of cognitive and functional degradation compared to the placebo was not significant enough and preliminary data suggested the drug would not meet the primary endpoint[25]. Kinetic studies on <sup>ch</sup>aducanumab could show that the antibody specifically suppresses secondary nucleation with no observable effect on  $A\beta(42)$  elongation (unpublished work by Sara Linse). The murine precursor of bapineuzumab, 3D6, on the other hand, has been shown to suppress secondary nucleation of  $A\beta(42)$  at low concentrations and even elongation at higher inhibitor concentrations (unpublished work by Sara Linse), yet failed to produce significant cognitive improvements in patients in two major trials[184]. The other two antibody types tested, gantenerumab and solanezumab are still in phase 3 trials with solanezumab expected to fail as the antibody already shows no significant changes in the disease phenotype compared to placebos[143, 196]. Experiments show that gantenerumab specifically binds to fibril ends and blocks elongation whereas m266 specifically suppresses primary nucleation (unpublished work by Sara Linse). Together with Sara Linse from Lund University, I have analysed the binding behaviour of the antibodies to  $A\beta$  monomers and fibrils mentioned above. The goal was to correlate the characteristic inhibition behaviour of those antibodies, previously studied by Sara Linse, to their individual binding parameters.

## **2.2 How the interaction of the small heat-shock protein $\alpha$ B-crystallin to $\alpha$ -synuclein fibrils is driven by entropic forces and what that means for the binding mechanism**

### **2.2.1 Microfluidic measurements of protein interactions in the condensed phase**

The microfluidic diffusional sizing relies on fluorescent labelled molecule in order to track their diffusional behaviour in complex solutions. Therefore, our protein of interest,  $\alpha$ B-c, was tagged with GFP label. First, the diffusion profiles of GFP-labelled  $\alpha$ B-c were acquired by epifluorescence microscopy in the absence and presence of unlabelled  $\alpha$ -syn

fibrils. By exploiting the difference in diffusion coefficient between amyloid fibrils and free molecular chaperones in solution, I have detected changes in size distributions upon the formation of the complex between the chaperone  $\alpha$ B-c and amyloid fibrils (Fig. 2.3 a and c). When a labelled chaperone binds to a fibril, the complex formed exhibits a diffusion coefficient about one order of magnitude smaller than the diffusion coefficient of the free chaperone. This difference has allowed me to deconvolve the diffusion profiles into the relative contribution of the two components: the rapidly diffusing free chaperones and the slowly diffusing chaperone-fibril complexes, thus determining the absolute concentrations of both binding partners in the condensed phase.

Prior to measuring the binding parameters, I verified by means of kinetic analysis that the GFP-tag on the  $\alpha$ B-c does not affect the chaperone's capability to inhibit  $\alpha$ -syn

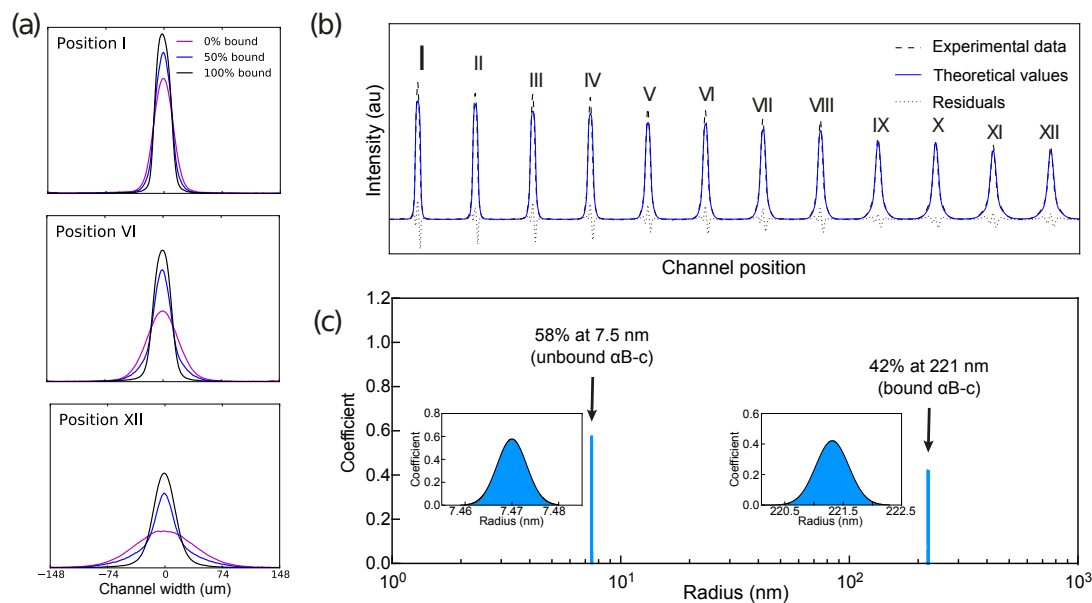


**Figure 2.3:** Experimental diffusion profiles and analysis a) Diffusion profiles of three chaperone-fibril samples exhibit different extent of binding: 0% (purple), about 50% (blue), and 100% (black) of total chaperones bound to fibrils. Normalised profiles are shown for three channel positions. The sample with 0% bound chaperone diffuses the most, while the sample with 100% bound chaperone stays localised in the centre of the channel. Partially bound samples exhibit superposition of two peak shapes - diffuse (corresponding to free chaperone) and localised (corresponding to bound chaperone). (b) Experimental profiles of  $\alpha$ B-c ( $1 \mu\text{M}$ ) binding to  $\alpha$ -syn fibrils ( $10 \mu\text{M}$ ) at  $25^\circ\text{C}$  at 12 diffusion positions along the channel together with the simulated profiles for the 50% bound sample showing the best fit for this data set. (c) The fitting of the model simulations to the experimental data provides a direct measure of the fraction of particles in each size bin. Inserts in (c) show error distribution of the individual radii determined by first order Taylor expansion of the least square equation.

amyloid formation. To this effect, I followed the aggregation kinetics of a solution of 70  $\mu\text{M}$   $\alpha\text{-syn}$  to which 5% w/w pre-formed seeds had been added in the presence and absence of different concentrations of GFP by itself, and both unlabelled and labelled  $\alpha\text{B-c}$  (see Supplementary Fig. B.1). I observed very similar aggregation profiles for the labelled and unlabelled chaperone, indicating that the GFP-tag does not significantly modify the binding properties of  $\alpha\text{B-c}$  to  $\alpha\text{-syn}$  fibrils and its ability to inhibit their aggregation. Furthermore, no effect on  $\alpha\text{-syn}$  aggregation by the presence of GFP by itself was detected. This indicates there are no interactions between GFP and the aggregation-relevant binding sites of  $\alpha\text{-syn}$ .

By using the described microfluidic approach, I measured the average hydrodynamic radius,  $R_{\text{H}}$ , of the polydisperse  $\alpha\text{B-c}$  oligomer distribution to be  $7.45 \pm 0.01$  nm at  $21^\circ\text{C}$  (see Supplementary Fig. B.2). This value is in good agreement with previously reported values measured by size exclusion chromatography and dynamic light scattering ( $R_{\text{H}}=7.25$  nm), with the attached GFP moiety being responsible for the increased measured size relative to the wild-type[182]. The measured  $R_{\text{H}}$  indicates that  $\alpha\text{B-c}$  is present as an ensemble of oligomers, which is in agreement with mass spectrometric analysis (see Supplementary Fig. B.3). When  $\alpha\text{-syn}$  fibrils were introduced into the system and the distribution of hydrodynamic radii was measured using the microfluidic platform, a second species in the  $R_{\text{H}}$  distribution emerged with size in the range of 220.5-222.5 nm (Fig. 2.3 c). This second population, with a larger radius, corresponds to the complex formed by  $\alpha\text{B-c}$  and  $\alpha\text{-syn}$  fibrils, and thus reports on the interactions between these two species.

### **2.2.2 Experiments under native conditions reveal a nanomolar affinity for $\alpha\text{B-c}$ crystallin binding to $\alpha\text{-syn}$ fibrils**

I next exploited the quantitative power of the MDS to evaluate the affinity of the chaperone-fibril interactions in the condensed phase under native conditions. To this effect, I characterised the kinetics of the binding reaction by incubating a solution of 1  $\mu\text{M}$   $\alpha\text{B-c}$  with a suspension of 10  $\mu\text{M}$   $\alpha\text{-syn}$  fibrils and measuring the size distribution of aliquots taken at discrete time points over the course of 50-150 hours. In a wide range of  $\alpha\text{B-c}$  concentrations, the distribution of the oligomer distribution has been shown to be rather narrow and defined[182]. I carried out the measurements at seven different

temperatures (7°C, 10°C, 17°C, 20°C, 25°C, 30°C, and 37°C) (Fig. 2.4) to obtain both the thermodynamic parameters and the activation free energy involved in this binding process. In order to analyse quantitatively the binding kinetics at individual temperatures, I fitted the binding site concentration globally as its value should be identical under all seven conditions tested.

My data reveal that the reaction exhibits kinetic characteristics of a first order reaction (Fig. 2.4 a) in both the chaperone and the fibril concentration, and hence second order overall. I obtained values for the association rate constants (e.g.,  $k_{\text{on},25^\circ\text{C}} = 7.1 \pm 2.6 \text{ M}^{-1} \text{ s}^{-1}$ ) and dissociation rate constants (e.g.,  $k_{\text{off},25^\circ\text{C}} = 2.7 \cdot 10^{-6} \pm 8.6 \cdot 10^{-7} \text{ s}^{-1}$ ). The accuracy of the fitted dissociation rates have been tested separately

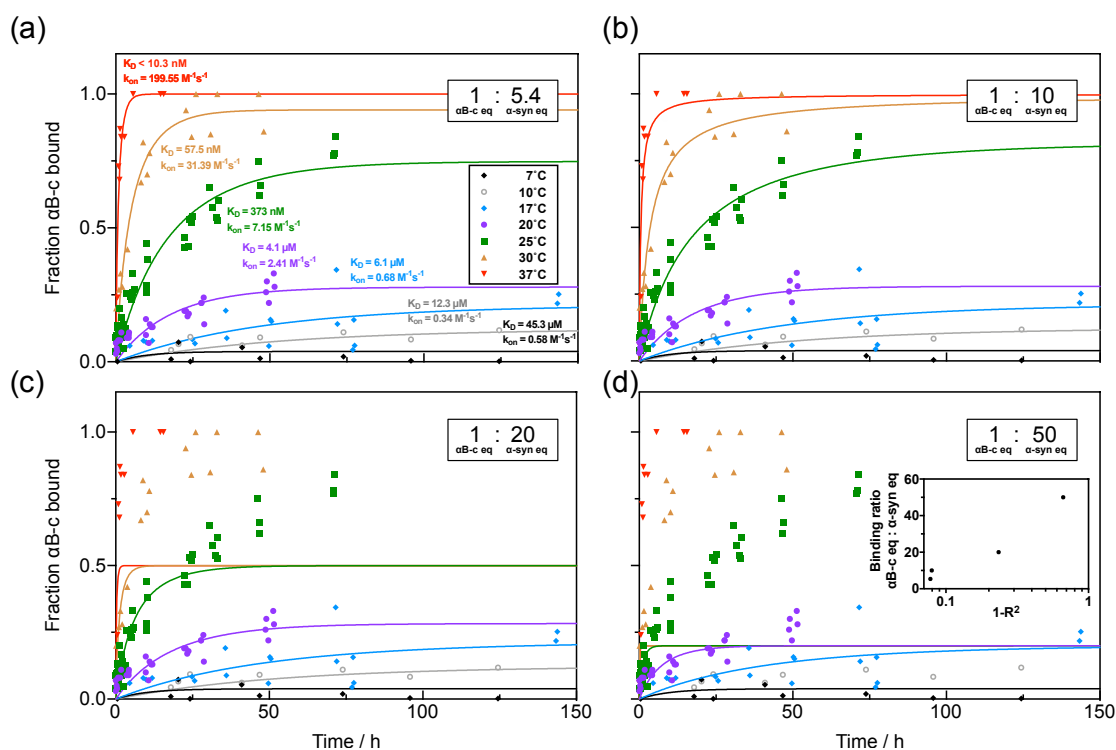


**Figure 2.4:** Kinetic data of  $\alpha\text{B-c}$  ( $1 \mu\text{M}$ ) binding to  $\alpha\text{-syn}$  fibrils ( $10 \mu\text{M}$ ) reveal the kinetic parameters of binding. Kinetic traces at different temperatures were fit to a second order rate equation to obtain the association ( $k_{\text{on}}$ ) and dissociation ( $k_{\text{off}}$ ) rate constants, from which an apparent dissociation constant  $K_{\text{D,app}}$  was calculated. Different binding ratios of  $\alpha\text{B-c}$  equivalents (eq) to  $\alpha\text{-syn}$  fibril mass eq with (a)  $1:5.4 \pm 1.1$  ( $R^2 = 0.922$ ), (b)  $1:10$  ( $R^2 = 0.921$ ), (c)  $1:20$  ( $R^2 = 0.766$ ) and (d)  $1:50$  ( $R^2 = 0.336$ ) were fitted. The optimal fit (a) is given with a stoichiometry of  $1:5.4$  with a lower boundary for the stoichiometry at  $1:8$  given by the standard deviation. The resulting  $R^2$  values are plotted against the corresponding binding ratios as an insert in (d). List of estimated values for  $k_{\text{on}}$ ,  $k_{\text{off}}$  and  $K_{\text{D,app}}$  including standard deviation at individual temperatures can be found in Supplementary Table B.1.

by following the dissociation of bound  $\alpha$ B-c in a saturated  $\alpha$ -syn fibril solution at 7°C (see Supplementary Fig. B.5). The dissociation rate constant measured in this experiment is consistent with the  $k_{\text{off},7^\circ\text{C}} = 5.6 \cdot 10^{-5} \pm 1.2 \cdot 10^{-5} \text{ s}^{-1}$ , similar to the dissociation rate calculated from the association kinetics  $k_{\text{off},7^\circ\text{C}} = 2.6 \cdot 10^{-5} \pm 1.6 \cdot 10^{-5} \text{ s}^{-1}$ . The dissociation equilibrium constants are computed from the ratio of the rate constants (e.g.,  $K_{\text{D,app},25^\circ\text{C}} = 373 \pm 238 \text{ nM}$  and  $K_{\text{D,app},20^\circ\text{C}} = 4.1 \pm 1.7 \text{ }\mu\text{M}$ ). Similar affinities at low micromolar range have been reported for  $\alpha$ B-c binding to other amyloid fibrils, including A $\beta$ 42 fibrils ( $K_{\text{D}} = 2.1 \text{ }\mu\text{M}$ ), A $\beta$ 42<sub>arc</sub> mutant fibrils ( $K_{\text{D}} = 0.34 \text{ }\mu\text{M}$ )[207], and apoC-II fibrils ( $K_{\text{D}} = 5.4 \text{ }\mu\text{M}$ )[24]. Moreover, using the MDS platform, I further obtained information on the number of binding sites present on the fibrils; to this effect, I examined the global influence of the binding stoichiometry on the binding kinetics by comparing the model predictions for different binding ratios of  $\alpha$ B-c to  $\alpha$ -syn between 1:5.4 and 1:50 (Fig. 2.4 a-d). The modelled data do not match the measured data points if the binding ratio of  $\alpha$ -syn equivalents to  $\alpha$ B-c equivalents increases beyond 8 (Fig. 2.4 b-c). This observation yields a lower limit with a binding-site concentration of 1.2  $\mu\text{M}$  under the conditions used and given by the standard deviation of the optimal fit. This best fit gives a concentration of binding-sites of 1.86  $\mu\text{M}$ , corresponding to one  $\alpha$ B-c equivalent binding to, on average, every 5.4  $\alpha$ -syn equivalents. At the highest temperature (37°C) the fraction bound was within error of 100%, hence yielding only an upper bound on  $K_{\text{D}}$ . For this reason the  $K_{\text{D}}$  measured at 37°C was not used for any further analysis.

In order to probe whether the binding reaction could be described as a two state process, I next sought to measure the value of the apparent equilibrium dissociation constant directly from equilibrium titration measurements, and compared the value obtained to that of the estimated affinities given by the kinetic analysis. Concentrations of  $\alpha$ -syn fibrils between 1 and 100  $\mu\text{M}$  were incubated with 1  $\mu\text{M}$   $\alpha$ B-c at 25°C for three days to ensure that the binding reaction had reached equilibrium (see Supplementary Fig. B.4). A non-cooperative, single-site binding model (see Materials and Methods) was found to describe the titration data, using the previously calculated  $\alpha$ -syn binding site ratio of 0.186 binding sites per  $\alpha$ -syn monomer (inverse value of 5.4 binding ratio derived from Fig. 2.4 a) as a fixed input parameter. The apparent dissociation constant given by the titration experiment is  $K_{\text{D,app},25^\circ\text{C}} = 261 \pm 76 \text{ nM}$  (see Supplementary Fig. B.4), which is in agreement with the  $K_{\text{D}} = 373 \pm 238 \text{ nM}$  obtained from the kinetic experiments at the same temperature in Fig. 2.4 a, showing that both experiments probe the same

thermodynamic landscape.

### 2.2.3 The binding of $\alpha$ B-crystallin to $\alpha$ -syn fibrils exhibits strong entropy/enthalpy compensation

The apparent dissociation constants estimated at different temperatures allowed me to deconvolve the enthalpic and entropic components of the free energy of binding using a non-linear van't Hoff analysis (Fig. 2.5 b). The values obtained indicate that the binding between  $\alpha$ B-c and  $\alpha$ -syn fibrils is endothermic at 37°C ( $\Delta H_{37^\circ\text{C}} = 443 \pm 107 \text{ kJ mol}^{-1}$ ), and that the enthalpic loss upon binding is compensated by a gain in entropy ( $\Delta S_{37^\circ\text{C}} = 1.6 \pm 0.4 \text{ kJ mol}^{-1} \text{ K}^{-1}$ ), resulting in an overall spontaneous process at a physiological temperature ( $\Delta G_{37^\circ\text{C}} = -52 \pm 154 \text{ kJ mol}^{-1}$ ) (Fig. 2.5 c). The gain in entropic energy that drives the binding of the chaperone to the surface can originate from two processes, illustrated in Fig. 2.6. A first possibility involves the reduction of the translation and rotational degrees of freedom of the proteins upon binding to the fibrils. In this case, the increase in entropy originates from the release of constraints on hydrogen bonding of water molecules resulting from the burial of hydrophobic protein patches upon binding or other solvent-mediated interactions (Fig. 2.6 a). The release of water molecules and therefore an overall increase in entropy is typically the signature of binding driven by hydrophobic interactions. A second explanation for the entropically driven binding reaction is the increase of degrees of freedom induced by conformational changes of the interacting molecules. In this case, the entropic gain would be mainly given by the disassembly of the oligomeric chaperones (Fig. 2.6 b), while the interactions between fibrils and chaperones would be specific and mediated by the surface chemistry of the two binding partners. I measured a positive change in heat capacity ( $\Delta C_p = 13.3 \pm 5.5 \text{ kJ mol}^{-1} \text{ K}^{-1}$ ), indicating that the entropic-driven binding is due to the disassembly of the chaperone oligomers into smaller subunits, rather than to a hydrophobic effect. The assumption can be deduced from the fact that more water molecules become coordinated by unveiling hydrophobic patches and/or and increase of electrostatic interactions which finally lead to an overall negative change in heat capacity. Furthermore, the idea of dissociating oligomers prior to binding to  $\alpha$ -syn binding is in good agreement with previous studies on  $\alpha$ B-c subunit exchange kinetics. The exchange of  $\alpha$ B-c subunits occurs on a similar timescale of the binding between  $\alpha$ B-c and  $\alpha$ -syn fibrils[112]. The described system can therefore be described by a chaperone activation

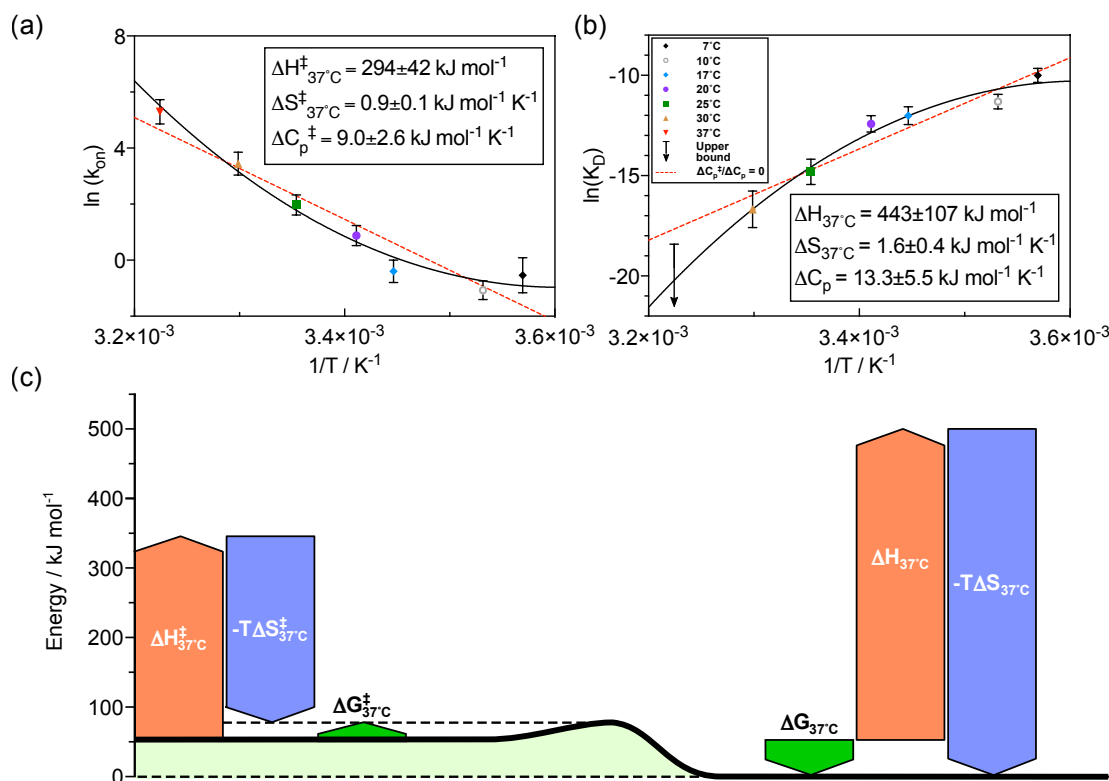


**Figure 2.5:** Thermodynamic parameters of  $\alpha$ B-c ( $1 \mu\text{M}$ ) binding to  $\alpha$ -syn fibrils ( $10 \mu\text{M}$ ) derived from the kinetic parameters of binding. (a) The enthalpic ( $\Delta H_{37^\circ\text{C}}^\ddagger = 294 \pm 42 \text{ kJ mol}^{-1}$ ) and entropic ( $\Delta S_{37^\circ\text{C}}^\ddagger = 0.9 \pm 0.1 \text{ kJ mol}^{-1} \text{ K}^{-1}$ ) contribution together with the change in heat capacity ( $\Delta C_p^\ddagger = 9 \pm 1.1 \text{ kJ mol}^{-1} \text{ K}^{-1}$ ) involved in the formation of the activated state of the binding partners were estimated using a model which combines polymer theory and Kramer’s problem of escape from a metastable state. Therefore, the free energy barrier of binding is  $\Delta G_{37^\circ\text{C}}^\ddagger = 24 \pm 61 \text{ kJ mol}^{-1}$ . The large barrier suggests the binding is a highly activated process. (b) Values of  $K_{D,app}$  were plotted according to the van’t Hoff equation to obtain the binding enthalpy ( $\Delta H_{37^\circ\text{C}} = 443 \pm 107 \text{ kJ mol}^{-1}$ ) and entropy ( $\Delta S_{37^\circ\text{C}} = 1.6 \pm 0.4 \text{ kJ mol}^{-1} \text{ K}^{-1}$ ) together with the change in heat capacity ( $\Delta C_p = 13.3 \pm 5.5 \text{ kJ mol}^{-1} \text{ K}^{-1}$ ). The binding is enthalpically unfavourable and entropically favourable. Value at  $37^\circ\text{C}$  was not included in the analysis and is only given as an upper bound. The dashed red lines in (a) and (b) show similar fits with  $\Delta C_p^\ddagger$  and  $\Delta C_p = 0$  indicating that the change in heat capacity is positive. The resulting  $R^2$  values are for a)  $R^2 = 0.91$  (red dashed curve) and  $R^2 = 0.98$  (black curve), for b)  $R^2 = 0.92$  (red dashed curve) and  $R^2 = 0.97$  (black curve).

(c) The reaction diagram shows the fraction of the individual thermodynamic parameters and shows that the overall chaperone-fibril binding is spontaneous with a free energy of  $\Delta G_{37^\circ} = -55 \pm 216 \text{ kJ mol}^{-1}$ .

through substrate/temperature dependent disassembly of chaperone complexes which e.g. is known from Hsp27 and adds up to the findings of substrate activated and thermosensitive disassembly of other sHsps in order to prevent protein aggregation[78, 224].

### 2.2.4 Analysis of thermodynamic contributions to the activated state

The association rate constants ( $k_{\text{on}}$ ) for chaperone-fibril binding increases with elevated temperature. Together with the  $k_{\text{off}}$ , these measurements indicate that the binding affinity is higher at elevated temperatures. These findings provide a thermodynamic explanation for the reported greater efficiency of  $\alpha\text{B-c}$  in inhibiting  $\alpha\text{-syn}$  aggregation at higher temperatures[193]. From the association rate of  $\alpha\text{B-c}$  to the fibrils as a function of temperature, I estimated a free energy barrier of  $\Delta G_{37^\circ\text{C}}^\ddagger = 24 \pm 61 \text{ kJ mol}^{-1}$  (Fig. 2.5 c). Moreover, I measured the individual enthalpic ( $\Delta H_{37^\circ\text{C}}^\ddagger = 294 \pm 42 \text{ kJ mol}^{-1}$ ) and entropic ( $\Delta S_{37^\circ\text{C}}^\ddagger = 0.9 \pm 0.1 \text{ kJ mol}^{-1} \text{ K}^{-1}$ ) contributions at  $37^\circ\text{C}$  as well as the change in heat capacity ( $\Delta C_p^\ddagger = 9 \pm 2.6 \text{ kJ mol}^{-1} \text{ K}^{-1}$ ) necessary to reach this activated state (Fig. 2.5 a) (see Materials and Methods)[31, 32]. The observed high free energy barrier could be related to  $\alpha\text{B-c}$  conformational changes, including changes in the oligomeric

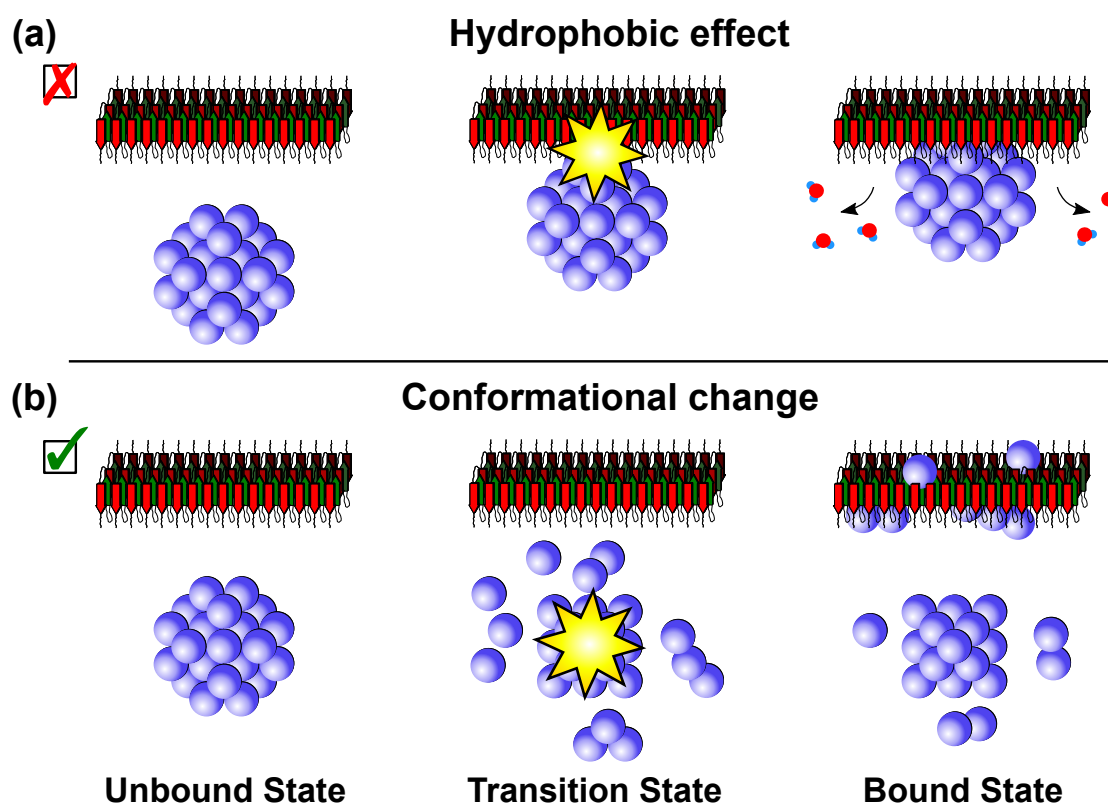


**Figure 2.6:** Potential binding mechanisms of  $\alpha\text{B-c}$  to  $\alpha\text{-syn}$  fibrils. The gain of entropy during the binding reaction of  $\alpha\text{B-c}$  to  $\alpha\text{-syn}$  fibrils can be explained either by (a) a solvent-mediated interaction through release of water molecules or (b) a conformational change of the binding partners. The observed positive change in heat capacity ( $\Delta C_p$ ) supports the latter explanation.

state upon binding to the surface of the fibrils. Crucially, these results show that interactions between chaperones and amyloid fibrils are highly regulated and specific, which is reflected in the high free energy barriers.

### 2.2.5 Discussion

The quantification of the thermodynamic and the kinetic parameters associated with the binding of  $\alpha$ B-c to  $\alpha$ -syn fibrils provides important insights into the mechanisms through which molecular chaperones are able to recognise misfolded protein aggregates and interfere with their proliferation. The client-binding region of  $\alpha$ B-c is still unconfirmed, yet it has been hypothesised to involve the N-terminal domain and the conserved  $\alpha$ B-c domain[23, 80, 105, 116, 228]. In fact, different residues of the chaperone may be relevant for its binding to different clients. Recent studies have shown that  $\alpha$ B-c is a potent aggregation inhibitor in cells and that the  $\alpha$ B-c core domain inhibits the aggregation of  $\alpha$ -syn with similar efficacy to the wild-type (full-length) protein *in vitro*[49, 50]. Furthermore, it has been shown that  $\alpha$ B-c binds to an amorously aggregating client protein (reduced lysozyme) *via* its unstructured N-terminal domain, but interactions with an amyloid aggregating client (amyloid- $\beta_{1-40}$ ) were mediated by the structured  $\alpha$ -crystallin domain[105, 149]. Both areas are predicted to be hydrophobic and are buried in the oligomeric state of the protein. My findings provide direct thermodynamic evidence that the recognition of amyloid fibrillar structures by  $\alpha$ B-c is driven by entropic forces, which include disassembly of the chaperone and its local structural ordering and disordering upon binding. The latter can be described as an “entropy transfer” model, where entropic costs of binding are paid for by entropy-increasing conformational changes within the protein[191, 226]. Moreover, the high activation barrier associated with the binding process for  $\alpha$ B-c supports the hypothesis that some structural or conformational rearrangements are necessary for binding to occur.

An intriguing possible consequence of the interactions between chaperones and amyloid fibrils in living systems is the sequestration of chaperones by amyloid fibrils, with subsequent loss of function and the development of toxicity. Sequestration and reduced activity of chaperones is particularly dangerous since it can have a sequential effect, due to the reduced ability of the cell to cope with any subsequent misfolding and aggregation[172]. By contrast, a favourable effect of the binding of  $\alpha$ B-c to  $\alpha$ -syn fibrils is that the surface

coverage by the chaperone may hinder  $\alpha$ -syn secondary nucleation, although no studies have investigated this effect specifically to date.

## **2.3 Brichos and clusterin - a model system that shows how secondary nucleation and elongation occurs at distinct sites along amyloid fibrils**

### **2.3.1 Clusterin suppresses specifically the elongation step of $A\beta$ (M1-42) aggregation**

In order to investigate the capability of clusterin to inhibit the aggregation process of  $A\beta$ (M1-42), I first incubated the peptide in the absence and presence of different concentrations of the molecular chaperone, and monitored the time evolution of fibril formation by recording the fluorescence signal of the dye thioflavin T (ThT), which is strongly enhanced by its interaction with beta-sheet structures (Fig. 2.7). I observed a delay in the fibril formation process that is proportional to the concentration of clusterin present in the system, even at a very low substoichiometric molar ratios (including 1:500) of clusterin. I then carried out a series of kinetic experiments at different concentrations of  $A\beta$ (M1-42), see Supplementary Fig. B.7, in order to explore the dependence of the various microscopic steps in the aggregation cascade and the presence of the molecular chaperone by means of kinetic analysis[10]. According to this strategy, the experimental kinetic profiles determined at a range of  $A\beta$ (M1-42) concentrations are compared to simulations in which individual events are specifically suppressed (Fig. 2.7 a-c). The least-squared error function, defined in the Materials and Methods section, at a clusterin concentration of 135 nM is 1.5, 0.2 and 1.5 for the specific inhibition of  $k_n$ ,  $k_+$ , and  $k_2$ , respectively. This comparison suggests that clusterin inhibits the overall aggregation process by suppressing specifically the rate of elongation of the  $A\beta$ (M1-42) fibrils, while having no detectable effect on primary and secondary nucleation events.

In order to test this concept experimentally, Paolo Arosio performed kinetic experiments where a solution of 5% (w/w) of pre-formed seed fibrils were added to solutions of monomeric  $A\beta$ (M1-42) (Fig. 2.7 d); under these conditions, primary and secondary

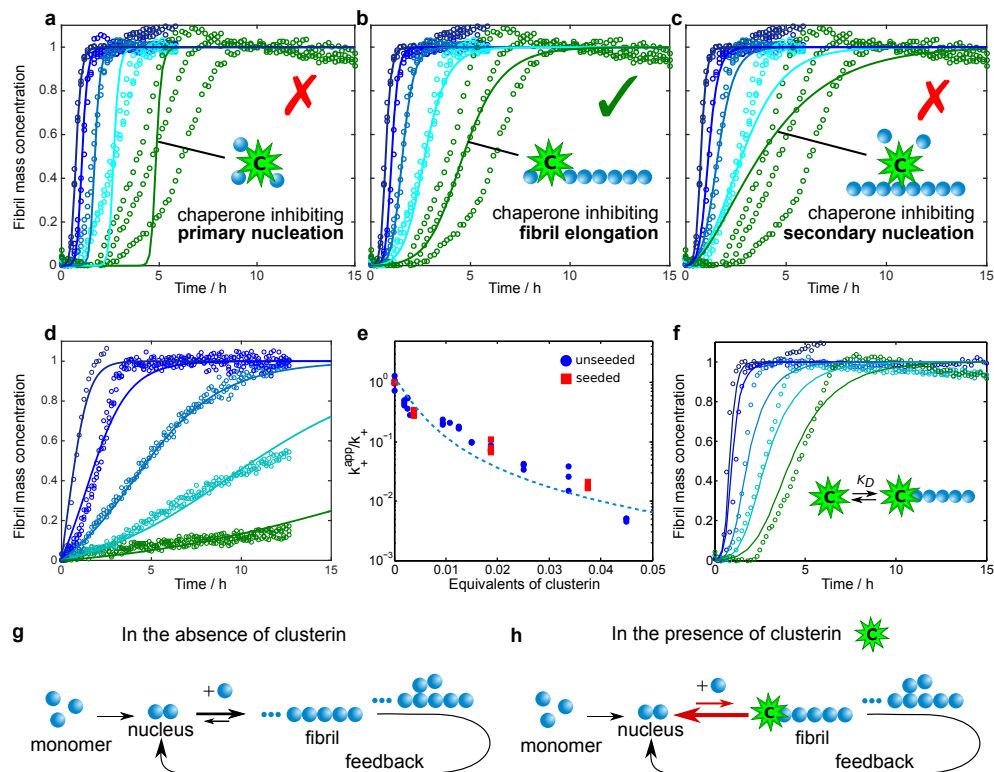


**Figure 2.7:** Analysis of the effects of clusterin on the aggregation kinetics of A $\beta$ (M1-42). (a-c) Kinetic reaction profiles for the aggregation of 4  $\mu$ M A $\beta$ (M1-42) solutions are shown in each panel from left (blue) to right (green) in the absence and presence of 7.5 nM, 37 nM, 75 nM and 135 nM of clusterin with each colour representing repetitions at the same concentration. The integrated rate law for A $\beta$ (M1-42) aggregation in the absence of clusterin using the rate constants, previously determined by a least-square error function, is shown as a dark blue line for each case[42]. Predicted profiles of the specific inhibition processes of (a) primary nucleation, (b) fibril elongation, and (c) secondary nucleation generated by clusterin are shown as continuous lines. Note the characteristic differences in the changes in the shape of the reaction profiles in each case. The prediction for the case where the molecular chaperone suppresses only elongation events matches closely the experimental data in the presence of different concentrations of clusterin. (d) Kinetic reaction profiles for the aggregation reaction of a 2  $\mu$ M A $\beta$ (M1-42) solution seeded with 100 nM pre-formed fibrils in the absence and presence of 7.5 nM, 37 nM, 75 nM and 135 nM clusterin. The lines represent the integrated rate laws for A $\beta$ (M1-42) aggregation where the elongation rate has been selectively reduced. The apparent elongation reaction rates as a function of the molecular chaperone concentration evaluated from the fitting in (b) and (d) are reported in (e) for both unseeded and seeded reactions. The continuous line in (e) represents a simplified correlation between the elongation rate and the binding affinity constant (see Materials and Methods), from which a  $K_{D,37^\circ C} = 8$  nM is determined. (f) Comparison between the experimental data reported in (b) and theoretical predictions of the reaction profiles calculated from a kinetic model which considers the association and dissociation rate constants in the reaction scheme with a  $K_{D,37^\circ C} = 2.5$  nM. (g, h) Schematic diagrams showing the molecular pathways involved in A $\beta$ (M1-42) aggregation (g) and the mechanism by which clusterin perturbs the aggregation process (h).

nucleation events are negligible, and fibril elongation is the major contributor to the increase in fibril mass[7]. By increasing the concentration of clusterin, he observed a progressive reduction in the rate of aggregation, supporting the conclusion that the molecular chaperone inhibits this specific microscopic process. In addition, the elongation rate constants calculated from simulations of the experimental data under seeded conditions are in excellent agreement with the values determined under unseeded conditions, confirming the robustness of the analysis (Fig. 2.7 e).

Previous kinetic analysis of  $A\beta$ (M1-42) profiles indicates that monomeric species participate directly in elongation and primary/secondary nucleation rates[42]. In particular, the elongation reaction involves the addition of monomers to fibril ends and smaller propagons, such as oligomers and other pre-fibrillar species and therefore the inhibition effect of clusterin could result from its interactions with either of the three species[45, 130]. Significant binding of the molecular chaperone to monomeric  $A\beta$ (M1-42) would, however, also affect primary and secondary nucleation reactions, since these processes also depend on the concentration of monomers. As the kinetic analysis reveals that clusterin inhibits only the elongation rate, I can conclude that it interacts preferentially with the fibril ends and all species capable of elongation. The fact that inhibition is observed at very low substoichiometric ratios is completely associated with the interaction of clusterin with the ends of fibrils or pre-fibrillar species, as interactions with monomeric  $A\beta$ (M1-42) would require a much higher stoichiometric concentration of clusterin to affect the rates to such a significant extent.

In order to interpret the kinetic effects in a more quantitative manner, he compared the experimental data with the prediction of a kinetic model that considers explicitly binary interactions between clusterin and the ends of  $A\beta$ (M1-42) fibrils (see Materials and Methods). The theoretical predictions account well for the concentration-dependence of the inhibition at 37°C by using the fitting parameters  $k_{\text{on},37^\circ\text{C}} = 4 \cdot 10^5 \text{ M}^{-1}\text{s}^{-1}$  and  $k_{\text{off},37^\circ\text{C}} = 1 \cdot 10^{-3} \text{ s}^{-1}$  (Fig. 2.7 f), corresponding to  $K_{\text{D},37^\circ\text{C}} = 2.5 \text{ nM}$ . From an analysis of the dependence of the apparent elongation rate constant on the molecular chaperone concentration (Fig. 2.7 f) using a simplified kinetic model, in which the binding reaction process is assumed to be under equilibrium conditions (see Materials and Methods), he obtains a similar value of  $K_{\text{D},37^\circ\text{C}} = 8 \text{ nM}$ . I further extended this approach at a temperature of 21°C, and obtained a value of  $K_{\text{D},21^\circ\text{C}} = 1 \text{ nM}$  (Supplementary Fig. B.8),

indicating that the binding is exothermic. The exergonic binding and the high interaction affinity are consistent with the fact that clusterin interacts with A $\beta$ (M1-42) fibrils in an ATP-independent manner[186].

The interactions between clusterin and fibrils of A $\beta$ (M1-42) were probed in additional kinetic experiments. To this effect, A $\beta$ (M1-42) fibrils were generated in the presence or absence of clusterin and then added to freshly prepared monomer solutions in the presence or absence of clusterin (Supplementary Fig. B.9). Even in the absence of clusterin in the monomer solution (Supplementary Fig. B.9 b), the pre-formed fibrils that had been produced in the presence of clusterin accelerated aggregation to a smaller extent than did fibrils produced in the absence of the chaperone (Supplementary Fig. B.9 a). Application of the kinetic analysis reveals a reduction of ca. 40% in the elongation rate in this latter case (Supplementary Fig. B.9 b), indicating that a significant fraction of the molecular chaperone must have remained bound to the aggregates during the time course of the reaction, and indeed immunogold transmission electron microscopy (TEM) analysis performed by Janet Kumita (Fig. 2.8 b, d and e) indicates that clusterin is bound to these A $\beta$ (M1-42) fibrils. Furthermore, the ability of fibril ends to grow was also observed to be substantially reduced when pre-formed aggregates generated in the absence of the chaperone were added to a mixture of clusterin and monomeric A $\beta$ (M1-42) (Supplementary Fig. B.9 c), demonstrating the ability of clusterin to inhibit ongoing reactions. By contrast, in this set of experiments the fibrils that had not been exposed to the molecular chaperone at any stage maintained their full ability to elongate (Supplementary Fig. B.9 a).

### **2.3.2 Quantification of interactions between clusterin and A $\beta$ (M1-42) fibrils by microfluidic diffusional sizing**

Taken together, the kinetic data described in the previous sections suggest that clusterin is highly effective at inhibiting the aggregation of A $\beta$ (M1-42) at low substoichiometric ratios by specifically reducing the rate of elongation, and provide strong evidence that this process is mediated by the non-covalent association of clusterin with A $\beta$ (M1-42) fibril ends and pre-fibrillar species. The interactions between the molecular chaperone

and the fibrils, therefore, represent the key molecular process underlying the inhibition of fibril elongation.

Evidence of these interactions between clusterin and the fibril ends is provided by immunogold (TEM) (Fig. 2.8 a-d) when the presence of clusterin on the A $\beta$ (M1-42) fibrils have been specifically probed under a variety of conditions which implement stringent washing steps and the use of bovine serum albumin (BSA) incubation to reduce non-specific binding, it is apparent that clusterin binds to the A $\beta$ (M1-42) fibrils. This becomes particularly clear by looking at the absolute quantification of immunogold particles per quantified area occupied by aggregates (Fig. 2.8 e). A significant increase of particles can be observed in the presence of clusterin. Although it appears that the gold labelling is occurring mainly at the fibril ends, it is not possible to conclude that there

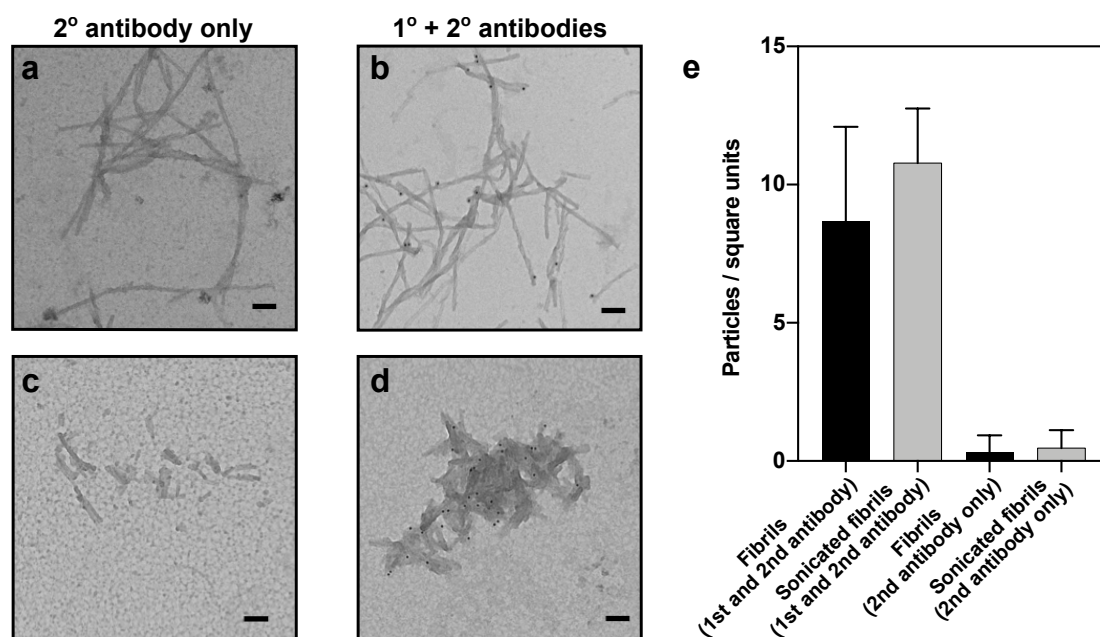


**Figure 2.8:** Analysis of clusterin interactions with A $\beta$ (M1-42) fibrils using immunogold TEM. A $\beta$ (M1-42) fibrils formed under quiescent condition imaged as is (a,b) and after sonication (c,d), were incubated with BSA and clusterin and stringently washed. Incubation with an anti-mouse secondary antibody conjugated to a gold particle showed no non-specific labelling (a,c) whereas incubation with an anti-clusterin monoclonal antibody followed by an anti-mouse secondary antibody conjugated to a gold particle shows the presence of clusterin interacting with the A $\beta$ (M1-42) fibrils (black dots). Scale bars represent 100 nm. (d) Quantification of TEM images given as bar plots showing the individual ratio of immunogold particles per area occupied by aggregates. Area quantity was determined using ImageJ. Reported mean and standard deviation are of at least five independent frames.

are no interactions of clusterin with the surfaces of the fibrils (Fig. 2.8 e). Interestingly, the quantity of bound clusterin can be seen to be slightly increased when the molecular chaperone was incubated with fibrils that were exposed to mechanical breakage by sonication. These shorter fibrils possess a larger number of ends at constant surface area compared to the unsonicated fibrils (Fig. 2.8 e). Although imaging analysis is highly limited by the quality and uniformity of the TEM images, this result suggests that the molecular chaperone interacts preferentially with fibril ends, in agreement with the conclusion from the specific inhibition of the elongation rate observed in this study by the kinetic analysis and discussed earlier.

In order to characterise the interactions between clusterin and A $\beta$ (M1-42) fibrils in a more quantitative manner, I made use of microfluidic diffusional sizing that has recently been developed to measure the interactions between biomolecules directly in solution under native conditions[9, 257]. Briefly, the principle of this technique consists of acquiring, in both space and time, the longitudinal diffusion profiles of molecules in a solution flowing in a microfluidic channel (Fig. 1.3). The diffusion profiles acquired in such experiments can then be analysed by considering advection-diffusion processes to extract the distribution of diffusion coefficients, and therefore the distributions of the hydrodynamic radii of the individual species present in solution[9]. With this technique, interactions between macromolecules can be detected by monitoring the increase in size associated with such events.

I therefore monitored the binding of clusterin to A $\beta$ (M1-42) fibrils by measuring the diffusion of clusterin labelled with the fluorescent dye Alexa-488 in the absence and presence of A $\beta$ (M1-42) fibrils (Fig. 2.9 b and Supplementary Fig. B.11). Clusterin bound to a fibril will diffuse significantly slower than the unbound species because of the much greater size of the fibrils related to the molecular chaperones, and hence exhibit a distinct diffusion profile (Fig. 2.9 b). The size distributions extracted from the diffusion profiles are shown in Fig. 2.9 c; in the absence of A $\beta$ (M1-42) fibrils, clusterin exhibits a monomodal distribution centred at a hydrodynamic radius of about 8 nm. In the presence of the fibrils, however, a bimodal distribution is observed, with a population similar to the hydrodynamic radius of the monomodal distribution corresponding to unbound molecular chaperone, and a peak in the larger size range, corresponding to complexes formed by clusterin and amyloid fibrils. The integral of the area under the two subpopulations is proportional to the concentration of free and bound clusterin. From the

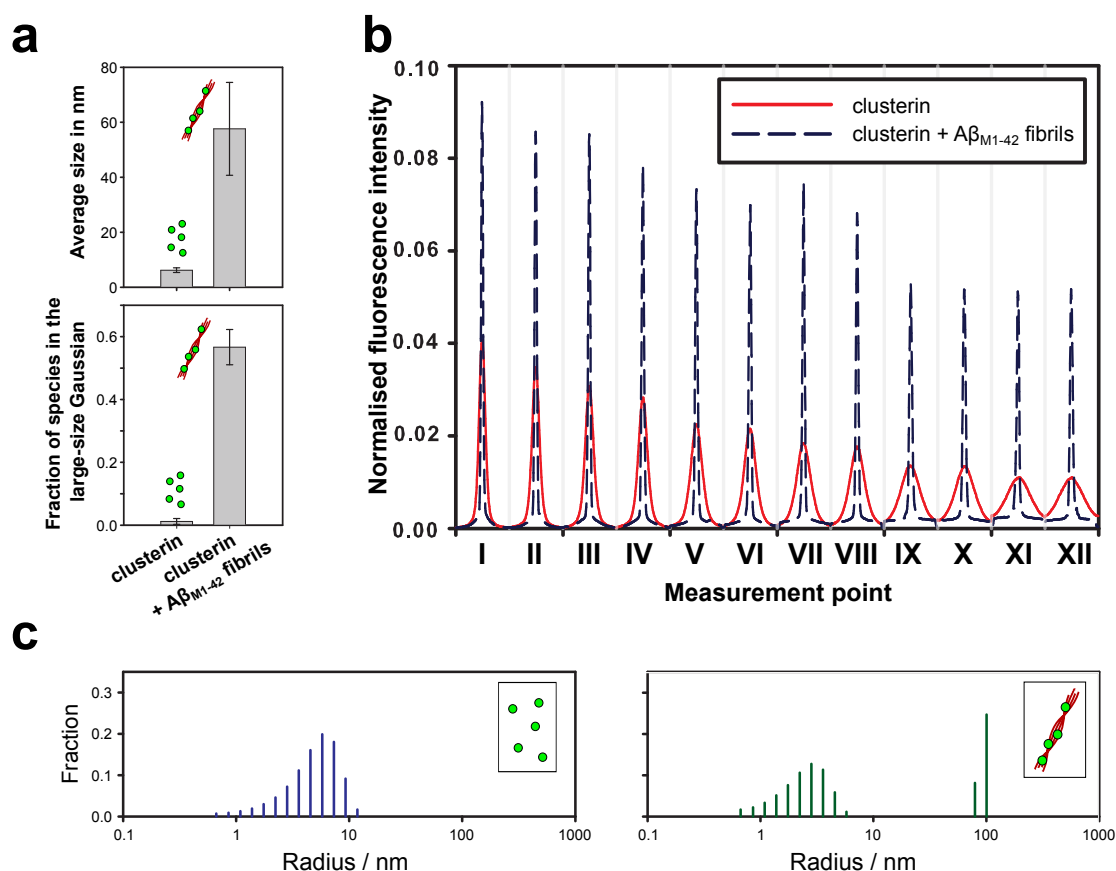


**Figure 2.9:** Microfluidic analysis of clusterin binding to A $\beta$ (M1-42) fibrils. (a) The bar charts show the average size and fraction of the species in the large-size range in the absence and presence of A $\beta$ (M1-42) fibrils. The average sizes and the fraction of species in the large-size range reported have the means and the standard deviations of at least three independent repetitions. (b) Diffusion profiles acquired at 12 different positions along the microfluidic channel for a 0.8  $\mu$ M clusterin solution in the absence (red curves) and presence of 17.5  $\mu$ M pre-formed A $\beta$ (M1-42) fibrils (black dashed curves) in 20 mM sodium phosphate buffer at pH 8.0; (c) The size distributions in the absence (blue) and presence (green) of 2  $\mu$ M A $\beta$ (M1-42) fibrils were evaluated by fitting model simulations based on advection-diffusion equations to the experimental diffusion profiles reported in (b) (more profiles see Supplementary Fig. B.11).

titration curve, obtained by performing experiments at different clusterin concentrations between 0 and 4.5  $\mu$ M with a fibril concentration of 17.5  $\mu$ M, (Fig. 2.10), I obtained a value  $K_{D,21^{\circ}\text{C}}$  of 670 nM. This value is two orders of magnitude larger than the  $K_D$  estimated from the kinetic analysis at the same temperature ( $K_{D,21^{\circ}\text{C}} = 1$  nM); the difference may arise from the specific types of information provided by the two approaches. As can be seen by TEM images, clusterin binds both to the surfaces and the ends of the fibrils, and the microfluidic diffusion technique detects the total quantity of bound

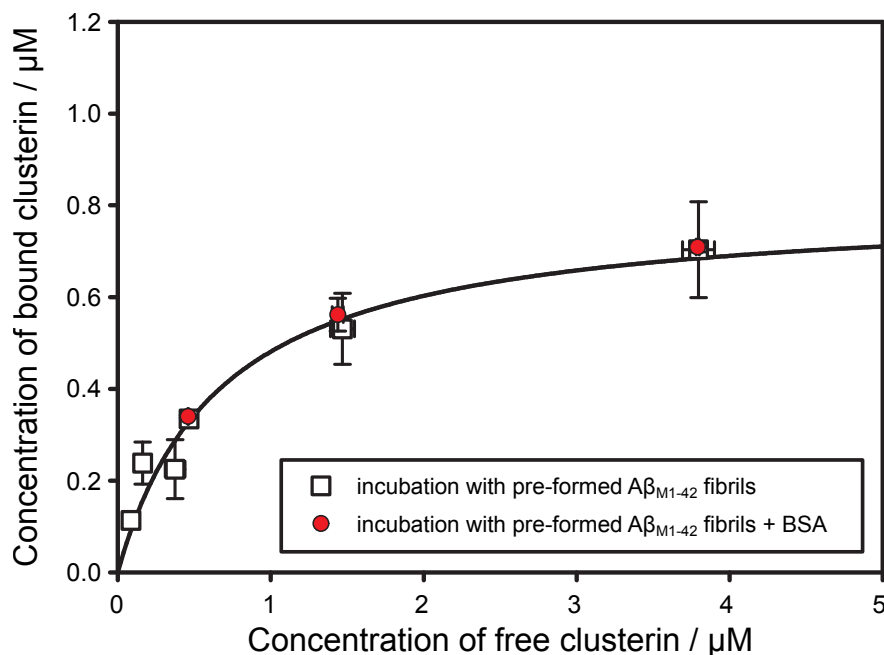


**Figure 2.10:** Binding curve of clusterin to  $17.5 \mu\text{M}$   $\text{A}\beta(\text{M1-42})$  fibrils in  $20 \text{ mM}$  sodium phosphate at  $\text{pH } 8.0$  and  $21^\circ\text{C}$  measured by the microfluidic diffusion technique. In a first set of experiments (squares), different concentrations of clusterin were incubated with previously generated  $\text{A}\beta(\text{M1-42})$  fibrils and size distributions were acquired after  $48 \text{ h}$  of incubation to ensure equilibrium conditions. In a second set of experiments (circles), different concentrations of clusterin were incubated with  $17.5 \mu\text{M}$   $\text{A}\beta(\text{M1-42})$  fibrils and BSA at an equimolar concentrations to clusterin. Each point represents the mean, and the standard deviation of at least two independent repetitions. The regression line represents the best fit to the non-linear Langmuir binding isotherm with  $K_D = 0.67 \pm 0.19 \mu\text{M}$  and  $M = 0.80 \pm 0.08 \mu\text{M}$  (corresponding to one clusterin molecule per  $21.9 \pm 2.2$   $\text{A}\beta(\text{M1-42})$  monomers), with  $R^2 = 0.97$ .

clusterin resulting from these two interactions. By contrast, the kinetic analysis is sensitive only to interactions with the growing fibril ends and the smaller propagons which determine the modulation of the elongation rate, and therefore reports a higher affinity. These findings indicate that clusterin is capable of suppressing  $\text{A}\beta(\text{M1-42})$  aggregation under physiological concentration but higher concentrations of molecular chaperone are needed to reduce substantially the effect of toxic species, in agreement with previously reported results[67, 261]. As a control experiment, I studied the interaction and the inhibition effects of clusterin when a non-chaperone protein, BSA is added into the system (Fig. 2.10 and Supplementary Fig. B.12), and detected no effect on binding.

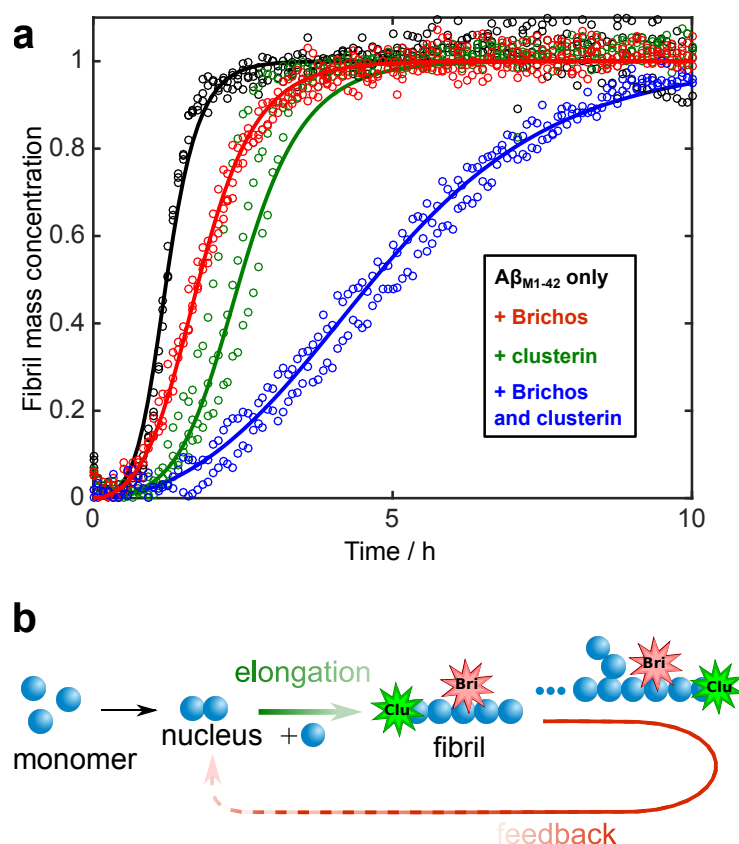


**Figure 2.11:** Brichos and clusterin exhibit modular and additive behaviour of their specific inhibition processes. (a) Kinetic profiles of  $3 \mu\text{M}$   $\text{A}\beta(\text{M1-42})$  solutions in 20 mM sodium phosphate buffer at pH 8.0 in the absence and presence of 18 nM clusterin and  $2 \mu\text{M}$  proSP-C Brichos, added either individually or together as indicated, at  $37^\circ\text{C}$ . (b) The additivity of the inhibition effects reveals that the sites associated with the two different microscopic steps of elongation and secondary nucleation are distinct. Continuous lines represent model simulations where either the elongation rate constant (green line), secondary nucleation rate constant (red line) or both (blue line) have been selectively inhibited.

### 2.3.3 Modulation of $\text{A}\beta(\text{M1-42})$ aggregation by Brichos reveals that the reactive sites of secondary nucleation and elongation are distinct

Although there is evidence deduced from the immunogold labelling and the diffusion experiments that clusterin may be able to bind along the surface of the fibrils, as well as to their ends, the kinetic experiments show that clusterin does not inhibit detectable surface-catalysed secondary nucleation. By contrast, a molecular chaperone belonging

to the Brichos family (proSP-C Brichos), has been found to inhibit the secondary nucleation rate associated with A $\beta$ (M1-42) aggregation but not the rate of elongation[41]. This observation suggests that inhibition of secondary nucleation processes requires specific interactions with defined reactive sites on the fibrils rather than non-specific binding along their surfaces. It also suggests that the sites involved in the nucleation and elongation processes are likely to be distinct. To address this question, as well as to conclude whether or not the effect of the two molecular chaperones is additive, I added 18 nM clusterin and 2  $\mu$ M proSP-C Brichos, both individually and together, to a solution of 2.5  $\mu$ M A $\beta$ (M1-42) and monitored the aggregation over time. I observed a larger inhibition of the aggregation kinetics when the two molecular chaperones are present together in the solution (Fig. 2.11). Moreover, the kinetic profiles can be described very closely by simulation using the rate constants determined from the experiments where the two molecular chaperones were added individually. In particular, the results show that inhibition by proSP-C Brichos on the secondary nucleation rate is essentially the same in the presence or absence of clusterin, and reduction of the elongation rate constant is not detectably affected by the presence of proSP-C Brichos (corresponding to the values reported in Fig. 2.7 e).

The inhibition effects of the two molecular chaperones studied here have been found to be additive and present a number of important implications: it indicates that the sites on the amyloid fibrils involved with the two different microscopic processes of elongation and secondary nucleation pathways are distinct, a result consistent with a recent study showing the development of antibodies able to target specifically distinct steps[5, 165]. Moreover, biologically relevant molecular chaperones can interact with these different sites in an additive non-cooperative way. Experimental repetitions (Supplementary Fig. B.14) at different inhibitor concentrations confirm the additive and non-cooperative inhibition effect of the two individual chaperones.

### 2.3.4 Discussion

Increasing evidence indicates that the aggregation networks leading to the formation of amyloid fibrils are composed of a series of distinct microscopic reactions[43, 43, 130]. For A $\beta$ (M1-42), secondary nucleation under the *in vitro* conditions studied has emerged as the most important source of toxic oligomeric species[42, 227]. Understanding the

molecular details of this process, which is now feasible through the development of chemical kinetic analysis, is therefore of vital importance for understanding the fundamental processes that are likely to be involved in AD. In this work, I have built on the ability of this kinetic platform to identify the different microscopic mechanisms of the inhibitory effects of two molecular chaperones on amyloid formation by A $\beta$ (M1-42). I have observed that clusterin induces a similar reduction of the parameters  $k_+k_2$  and  $k_+k_n$ , in agreement with previous findings[19]. Moreover, my analysis of seeded aggregation profiles demonstrates that, for my recombinant peptide, this observation can be explained at the microscopic level by a reduction of the elongation rate constant, and not by an equal reduction of primary and secondary nucleation rates. In particular, I have shown that the additive nature of the inhibition by the different molecular chaperones implies a selective inhibition of two different microscopic reactions, namely elongation and surface-induced secondary nucleation. This result suggests that the natural protective mechanisms that have evolved to maintain protein homeostasis network are highly sophisticated, and work together to suppress different steps in the series of events that give rise to protein aggregation and amyloid formation. Specific inhibition of elongation reactions alone would inhibit the formation of surface available for secondary nucleation, but could lead to an accumulation of soluble intermediates and an increase in toxicity. For a complete inhibition of the aggregation process, therefore, additional interactions with the surfaces of the fibrils are required to suppress secondary nucleation events, a finding in good agreement with previous reports[67]. Future developments of the analysis described in this work may also clarify the behaviour observed in the more complex environment of *in vivo* systems, for example where overexpression of clusterin has been shown to accelerate amyloid deposition in mice but to decrease the risk of AD in humans[57, 220, 247]. More generally, understanding how the aggregation process is altered by specific molecules is crucial to evaluate the consequences for the generation of potential toxic oligomeric species. These molecular details are particularly relevant in the context of the rational design of drug molecules that could, potentially in combination, target multiple specific aggregation steps in a selective manner.

Interestingly, these findings correlate well with another study, where it has been shown that at a very low clusterin:A $\beta_{42}$ -ratio the toxicity of the aggregates is enhanced, suggesting that clusterin stabilises pre-fibrillar oligomers[259]. This result supports the

inhibition of fibril elongation events in favour of primary and secondary nucleation processes.

In particular, experiments with synthetic A $\beta$ 40 and A $\beta$ 42 have shown that clusterin can bind to oligomers and pre-fibrillar species, while my experiments on recombinant A $\beta$ (M1-42) demonstrate that clusterin is highly effective in retarding the aggregation process of A $\beta$ (M1-42) at low substoichiometric ratios and physiological concentrations by inhibiting specifically the elongation process[19, 166, 243, 259].

## **2.4 Thermodynamic evaluation of the enthalpic Brichos binding reveals very limited catalytic sites along amyloid-beta fibrils**

Molecular chaperones and amyloid fibrils are characterised by significantly different diffusion coefficients; indeed, at the end of the channel, corresponding to a diffusion time on the order of seconds, I observed that the amyloid fibrils remain concentrated in the central region of the channel, while the molecular chaperones have diffused all the way to the sides of the channel. However, any molecular chaperones interacting with the fibrils remain localised in the centre of the channel together with the slow-diffusing fibrils; by contrast, unbound molecular chaperones are free to diffuse along the width of the channel (Fig. 1.3 C). This behaviour results in a large difference in the characteristic diffusion profiles of the interacting and the non-interacting molecular chaperones, which can be quantified using this approach.

In order to track the mass transport of the molecular chaperones, I labelled the chaperone, the Brichos domain, with an Alexa-488 dye (see Materials and Methods), required for the detection of the diffusion profiles by epifluorescence microscopy. Before initiating the measurements, I verified by means of kinetic analysis that the labelling does not affect its capability to inhibit A $\beta$ (M1-42) amyloid formation. To this effect, I followed the aggregation kinetics of a 3  $\mu$ M A $\beta$ (M1-42) solution in the absence and presence of different concentrations of both unlabelled and labelled Brichos domains. I observed very similar aggregation profiles for the two cases (Fig. B.15), indicating that the presence of the fluorescent label does not detectably modify the binding properties of Brichos and its capability of inhibiting the secondary nucleation reactions.

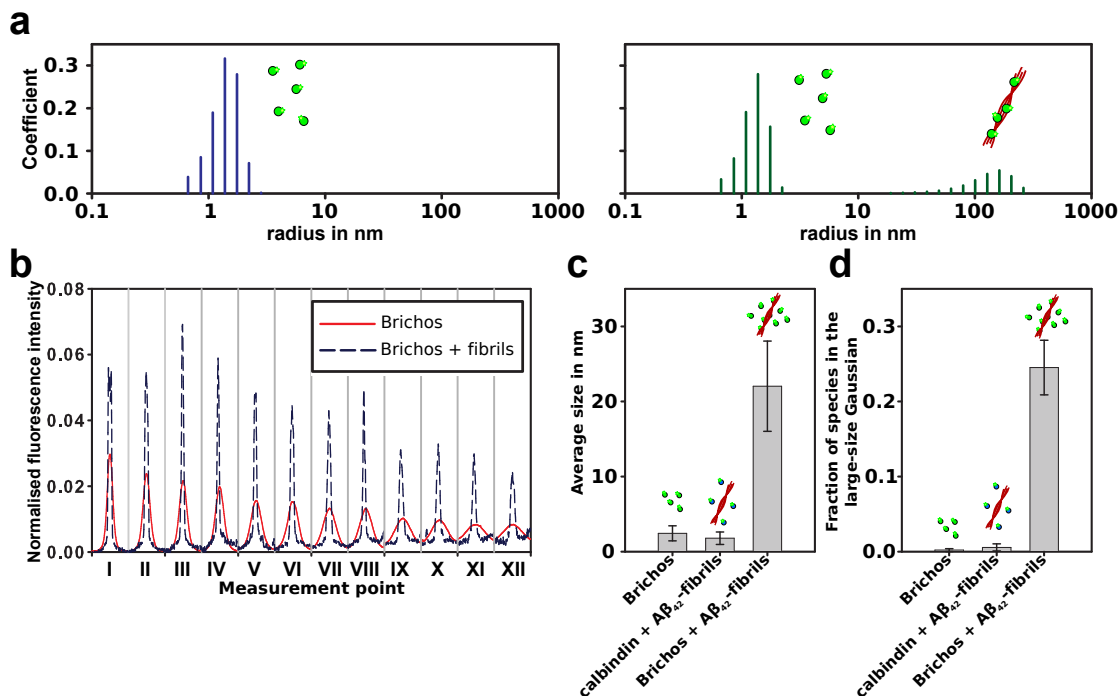


**Figure 2.12:** (a) The size distributions in the absence (blue) and presence (green) of A $\beta$ (M1-42) fibrils were evaluated by fitting model simulations based on advection-diffusion equations to the experimental diffusion profiles. (b) Corresponding diffusion profiles acquired at 12 different positions along the microfluidic channel for a 2  $\mu$ M proSP-C Brichos solution (red curve) and a 0.25  $\mu$ M proSP-C Brichos solution in the presence of 24  $\mu$ M A $\beta$ (M1-42) fibrils (black dashed curve) in 20 mM sodium phosphate buffer at pH 8.0. (c-d) The average size and fraction of the species in the large-size range in the absence and presence of A $\beta$ (M1-42) fibrils at 21 $^{\circ}$ C. In the presence of the fibrils, complexes of the molecular chaperone with amyloid aggregates are observed. The specificity of the binding between Brichos and A $\beta$ (M1-42) fibrils was confirmed by measurements of the size distribution of 6  $\mu$ M calbindin in the absence and presence of 24  $\mu$ M A $\beta$ (M1-42) fibrils. The reported average sizes and the fraction of species in the large-size range are the mean and the standard deviation of at least three independent repetitions.

A mixture of 0.25  $\mu$ M proSP-C Brichos in 20 mM sodium phosphate buffer at pH 8.0 in the absence and presence of 24  $\mu$ M A $\beta$ (M1-42) fibrils were investigated using a microfluidic diffusion device described above and diffusion profiles were acquired at 12 different positions along the channel length (Fig. 2.12 b). From the diffusion profiles shown in Fig. 2.12 b, it can clearly be seen that in the presence of A $\beta$ (M1-42) fibrils the average translational diffusion coefficient of the molecular chaperone decreases dramatically, thereby indicating an increase in its apparent hydrodynamic radius (defined as the Stokes radius,  $R_H$ ) upon binding to the fibrils. To provide a quantitative description of this behaviour, the measured diffusion profiles were fitted by model simulations

based on advection-diffusion equations where a bimodal Gaussian distribution of sizes has been assumed to account for the possible presence of both bound and unbound chaperones[164] (see Materials and Methods and Supplementary Fig. B.17); representative size distributions measured in the absence and presence of fibrils are shown in Fig. 2.12 a. In the absence of fibrils, proSP-C Brichos exhibits a monodisperse size distribution of hydrodynamic radii centred at ca. 1.5 nm. In the presence of 24  $\mu\text{M}$  A $\beta$ (M1-42) fibrils, a bimodal size distribution is observed, with one peak in the range of hydrodynamic radii corresponding to the free molecular chaperone, and a second peak centred at ca. 200 nm, corresponding to Brichos bound to the fibrils. The average sizes of the complete distributions, as well as the fraction of the sub-population characterised by the second peak, are reported in Fig. 2.12 c and 2.12 d, respectively.

I investigated the specificity of the interactions between Brichos and the A $\beta$ (M1-42) fibrils by measuring the size distribution of the protein calbindin in the absence and presence of A $\beta$ (M1-42) fibrils. The consistent hydrodynamic radius of calbindin under changing conditions indicates (Fig. 2.12 c) the lack of interactions between calbindin and the fibrils, and the specificity of the microfluidic binding assay.

The quantitative nature of the diffusion measurements enables readily the evaluation of binding affinity from the experimental data, and therefore the measurement of the dissociation constants ( $K_D$ ) of the binding process by determining the fraction of bound protein at different total initial concentrations of chaperone. To this effort, I measured the fraction of Brichos molecules at constant A $\beta$ (M1-42) fibril concentration of 24  $\mu\text{M}$  and at Brichos concentrations ranging between 0 and 1.5  $\mu\text{M}$  (Fig. 2.13). Two different incubation procedures followed: in a first approach, I measured the binding of Brichos to mature A $\beta$ (M1-42) fibrils generated previously in the absence of the molecular chaperone (Fig. 2.13, black open squares). In a second set of experiments, the chaperone was incubated together with monomeric A $\beta$ (M1-42) at 37°C until essentially all monomers had converted into fibrils, and the binding was later evaluated after 48 h incubation at 21°C (Fig. 2.13, red circles); in this latter approach, the molecular chaperone binds to the peptide fibrils during the aggregation reaction. In Fig. 2.13 it can be seen that the data obtained through the two procedures are similar.

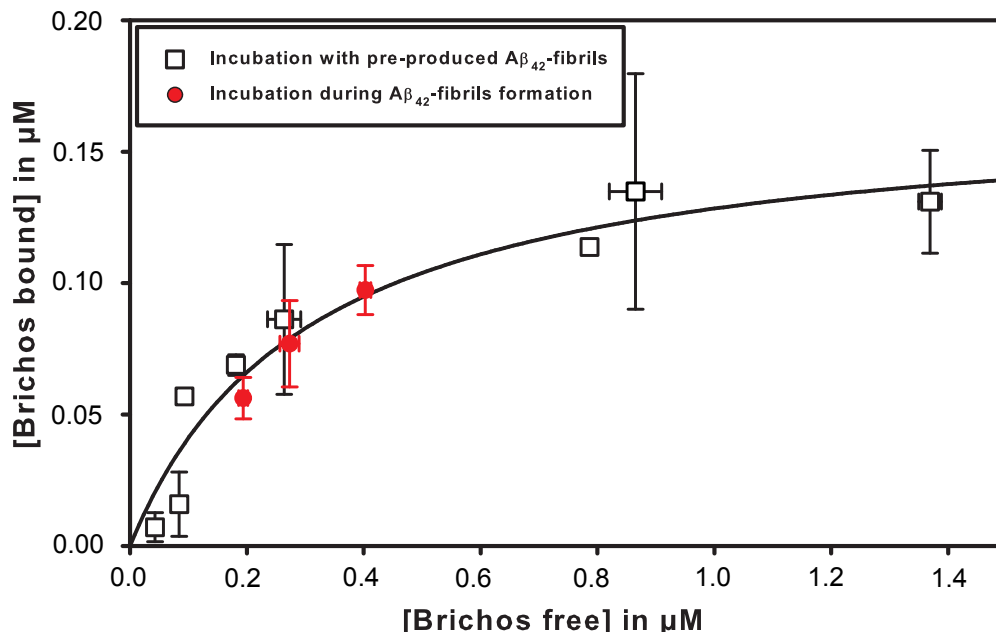


**Figure 2.13:** Binding of proSP-C Brichos to 24  $\mu\text{M}$   $\text{A}\beta(\text{M1-42})$  fibrils in 20 mM sodium phosphate at pH 8.0 and 21°C measured by the microfluidic diffusion technique. In a first set of experiments (squares), different concentrations of Brichos were incubated with pre-generated  $\text{A}\beta(\text{M1-42})$  fibrils and size distributions were measured after at least 48 h of incubation to ensure that equilibrium was established prior to measurement. In a second set of experiments (circles), different concentrations of Brichos were mixed with monomeric  $\text{A}\beta(\text{M1-42})$  and incubated at 37°C until all monomers converted into fibrils. Samples were analysed after 48 h incubation at 21°C by the microfluidic diffusion method. In this second approach, Brichos molecules bind to  $\text{A}\beta(\text{M1-42})$  fibrils during their formation. Each point represents the mean and the standard deviation of at least two independent repetitions. The regression line represents the best fit to the non-linear Scatchard equation with  $K_{D,21^\circ\text{C}} = 310 \pm 80$  nM and  $M = 168 \pm 17$  nM (corresponding to one Brichos molecule per  $143 \pm 14.5$   $\text{A}\beta(\text{M1-42})$  monomers), with  $R^2 = 0.93$ .

#### 2.4.1 Binding affinity determination

By fitting the experimental data to a non-cooperative, single binding-site model (using the Scatchard equation, see Materials and Methods), I obtained a  $K_{D,21^\circ\text{C}}$  of  $310 \pm 80$  nM, and a maximum surface coverage of one Brichos domain per  $\sim 143$   $\text{A}\beta(\text{M1-42})$  monomers. I note that the measured  $K_{D,21^\circ\text{C}}$  is of the same order of magnitude but about seven fold larger than the value defined by previous SPR experiments with a  $K_D$  of about 40 nM,[41] a result that can be attributed to the well-established non-specific binding to the surface of the chip in the SPR technique, which is likely to lead to an overestimation of the quantity of bound Brichos[171]. By contrast, the microfluidic platform enables the interactions between the species to be measured in a solution that is

closer to physiological conditions.

The measured  $K_{D,21^{\circ}\text{C}}$  value indicates a very high affinity of Brichos to the A $\beta$ (M1-42) amyloid fibrils, yet the very low value of surface coverage demonstrates the remarkable efficiency of this molecular chaperone in suppressing the secondary nucleation events catalysed by the fibril surface. This high level of efficiency is likely to be due to the ability of the Brichos domain to interact highly selectively with the more active catalytic sites on the surfaces of the fibrils.

### 2.4.2 Thermodynamic parameters of Brichos binding to A $\beta$ (M1-42) fibrils

A further possibility opened up by the microfluidic diffusion technique proposed in this work is the measurement of the thermodynamic parameters of the binding reaction in solution by evaluating the temperature dependence of the dissociation constants. To this effect, I measured the binding curve at different temperatures in the range of 21-37°C using the procedure described in the previous paragraphs (Fig. 2.14 a). I verified by SDS-PAGE analysis that the attachment of the fluorescent label to Brichos is stable at a higher incubation temperature for several hours (see Supplementary Fig. B.18). As the image acquisition on the microscope for diffusional sizing is in the range of seconds there is still a risk of molecules dissociating caused by the dilution through co-flow buffer. However, this only affects very transient or weak or unspecific interactions with dissociation constants conventionally above millimolar range and dissociation rate constants above  $k_{\text{off}} = 10^{-3}\text{sec}^{-1}$ [118]. The fitting, based on the non-linear Scatchard equation, where the amount of maximum fibril binding sites  $[M] = 168 \pm 17$  nM, was assumed to be temperature-independent and indicates a progressive increase of the dissociation constant. Therefore a decrease in the binding affinity, with increasing temperature ( $K_{D,21^{\circ}\text{C}} = 0.3 \mu\text{M}$ ,  $K_{D,27^{\circ}\text{C}} = 1.4 \mu\text{M}$ ,  $K_{D,30^{\circ}\text{C}} = 5.3 \mu\text{M}$ , and  $K_{D,37^{\circ}\text{C}} = 15.1 \mu\text{M}$ ) can be observed. From the corresponding van't Hoff plot (Fig. 2.14 b, see also Materials and Methods), values of a standard molar-binding enthalpy  $\Delta H^{\ominus} = -141.31 \pm 22.16$  kJ/mol and of a -binding entropy  $\Delta S^{\ominus} = -0.36 \pm 0.07$  kJ/(mol·K) were obtained. These parameters can be combined through the Gibbs-Helmholtz equation to yield a value of the standard molar binding free energy  $\Delta G_{37^{\circ}\text{C}}^{\ominus} = -30.38 \pm 35.01$  kJ/mol, indicating that under native conditions the binding of Brichos to A $\beta$ (M1-42) fibrils is a spontaneous

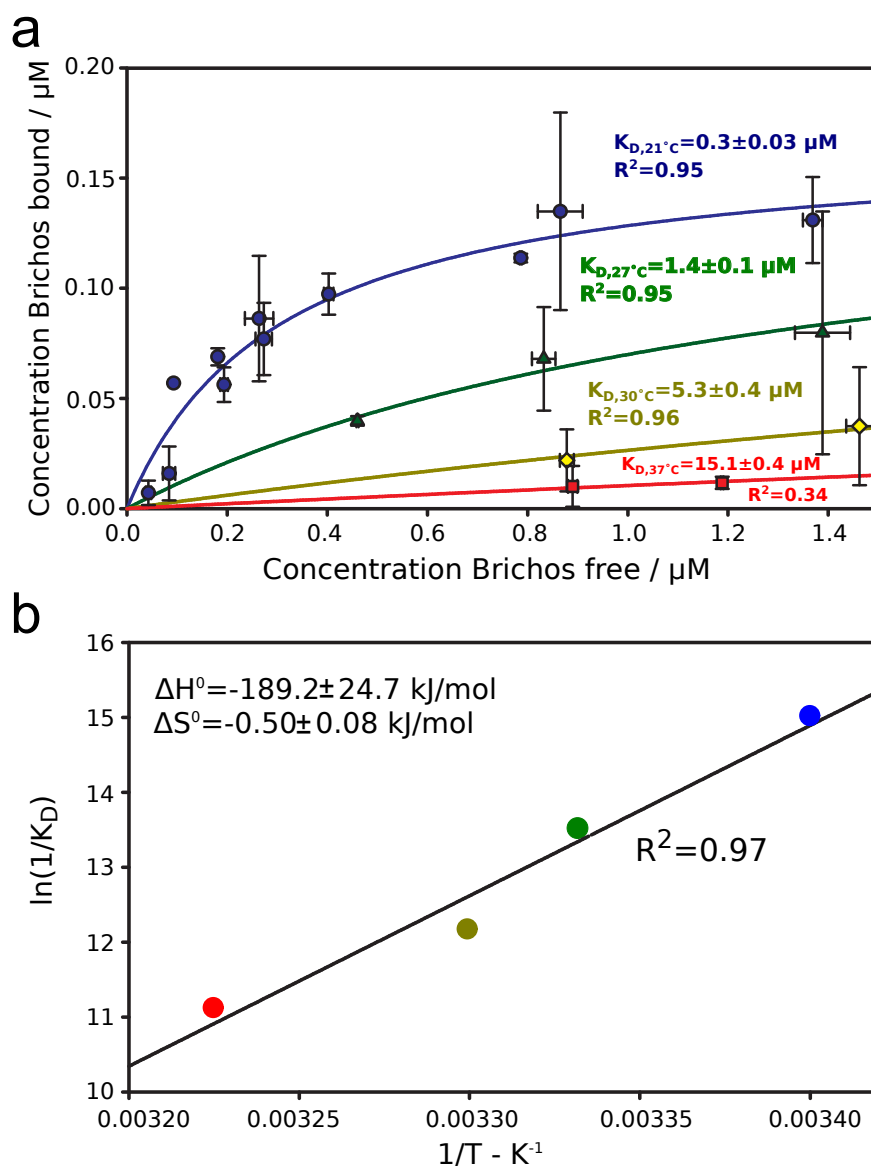


**Figure 2.14:** Thermodynamic evaluation of Brichos binding to  $A\beta(M1-42)$  fibrils. (a) Binding curves of proSP-C Brichos to  $A\beta(M1-42)$  fibrils in 20 mM sodium phosphate at pH 8.0 measured by the microfluidic diffusion method at 21°C (blue circles), 27°C (green triangles), 30°C (yellow diamonds) and 37°C (red squares). Each point represents the mean and the standard deviation of at least two independent repetitions. The regression lines represent the best fit based on a non-linear Scatchard equation. For the regression lines for the data points at 27°C, 30°C and 37°C an  $[Brichosbound_{max}] = 0.1680 \pm 0.0167 \mu\text{M}$  were assumed which was adopted of the more high graded regression line of 21°C. (b) van't Hoff plot corresponding to the dissociation constants measured at different temperatures in (a) (see Materials and Methods), providing a standard binding enthalpy of  $\Delta H^\ominus = -189.2 \pm 24.7 \text{ kJ/mol}$ , a standard binding entropy of  $\Delta S^\ominus = -0.5 \pm 0.08 \text{ kJ/(mol} \cdot \text{K)}$  (B) and a free energy of binding  $\Delta G_{37^\circ\text{C}}^\ominus = -34.125 \pm 35.01 \text{ kJ/mol}$  with  $R^2 = 0.97$ .

exothermic process where the binding enthalpy more than compensates for the loss in entropy. As of the result of the error propagation of combining the free enthalpy and entropy to obtain the free energy, the standard deviation of the free energy is in range where also an endergonic reaction could theoretically occur. However, as no other proteins are present and an enzymatic reaction can be excluded, the binding has to occur spontaneous. Nevertheless, in order to validate the findings, further investigation would be recommended. Measuring the enthalpy directly with ITC would help to minimise the error on th free energy. Also varying the fibril concentration using microfluidic sizing would be a potential solution.

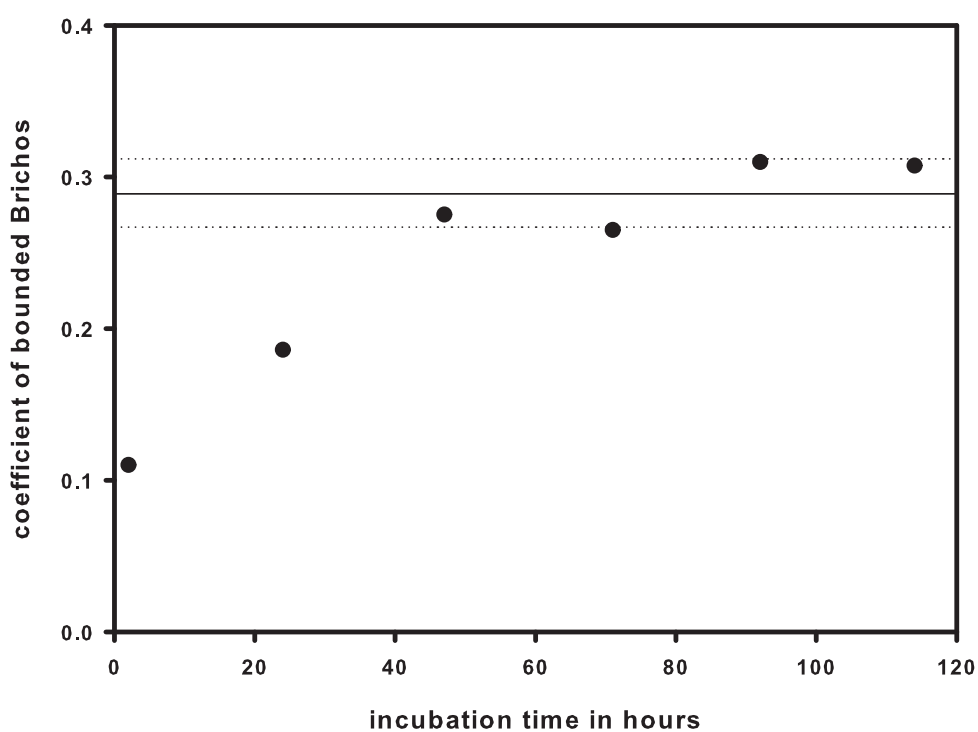


**Figure 2.15:** Fraction of Brichos bound to a mixture of 24  $A\beta(M1-42)$  fibrils and  $0.25 \mu\text{M}$  Alexa-488 labelled Brichos, measured at different incubation times over a time period of 114 h by the space-time diffusion microfluidic approach. The binding reaction reaches equilibrium after about 48 hours. The continuous line represents the mean of the last four data points, while the dotted lines represent the standard deviation.

### 2.4.3 Brichos binding kinetics indicate a limitation of secondary nucleation sites

The exothermic binding behaviour of Brichos to A $\beta$ (M1-42) fibrils results in all smaller fraction of Brichos bound at higher temperatures. Furthermore, kinetic binding analysis of Brichos to A $\beta$ (M1-42) fibrils at 21°C exhibits a two state binding behaviour (see Fig. 2.15, indicating a fast binding to high affine binding sites, potentially responsible for inhibitory activity, within several minutes and a rather slow, more unspecific binding occurring over several hours up to days. Previous studies on Brichos binding to A $\beta$ (M1-42) fibrils with SPR only focussed on the initial binding, not including the system reaching an equilibrated state[41]. Taken both information together indicates that the actual amount of secondary nucleation sites is even lower than the measured stoichiometry of 1 Brichos molecule per 143 A $\beta$ (M1-42). Preliminary kinetic experiments at physiological temperature exhibited at a very low stoichiometry of one Brichos molecule per about 70 000 A $\beta$ (M1-42) monomers (see Supplementary Fig. B.16). These results have to be validated with varying Brichos or A $\beta$ (M1-42) fibril concentration. However, the kinetic analysis and equilibrium binding experiments of Brichos binding to A $\beta$ (M1-42) fibrils suggest that secondary nucleation sites along fibrils a rather rare event or artefact which might not even presented on every fibril rather than a repetitive structure universal for all A $\beta$ (M1-42) fibrils.

### 2.4.4 Discussion

I have described microfluidic diffusion measurements to probe directly in solution in a non-invasive manner the thermodynamic parameters of a binding reaction between biomolecules. I have demonstrated the value of this approach by characterising the binding reaction between the proSP-C Brichos domain and A $\beta$ (M1-42) amyloid fibrils, a process which underlies the inhibition of the secondary nucleation events catalysed by the surfaces of A $\beta$ (M1-42) fibrils. The results reveal that under physiological conditions the binding of Brichos to A $\beta$ (M1-42) fibrils is a spontaneous exothermic process characterised by the conjunction of entropic and enthalpic factors. Remarkably, the results also reveal this molecular chaperone is able to inhibit the aggregation process of A $\beta$ (M1-42) even at very low fibril surface coverage, indicating preferential binding to sites that

are active in secondary nucleation process generating new aggregates on the surfaces of existing fibrils.

## 2.5 How the binding characteristics of therapeutic antibodies control their inhibitory capabilities

### 2.5.1 Kinetic and mechanistic analysis of potential Alzheimer's therapeutics

The investigation of protein binding can give insights into the inhibition behaviour of aggregation suppressors and *vice versa*. Through combining binding and kinetic information together, broader mechanistic understanding of the aggregation homeostasis can be achieved, leading to new insights of how to approach toxicity and disease phenotypes for future therapies. One key step in achieving this goal should be to minimise the amount of toxic oligomeric  $A\beta(1-42)$  species. The main contributing microscopic step for the formation of toxic  $A\beta(1-42)$  oligomers has been found to be secondary nucleation. Inhibiting this particular process and destabilising  $A\beta(1-42)$  oligomers should be the main target for therapeutic applications.

Whereas Sara Linse focused on the analysis of the inhibitory effects of a selection of therapeutic antibodies in a collaborative project, I characterised the general binding behaviour of those antibodies to  $A\beta(42)$  monomers and fibrils. We used the murin counterparts of aducanumab, bapineuzumab, gantenerumab and solanezumab, all have been or still are in clinical trial as potential Alzheimer's therapeutics.

#### 2.5.1.1 Aducanumab

In the beginning of 2019, the clinical trial of aducanumab was halted after promising early 1b trials due to no significant improvement compared to given placebos for the recent phase 3 stage[25, 206]. Accordingly, the kinetic analysis of  $A\beta(M1-42)$  aggregation in the presence of aducanumab *in vitro* performed by Sara Linse reveals a specific and dramatic retardation of secondary nucleation, lowering the effective rate constant for this process by ca. 40% even at the lowest concentrations of antibody tested with

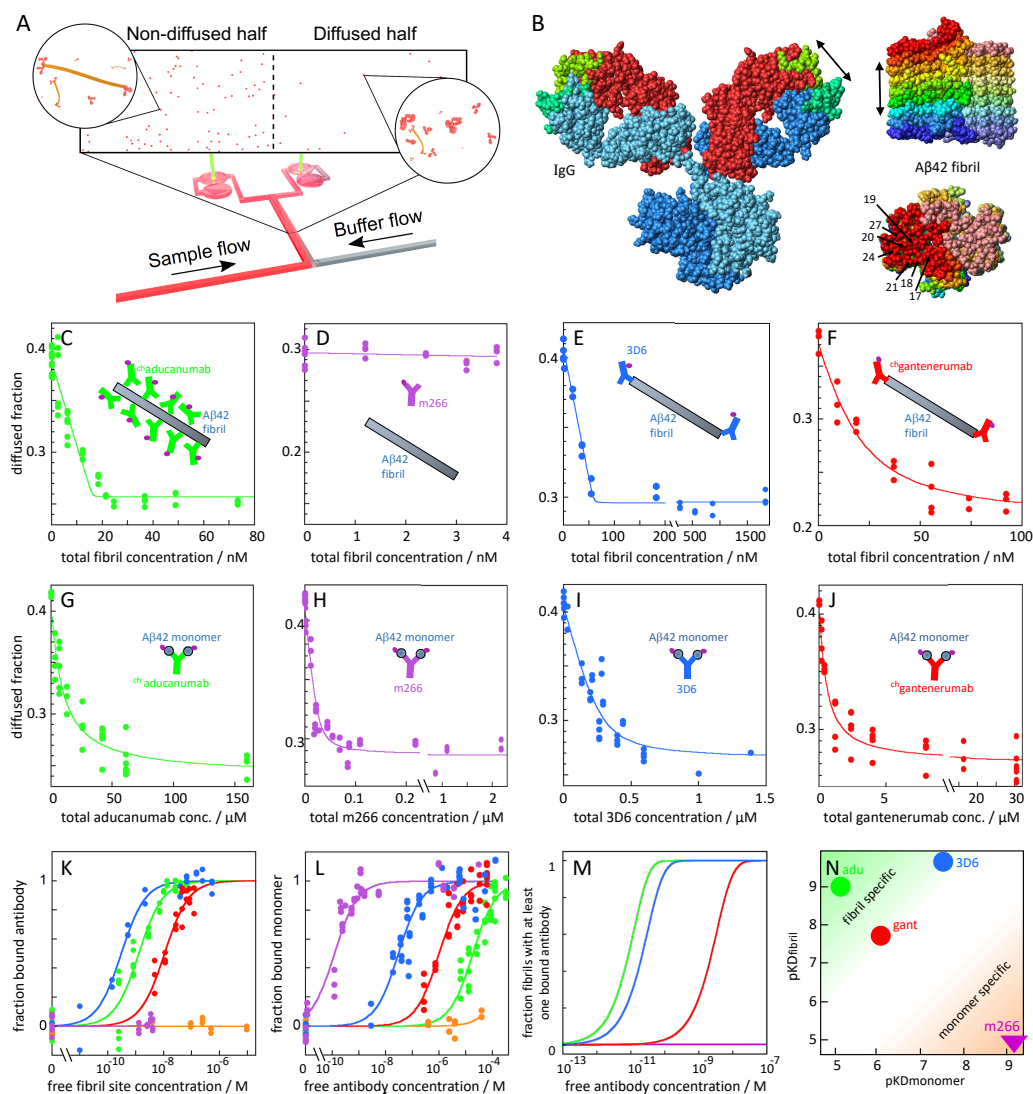


**Figure 2.16:** Investigation of the interactions between therapeutic antibodies to  $A\beta(1-42)$  monomers and fibrils using diffusional sizing. (A) Microfluidic architecture and experimental strategy used to study labelled molecules (red) interacting with ligand (orange). (B) Size of a full-length IgG (1igy.pdb) compared with  $A\beta(1-42)$  fibril (5kk3.pdb): 9 planes of one filament are viewed from the side (top) and fibril end (bottom). Each plane contains two monomers in darker and paler colour, with buried epitope residues indicated in one monomer. Each double-headed arrow corresponds to 2.5 nm. Structural models were prepared using MOLMOL[132]. (C-F) Diffused fraction of Alexa647-antibodies in the absence and presence of increasing concentrations of unlabeled  $A\beta(1-42)$  fibrils, concentration given in monomer units. (G-J) Diffused fraction of Alexa647- $A\beta(1-42)$  monomers in the absence and presence of increasing concentrations of each antibody. Examples of data for  $^{ch}$ aducanumab are in panels C,G; m266 D,H; 3D6 E,I;  $^{ch}$ gantenerumab F,J. (K) Antibody saturation versus free fibril site concentration, calculated from the fits in panels C-F and an isotype control. (L) Monomer saturation versus free antibody concentration, calculated from the fits in panels G-J and an isotype control. (M) Fraction of fibrils with at least one antibody bound calculated using the fitted values of  $KD$  and  $n$ . (N) Summary of obtained affinities of each antibody for fibrils (pKDfibril) versus monomers (pKDmonomer). All data were analysed by fitting directly to the observed diffused fraction of fluorescent species at the end of the microfluidic channel. For detailed description of the applied binding equation, see Material and Methods. The illustration was used with permission of Sara Linse.

500 pM (Supplementary Fig. B.19 A and B.20 A). In addition, I could detect by diffusional sizing, using the commercial Fluidity One-W system of Fluidic Analytics Ltd. (Fig. 2.16 A), that <sup>ch</sup>aducanumab preferentially binds to A $\beta$ (M1-42) fibrils with a relatively high apparent affinity of  $1 \pm 0.2$  nM (Fig. 2.16 C). On the other hand, the affinity to A $\beta$ (M1-42) monomers is with  $9 \pm 2$   $\mu$ M about 4-5 magnitudes lower (Fig. 2.16 G). This is in agreement with previous estimates by surface assays[6]. Furthermore, my measurements provided a binding stoichiometry of 1 <sup>ch</sup>aducanumab per about 5 A $\beta$ (M1-42) monomer units in the fibril, indicating that the fibril is completely coated with antibodies at saturation. Indeed, the width of an IgG antigen-binding region is approximately the summed pitch of 5 planes of a fibril (Fig. 2.16 B). Therefore, in good agreement with our findings, Biogen Idec Inc. announced in October 2019 to file an application for aducanumab for approval by the Food and Drug Administration (FDA). New analysis of a larger dataset from phase 3 studies could show reduced clinical decline in patients with early Alzheimer's disease as measured by the pre-specified primary and secondary endpoints[26].

### 2.5.1.2 Bapineuzumab

In contrast to aducanumab, bapineuzumab failed two major clinical trials and was discontinued in 2012[184]. Following an initial indication of plaque burden reduction in AD patients, no further indication of significant cognitive improvements could be observed. The corresponding mouse antibody, 3D6, shows high affinity to both the monomeric as well as the fibrillar form of A $\beta$ (1-42) with  $38 \pm 8$  nM and  $0.27 \pm 0.2$  nM, respectively (Fig. 2.16 E and I). It should be highlighted here, that a free Asp1 at the N-terminus of A $\beta$ (1-42) had to be used as the recognised epitope covers residues 1-5[73, 176]. The binding stoichiometry of antibodies to monomer units in the fibrils was 1 to  $47 \pm 10$ . The kinetic analysis of the inhibitory effects of 3D6 of the individual microscopic aggregation steps showed specific reduction of fibril elongation (Supplementary Fig. B.19 C and B.20 E).

### 2.5.1.3 Gantenerumab

Even though gantenerumab failed to show efficacy against AD in clinical phase 3 trial, another phase 3 trial was initiated in 2018 for an additional 4 years[16, 173]. The

kinetic analysis of A $\beta$ (M1-42) aggregation together with the murine counterpart of gantenerumab, *ch*gantenerumab, showed a selective inhibitory effect on fibril elongation (Supplementary Fig. B.19 D and B.20 D). The microfluidic binding experiment depicted in Fig. 2.16 F showed, with a  $K_D = 30 \pm 15$  nM, a high affinity of the antibody to A $\beta$ (M1-42) fibrils with a stoichiometry of one antibody per  $43 \pm 4$  monomers in the fibrils and is reflecting the limited amount of binding sites at fibril ends. The finding that *ch*gantenerumab inhibits elongation conforms with the fact that the epitope side-chains of A $\beta$ (M1-42) are buried within the fibril core and are only accessible at the fibrillar ends, according to two high-resolution solid state NMR structures of A $\beta$ (1-42) fibrils[46, 234]. The affinity of *ch*gantenerumab to A $\beta$ (M1-42) monomers is significantly lower with  $485 \pm 100$  nM.

#### 2.5.1.4 Solanezumab

Solanezumab is still on clinical phase 3 trial but is expected to fail, as it shows no significant difference to placebos thus far. However, it exhibited improvements for early AD patients in early trials[107]. In contrast to all previous antibodies described, its murine analogue, m266, specifically inhibits primary nucleation (Supplementary Fig. B.19 B and B.20 B). Similar to gantenerumab, the side-chains of A $\beta$ (1-42) forming the epitope are in the central part of the sequence (residues 16-26)[6]. This again means that the epitope is in the fibrillar core and not accessible for the antibodies, as it has been shown by solid state NMR[46, 234]. Therefore, the binding experiments show a high affinity of  $3 \pm 2$  nM to A $\beta$ (M1-42) monomers but no binding to the fibrillar form (Fig. 2.16 D and H).

#### 2.5.2 Discussion

My work demonstrates the power of detailed analyses of molecular interactions in establishing the mechanism of action for amyloid inhibitors. Understanding the specific effects and relevant interactions of inhibitors allows to identify which individual microscopic steps of the aggregation process are targeted. This can pave the way for predicting how toxicity is affected. All antibodies studied here show a distinct mechanism for inhibiting A $\beta$ (1-42) aggregation (Fig. 2.17). This specific behaviour is reflected in the measured binding properties, such as affinity, specificity and stoichiometry, and allow

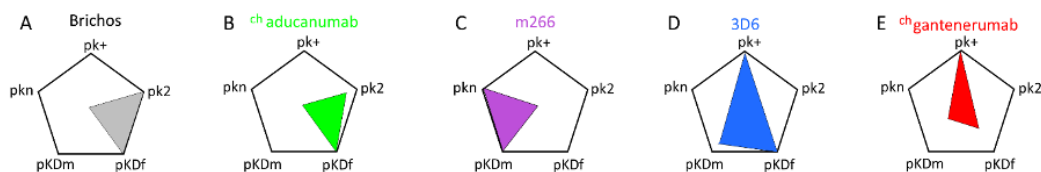


**Figure 2.17:** Summary of kinetic and binding analysis of selected therapeutic antibodies and their effects on the aggregation mechanism. Effect of proSPC-Brichos as an example for a selective secondary nucleation inhibitor (A), *ch*aducanumab (B), m266 (C), 3D6 (D) and *ch*gantenerumab (E) on the microscopic rate constants (pkn, pk+ and pk2) pictured in a pentagon together with the affinity for monomer (pKDm) and fibril (pKDf). The centre of each pentagon corresponds to unperturbed rate constants and a high pk value signifies a large reduction in rate constant, e.g. the molecular chaperone proSP-C Brichos dramatically inhibits specifically secondary nucleation by binding fibrils with a relative high affinity

[41]. The illustration was used with permission of Sara Linse.

mechanistic evaluation of their function. However, not being able to fully quantify their binding to oligomers is a major drawback. A general technical problem of measuring  $A\beta(1-42)$  oligomer interactions is that they only make up a minor fraction of the entire  $A\beta(1-42)$  content, are highly heterogeneous, transient and converge quickly either to fibrils or other forms of oligomers. Therefore, a stabilisation of oligomers by antibodies can not be excluded, factors which may counteract its beneficial effect. Further microfluidic technique developments or other biophysical tools need to be applied to investigate  $A\beta(1-42)$  oligomer antibody binding and their toxicity. One potential application could use the advantage of chromatographic separation prior to microfluidic analysis, as described in the following chapter. However, none of the antibodies shown interferes strongly with the generation of oligomers. The presented strategy of uncovering specific secondary nucleation inhibitors by kinetic and mechanistic analysis is a powerful tool for the identification and assessment of potential therapeutics at early stages to streamline drug development.

## 2.6 Conclusion

The results discussed in this chapter demonstrate the inherent potential of microfluidic binding measurements in solution and that they can prove beneficial as a further biophysical techniques extending current technical limitations. This chapter has focused

on natural evolved and synthetically produced aggregation inhibitors and their interactions with protein aggregates or their monomeric subunits. The binding of these natural evolved chaperones are highly regulated. Recent results have indicated on the emergence of secondary nucleation during aggregation as the key process in the formation of the toxicity of those aggregation events. Therefore, inhibiting other microscopic events, such as elongation, can have contrary effects e.g. by providing more monomers for secondary nucleation and increasing the overall oligomer content. The result show that chaperones are part of a highly balanced system and that their activity can be dependent on the heterogeneous dynamic of chaperone assembly and disassembly. Clusterin is a specific elongation inhibitor and, as such, is shown to accelerate amyloid deposition in mice when overexpressed[57]. Similar effects have to be considered for drug development. I have shown that therapeutic antibodies, which were or still are under clinical trial, lack sufficient capability of suppressing secondary nucleation due to their binding properties. A general biophysical characterisation of potential drugs can accelerate and identify new therapies for neurodegenerative diseases.

# Chapter A

---

## Methods and Analysis

---

### A.1 Proteins

#### A.1.1 $\alpha$ B-crystallin

GFP (green fluorescent protein) labelled  $\alpha$ B-crystallin ( $\alpha$ B-c) was prepared by purifying a construct with the following arrangement:  $\alpha$ B-c-TEV site-GFP-His tag. This construct was expressed recombinantly in *E. coli* BL 21 (DE3). Cells were lysed using a microfluidiser, centrifuged to remove insoluble material and the fusion protein was isolated using Ni affinity chromatography, HisTrap column (GE Healthcare, Chicago, US), using standard procedures. The protein was further purified by size exclusion chromatography on a Superdex 200 16/60 column (GE Healthcare, Chicago, US). The resultant protein was in a solution of 300 mM NaCl, 50 mM Tris (pH 8) made up in 20% glycerol (aq).

#### A.1.2 $\alpha$ -Synuclein

$\alpha$ -syn was expressed and purified in PBS, pH 7.2 as described previously[4, 108]. To prepare fibrils, a solution of 70  $\mu$ M monomeric  $\alpha$ -syn and 0.1% NaN<sub>3</sub> in PBS, pH 7.2 was incubated in an Eppendorf tube at 37°C under constant shaking at 200 rpm for 5 days.

The visibly cloudy sample was centrifuged at 15,000 rpm for 5 min and the pellet was washed once with PBS, pH 7.2 with 0.1% NaN<sub>3</sub> to remove residual monomer. The fibrils were resuspended at 100  $\mu$ M and sonicated with the probe sonicator SONOPULS HD 2070 (BANDELIN electronic, Berlin, DE) at 10% power, 30% cycles for 1 min. Fibril concentration (measured in constituent monomer concentration) was measured by denaturing a fibril aliquot in 5.5 M GuHCl and measuring the resultant  $\alpha$ -syn monomer absorbance. All chemicals were of analytical grade and purchased from Sigma Aldrich unless otherwise stated.

### A.1.3 Amyloid- $\beta$ (M1-42)

The expression and purification procedure for the peptide A $\beta$ (M1-42) (MDAEFRHDS-GYEVHHQKLVFFAEDVGSNKGAIIGLMVGGVVIA), the molecular chaperones clusterin and proSP-C Brichos were carried out as described in previous papers[54, 119, 233, 242]. In short, A $\beta$ (M1-42) inclusion bodies were extracted from *E. coli* cells by sonication and dissolved in 8 M urea. Further purification was performed by ion exchange in batch mode on DEAE cellulose resin with additional lyophilisation and gel filtration on a 3.4 cm x 200 cm gel-filtration column at 4°C[233].

### A.1.4 Amyloid- $\beta$ (1-42)

*The expression and purification was performed by Sara Linse.* The peptide version without the N-terminal methionine had to be used for the experiments with the therapeutic antibody bapineuzumab. The expression of A $\beta$ (1-42) thus requires a fusion tag, the self-cleavable tag nPro in the form of its EDDIE mutant[123]. The peptide was expressed and purified similar to the M1-42 version. However, the EDDIE- $\beta$ (1-42) was diluted 15 times with 1 M Tris, 1 mM EDTA, 5 mM DTT, pH 7.9 and allowed to stand at 4° for 48 h. During this time EDDIE slowly folds leading to auto-cleavage and release of  $\beta$ (1-42). The solutions were then transferred to dialysis bags with 3.5 kDa MW cutoff and dialysed in 5 mM Tris/HCl, 0.5 mM EDTA, pH 8.5, with three shifts. Further purification was applied similar to the procedure for the M1-42 version.

### A.1.5 proSP-C Brichos

In order to obtain the proSP-C Brichos domain, *E. coli* cells were lysed by lysozyme (1 mg/ml) for 30 min and incubated with DNase and 2 mM MgCl<sub>2</sub> for another 30 min on ice. The centrifuged cell pellet was dissolved in 2 M urea in 20 mM Tris, 0.1 M NaCl, pH 8, and sonicated for another 5 min. After another centrifugation step, the supernatant was filtered through a 5- $\mu$ m filter and purified with a 2.5 ml nickel-agarose column. The thioredoxin and His<sub>6</sub> tag were removed by adding thrombin for 16 h at 4°C followed by another run through a nickel column. The protein was further purified using ion exchange chromatography[119, 242].

### A.1.6 Clusterin

Clusterin was extracted from human blood plasma obtained from Wollongong Hospital (Wollongong, NSW, Australia). Complete protease inhibitor was added and the mixture was filtered through (i) a GFC glass fibre filter and then (ii) a 0.45 mm cellulose nitrate filter. The filtrate was further purified on a 5 ml G7 anti-CLU monoclonal antibody column. After severe washing steps the specifically bound material was eluted using 2 M GdnHCl in PBS. The fraction was dialysed against 20 mM MES, pH 6.0 and loaded on a 1 ml HiTrap SP XL cation exchange column, collecting the flow through. Finally, the pure protein was obtained by SEC on a Superose 6 10/300 column[54]. For the microfluidic experiments clusterin was covalently labelled with Alexa Fluor 488 NHS ester (Thermo Fisher, Waltham, US). To achieve this, the protein (2 mg/ml) was incubated with a 10-fold molar excess of the fluorophore (added from a 10 mM stock in DMSO) (1 h, RT). Unconjugated dye was removed by buffer exchange into PBS using a PD-10 column (GE Healthcare, Chicago, US). The final protein concentration and labelling efficiency was measured according to the manufacturer's instructions. I carried out kinetic experiments to show that the labelling with the Alexa dye, required for the fluorescence detection does not modify the inhibition and the binding properties of clusterin (Supplementary Fig. B.13). Bovine serum albumin, obtained from Sigma Aldrich (St. Louis, US), was used. All aggregation assays and binding reactions were carried out in 20 mM sodium phosphate buffer at pH 8.0. All chemicals were of analytical grade and purchased from Sigma Aldrich unless otherwise stated.

### A.1.7 Generation and purification of anti-A $\beta$ antibodies

*The expression and purification was performed by Sara Linse.* <sup>ch</sup>Aducanumab, <sup>ch</sup>gantenerumab, 3D6 and m266 were generated as described before[6]. All antibodies were expressed in CHO cells and purified by protein-A-affinity followed by ion-exchange chromatography.

### A.1.8 Alexa-647 labelling of A $\beta$ peptides and antibodies

*The expression and purification was performed by Sara Linse.* A $\beta$ (MC1-42), a mutant with an extra Cys residue placed between the starting Met and Asp1 was used for fluorophore labelling. An aliquot of purified peptide monomer was dissolved in 6 M GuHCl, 10 mM DTT, pH 8.5, incubated for 1 h and the monomer was isolated by gel filtration in 20 mM sodium phosphate buffer, pH 8.0. Two molar equivalents of Alexa-647 C2 maleimide (Thermo Fisher A20347) were added from a concentrated stock in DMSO. The solution was incubated overnight in darkness on ice. Labelled monomer was isolated from free dye by two rounds of gel filtration in 20 mM sodium phosphate buffer, pH 8.0. Antibodies were labelled by mixing with Alexa-647 N-hydroxy succinimidyl ester (Thermo Fisher A20006) after gel filtration of each antibody in PBS. Two molar equivalents of Alexa-647 were added to each antibody, and the solutions were incubated for 2 h at 4°C, followed by gel filtration twice to remove free dye. The absence of free dye was confirmed using microfluidic diffusional sizing with fluorescence detection using a Fluidity One-W instrument (Fluidic Analytics Ltd, Cambridge, UK).

## A.2 Fabrication and use of microfluidic diffusion devices

The fabrication and the operation of the microfluidic diffusion device used in the present studies have been described in previous papers[9, 164]. Briefly, the microfluidic chips were fabricated by using standard soft lithography. The sample to be analysed and the buffer were introduced into the system through reservoirs connected to the inlets, and the flow rate in the channel was controlled by applying a negative pressure at the outlet by a syringe pump (Cetoni neMESYS, Korbussen, DE); at typical flow rates in the range from 90  $\mu$ l/h to 150  $\mu$ l/h. Lateral diffusion profiles were recorded at twelve different positions

(3.5 mm, 5.3 mm, 8.6 mm, 10.3 mm, 18.6 mm, 20.3 mm, 28.6 mm, 30.4 mm, 58.7 mm, 60.4 mm, 88.7 mm and 90.5 mm) by standard epifluorescence microscopy using a cooled CCD camera (Photometrics Evolve 512, Tucson, US). The diffusion profiles were fitted to model simulations based on advection-diffusion equations assuming a bimodal Gaussian distribution[164]. From the area under the curves of the two Gaussian populations, the concentrations of the bound and the free molecular chaperones were evaluated.

## **A.3 Aggregation kinetics**

### **A.3.1 $\alpha$ -synuclein**

The aggregation of 70  $\mu\text{M}$   $\alpha$ -syn in the absence and presence of 0.5  $\mu\text{M}$ , 1  $\mu\text{M}$  and 2  $\mu\text{M}$  GFP and unlabelled/labelled  $\alpha\text{B-c}$  in PBS, pH 7.2 with 0.1%  $\text{NaN}_3$  were followed by recording the increase in ThT fluorescence at 480 nm upon excitation at 440 nm. 100  $\mu\text{L}$  samples were incubated in a 96 well plate in a plate reader Fluostar Optima (BMG Labtech, Ortenberg, Germany) at 37°C. ThT concentration was 20  $\mu\text{M}$ . All aggregation experiments were operated in the presence of 5% pre-formed second generation fibrils[4].

### **A.3.2 Clusterin and proSP-C Brichos**

Aggregation reactions in the presence and absence of clusterin and proSP-C Brichos were followed by recording thioflavin T (ThT) fluorescence emission at 480 nm after excitation at 440 nm. 100  $\mu\text{L}$  samples were incubated in a Corning® (Corning, US) 96-Well (COSTAR) Half Area Black with Clear Flat Bottom Polystyrene NBS™ Microplate and measurements were recorded in a FLUOstar OPTIMA (BMG LABTECH, Ortenberg, DE) plate reader at 21°C or 37°C under quiescent conditions[42]. For seeded reactions, fibrils were freshly prepared before each experiment and mixed with freshly purified monomeric  $\text{A}\beta(\text{M1-42})$  at the desired concentrations. The concentrations of clusterin, monomeric and fibrillar  $\text{A}\beta(\text{M1-42})$  for the different experiments are reported in the main and supplementary text as well as in the captions of the figures. The concentration of ThT was 20  $\mu\text{M}$  in all experiments that I carried out at 37°C unless otherwise stated.

### A.3.3 Anti-Amyloid- $\beta$ antibodies

Monomers of A $\beta$ (1-42) or A $\beta$ (M1-42) as well as all antibodies were freshly isolated by size exclusion chromatography in experimental buffer on each day, and mixed on ice just prior to starting the kinetics experiment. The samples were loaded as multiple (3-6) replicates in a 96-well plate (Corning 3881) and the experiments were initiated by a temperature jump from zero to 37°C, thus creating supersaturated A $\beta$ 1-42 solutions. The ThT fluorescence intensity was monitored as a function of time in a plate reader (BMG Omega, Optima and Fluostar were used) with excitation at 44 nm and emission at 480 nm.

Reactions were started from 3 or 4  $\mu$ M A $\beta$ 42 monomer with 10  $\mu$ M ThT in the absence and presence of 0.00025–2  $\mu$ M <sup>ch</sup>aducanumab (a murine analog of aducanumab), 0.03–2  $\mu$ M 3D6 (the murine precursor of bapineuzumab), 0.03–2  $\mu$ M <sup>ch</sup>gantenerumab (a murine analog of gantenerumab), 0.03–2  $\mu$ M <sup>ch</sup>solaneumab (a murine analog of solanezumab) or 0.03–2  $\mu$ M isotype control, all of which were blinded. I performed at least three separate experiments as a function of antibody concentration and in each experiment there were 2-5 replicates of each condition.

### A.3.4 Kinetic analysis and simulations

*The inhibition kinetic analysis of the A $\beta$  aggregation was performed by Paolo Arosio. The inhibition kinetic analysis of A $\beta$  aggregation by therapeutic antibodies was performed by Sara Linse.* The aggregation profiles in the absence and presence of different concentrations of molecular chaperones were simulated individually according to the following equation:

$$\frac{M(t)}{M(\infty)} = 1 - \left( \frac{B_+ + C_+}{B_+ + C_+ e^{\kappa t}} \frac{B_- + C_+ e^{\kappa t}}{B_- + C_+} \right)^{\frac{\kappa_\infty^2}{\kappa \tilde{\kappa}_\infty}} e^{-\kappa_\infty t}, \quad (\text{A.1})$$

where the kinetic parameters  $B_\pm$ ,  $C_\pm$ ,  $\kappa$ ,  $\kappa_\infty$ , and  $\tilde{\kappa}_\infty$  are functions of the mass and number concentrations of seeds as well as of the two combinations of the microscopic rate constants  $k_+k_2$  and  $k_nk_2$ , where  $k_n$ ,  $k_+$ , and  $k_2$  are the rate constants of primary nucleation, elongation, and secondary nucleation, respectively[43, 43].

The microscopic rate constants in the absence of the molecular chaperones were considered equal to the values estimated in previous work[42]. The rate constants in

the presence of different concentrations of clusterin were determined by fitting the individual reaction profiles by minimising a least-squared error function defined as  $y = \sum_{i=1}^{t_{\text{exp}}} (M_{\text{sim}}(t_i) - M_{\text{exp}}(t_i))^2$ , where  $M_{\text{sim}}(t_i)$  and  $M_{\text{exp}}(t_i)$  are the simulated and the experimental total fibril mass fractions at time  $t_i$ , respectively. In the simulations shown in Fig. 2.7,  $k_n$ ,  $k_+$ , and  $k_2$  were varied individually, but in the simulations shown in the other figures, only  $k_+$  has been modified.

The experimental data in the absence and presence of clusterin were described by a second kinetic model which considers binary interactions between clusterin and fibril ends. The detailed description of the corresponding equations can be found in ref. 8. In this model, the rate constants  $k_n$ ,  $k_+$ , and  $k_2$  were assumed to be equal to the values estimated in the absence of the chaperone and considered to be independent of the concentration of clusterin, the effect of which is included in the association and dissociation rates. The association and dissociation rate constants were estimated by the global analysis of the reaction profiles at different concentrations of clusterin by minimising a least-squared error function similar to that described above[8]. The simulation reported in Fig. 2.7 e is based on a simplified expression which can be derived from this second kinetic model and relates the apparent elongation rate constant to the total concentration of chaperone ( $C_i^{\text{Tot}}$ ) and the equilibrium constant of the association reaction:[8]

$$k_+^{\text{app}}/k_+ = \frac{2 + K_{\text{eqEnd}} C_i^{\text{Tot}}}{2 + 2K_{\text{eqEnd}} C_i^{\text{Tot}} + 2 (K_{\text{eqEnd}} C_i^{\text{Tot}})^2} \quad (\text{A.2})$$

In the thesis I report the dissociation constant  $K_d = 1/K_{\text{eqEnd}}$ .

For the kinetic analysis of  $A\beta$  aggregation in chapter 2.5, the idea was to determine the microscopic process which was most inhibited in the presence of therapeutic antibodies. Therefore, experimental values were fitted assuming either specific secondary nucleation or primary nucleation. If the fitting showed a smaller root-mean-square deviation for primary nucleation, the process was determined to be most inhibited. In case of a more favourable fit for secondary nucleation, further experiments with low and high concentration of  $A\beta$  seeds needed to be conducted as similar kinetics can be compensated by elongation processes. Higher seeding conditions are dominated by elongation and therefore make it easier to distinguish between both processes.

## A.4 Sample preparation for binding experiments

### A.4.1 $\alpha$ -Synuclein

*The kinetic binding experiments of  $\alpha$ -synuclein were performed together with Jacqueline Carozza.* Fibrils were diluted to the indicated concentrations in PBS, pH 7.2 with 0.1%  $\text{NaN}_3$  and incubated with 1  $\mu\text{M}$   $\alpha\text{B-c}$ . For equilibrium experiments at 25°C, endpoint measurements were taken after 3 days. Aliquots of the chaperone-fibril system were measured on the microfluidic diffusion device at the same temperature at which they were incubated to avoid disturbing equilibrium. To minimise protein sticking to the sides of the PDMS devices, 0.1% Tween-20 was added to the flanking buffer streams (this is not expected to interfere with the sample, since contact between the sample and the buffer streams is minimal and short-lived).

### A.4.2 Clusterin and proSP-C Brichos

$\text{A}\beta(\text{M1-42})$  fibrils were generated by incubating 17  $\mu\text{M}$  monomeric  $\text{A}\beta(\text{M1-42})$  in 20 mM sodium phosphate buffer at pH 8.0 in a 96 well plate in a plate reader FLUOstar OPTIMA (BMG LABTECH) at 37°C with double orbital rotation (400 rpm). Aggregation was monitored by following the increase in the fluorescence emission of a similar sample implemented with 20  $\mu\text{M}$  ThT dye initiated upon its binding to amyloid fibrils. After completion of the aggregation reaction, the fibrils were collected, supplemented with Alexa-488-labelled clusterin in the concentration range between 0 and 4.5  $\mu\text{M}$ , and incubated for at least 2 d at 21°C to ensure equilibrium was obtained. Diffusion sizing measurements were then performed at 21°C as described below. In a second set of experiments, three more points were evaluated with the addition of BSA (at the same concentration as used in the clusterin experiments, i.e. 0.8  $\mu\text{M}$ , 2  $\mu\text{M}$  and 4.5  $\mu\text{M}$ ) added to a mixture of clusterin and fibrils as described above to examine the specificity of the binding with 17.5  $\mu\text{M}$   $\text{A}\beta(\text{M1-42})$  fibrils. The samples were analysed again by microfluidic diffusion methods.

### A.4.3 proSP-C Brichos only

A $\beta$ (M1-42) fibrils were formed by incubating a solution of 25  $\mu$ M A $\beta$ (M1-42) peptide and 20  $\mu$ M Thioflavin-T (ThT) in a non-binding 96 well plate in a plate reader Fluostar Optima (BMG Labtech, Ortenberg, Germany) at 37°C with double orbital rotation (400 rpm). The aggregation process was monitored by following the increase in the fluorescence of the ThT dye upon binding to amyloid fibrils. Aliquots of Alexa-488 labelled Brichos in the concentration range between 0 and 1.5  $\mu$ M were added to mature A $\beta$ (M1-42) fibrils and incubated for at least 2 days (see Fig. 2.15) at 21°C to ensure equilibrium conditions; for measurements in the range 27-37°C the incubation time could be decreased to 5 hours. Diffusional sizing measurements were performed at the same temperature as that of which the incubation was carried out in order not to perturb the equilibrium distribution. In order to evaluate the binding between Brichos and A $\beta$ (M1-42) fibrils during the aggregation process, samples with Alexa-488 labelled Brichos at concentrations of 0.25, 0.35 or 0.50  $\mu$ M were mixed with 24  $\mu$ M A $\beta$ (M1-42) monomers and 20  $\mu$ M ThT and incubated in a 96 well plate in a Fluostar Optima plate reader (BMG Labtech, Ortenberg, Germany) at 37°C under quiescent conditions. The aggregation kinetics were monitored by following the associated increase in ThT fluorescence. After completion of the reaction, samples were further incubated for 48 hours at 21°C and analysed by microfluidic diffusion sizing.

### A.4.4 Anti-Amyloid- $\beta$ antibodies

Antibody binding interactions were assessed by a Fluidity One-W instrument (Fluidic Analytics Ltd, Cambridge, UK) which measures the hydrodynamic radius of fluorescently labelled species in their native state in solution by microfluidic diffusional sizing, the principles of which have been described previously. Binding interactions were monitored between Alexa-647-A $\beta$ (M1-42) and unlabelled antibodies, or Alexa-647-antibodies and unlabelled A $\beta$ 1-42 fibrils. All binding measurements were performed at 27-28°C in PBS, pH 7.8. A $\beta$ 1-42 fibrils were sonicated (20/20 s on/off cycles) for 6 min on ice and shaken for 30 min at 1800 rpm before use in the binding experiments.

## A.5 Diffusion image analysis and fitting

*The derivation of the code was done by Thomas Müller and Quentin Peter. The actual analysis was done by me.* Through out the thesis two different approaches were used for analysis of diffusion images. This is caused by the evolution of the coding the analysis is based on. The procedure used for the data found in chapter 2.2-2.4 and Fig. 3.2-3.4 were processed as follows, the three-dimensional information of the 12 images taken along the diffusion channel were converted into two-dimensional profiles with intensities normalised to the intensity of the first frame. Afterwards a least square fitting to a series of simulated basis functions was applied[9, 164]. A basin hopping algorithm with a Broyden-Fletcher-Goldfarb-Shannon (BFGS) minimisation is used to find the linear combination of radii that gives the lowest residuals. Minimisations were run with an accuracy value (criteria for accepting a minimum) of  $10^{-8}$  and epsilon value (step width of optimisation) of  $10^{-8}$ . The fit is also penalised by a term multiplied by an empirically determined regularisation coefficient  $\alpha$ , which serves to reduce overfitting.

Each fit was run 10-13 times increasing  $\alpha$  from  $10^{-6}$  to  $10^{-2}$  taking three steps per order of magnitude, which causes the number of radii with non-zero coefficients to decrease and the residuals to increase as the fits become more constrained (see Supplementary Fig. B.6 a). While  $\alpha$  is low, the residuals remain almost constant since decreasing the number of radii fit to the experimental profiles does not dramatically impact the quality of the fit.

At some  $\alpha$  (the value varies for each fit), there is a relatively large increase in the residuals. The magnitude of this jump reports on whether the sample is monodisperse or polydisperse[9]. Empirically, if the residuals jump is smaller than  $10^{-7}$ , the sample is described best as monodisperse. If it is larger than  $10^{-7}$ , the sample is described best as polydisperse (see Supplementary Fig. B.6 b). The fit immediately before the jump in residuals was taken as the best fit and used for further analysis. The tunable regularisation coefficient allows me to find the simplest fit that also fully describes the data for various sets of data profiles, since the best fit differs for each.

The fitting program always includes a peak at the smallest possible radii in the range of simulated basis functions, attributing 0-10% of diffusion to this small radius. This artefact is due to a mismatch between the simulated diffusion profiles and the channel

geometry. The artefact peak was removed by summing the two remaining populations and re-calculating the percentages of free and bound chaperone.

For diffusion data in chapter 3, 4, Fig. 2.3 and Fig B.2 the analysis procedure started with the creation of two masks from the known channel and inter-channel width. These masks were shaped as the top of a Gaussian function to decrease interfaces effects. Thus, the fluorescence from the channels could be maximised while the fluorescence from the walls were minimised. The same procedure was repeated for a range of pixel sizes around the expected value with the final pixel size selected with the best channel to wall fluorescence ratio selected as being the most probable value. Afterwards, the diffusion profiles can be extracted and converted into two-dimensional profiles. Basis functions (theoretical diffusion profiles) are simulated from the first measured profile. A global fitting was used to find the best solution over all positions. The least square error between the recordings and the simulations was calculated. The best solution can be extracted from the two lowest least square errors.

The diffusion profile depends on the channel cross section, the flow rate ( $Q$ ), the detection position along the diffusion channel ( $x$ ), and the sample diffusion coefficient ( $D$ ). All these quantities can be combined to a dimensionless variable that is introduced as the amount of diffusion ( $\phi$ ):

$$\phi = x \frac{D\beta}{Q} \quad (\text{A.3})$$

This variable, together with the channel height over width ratio ( $\beta$ ) uniquely describes the diffusion system. The error on the diffusion profiles can be estimated with first order Taylor expansion of the least square equation for single measurements[195]. The standard error on the radius not only comes from the error on  $\phi$  but also on all other errors:

$$\sigma_r^2 = r^2 \left( \frac{\sigma_\phi^2}{\phi^2} + \frac{\sigma_x^2}{x^2} + \frac{\sigma_Q^2}{Q^2} + \frac{\sigma_\beta^2}{\beta^2} + \frac{\sigma_T^2}{T^2} + \frac{\sigma_\eta^2}{\eta^2} \right) \quad (\text{A.4})$$

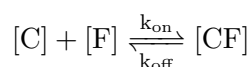
The fitting algorithm cannot account for other errors and will therefore only take the error on  $\phi$  into account, but these others error can and will have an effect on the radius estimation. In the end, the total error on the overall radius and the individual amount of each species in a bimodal distribution was determined via repeats.

## A.6 Native mass spectrometry

*The experiments were performed by Justin Benesch and Olga Tkachenko.* Spectra were acquired on a modified quadrupole-time-of-flight instrument (Waters Limited, Elstree, UK) following a previously described protocol[131]. Samples at 20  $\mu\text{M}$  were electro-sprayed from gold-coated glass capillaries made in house. The instrument parameters were as followed.  $\alpha\text{B-c WT}$ : source pressure 6.0 mbar, cone 50 V, extractor 3 V, collision gas Ar, collision energy 50 V, ToF pressure  $3.1 \cdot 10^{-6}$  mbar.  $\alpha\text{B-c-GFP}$ : as above except cone 200 V, extractor 9 V, collision gas  $\text{SF}_6$ , collision energy 200 V. Spectra are shown with linear background subtraction and Gaussian smoothing with a window of 50 points. The spectra were fit with the UniDec software using an oligomer mass list of between 5-50 subunits and a peak width of 20 m/z units[154].

## A.7 Equilibrium and kinetic curve fitting

*The derivation of the kinetic equation was done by Matthias Bellaiche and the analysis of the kinetic data is my work.* I fit the data with a non-cooperative, single-site binding model, where free chaperones C bind to free fibril binding sites F, forming a complex CF. The equilibrium between free and bound states is governed by the forward and reverse reaction rates, which are described by rate constants  $k_{\text{on}}$  and  $k_{\text{off}}$ , respectively.



The rate of the reaction can be expressed

$$\frac{d[\text{CF}]}{dt} = k_{\text{on}}[\text{C}][\text{F}] - k_{\text{off}}[\text{CF}] \quad (\text{A.5})$$

I substitute the expressions obtained from the conservation of mass  $[\text{C}] = [\text{C}_t] - [\text{CF}]$  and  $[\text{F}] = [\text{F}_t] - [\text{CF}]$  into Eq. A.5 to obtain a quadratic expression:

$$\frac{d[\text{CF}]}{dt} = k_{\text{on}}[\text{CF}]^2 - (k_{\text{on}}([\text{C}_t] + [\text{F}_t]) + k_{\text{off}}) [\text{CF}] + k_{\text{on}}[\text{C}_t][\text{F}_t] \quad (\text{A.6})$$

where  $[C_t]$  and  $[F_t]$  are the total chaperone and fibril mass concentration, respectively. At equilibrium, the forward and reverse rates are equal and therefore

$$\frac{d[CF]}{dt} = 0 \quad (\text{A.7})$$

Setting Eq. A.6 equal to zero, substituting the definition of the apparent dissociation constant  $K_D = \frac{k_{\text{off}}}{k_{\text{on}}}$ , and solving for the fractional occupancy  $\frac{[CF]}{[C_t]}$ , I arrive at the expression used to fit the equilibrium data:

$$\frac{[CF]}{[C_t]} = \frac{([F_t] + K_D + [C_t]) - \sqrt{(-[F_t] - K_D - [C_t])^2 - 4[F_t][C_t]}}{2[C_t]} \quad (\text{A.8})$$

To fit the kinetic data, I solve Eq. A.6 by the method of partial fractions to find

$$\frac{[CF]}{[C_t]} = [F_t] \frac{1 - e^{k_{\text{on}}(x_+ - x_-)t}}{x_- - x_+ e^{k_{\text{on}}(x_+ - x_-)t}} = \frac{1}{[C_t]} \frac{1 - \exp(k_{\text{on}}(x_+ - x_-)t)}{x_+^{-1} - x_-^{-1} \exp(k_{\text{on}}(x_+ - x_-)t)} \quad (\text{A.9})$$

where

$$x_{\pm} = \frac{k_{\text{on}}([C_t] + [F_t]) + k_{\text{off}} \pm \sqrt{k_{\text{on}}^2([C_t] - [F_t])^2 + k_{\text{off}}^2 + 2k_{\text{on}}k_{\text{off}}([C_t] + [F_t])}}{2k_{\text{on}}} \quad (\text{A.10})$$

In this expression, I constrain the value of  $[C_t]$  and take the following terms as fitting parameters:  $k_{\text{on}}$ ,  $k_{\text{off}}$ , and  $[F_t]$ , as I do not know the actual number of fibril binding sites.

In the limit where time recovers infinity, Eq. A.9 goes to the equilibrium solution (Eq. A.8).

The binding stoichiometry, describing the amount of  $\alpha$ -synuclein molecules per single  $\alpha$  B-crystallin molecule, is derived from

$$\frac{\alpha\text{-synuclein molecules}}{\alpha\text{B-crystallin molecule}} = \frac{[\alpha\text{-synuclein}_{\text{total}}]}{[F_t]} \quad (\text{A.11})$$

where  $[\alpha\text{-synuclein}_{\text{total}}]$  is the total concentration of monomeric  $\alpha$ -synuclein equivalents used.

## A.8 Determination of Binding parameters

### A.8.1 Curve fitting to obtain thermodynamic and kinetic parameters of $\alpha$ -synuclein

The van't Hoff equation gives the relationship between the equilibrium constant  $K_{\text{eq}}$  (related to the apparent dissociation constant by  $K_{\text{eq}} = 1/K_{\text{D}}$ ) and temperature  $T$ :

$$\frac{d \ln K_{\text{eq}}}{d(1/T)} = -\frac{\Delta H}{R} \quad (\text{A.12})$$

where  $\Delta H$  is the enthalpy, and  $R$  is the gas constant. I arrive at the linear form of the van't Hoff equation, using  $K_{\text{D}}$  instead of  $K_{\text{eq}}$  by combining Eq. A.12 with the relationship between Gibbs free energy and the equilibrium constant  $\Delta G = -RT \ln K_{\text{eq}}$ , and the definition of Gibbs free energy  $\Delta G = \Delta H - T\Delta S$ :

$$\ln K_{\text{D,app}} = \frac{\Delta H}{RT} - \frac{\Delta S}{R} \quad (\text{A.13})$$

By adding the contribution of the change in heat capacity  $\Delta C_{\text{p}}$  to the enthalpy and entropy (Eq. A.14 and A.15)

$$\Delta H = \Delta H_{\text{Tref}} + \Delta C_{\text{p}}(T - T_{\text{ref}}) \quad (\text{A.14})$$

$$\Delta S = \Delta S_{\text{Tref}} + \Delta C_{\text{p}}(\ln T - \ln T_{\text{ref}}) \quad (\text{A.15})$$

I derive:

$$\ln K_{\text{D,app}} = \frac{\Delta H_{\text{Tref}}}{RT} - \frac{\Delta S_{\text{Tref}}}{R} + \frac{\Delta C_{\text{p}}}{R} \left(1 - \frac{T_{\text{ref}}}{T}\right) - \frac{\Delta C_{\text{p}}}{R} \ln \left(\frac{T}{T_{\text{ref}}}\right) \quad (\text{A.16})$$

where  $\Delta H_{\text{Tref}}$  and  $\Delta S_{\text{Tref}}$  are the enthalpy and entropy changes at a reference temperature. The reference temperature  $T_{\text{ref}}$  is chosen to be 310 K.

I also estimate the free energy barrier of the binding reaction from this data set by constructing a model, which combines polymer theory and Kramer's problem of escape

from a metastable state considering the change in association rate constant  $k_{\text{on}}$  of  $\alpha\text{B-c}$  binding to the fibrils ( $\Phi$ ) as a function of temperature[32].

$$k_{\text{on}} = 1000 \cdot D \cdot N_A \cdot r_{\text{eff}} \cdot e^{-\beta\Delta G^\ddagger} = 1000 \cdot D \cdot N_A \cdot r_{\text{eff}} \cdot e^{-\beta\Delta H^\ddagger} e^{\beta T\Delta S^\ddagger} \quad (\text{A.17})$$

In order to respect the contribution of the heat capacity change to the activated state  $\Delta C_p^\ddagger$  I combined Eq. A.14, A.15 and A.17 to:

$$k_{\text{on}} = 1000 \cdot D \cdot N_A \cdot r_{\text{eff}} \cdot e^{-\beta\Delta H_{\text{Tref}}^\ddagger + \Delta C_p^\ddagger(T - T_{\text{ref}})} e^{\beta T\Delta S_{\text{Tref}}^\ddagger + \Delta C_p^\ddagger(\ln T - \ln T_{\text{ref}})} \quad (\text{A.18})$$

$D$  is the diffusion constant of a segment of the protein (comprising 3 amino acids, the Kuhn length of a polypeptide chain) and has a numerical value of approx.  $5 \cdot 10^{-10} \text{m}^2 \text{s}^{-1}$ ,  $N_A$  is the Avogadro constant and  $r_{\text{eff}}$  is the characteristic distance that can be computed from

$$r_{\text{eff}} = \frac{b_0}{\pi\sqrt{2n}} \quad (\text{A.19})$$

with  $b_0$  being around 1 nm, the Kuhn length of a polypeptide chain, and  $n$  the number of protein residues.

### A.8.2 Thermodynamic equilibrium analysis of proSP-C Brichos

The dissociation constant  $K_D$  was calculated by direct non-linear regression based on the Scatchard equation[240]

$$[\text{Brichos}_{\text{bound}}] = \frac{[\text{Brichos}_{\text{free}}] \cdot [M]}{K_D + [\text{Brichos}_{\text{free}}]} \quad (\text{A.20})$$

where  $M$  is the total concentration of binding sites available on an  $A\beta(\text{M1-42})$  fibril surface, representing the maximum concentration of bound molecular chaperone,  $\text{Brichos}_{\text{bound}}$  and  $\text{Brichos}_{\text{free}}$  are the concentrations of the bound and free chaperone, respectively, evaluated by the size distributions measured by the microfluidic diffusion technique. The binding stoichiometry, describing the amount of  $A\beta(\text{M1-42})$  molecules within the fibril bound per single proSP-C Brichos molecule, is derived from

$$\frac{\text{A}\beta(\text{M1-42}) \text{ molecules}}{\text{proSP-C Brichos molecule}} = \frac{[\text{A}\beta(\text{M1-42})_{\text{total}}]}{[\text{M}]} \quad (\text{A.21})$$

where  $[\text{A}\beta(\text{M1-42})_{\text{total}}]$  is the total concentration of monomeric  $\text{A}\beta(\text{M1-42})$  equivalents used. The standard binding free energy, enthalpy and entropy ( $\Delta G^\ominus$ ,  $\Delta H^\ominus$  and  $\Delta S^\ominus$ , respectively) were calculated by linear regression to the van't Hoff equation:

$$\log(K_D) = \frac{\Delta H^\ominus}{R \cdot T} - \frac{\Delta S^\ominus}{R} \quad (\text{A.22})$$

where  $K_D$  is the dissociation constant,  $R$  is the gas constant and  $T$  is the temperature, in combination with the Gibbs-Helmholtz equation:

$$\Delta G^\ominus = \Delta H^\ominus - T\Delta S^\ominus \quad (\text{A.23})$$

assuming  $\Delta H^\ominus$  and  $\Delta S^\ominus$  to be temperature independent.

### A.8.3 Binding constant determination for anti-Amyloid- $\beta$ antibodies

Equilibrium binding parameters (affinity and stoichiometry) were obtained by fitting directly to the raw data. Because relatively dilute solutions used, activities were replaced with concentrations and the apparent dissociation constant  $K_D$  was estimated by global non-linear regression to the measured quantities,  $I_D$  and  $I_N$ , using the following equations:

$$I_D = I_{D1} + (I_{D2} - I_{D1}) \cdot \frac{0.5(nL_{\text{tot}} - K_D - C_P) + \sqrt{0.25(nL_{\text{tot}} - K_D - C_P)^2 + nL_{\text{tot}}K_D}}{K_D + 0.5(nL_{\text{tot}} - K_D - C_P) + \sqrt{0.25(nL_{\text{tot}} - K_D - C_P)^2 + nL_{\text{tot}}K_D}} \quad (\text{A.24})$$

$$I_N = I_{N1} + (I_{N2} - I_{N1}) \cdot \frac{0.5(nL_{\text{tot}} - K_D - C_P) + \sqrt{0.25(nL_{\text{tot}} - K_D - C_P)^2 + nL_{\text{tot}}K_D}}{K_D + 0.5(nL_{\text{tot}} - K_D - C_P) + \sqrt{0.25(nL_{\text{tot}} - K_D - C_P)^2 + nL_{\text{tot}}K_D}} \quad (\text{A.25})$$

where  $C_P$  is the total concentration of labelled protein (monomer or antibody),  $I_{D1}$  and  $I_{N1}$  are the intensities of labelled protein in the respective half of the channel.  $I_{D2}$  and  $I_{N2}$  is the intensity of labelled protein-ligand complex (monomer-antibody or antibody-fibril) in the respective half of the channel, and  $n$  is the stoichiometry of the interaction. For data with Alexa-647-labelled  $\text{A}\beta(1-42)$  monomer,  $n$  was fixed to 2, while  $I_{D1}$ ,  $I_{D2}$

and  $K_D$  were fitted parameters. For data with Alexa-647 labelled antibodies,  $n$ ,  $I_{N1}$ ,  $I_{N2}$  and  $K_D$  were fitted parameters.

After fitting, the fractional saturation of the labelled species,  $Q$ , was calculated from each data point,  $I_D$  or  $I_N$ , using the fitted values of  $I_{D1}$  and  $I_{D2}$ , or  $I_{N1}$  and  $I_{N2}$  as follows

$$Q = \frac{I_D - I_{D1}}{I_{D2} - I_{D1}} \quad (\text{A.26})$$

$$Q = \frac{I_N - I_{N1}}{I_{N2} - I_{N1}} \quad (\text{A.27})$$

The average of these two values was plotted versus free ligand concentration, which was calculated at each total concentration of added ligand,  $C_L$ , as follows:

$$[L] = 0.5(nL_{tot} - K_D - C_P) + \sqrt{0.25(nL_{tot} - K_D - C_P)^2 + nL_{tot}K_D} \quad (\text{A.28})$$

using in the case of Alexa-647- $A\beta(1-42)$  interacting with antibody the fitted value of  $K_D$  and the fixed value of  $n$  and  $C_P$ , and in the case of Alexa-antibody interaction with fibrils the fitted values of  $n$  and  $K_D$  and the fixed value of  $C_P$ . Based on the ratio of the  $I_N$  and  $I_D$ , the instrument reports an apparent hydrodynamic radius of the fluorescent labelled species.

## A.9 Immunogold-labelling Transmission Electron Microscopy (TEM)

*The experiments were performed by Janet Kumita. The actual quantification was performed by me.*  $A\beta(M1-42)$  fibrils (1.5  $\mu\text{M}$   $A\beta(M1-42)$  monomer equivalents) were incubated with BSA (1  $\mu\text{M}$ ; NEB) in 20 mM phosphate buffer, pH 8.0 (10 min, RT). Clusterin (0.15  $\mu\text{M}$ ) was added to the solution and this was further incubated (10 min, RT). The fibril sample was centrifuged (15,000 rpm, 20 min, 4°C) and the supernatant was removed. The pellet was resuspended in PBS containing 0.01% (v/v) Triton and 0.01% (v/v) Tween-20 (15  $\mu\text{L}$ ) then the sample was centrifuged (15,000 rpm, 20 min, 4°C). The pellet was resuspended in PBS (10  $\mu\text{L}$ ). For the sonicated samples,  $A\beta(M1-42)$

fibrils (1.5  $\mu\text{M}$ ) were sonicated using a probe sonicator (Bandelin, Sonopuls HD 2070) for 1 min with 10% maximum power and 30% cycles prior to incubation with BSA and clusterin. The prepared fibril samples (5  $\mu\text{L}$ ) were applied to a carbon support film, 400 mesh, 3 mm nickel grid (EM Resolutions Ltd., Saffron Walden, UK) and incubated (5 min, RT). The grid was blocked with 1 mg/ml BSA in PBS for 15 min and incubated with 1:100 G7 mouse anti-human-clusterin monoclonal antibody (2 mg/ml stock solution) in PBS for 30 min. For the secondary antibody only negative controls, samples were incubated with PBS only at this step. The grid was washed (3 X 5 min); first in PBS/0.01%Triton/0.01%Tween-20 and then twice with PBS only, followed by incubation with 1:500 gold labelled, anti-mouse secondary antibody (BBI Solutions, Cardiff, UK) in PBS for 30 min. Finally, the grid was washed three times as described above, twice with water and then incubated for 2 min with 2% uranyl acetate (w/v). In order to remove excess uranyl acetate, the grid was washed twice with water and dried completely before imaging. The fibrils were imaged on a FEI Tecnai G2 transmission electron microscope (Cambridge Advanced Imaging Centre, University of Cambridge, UK). Images were analysed using the SIS Megaview II Image Capture system (Olympus, Tokyo, JP).

In order to quantify the amount of immunogold labels per fibril mass, a ratio of counted particles in a frame and the area occupied by aggregates were formed. Therefore, using ImageJ, the TEM image threshold was set to "Shanbhag" auto threshold and further applying the "analyze particles" function. The particle analysis settings were pixel size 1000-infinity and circularity 0-2. The sum of all quantified particles per frame was used for quantification[208].

## **A.10 SDS-PAGE analysis**

SDS-PAGE electrophoresis was run with Novex NuPAGE SDS-PAGE Gel System (Life Technologies). Brichos samples were incubated for 17 h at 30°C and loaded in the gel together with a Brichos sample at the same concentration which was freshly defrozen as a control. Samples were analysed under both reducing and non-reducing conditions. Samples under reducing conditions were analysed by Coomassie blue staining, while samples under non-reducing conditions were analysed by fluorescence detection by using a Typhoon Trio variable-mode imager (GE Healthcare, Little Chalfont, UK).

# Chapter B

---

## Supplementary information

---

**Table B.1:** Summary of the kinetic parameters  $k_{\text{on}}$  and  $k_{\text{off}}$  and the dissociation constants  $K_{\text{d}}$  for the binding of  $\alpha\text{B-c}$  to  $\alpha\text{-syn}$  fibrils at different temperatures. Values were obtained by fitting the kinetic data to Eq.

A.9 (Materials and Methods). Note that at 37°C where the binding curve reaches saturation, the value for  $k_{\text{off}}$  and therefore also the value of  $K_{\text{d}}$  obtained from the fit is subjected to be more error prone than the other dissociation constants at lower temperatures. The fit still gives us an estimate of the binding affinity, and still reports

T (°C)	$\alpha\text{B-c}$		
	$k_{\text{on}}$ ( $\text{M}^{-1}\text{s}^{-1}$ )	$k_{\text{off}}$ ( $\text{s}^{-1}$ )	$K_{\text{d}}$ (nM)
7	$0.6 \pm 0.4$	$2.6 \times 10^{-5} \pm 1.6 \times 10^{-5}$	$45310 \pm 15890$
10	$0.3 \pm 0.1$	$4.2 \times 10^{-6} \pm 6.3 \times 10^{-7}$	$12330 \pm 4465$
17	$0.7 \pm 0.3$	$4.1 \times 10^{-6} \pm 1.9 \times 10^{-6}$	$6118 \pm 2722$
20	$2.4 \pm 0.9$	$9.8 \times 10^{-6} \pm 2.8 \times 10^{-6}$	$4075 \pm 1701$
25	$7.1 \pm 2.6$	$2.7 \times 10^{-6} \pm 8.6 \times 10^{-7}$	$373 \pm 238$
30	$31.4 \pm 12.9$	$1.8 \times 10^{-6} \pm 1.1 \times 10^{-6}$	$58 \pm 53$
37	$199.5 \pm 86.8$	$1.2 \times 10^{-16} \begin{smallmatrix} +1.9 \times 10^{-6} \\ -1.2 \times 10^{-16} \end{smallmatrix}$	$\leq 10$

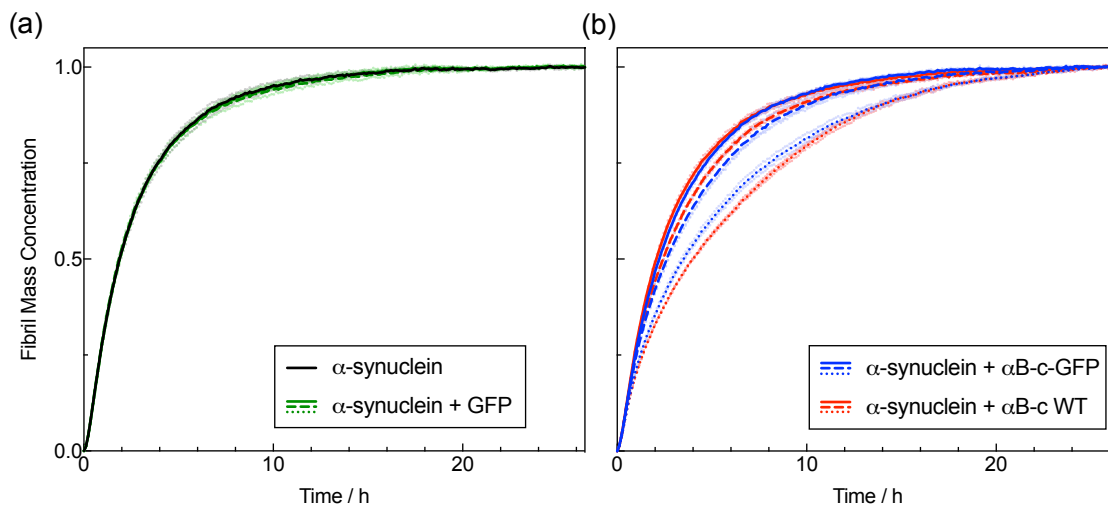


**Figure B.1:** Kinetic reaction profiles of 70  $\mu\text{M}$   $\alpha\text{-syn}$  solutions are shown (a) in the absence (black curve) or in the presence of either 0.5  $\mu\text{M}$  (solid curve), 1  $\mu\text{M}$  (dashed curve) and 2  $\mu\text{M}$  (dotted curve) of GFP (green curves) or (b) unlabelled/labelled  $\alpha\text{B-c}$  including 5% seeds in PBS, pH 7.2 with 0.1%  $\text{NaN}_3$  (red and blue, respectively). Each curve is an average of three independent measurements with individual measured points shown in each plot (faded colors).

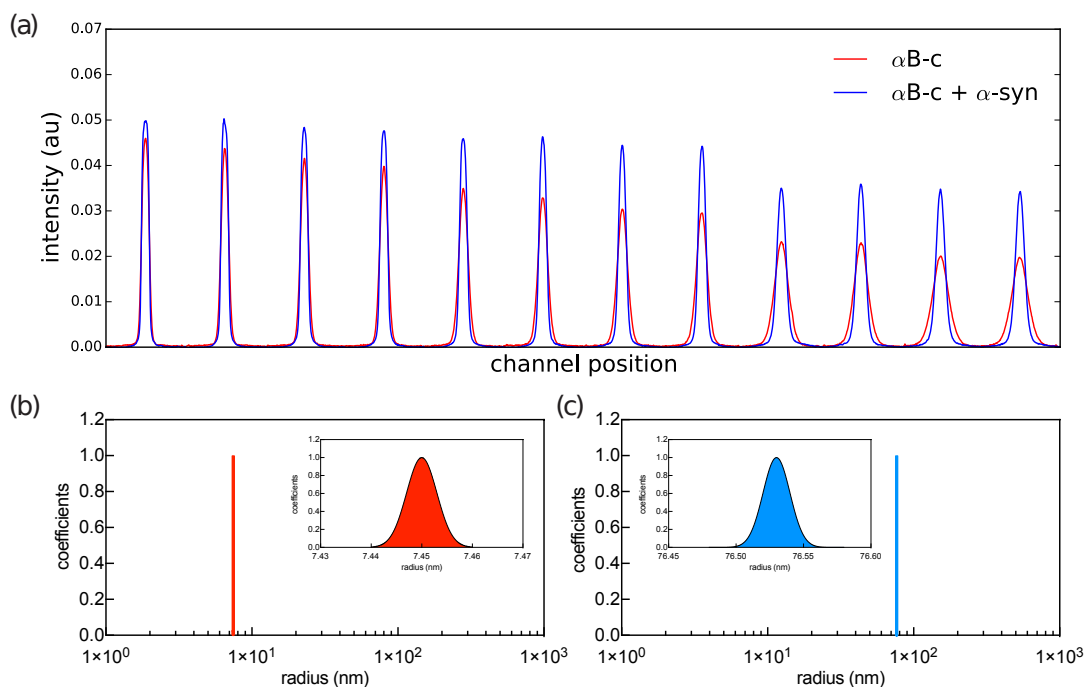


**Figure B.2:** (a) Complete set of 12 diffusion profiles for  $\alpha\text{B-c}$  alone and  $\alpha\text{B-c}$  incubated with  $\alpha\text{-syn}$  fibrils and exhibiting 100% binding. Histograms of the sample size distribution for (b)  $\alpha\text{B-c}$  alone and (c)  $\alpha\text{B-c}$  with  $\alpha\text{-syn}$  fibrils. Inserts in b) and c) show error distribution of the individual radii determined by first order Taylor expansion of the least square equation.

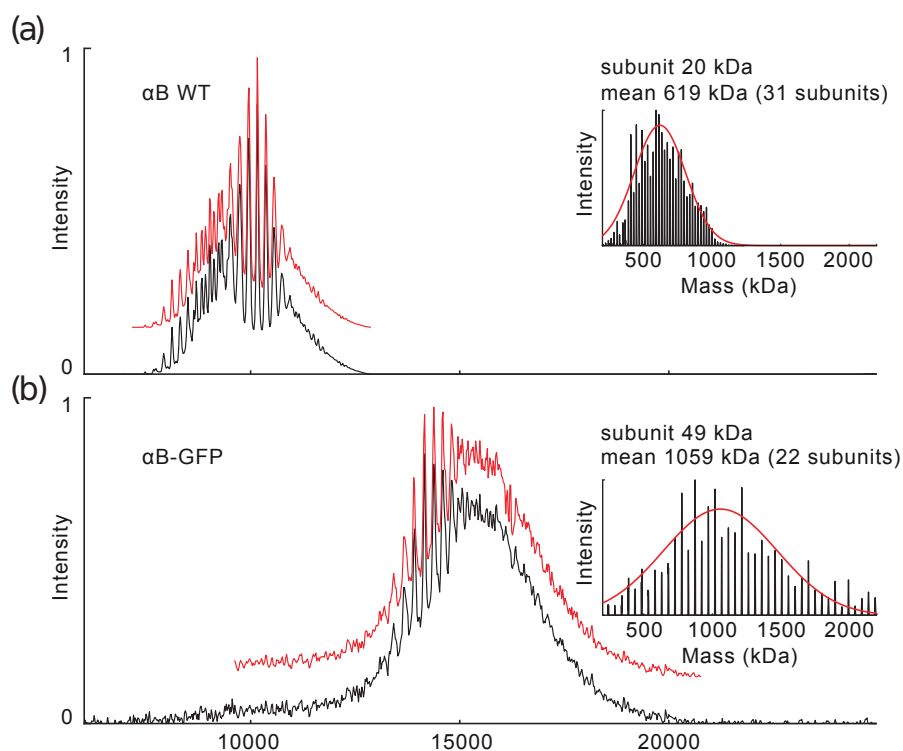


**Figure B.3:** Native mass spectrometry of (a) wild-type  $\alpha$ B-c and (b)  $\alpha$ B-c-GFP fusion. The mass spectra are shown in black with a Bayesian deconvolution fit in red[154]. Charge-deconvoluted mass distributions underlying the fit are shown as insets. The mean and standard deviation for the fit mass distributions was  $619 \pm 187$  kDa ( $31.0 \pm 9.3$  subunits) for  $\alpha$ B-c WT and  $1059 \pm 417$  kDa ( $21.6 \pm 8.5$  subunits) for  $\alpha$ B-c-GFP. Please note that, at this mass spectral resolution, the fit enables only an estimate of the average mass distribution and detailed interpretation of relative intensities of the different oligomers is not appropriate.

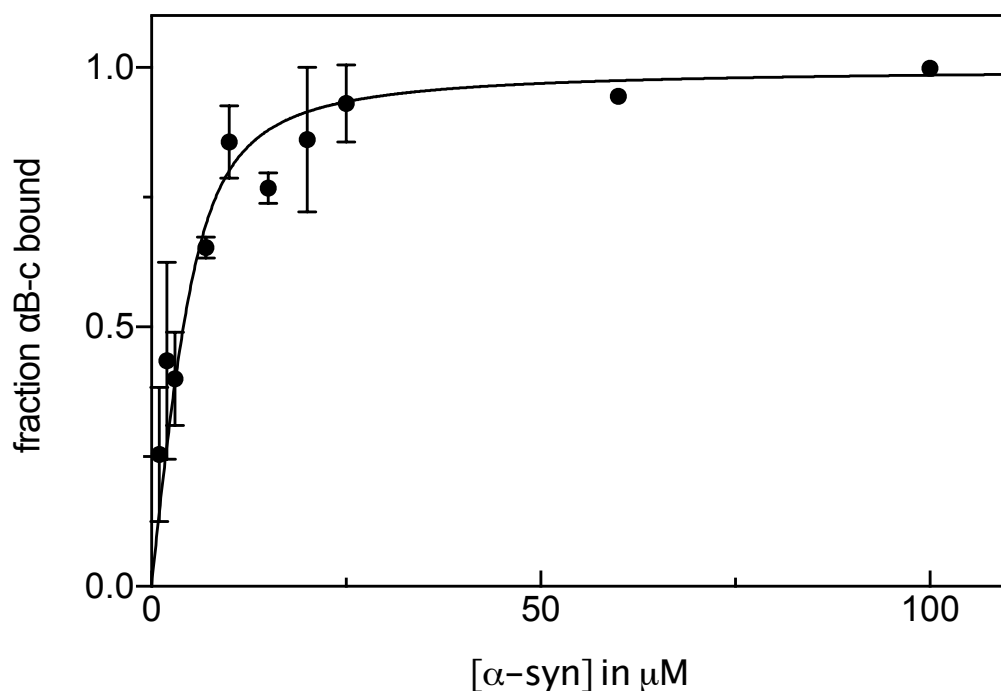


**Figure B.4:** The chaperone  $\alpha\text{B-c}$  binds to  $\alpha$ -syn fibrils in the high nanomolar affinity range  $K_{\text{D},25^{\circ}\text{C}} = 261 \pm 76$  nM. The concentration of  $\alpha\text{B-c}$  was kept at  $1 \mu\text{M}$  and the concentration of  $\alpha$ -syn fibrils was varied over two orders of magnitude to obtain a titration curve, and the data were fit according to a single-site binding model, with an  $\alpha$ -syn binding site ratio of 0.186 binding sites per  $\alpha$ -syn monomer. The fit gives a  $R^2 = 0.903$ .

Error bars represent standard deviations from at least two independent measurements.

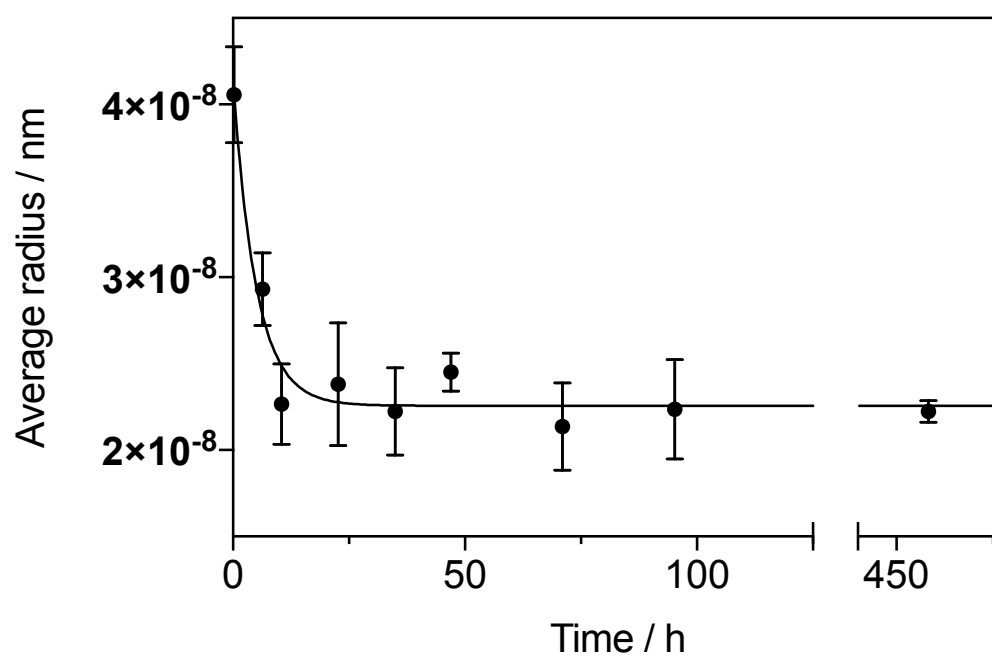


**Figure B.5:** Dissociation kinetic of  $\alpha$ B-c ( $1 \mu\text{M}$ ) in a saturated  $\alpha$ -syn fibril solution at  $7^\circ\text{C}$ . The data was fitted to a one phase exponential decay equation and the rate constant is  $k_{\text{off},7^\circ\text{C}} = 5.6 \times 10^{-5} \pm 1.2 \times 10^{-5} \text{ s}^{-1}$  with  $R^2 = 0.95$ .

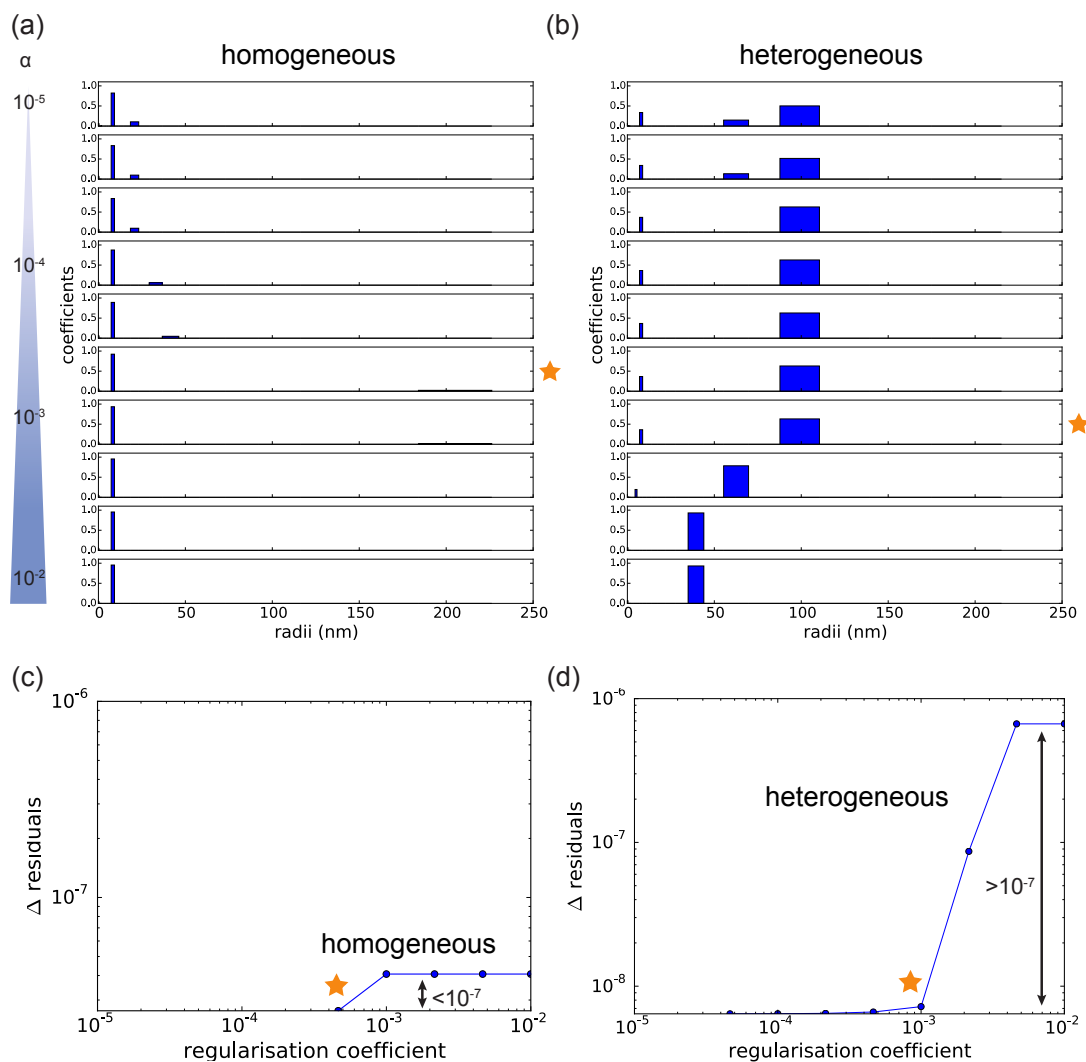


**Figure B.6:** Representative fits for (a) homogeneous ( $\alpha$ B-c alone) and (b) heterogeneous compositions ( $\alpha$ B-c incubated with fibrils), exhibiting binding. Higher regularisation coefficients penalise the number of individual components considered in the fitting. The change in the residuals relative to the sum of the residuals of the first fit ( $\alpha = 10^{-5}$ ) for the homogeneous (c) and heterogeneous (d) samples plotted against  $\alpha$  demonstrate that there is some critical value of  $\alpha$ , at which point there is a jump and the experimental profiles are no longer well described by the fit. The magnitude of that jump reports on whether the samples are homogeneous or heterogeneous (the cutoff value is  $\alpha \approx 10^{-7}$ ). The fit immediately before the jump in residuals (marked with a star) is taken as the best fit for that set of profiles.

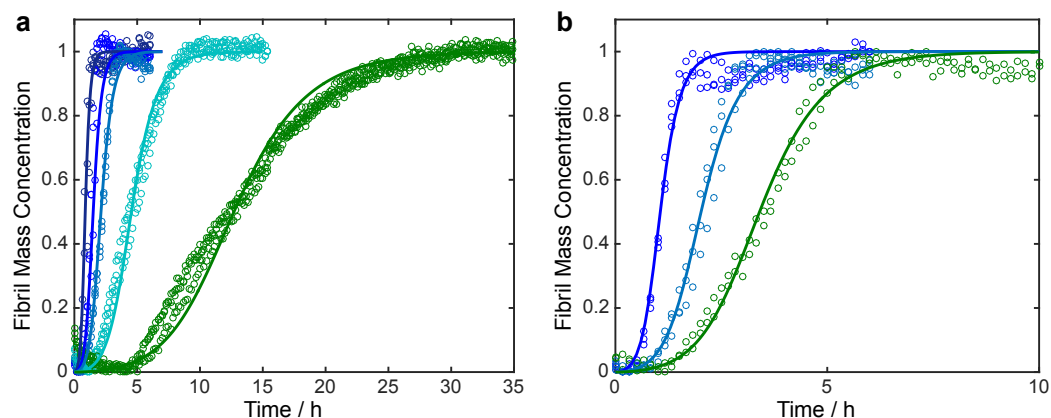


**Figure B.7:** Analysis of the effects of clusterin on the aggregation kinetics of  $A\beta(M1-42)$  at  $37^\circ\text{C}$ . (a) Kinetic reaction profiles at  $37^\circ\text{C}$  for the aggregation of  $3\ \mu\text{M}$   $A\beta(M1-42)$  solutions are shown from left (blue) to right (green) in the absence and presence of  $7.5\ \text{nM}$ ,  $37\ \text{nM}$ ,  $75\ \text{nM}$  and  $150\ \text{nM}$  of clusterin. Continuous lines represent integrated rate laws where the elongation rate constant has been specifically inhibited. b) Same as in a) in the absence and presence of  $37\ \text{nM}$  and  $75\ \text{nM}$  of clusterin. The average least-squares error function of these simulations, defined in the Materials and Methods section, is  $0.1$ .

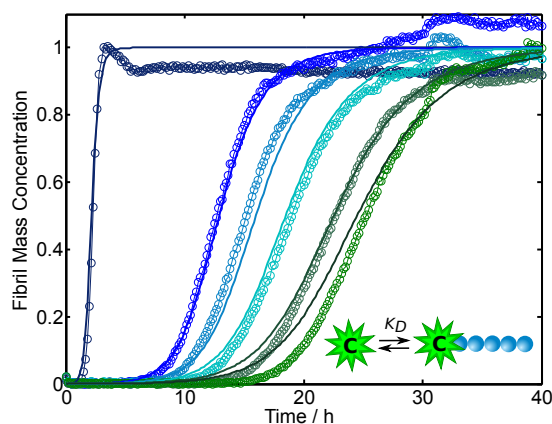


**Figure B.8:** Analysis of the effects of clusterin on the aggregation kinetics of  $A\beta(M1-42)$  at  $21^\circ\text{C}$ .  $A\beta(M1-42)$  aggregation kinetics are shown from left (blue) to right (green) in the absence and presence of  $40\ \text{nM}$ ,  $60\ \text{nM}$ ,  $80\ \text{nM}$ ,  $120\ \text{nM}$  and  $140\ \text{nM}$  of clusterin (symbols) with an  $A\beta(M1-42)$  monomer concentration of  $4\ \mu\text{M}$ . The data was globally fitted similar to the procedure at  $37^\circ\text{C}$  in Fig. S2 (continuous lines) in order to determine the dissociation constant  $K_{D,21^\circ\text{C}} = 1\ \text{nM}$  at this temperature.

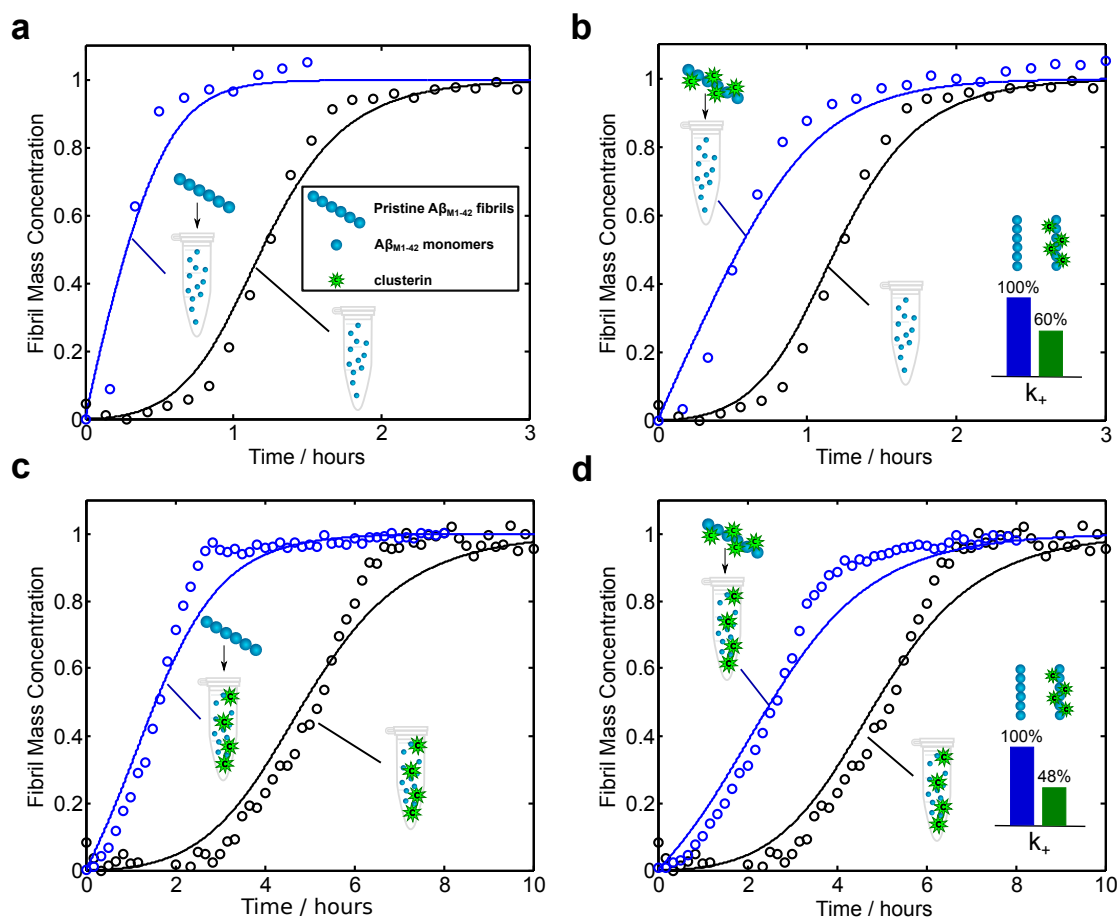


**Figure B.9:** Seeding experiments of  $A\beta(M1-42)$  in the presence and absence of clusterin. Aggregation profiles of reactions where pre-formed  $A\beta(M1-42)$  fibrils, grown in the presence or absence of clusterin, were added to monomeric solutions of  $A\beta(M1-42)$  in the presence or absence of the chaperone. (a) Pristine fibrils that had never been exposed to the chaperone (blue  $\circ$ ) were able to accelerate the aggregation reaction of  $A\beta(M1-42)$  monomers compared to the kinetics in the absence of added pre-formed fibrils (black symbols). (b) Fibrils grown in the presence of 37 nM clusterin (blue  $\circ$ ) did not accelerate the reaction to the same extent as pristine fibrils when added to monomer without the chaperone in solution (black  $\circ$ ), showing that clusterin binds to fibrils. (c, d) Clusterin added in solution is able to arrest the reaction and prevent the acceleration due to added fibrils (blue  $\circ$ ) even when the latter were grown in the absence of chaperone. The solution concentrations of  $A\beta(M1-42)$  and clusterin were  $2\ \mu\text{M}$  and 37 nM, respectively. The amount of added seeds has been 5% w/w for all seeded experiments. The dashed lines show predictions for the reaction profiles of seeded and unseeded reactions assuming (a) the value of the elongation rate constant measured previously in the absence of the chaperone, (b) the value in (a) reduced to 60% of its value, and (c,d) the elongation rate reduced to 48% with additional chaperones in the  $A\beta(M1-42)$  monomer solution.

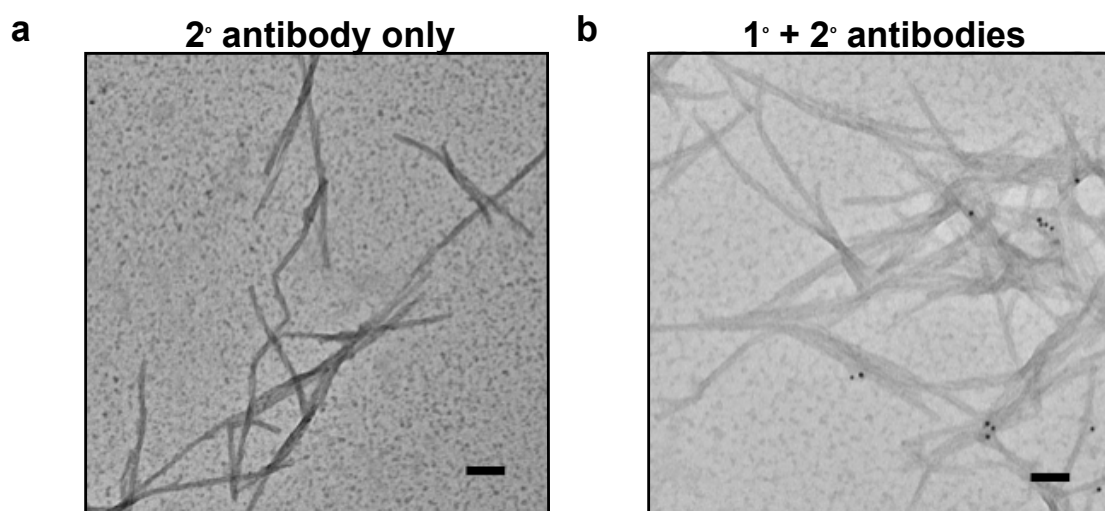


**Figure B.10:**  $A\beta$ (M1-42) fibrils formed in the presence of BSA and clusterin and probed for clusterin interaction using immunogold TEM. (a) sample probed with only the secondary antibody conjugated to a gold particle showing no non-specific labelling; (b) fibrils probed with an anti-clusterin monoclonal antibody followed by an anti-mouse secondary antibody conjugated to a gold particle. Black dots indicate the presence of clusterin interacting with the fibrils. Scale bar is 100 nm.

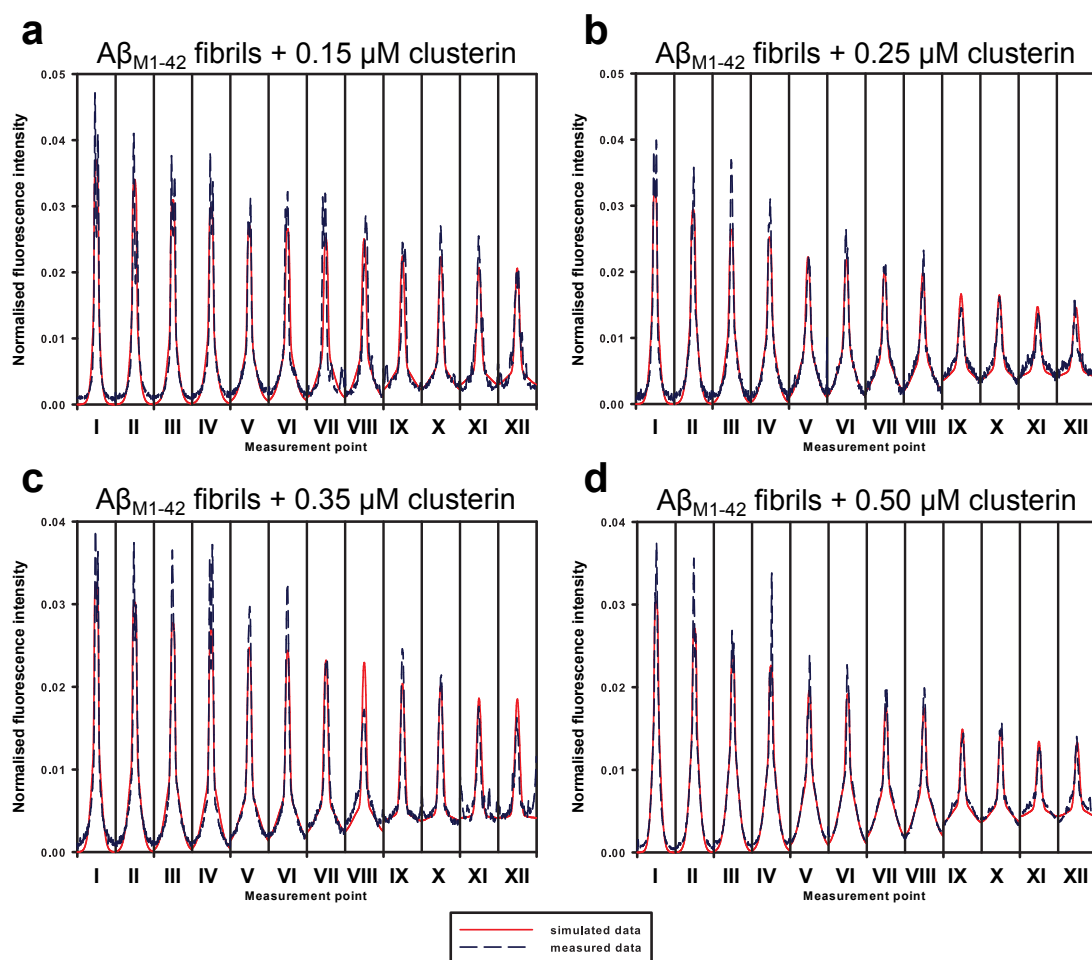


**Figure B.11:** Diffusion profiles of specific samples at twelve different positions in a microfluidic device. (a-d) Representative fluorescence diffusion profiles corresponding to solutions of  $17 \mu\text{M}$   $A\beta(M1-42)$  fibrils in the presence of different clusterin concentrations acquired at twelve different positions along the channel. The simulated diffusion profiles (red lines) were fitted to the measured data (black dashed lines) by a least square fit.

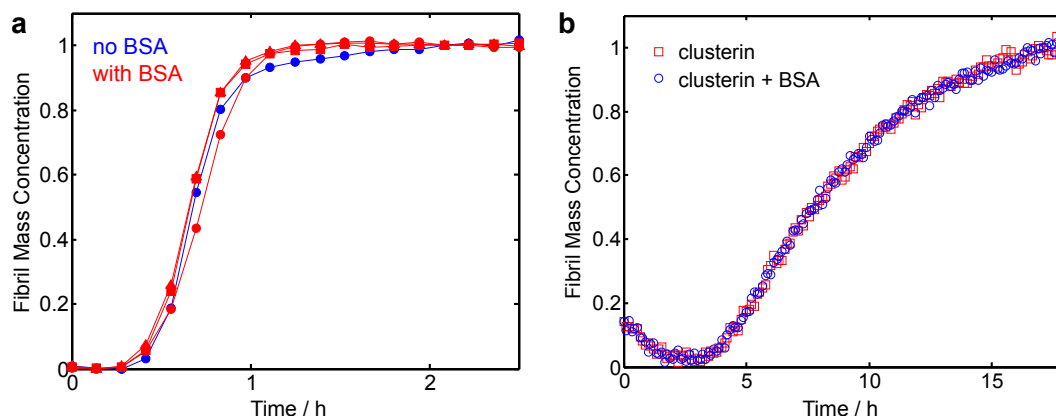


**Figure B.12:** Analysis of interfering effects of transient proteins on clusterins inhibition activity. (a) Kinetic reaction profiles for the aggregation of 2 μM Aβ(M1-42) in the absence (blue symbols) and presence (red symbols) of 7.5 nM, 37 nM and 75 nM of bovine serum albumin (BSA). (b) Same as in (a) but in the presence of 75 nM of BSA and 75 nM of clusterin, showing that the presence of BSA does not affect the inhibition activity of clusterin.

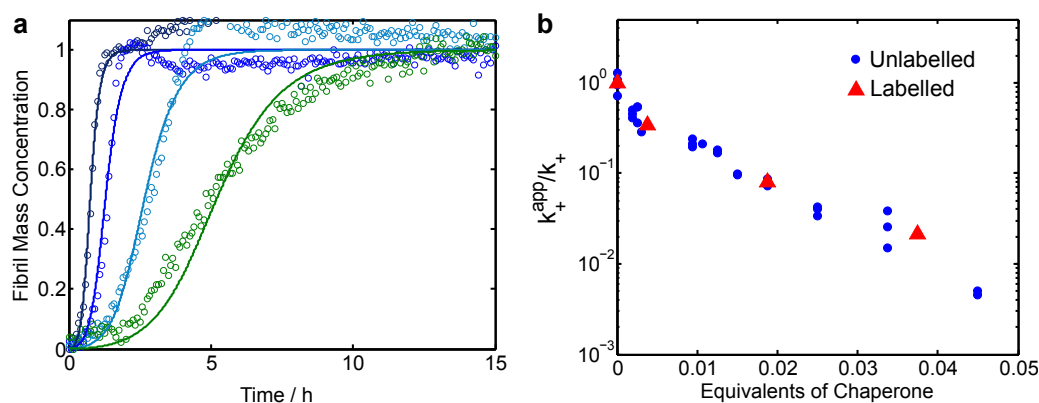


**Figure B.13:** Effects of the fluorescent label of clusterin on the inhibition process on Aβ(M1-42) aggregation. (a) Kinetic reaction profiles for the aggregation of 2 μM Aβ(M1-42) solutions are shown from left (blue) to right (green) in the absence and presence of 7.5 nM, 37 nM and 75 nM of labelled clusterin. Continuous lines represent model simulations where the elongation rate constant has been specifically inhibited; (b) The decrease in the apparent elongation rate constant as a function of molecular chaperone concentration is similar for labelled and unlabelled clusterin.

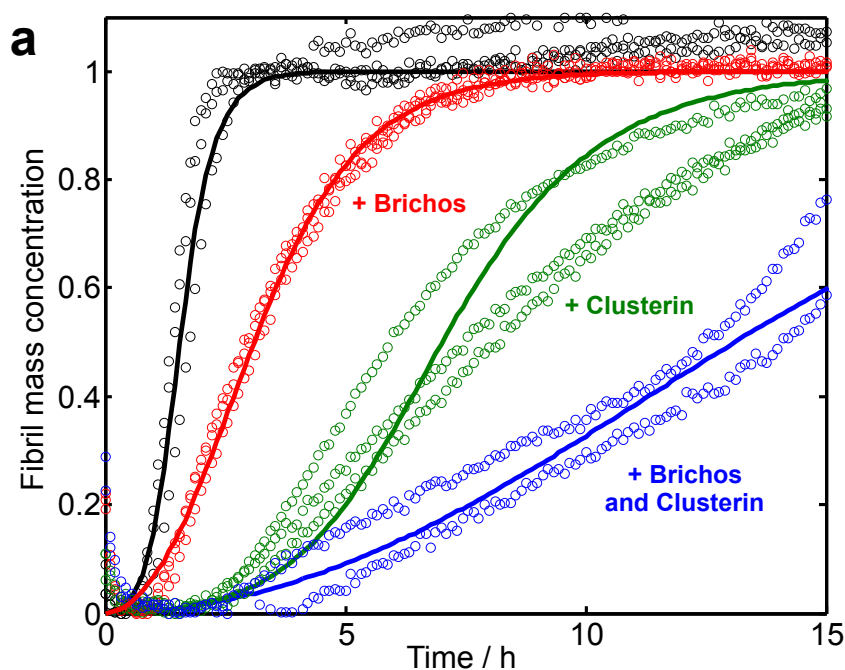


**Figure B.14:** Kinetic analysis on the aggregation kinetics of  $A\beta(M1-42)$  in the presence of Brichos and clusterin separately and combined. Kinetic reaction profiles for the aggregation of  $2.5 \mu\text{M}$   $A\beta(M1-42)$  solutions in 20 mM sodium phosphate buffer at pH 8.0 in the absence and presence of 37 nM clusterin and  $3 \mu\text{M}$  proSP-C Brichos, added either individually or together as indicated at  $37^\circ\text{C}$ . Continuous lines represent model simulations where either the elongation rate constant (green line), secondary nucleation constant (red line) or both (blue line) have been selectively inhibited.

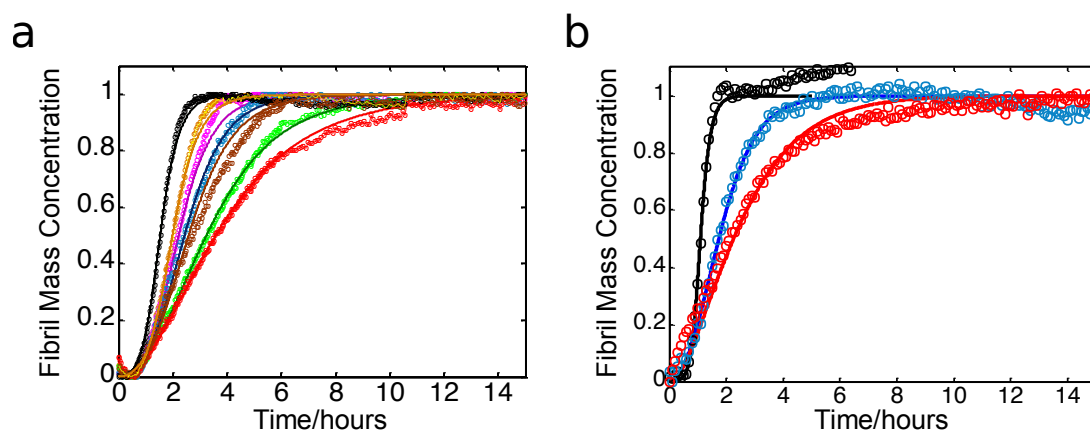


**Figure B.15:** (a) Kinetic reaction profiles of  $3 \mu\text{M}$   $A\beta_{42}$  solutions are shown from left to right for reactions in the absence of Brichos and with 10%, 22%, 35%, 50%, 75% and 100%  $A\beta(M1-42)$  monomer equivalents of unlabelled Brichos. (b) A similar  $A\beta(M1-42)$  aggregation behaviour was observed in the presence of Alexa-488 labelled Brichos. Shown from left to right are kinetic profiles without Brichos and with 50% and 100%  $A\beta_{42}$ -monomer equivalents of Alexa-488 labelled Brichos.

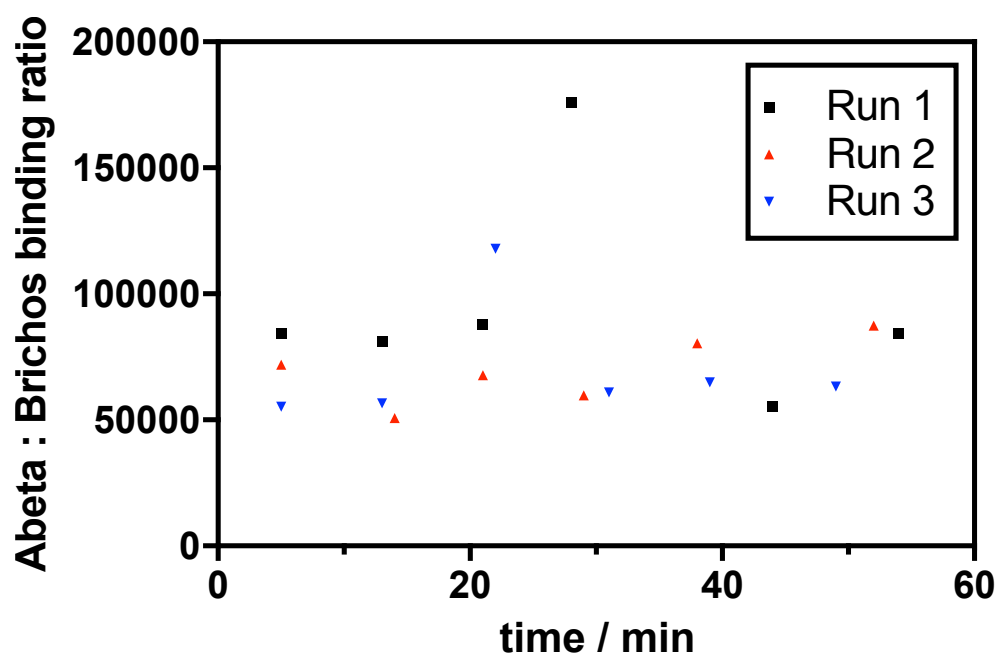


**Figure B.16:** Kinetics of Brichos binding to  $A\beta(M1-42)$  fibrils measured with Fluidity One-W. The kinetic was measured at  $37^{\circ}\text{C}$  in 20 mM sodium phosphate buffer at pH 8.0 with 9.2 nM Alexa-647 labelled Brichos and  $20.5\ \mu\text{M}$   $A\beta(M1-42)$  fibrils.

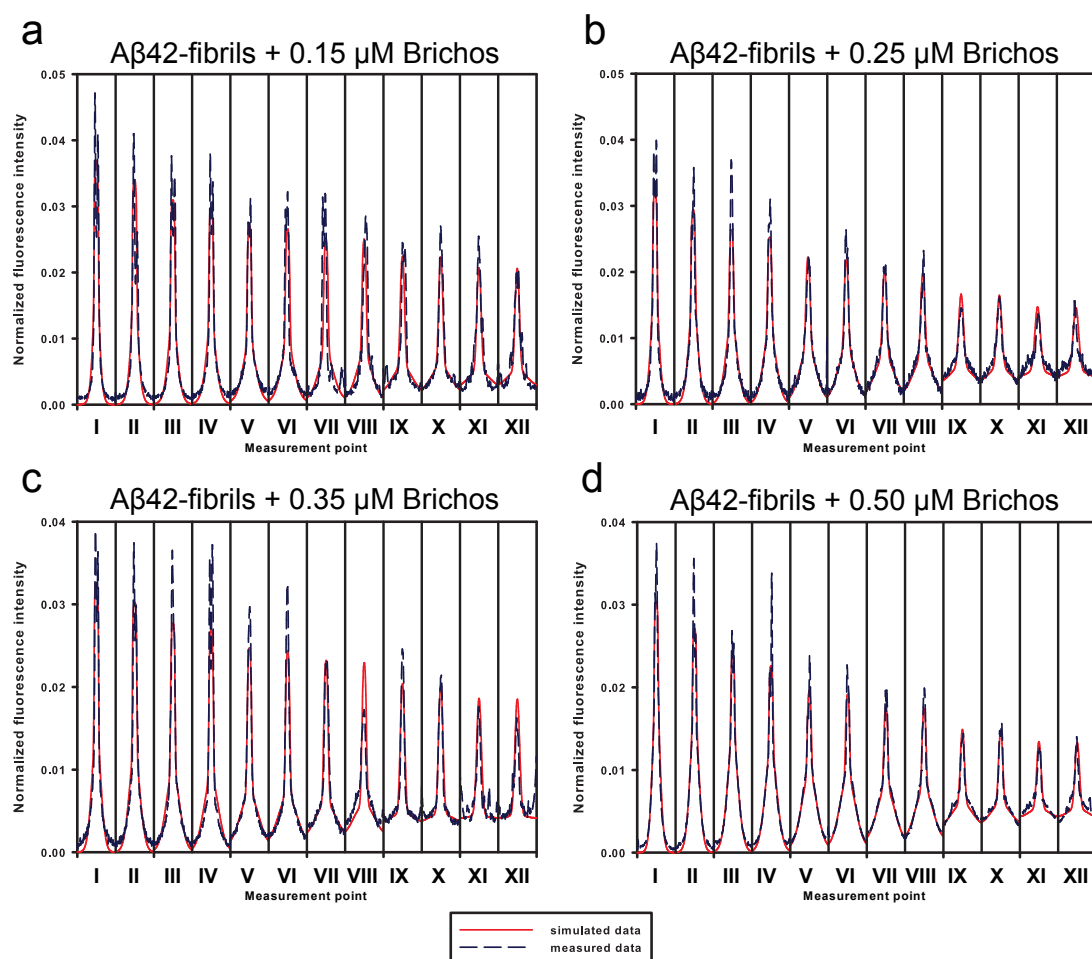


**Figure B.17:** (a-d) Representative fluorescence diffusion profiles corresponding to a solution of 24  $\mu\text{M}$   $\text{A}\beta(\text{M1-42})$  fibrils in the presence of different Alexa-488 labelled Brichos concentrations, acquired at twelve different channel positions. The simulated diffusion profiles (red lines) were fitted to the measured data (black dashed lines) by a least squared fit.

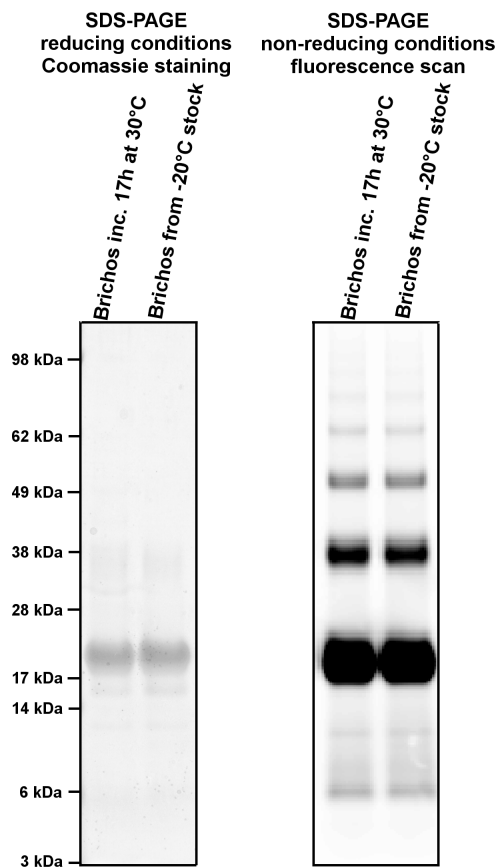


**Figure B.18:** SDS-PAGE analysis of Alexa-488 labelled Brichos samples freshly prepared or incubated at 30°C for 17 h. The assay was performed both under reducing with Coomassie blue staining (left box) and under non-reducing conditions with fluorescence detection (right box). Taken together, the two analyses show that both the Brichos and the Alexa-488 dye are stable upon incubation.

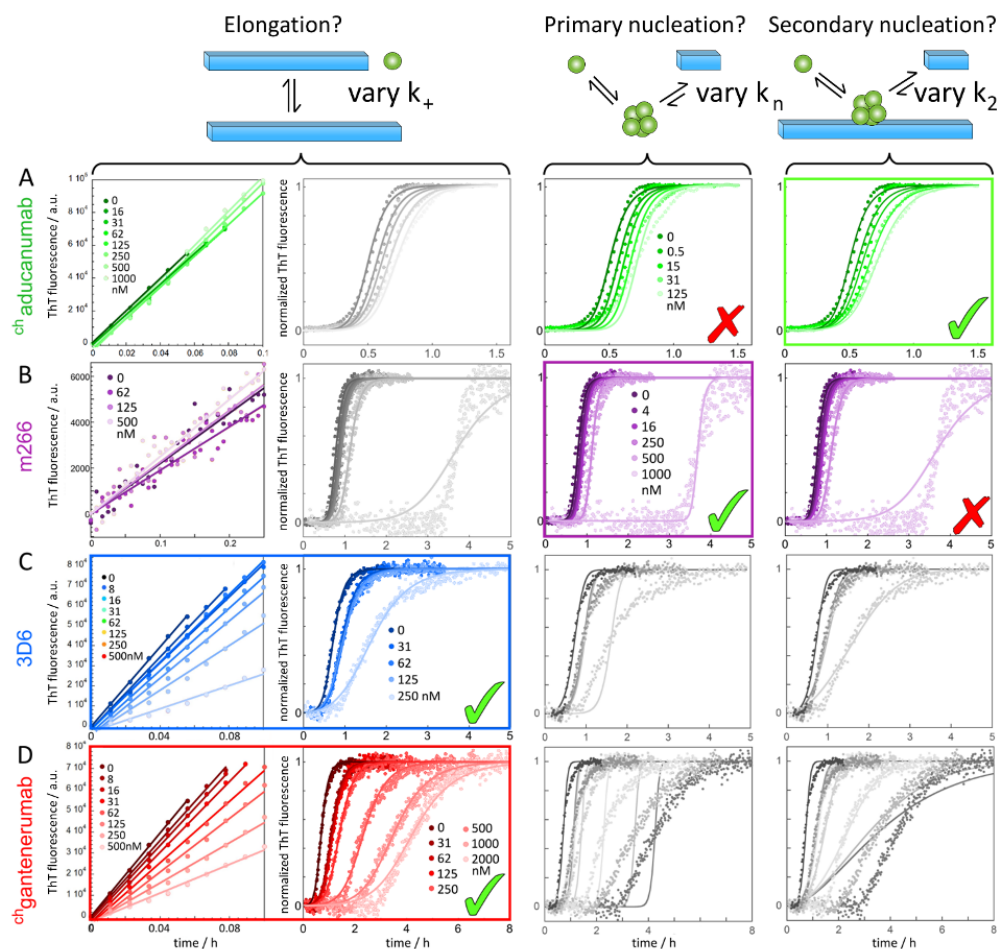


**Figure B.19:** (A-D) Thioflavin T (ThT) fluorescence as a function of time for reactions starting from 3-4  $\mu\text{M}$  recombinant  $\text{A}\beta(1-42)$  in 20 mM HEPES/-NaOH, 140 mM NaCl, 1 mM  $\text{CaCl}_2$ , pH 8.0 in the absence and presence of  $ch$  aducanumab (A), m266 (B), 3D6 (C) or  $ch$  gantenerumab (D). The first column shows data obtained for  $\text{A}\beta(1-42)$  monomer in the presence of 30% pre-formed  $\text{A}\beta(1-42)$  fibrils. The last three columns show data obtained for monomeric solutions in the absence of pre-formed fibrils. The colour codes for the antibody concentrations in nM are given on each row. The data are shown in normalised form. The solid lines are fits to the data and assume in the left two columns global values for  $k_2$  and  $k_n$  and curve-specific values for  $k_+$ , in the third column global values for  $k_+$  and  $k_2$  and curve-specific values for  $k_n$ , and in the right column global values for  $k_n$  and  $k_+$  and curve-specific values for  $k_2$ . The best fit in each case is indicated by a green tick. Grey colour indicates discarded mechanisms based on the results of heavy seeded data (first column). Note that the x-axes cover different ranges depending on the magnitude of the effect of each antibody.

The data was used with permission of Sara Linse.

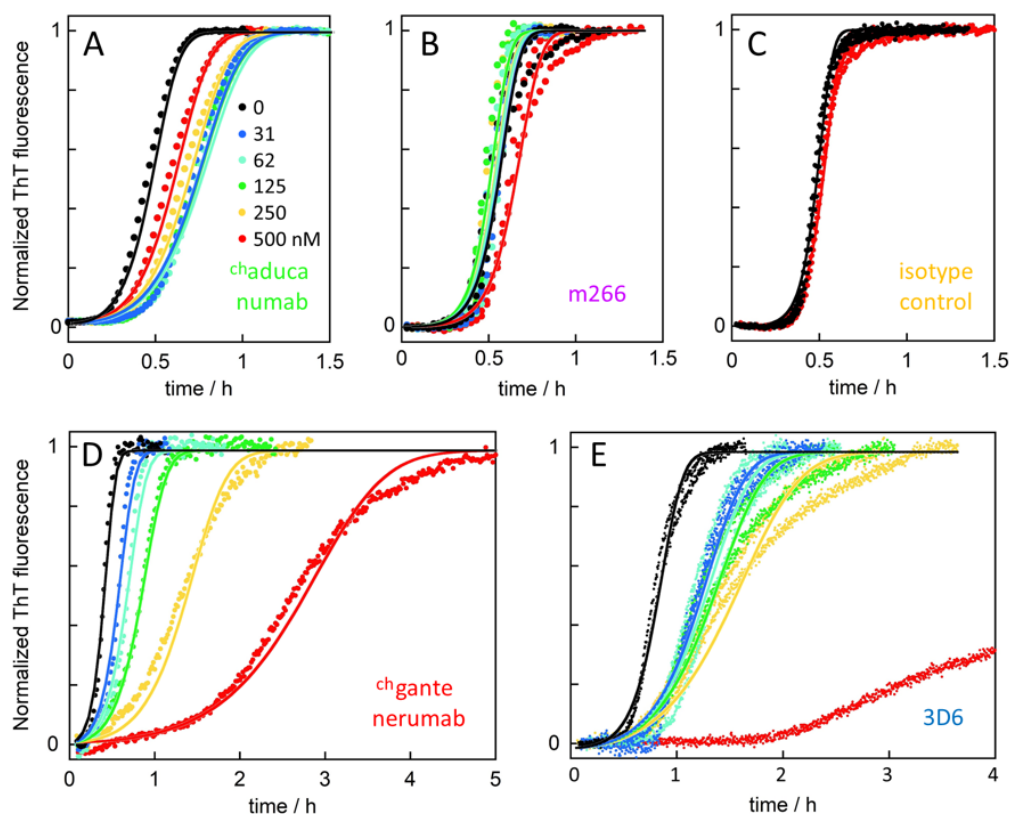


**Figure B.20:** Aggregation kinetics in the presence of pre-formed seed fibrils at low concentration (2%). The data show normalised ThT fluorescence as a function of time for reactions starting from 3 to 4  $\mu\text{M}$   $\text{A}\beta(1-42)$  monomer and 2% (60 to 80 nM)  $\text{A}\beta(1-42)$  fibrils in 20 mM HEPES/NaOH, 140 mM NaCl, 1 mM  $\text{CaCl}_2$ , pH 8.0 in the absence (black) and presence of A) *ch*gantenerumab, B) m266, C) isotype control antibody (yellow), D) *ch*aducanumab, or E) 3D6 at five concentrations as given by the colour code in panel A. The fitted curves in panels A-C and E allow only a variation of  $k_2$ , whereas the fitted curves in panel D allow only a variation of  $k_+$ . The data was used with permission of Sara Linse.



## Chapter 3

---

# Using microfluidic diffusional sizing for immunological screening

---

### List of publications

- MM Schneider, **T Scheidt**, M Hu, A Priddey, C Xu, S Devenish, G Meisl, CM Dobson, V Kosmoliaptsis, TPJ Knowles, In-solution characterisation of allo-antibodies in human serum, in preparation.

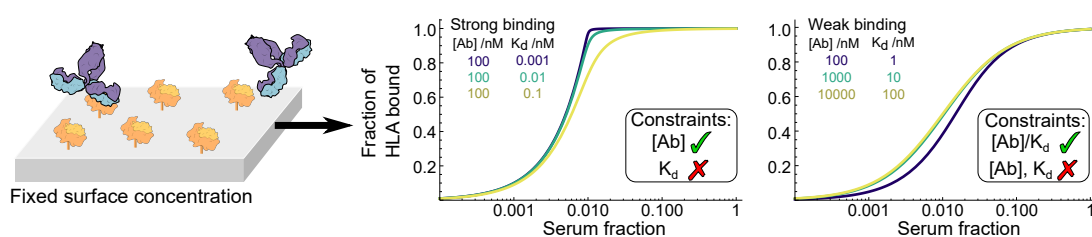
### 3.1 Clinical relevance of diffusional binding measurements for alloimmunisation detection

In order to understand characteristic behaviour and function of biomolecules, they have to be analysed under relevant conditions, ideally in biofluids, cells or systems which mainly adapt these properties. This plays a major role in medical applied science, e.g. drug screening, cancer treatment or pre/post-transplant alloimmunisation detection. In the latter case, due to a self-recognition process in every vertebrate, the body can start an immune response against foreign, mutated or infected cells. The recognition is therefore facilitated by the membrane protein human leukocyte antigen (HLA), also known as

major histocompatibility complex (MHC) in humans, which covers almost every cell in the body. Besides alloimmunisation, an association between HLA and diseases e.g. multiples sclerosis, Type I diabetes, celiac disease and up to 500 more, with or without a fortuitous correlation, could be identified[225]. The gene encoding the HLA-protein is highly polymorphic, which results in differences in the amino acid sequences between individuals and can influence the function to a major proportion.

The HLA is separated into two classes, class I and II. Class I is composed of two chains, one glycoprotein heavy chain anchored in the membrane and a non-covalently associated  $\beta$ -2 microglobulin, approximately 45 and 12 kDa, respectively[223]. In contrast, class II is formed by two membrane anchored glycoprotein heavy chains ( $\alpha$  and  $\beta$ ) with approximately 34 and 29 kDa, respectively[223]. Even if it is known that antibodies trigger the alloimmunisation by binding to non-self HLA, almost nothing is known about the role of binding affinity, antibody concentration, binding site location or the role of the

### Surface-based measurement



### Microfluidic diffusional sizing

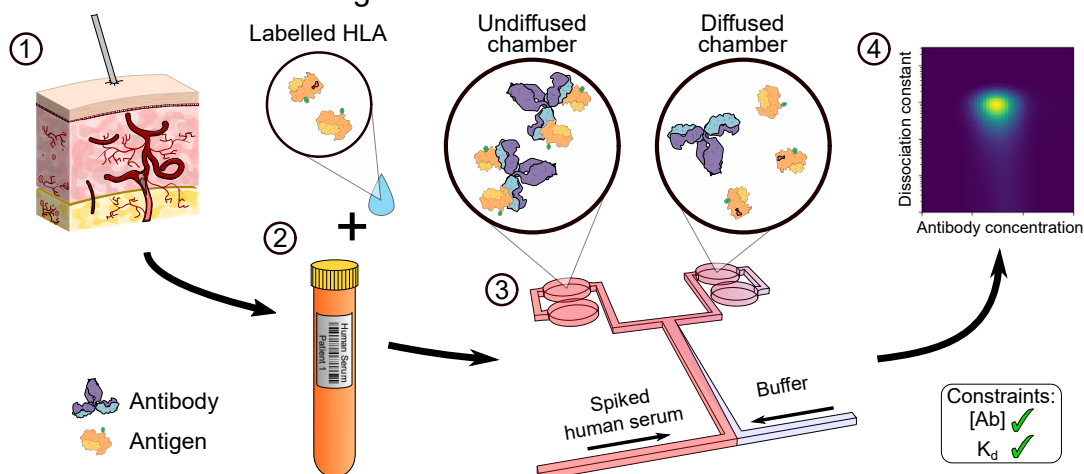


**Figure 3.1:** Basic principle of applying MDS for clinical samples. (1) Human serum is taken from a patient, which (2) is then incubated with labelled HLA to allow binding. (3) The size of the complex is, subsequently, determined by microfluidic diffusional sizing (scheme shows single side buffer co-flow but also surrounding buffer co-flow was used for experiments below), of which (4) the dissociation constant  $K_D$  and the antibody concentration  $[Ab]$  are evaluated.

peptide binding cleft during that process. However, nowadays semiquantitative binding measurements have to be done as part of an intensive screening for every transplantation patient[223]. Frequently used techniques are on the one hand cell-based assays such as the complement-dependent cytotoxicity test (CDC) or flow cytometry and on the other hand solid phase assays (SPA) as ELISA and Luminex, which is used in the field of solid-organ transplantation most frequently[134]. Although techniques of both assays can semiquantify relative amounts of binding HLAab directly in human blood serum, specific binding information is missing (Fig. 3.1). Usually, conventional measurement methods, together with extensive sample purification and preparation, are needed. The microfluidic diffusion device could be introduced here with its capabilities to acquire binding parameters directly in the condensed phase and highly heterogeneous solution as a novel type of binding studies with intact human samples. HLA interacting proteins will remain localised in the centre of the channel, whereas non-interacting molecules diffuse by their own diffusion coefficient (Fig. 1.3C).

As part of my Ph.D., I wanted to introduce this technique in the field of pre/post-transplant alloimmunisation detection. Furthermore, I wanted to test the capabilities of the microfluidic diffusion device of being able to probe specific molecular interactions in a complex environment such as human serum (Fig. 3.1). The human serum is an ideal representation of the extracellular space with its diverse protein composition, electrolytes, hormones and other exogenous substances.

### **3.2 Binding measurements of human leukocyte antigens and related antibodies in buffer**

To fulfil a detailed binding characterisation the diffusion-based microfluidic device was used. The acquired fluorescence profiles at twelve different positions along the diffusion-based microfluidic device correspond to the diffusion profile of the labelled HLA-tetramer. The comparison of the HLA diffusion profiles in the presence and absence of mABs showed a clear change in the diffusion behaviour of the HLA (Fig. 3.2). A dramatic decrease of the translational diffusion of 100 nM HLA class I A\*01:01 in the presence of 560 nM mABs WIM8E5 became clear and was connected to a decrease in the diffusion coefficient as well as an increase in the hydrodynamic radius ( $r_H$ ). The

change in the signal distribution indicated a binding between the Alexa-488 labelled HLA-complex and mABs. Through least-square fittings of simulated diffusion profiles to the measured diffusion profiles (see Supplementary Fig. D.3 for examples), an average  $r_H$  of the detected molecules was evaluated.

However, the advantage of the diffusion-based microfluidic device is not constricted on the qualitative investigation of the binding. The documentation of changing  $r_H$  by changing the mAB concentration provides the opportunity to calculate the dissociation constant ( $K_D$ ) and to describe the intensity of the binding. Experiments in PBS showed, if the Alexa-488 labelled HLA concentration is kept constant at 100 nM with a variation of the mAB concentration between 0-545 nM, a typical binding curve reaching a plateau with increasing ligand concentration was generated with the  $r_H$  against the used mAB concentration on the axes (Fig. 3.3). The experimental data points were fitted to a non-cooperative, single binding-site model (equation C.11, see Methods and Analysis). Accordingly, a  $K_D \leq 5.61$  nM and a maximum molar binding ratio (MMBR) of  $2.75 \pm 0.27$  mABs per HLA-complex could be estimated. In particular, the low dissociation constant

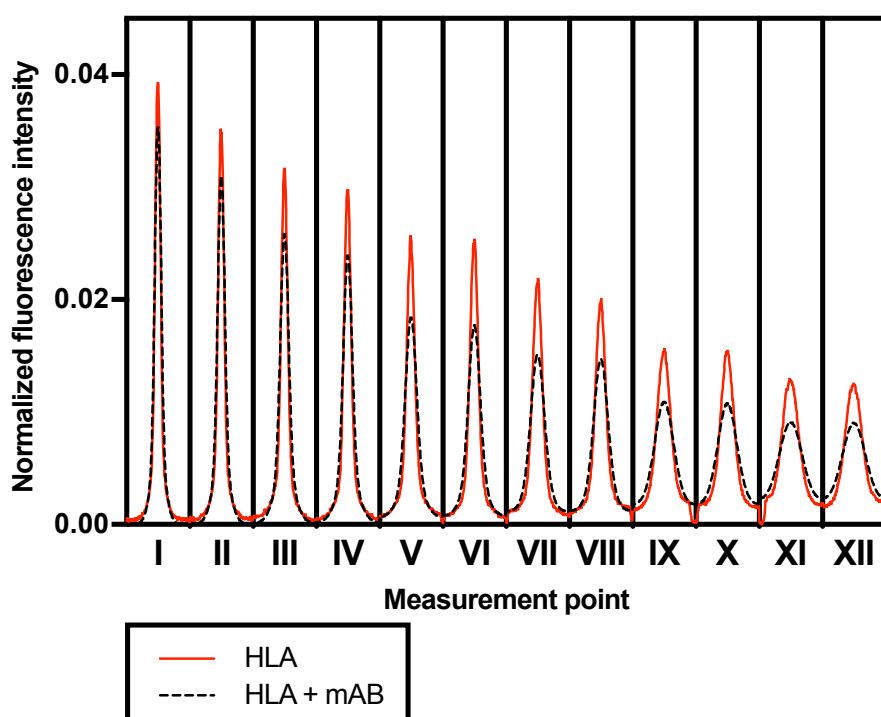


**Figure 3.2:** Diffusion profiles of 100 nM Alexa-488 labelled HLA (red curve) and 100 nM Alexa-488 labelled HLA (A\*01:01) in the presence of 560 nM monoclonal antibodies (WIM8E5) (black dashed curve) in PBS-buffer with 0.1% Tween at pH 7.4 measured at twelve different positions along a diffusion-based microfluidic device.

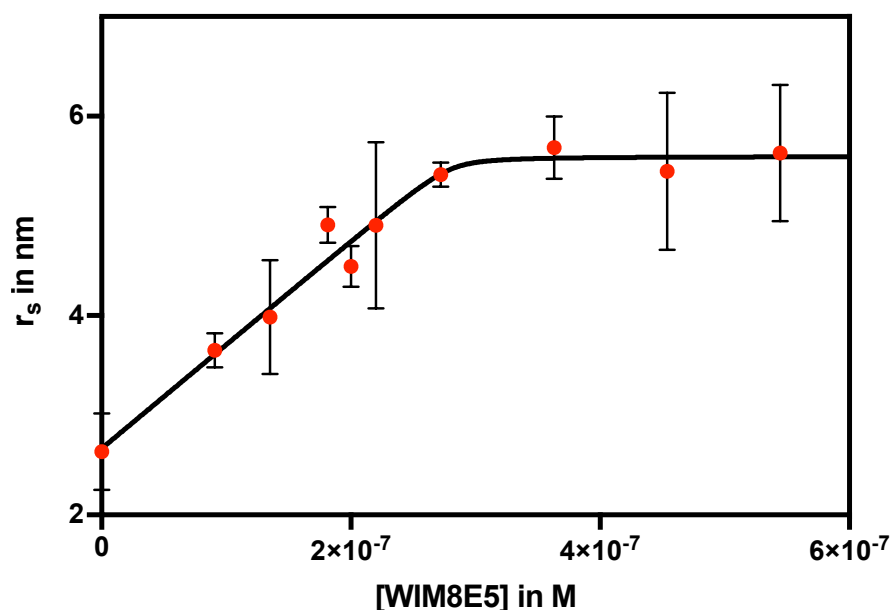


**Figure 3.3:** Binding curve for the mAB WIM8E5 interacting with HLA class I A\*01:01 in PBS-buffer with 0.1% Tween at pH 7.4 and 21 °C measured by microfluidic diffusion devices. In one set of experiments, different concentrations of mABs were incubated with 100 nM Alexa-488 labelled HLA (circles) and measured after a short incubation time of at least 30 minutes. Each point represents the mean and the standard deviation of at least two independent repetitions. The regression line represents the best fit to a non-linear binding equation (see equation C.11, Methods and Analysis), with  $K_D \leq 5.61$  nM,  $[mAB_{bound_{max}}] = 274.8 \pm 27.4$  nM and  $MMBR = 2.75 \pm 0.27$  with  $R^2 = 0.871$ .

indicated a very high affinity and the MMBR let suggest a stoichiometry of 2:1 or 3:1 for mABs and HLA-complex. The detected affinity of  $\leq 5.61$  nM is located in a low nanomolar range and is highly affine, as you would expect for a specific antibody. When I describe antibody affinity it takes into account the affinity of the entire antibody to the HLA-tetramer as it is not yet feasible to distinguish between affinity and avidity with the applied system.

### 3.3 Investigation of graft rejection factors in human serum

The ability of the diffusion-based microfluidic device to measure heterogeneous samples directly in the condensed phase, seems as an optimal set up for direct interaction measurements in biological samples. To resemble biological relevance binding parameters for HLAab, I measured the interaction of purified Alexa-488 labelled HLA and secreted antibodies directly in patient serum. The relative binding was measured beforehand by

the Luminex system[134], usually used for alloimmunisation tests before transplantation. The two HLA-types of interest gave a relative standard fluorescent intensity of 21108 for patient 1 blood serum in combination with HLA A\*02:01 and 6478 for HLA A\*01:01 (see Supplementary Fig. D.4). This is an indication for a clear binding of the beads to HLA A\*02:01 and just a weak binding to HLA A\*01:01, measured by the Luminex system. The measurements of both HLA types were repeated for patient 2. A negative result for binding in human serum with 0 was identified for A\*02:01. Nevertheless, also a weak signal could be detected for A\*01:01 with 7310 in human serum of patient 2. However, all four conditions were measured as well with the diffusion-based microfluidic device.

An indication for an interaction between Alexa-488 labelled HLA and HLAab was given by the change in the detected average molecule size (Fig. 3.4A). By fitting the resulting diffusion profiles to a convective-diffusion based model (see Supplementary Fig. D.5) considering a bimodal gaussian distribution, an average hydrodynamic radius was calculated. The significant increase in the average size of HLA A\*02:01 in the presence of human serum from patient 1 has to be related to the increased amount of formed HLA-HLAab complexes with a higher molecular weight and size. However, the exchange of the human serum of patient 1 against the serum of patient 2 showed no indication of binding. This suggests that the interaction between HLA A\*02:01 and HLAab is specific and furthermore not influenced by the dye. Both systems of HLA in human serum of patient 2 show a low average radius and indicate no binding which goes in line with the results from the Luminex platform. However, the results of the Luminex platform indicate an extremely low relative value for interaction of HLA A\*01:01 in patient 1 serum, caused by low affinity or by low concentration of HLAab, the sensitivity of the diffusion-based microfluidic device is not yet sufficient enough for measuring those small quantities.

Even though it is the first time that binding parameters were measured directly in unpurified patient samples, the binding characterisation of HLA and HLAab was studied in the same way as it was done with the mAB in the beginning of this paragraph. The only difference was the usage of a lower HLA concentration of 50 nM and using a human serum as fraction between 0 and 1, as the HLAab concentration in human serum is unknown. HLA A\*02:01 and human serum of patient 1 were the sample of choice for studying interactions in human serum as binding is indicated in previous studies (see

Fig. 3.4A). As the stoichiometry could not be verified clearly beforehand, the interaction was constrained to a stoichiometry of either 1:2 (dashed grey curve) or 1:3 (black curve) for the non-linear fitting of the binding curve. Both fittings were almost similar with minor differences in  $K_D$ , with  $K_{D,1:2} \leq 7.33$  nM and  $K_{D,1:3} \leq 9.22$  nM. In addition to the dissociation constant, the unknown HLAab concentration in the patients human serum can be estimated in respect to the stoichiometry. The individual concentration is  $[\text{HLAab}_{1:2}] = 306.9 \pm 83.4$  nM or  $[\text{HLAab}_{1:3}] = 459.6 \pm 117.7$  nM.

Although the labelling of HLA with fluorophores is well established *via* biotinylation[1, 188], the quality of the acquired HLA sample seems questionable. The measured hydrodynamic radius of the HLA species are significantly lower than expected for a tetrameric HLA species. By consideration of tetramerisation of biotin and streptavidin, a final

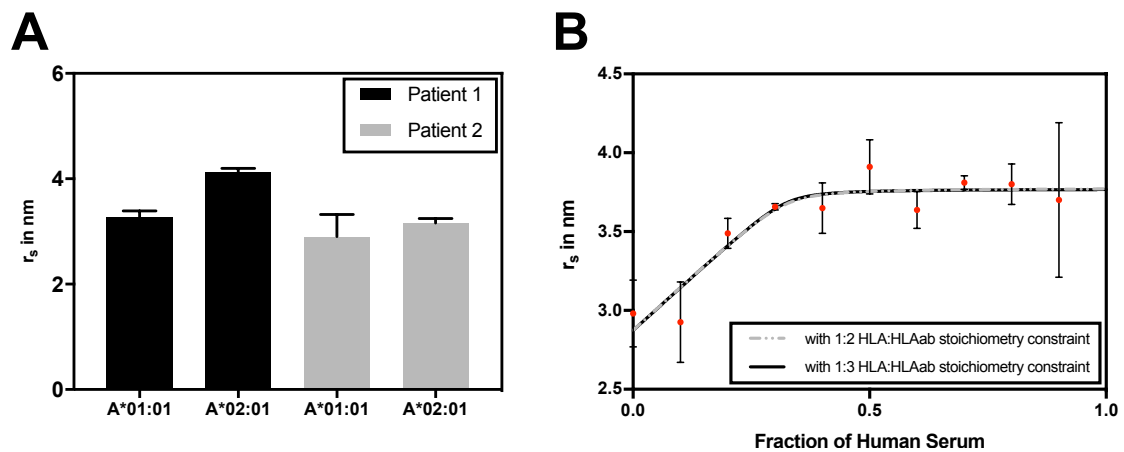


**Figure 3.4:** Binding measurements of Alexa-488 labelled HLA directly in human serum with a diffusion-based microfluidic approach. (A) Least-square fitting between simulated and measured diffusion profiles provided an average molecule radius of the detected species. The human serum of two patients were enriched with Alexa-488 labelled HLA A\*01:01 or A\*02:01, each. (B) Based on the functionality of the diffusion-based microfluidic devices to give an average  $r_H$  by adding different amount of human serum fraction a binding curve was generated. The binding curve represents the measured interaction between Alex-488 labelled HLA A\*02:01 with a constant concentration of 50 nM and various amount of HLAab containing human serum from patient 1 (circles). The experiments were done at 21 °C and human serum was diluted in PBS at pH 7.4. Tween was added to a total amount of 0.1%. Both regression line represent the best fit to a non-linear binding equation (see equation C.11 , Methods and Analysis) with  $R^2 = 0.69$

and constrained in the stoichiometry, assuming either binding 1:2 HLA:HLAab (dashed grey curve) or 1:3 HLA:HLAab (black curve). This results in a  $K_{D,1:2} \leq 7.33$  nM,  $[\text{HLAab}_{1:2}] = 306.9 \pm 83.4$  nM or  $K_{D,1:3} \leq 9.22$  nM,  $[\text{HLAab}_{1:3}] = 459.6 \pm 117.7$  nM. The reported average sizes in A and each point in B represents the mean and the standard deviation of at least two independent repetitions.

bioconjugate should be formed consisting of four biotinylated class I HLA molecules ( $\sim 57$  kDa each) and one streptavidin tetramer ( $\sim 67$  kDa). The total molecular mass of the HLA complex should be around 295 kDa and be equivalent to a hydrodynamic radius of  $\sim 5.9$  nm. Indeed, native polyacrylamide gel electrophoresis (PAGE) (see Supplementary Fig. D.1) indicate the presence of slight impurities. In addition, a chromatographic analysis of the HLA complex shows that the sample is not homogeneous and free dye is present (see Supplementary Fig. D.2). Free dye should not have any interfering effect on the binding measurements except for decreasing the average hydrodynamic radius. However, in order to overcome this problem, further experiments have been examined using Alexa-647 labelled monomeric HLA.

Using this labelling strategy, I was able to use the Fluidity One-W (Fluidic Analytics

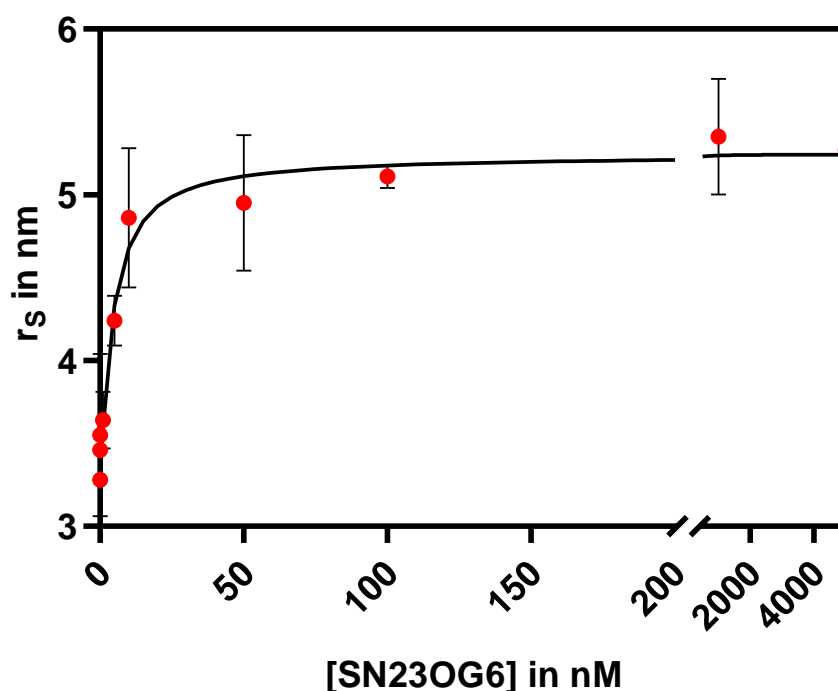


**Figure 3.5:** Binding curve of Alexa-647 labelled monovalent HLA and antibody infused human serum. Human serum was infused with a range of different concentrations of SN23OG6 antibody and 5 nM Alexa-647 labelled A\*02:01 HLA monomer. The plotted red points give the relative size increase, averaged over the data of at least three replicates, the black line represents the fitting with  $R^2 = 0.972$  according to the non-linear binding equation including background subtraction and a constrained stoichiometry of one antibody to two HLA molecules (see Methods and Analysis). From the fit, the dissociation constant  $K_D = 3.7 \pm 1.8$  nM could be determined. The results were obtained with the Fluidity One-W (Fluidic Analytics Ltd., UK).

Ltd., UK) diffusional sizing technology. The significantly higher sensitivity compared to the microscopic setup used beforehand made a more reliable sample acquisition possible. However, the general interest was whether such a commercial setup is capable of measuring biophysical parameters in a complex solution such as human serum. Due to the high sensitivity, the measurements were limited by the background given by the serum and had to be corrected by subtraction (see Methods and Analysis). The autofluorescence of human serum is attributable to the presence of porphyrin derivatives such as bilirubin, the metabolic product of hemoglobin. The porphyrin fluorophore was reported to exhibit fluorescence between 520 nm and 700 nm[155]. The increase in fluorescence is thought to be due to accumulation of porphyrin derivatives resulting from the degradation of bilirubin at the storage conditions. The labelled monomeric HLA version A\*0201 was added into a serum sample with a range of previously supplemented HLA specific antibody SN23OG6 concentrations (see Fig. 3.5). The constructed binding curve results in a dissociation constant of  $K_D = 3.7 \pm 1.8$  nM by applying a non-linear binding equation including background subtraction (see Methods and Analysis). The stoichiometry was constrained to one antibody binding to two HLA molecules, which was determined for monovalent HLA previously (see Supplementary Fig. D.6). The results exhibit that the Fluidity One-W is able to fully quantify binding of serum solved antibodies even at low probe concentrations. The lower limit of sufficient probe quantification is directly connected to the limit of detectable antibody concentration in patient sera.

### 3.4 Discussion

Notwithstanding, it has to be considered that besides the already used microfluidic devices which mimic the *in vivo* environment by perfusion cell cultures, extracellular matrix analogues, microscaffolds, spheroid formation and co-cultures [263], the ambience of the here presented microfluidic diffusion device is distant from realistic extracellular environment. The extracellular molecular heterogeneity, concentration and turnover is impossible to imitate. Hence, I have shown that measuring interactions directly in extracellular fluid rather mimicking them is possible with the used microfluidic diffusion device. Human serum is highly heterogeneous and represents the entire extracellular milieu in the blood stream except blood cells and clotting factor. In this way, the serum contains a huge variety of diverse proteins, nutrients, hormones, electrolytes and waste

material such as urea. Nevertheless, by using human serum from two patients I could distinguish a positive from a negative binding event by a change in the hydrodynamic radius. Consequently, the binding between the HLA and the HLAab in human serum is specific rather than generic or even induced by the method or label itself. Together with the determination of the dissociation constant it makes the diffusion-based device the first application for obtaining binding parameters from pure human samples in the condensed phase.

Nevertheless, even if a  $K_D$  in the nanomolar range could be detected and the unknown antibody concentration could be determined in serum, a more extensive characterisation of the system has to be done. Generating two different binding curves at different HLA concentrations would significantly decrease the error. It has to be pointed out that the hydrodynamic radius of unbound HLA seems too small by assuming a tetramer including a streptavidin. Therefore, further consideration has to be taken about sample quality and in selecting a specific probe, being monomeric, dimeric or tetrameric. Further studies will show whether avidity effects of multimeric probes are wanted in order to increase the sensitivity for rare antibodies in human serum. Measuring clinical samples or providing machines and facilities to do so are an emerging market with increasing economical interest. Rating the risk for graft rejection or determining the affinities of immunological factors in human serum is crucial for health care and it seems equipment such as the Fluidity One-W machine is a further application making those parameters accessible.

Although the system of HLA and interacting antibodies needs more characterisation, I was able to show the potential of a powerful tool for non-invasive real-time monitoring of protein-protein interactions in complex biological mixtures such as body fluids. The technique might be applicable for much more disease-related proteins such as antibodies generated by immune response against prion proteins or certain auto-immune diseases or allergies.

# Chapter C

---

## Methods and Analysis

---

### C.1 Sample preparation

#### C.1.1 Biotinylated HLA together with mAB in PBS or human serum

HLA class I was obtained from Emory Healthcare, US, and were biotinylated and assembled with Alexa-488 labelled streptavidin. They were solved in PBS with 0.02% sodium azide at pH 7.4. Used HLA forms were A\*01:01 and A\*02:01 with the cleft peptide STDHIPILY and VLHDDLLEA, respectively. The mABs on the other hand were provided in RPMI or IMDM medium with 10% FCS and sodium azide. The used mABs were WIM8E5 and W6/32. Human serum from anonymised patients were blended with EDTA to 0.3% in total, which diluted the serum by 2.5%. Labelled HLA and mABs/human serum were diluted and incubated in 1xPBS at pH 7.4 in the presence of 0.1% Tween.

### C.2 Labelling of non-biotinylated HLA with Alexa Fluor 647 fluorophore

*With assistance of Matthias M. Schneider.* To HLA (between 50 - 80  $\mu$ L in NaHCO<sub>3</sub>, 0.89 nmol, 1 equiv.), Alexa Fluor 647 N-Hydroxysuccinimide ester (in DMSO 3 equiv.)

was added. The reaction mixture was incubated for 1 h at approx. 20°C, protected from light. The sample was purified by size exclusion chromatography on a Superdex 200 increase 10/300 GL column (GE healthcare, US) with a flow rate of 0.5 mL/min and PBS (pH 7.3, supplemented with NaN<sub>3</sub> (0.02% (w/v))) as eluting buffer, to yield labelled HLA (1 mL, 370 nM, DOL between 0.33 to 2.25, depending on variant). The conjugated HLA was stored at 4°C until further use.

### C.3 Fabrication and use of microfluidic diffusion devices

The fabrication and use of microfluidic diffusion devices is explained in detail in section A.2. For the human serum experiment with the spiked antibody, chips for the Fluidity One-W from Fluidic Analytics Ltd. (Cambridge, UK) were used.

### C.4 Native-PAGE analysis

Native-PAGE electrophoresis was run with Novex NativePAGE Gel System (Life Technologies, US). The electrophoresis has been performed on ice in order to prevent to much heating. Samples were analysed by Coomassie blue staining.

### C.5 Binding analysis

#### C.5.1 Derivation of non-linear binding equation

$$K_D = \frac{[M_f] \cdot [L_f]}{[L_b]} \quad (\text{C.1})$$

$$[M] = [M_f] + [L_b] \quad (\text{C.2})$$

Equation C.1 in C.2 results in:

$$K_D = \frac{([M] - [L_b]) \cdot [L_f]}{[L_b]} \quad (\text{C.3})$$

$[L_b]$  and  $[L_f]$  are related to each other by:

$$[L_f] = [L_0] - [L_b] \quad (\text{C.4})$$

Equation C.4 in C.3 results in:

$$K_D = \frac{([M] - [L_b]) \cdot ([L_0] - [L_b])}{[L_b]} \quad (\text{C.5})$$

which can be formed to:

$$[L_b] = \frac{[L_0] + [M] + K_D}{2} - \sqrt{\left(\frac{[L_0] + [M] + K_D}{2}\right)^2 - [L_0] \cdot [M]} \quad (\text{C.6})$$

$[L_0] + [M]$  will be defined as:

$$q = [L_0] + [M] \quad (\text{C.7})$$

If  $[L_0]$  of undiluted ligand sample is unknown it can be extended by a fraction factor  $F$ , which is 1 in the undiluted form:

$$q_F = F \cdot [L_0] + [M] \quad (\text{C.8})$$

$[L_b]$  is related to the hydrodynamic radius by:

$$[L_b] = \frac{\Delta r_H \cdot [M]}{\Delta r_{H,tot}} \quad (\text{C.9})$$

Introducing equation C.9 in C.6 gives:

$$\Delta r_H = \left( \frac{q + K_D}{2} - \sqrt{\left(\frac{q + K_D}{2}\right)^2 - [L_0] \cdot [M]} \right) \frac{\Delta r_{H,tot}}{[M]} = r_{H,x} - r_{H,0} \quad (\text{C.10})$$

and can be formed to:

$$r_{H,x} = \left( \left( \frac{q + K_D}{2} - \sqrt{\left( \frac{q + K_D}{2} \right)^2 - [L_0] \cdot [M]} \right) \frac{\Delta r_{H,tot}}{[M]} \right) + r_{H,0} \quad (\text{C.11})$$

### C.5.2 Binding equation with background subtraction

Measurements with the Fluidity One-W (Fluidic Analytics Ltd., UK) with human serum were background subtracted under the assumption of additive fluorescence intensity. The hydrodynamic radius  $r_H$  was extracted from the measured apparent hydrodynamic radius  $r_H^{app}$  and the corresponding signal intensity  $I^{app}$  by using the following equation:

$$r_H = \frac{r_H^{app} - r_H^{serum} \cdot \frac{I^{serum}}{I^{app}}}{1 - \frac{I^{serum}}{I^{app}}} \quad (\text{C.12})$$

with  $r_H^{serum}$  and  $I^{serum}$  are the measured hydrodynamic radius and intensity of pure serum.

## Chapter D

---

### Supplementary information

---

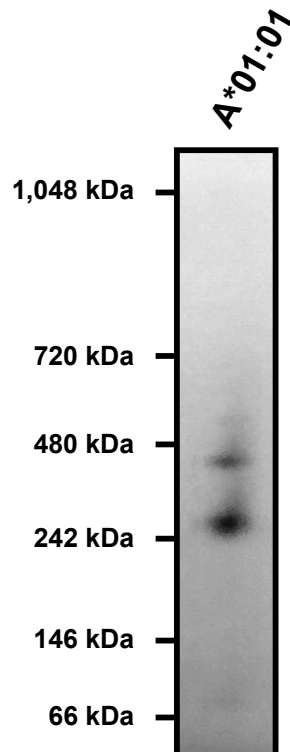


**Figure D.1:** Native-PAGE of Alexa-488 labelled HLA. Gel was stained with Instant Blue stain. The lower band at around 260 kDa is identical with the expected size of a tetrameric HLA complex. However, the upper band indicates some higher complex species which could be mediated by multiple unspecific biotinylation of some HLA molecules.

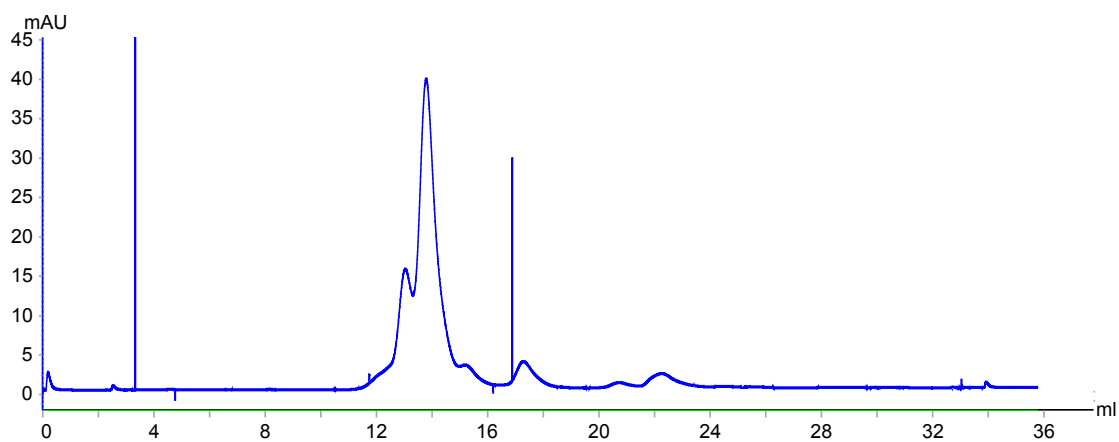


**Figure D.2:** Size-exclusion chromatogram of tetrameric HLA (Emory, US) with measured absorbance at 280 nm and eluted with PBS, pH 7.4. A Superdex 200 Increase column (GE healthcare, US) was used. As can be seen from the chromatogram, the provided sample shows a clear heterogeneous composition, however a pure tetrameric HLA entity was expected. Therefore peaks cannot reliably be assigned to specific protein species.

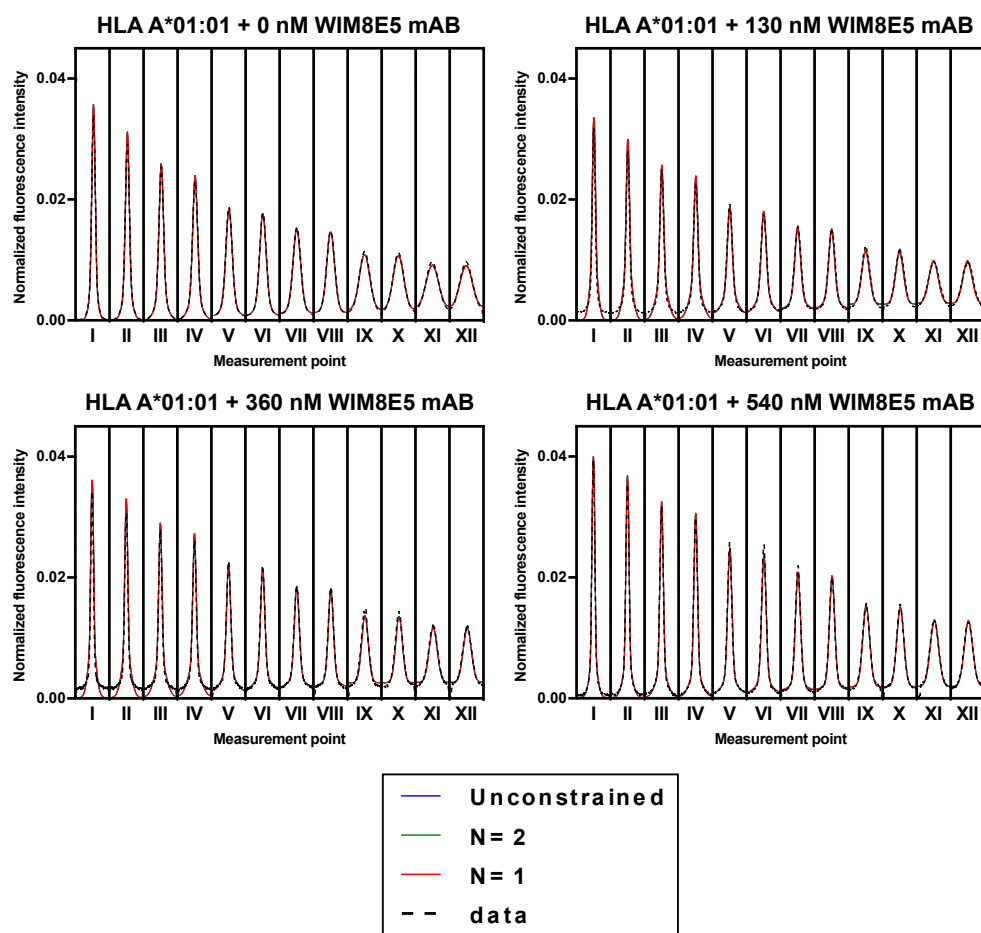


**Figure D.3:** Examples of normalized fluorescence profiles of 100 nM Alexa-488 labelled HLA A\*01:01 in the presence of different mAB WIM8E5 concentrations were acquired at twelve different channel positions at 21°C in PBS. The simulated diffusion profiles for one (red), two (green) or an infinite amount of species (blue line) were fitted to the measured data (black dashed line) by a least square fit depending on species restriction. The best fit to the measured profiles gives the size distribution and the referring amount of each species based on the simulated diffusion.

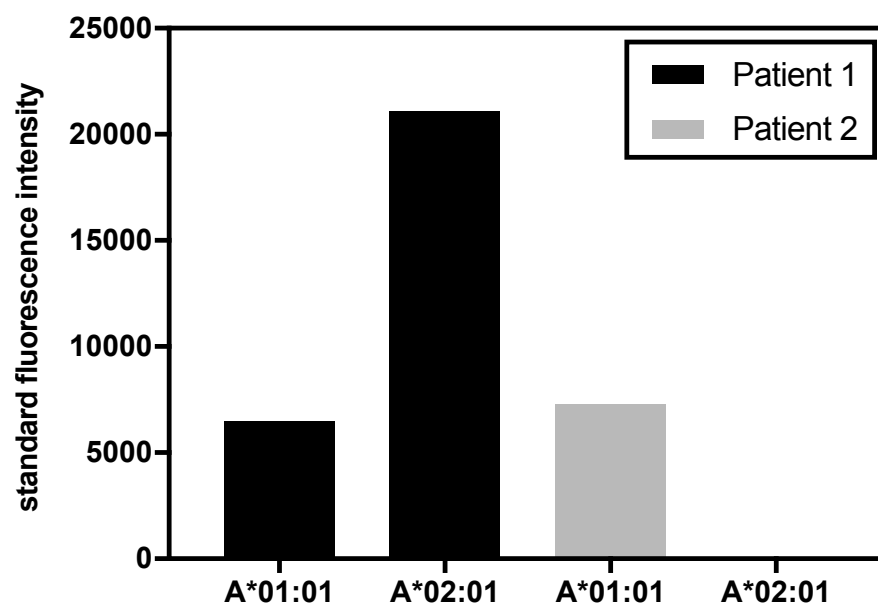


**Figure D.4:** The human serum of two patients were measured with the Luminex-bead system and gives a normalised standard fluorescence intensity for interactions with bead coated HLA A\*01:01 or HLA A\*02:01. (Measurements were done by members of the Addenbrooks hospital, Cambridge, UK)

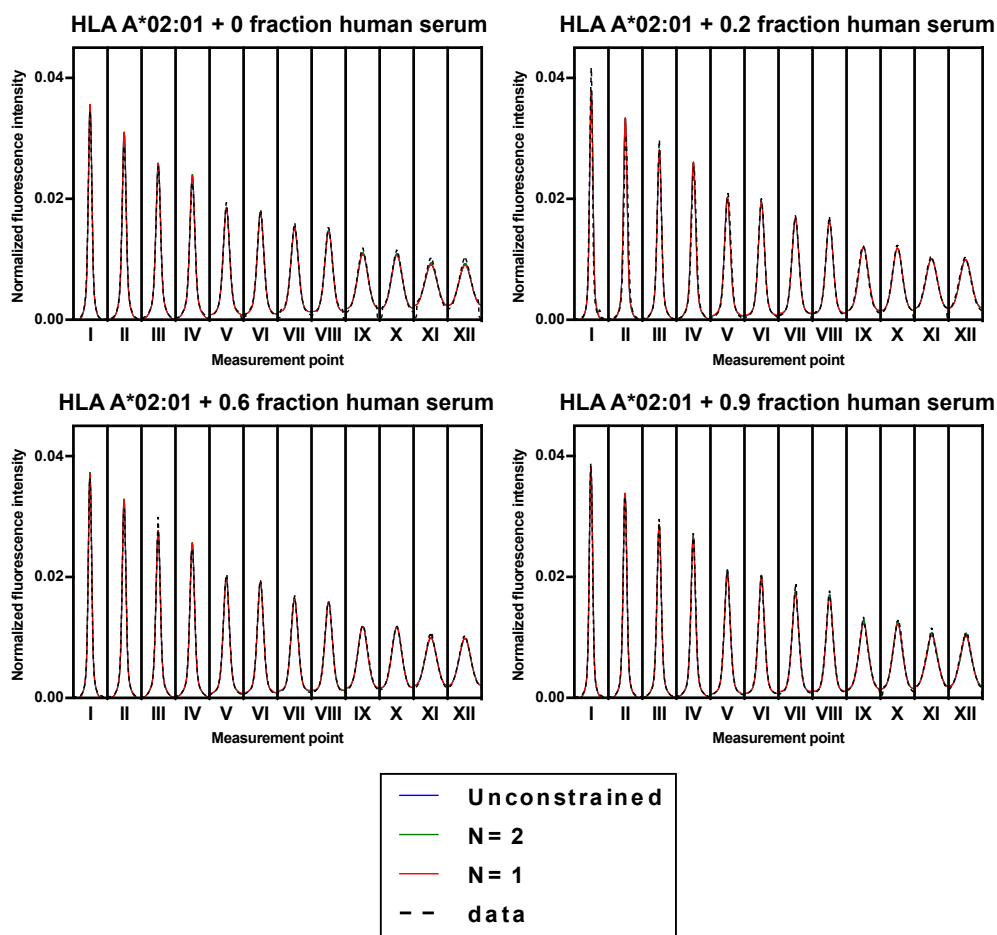


**Figure D.5:** Examples of normalized fluorescence profiles of 50 nM Alexa-488 labelled HLA A\*02:01 in the presence of different fractions of human serum were acquired at twelve different channel positions at 21°C. The simulated diffusion profiles (blue, green, red line) were fitted to the measured data (black dashed line) by a least square fit depending on species restriction. The best fit to the measured profiles gives the size distribution and the referring amount of each species based on the simulated diffusion.

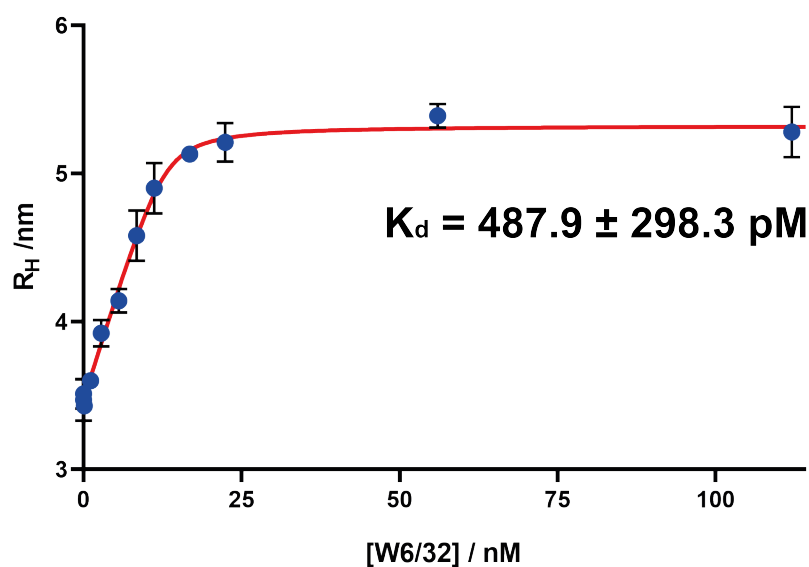


**Figure D.6:** Binding Curve of 25 nM HLA A\*03:01 with varying concentration of antibody W6/32. The blue points give the relative size increase, averaged over the data of at least three replicates, the red line to the fit according to the non-linear binding equation (see Methods and Analysis) with  $R^2 = 0.98$ . From the fit, the dissociation constant  $K_D = 487.9 \pm 298.3 \text{ pM}$  and the binding site concentration  $B = 12.98 \pm 1.00 \text{ nM}$  could be determined. This results in an overall stoichiometry of one antibody and two HLA molecules. *The experiment was performed by Matthias M. Schneider and Mengsha Hu.*

## Chapter 4

---

# Multidimensional characterisation of complex mixtures by microfluidic coupled size-exclusion chromatography

---

### List of publications

- **T Scheidt**, T Kartanas, Q Peter, MM Schneider, KL Saar, T Müller, PK Challa, A Levin, S Devenish, TPJ Knowles, Multidimensional Protein Characterisation Using Microfluidic Post-Column Analysis, *Lab Chip*, (2020).

### 4.1 Introduction

The formation of discrete structures by proteins is dictated by their ability to correctly fold, interact and assemble into hierarchically ordered complexes. Thus, the ability of proteins to serve as the basic machinery in cells is governed by their range of static and dynamic interactions enabling their flexible and specific functionality. Therefore, it is not surprising that over 80% of proteins do not appear on their own, but as part of complexes[22]. The nature of these interactions is defined by the specific amino acid sequences of the proteins and their post-translational modifications[146], thus modulating

their interactions[209, 229, 255, 262]. In particular, the direct electrostatic interactions are enabled by charged and polar groups at the protein surface that allow the formation of ion pairs, hydrogen bonds and other electrostatic interactions. The overall protein charge and formation of complexes in solution are dependent on the number and nature of the charged groups presented and is related to the isoelectric point (pI), known as the pH value at which the net charge is zero[161]. While electrostatic interactions can be highly specific and possess strong geometric constraints, hydrophobic interactions minimise water-exposed hydrophobic residues, and these are usually buried inside proteins or protein complexes[142]. Malfunctioning proteins that misfold and interact in an unregulated manner can lead to protein aggregation, a key feature in many neurodegenerative diseases. Thus, this wide range of interactions is a key feature of protein self-assembly and function, both *in vivo* and *in vitro*.

Techniques capable of characterising complex mixtures are limited and commonly only allow to determine unidimensional information. As protein complexes are highly dynamic and their composition is dependent on exogenous factors including temperature, pH, local salt concentration and viscosity, it is challenging to determine their biophysical

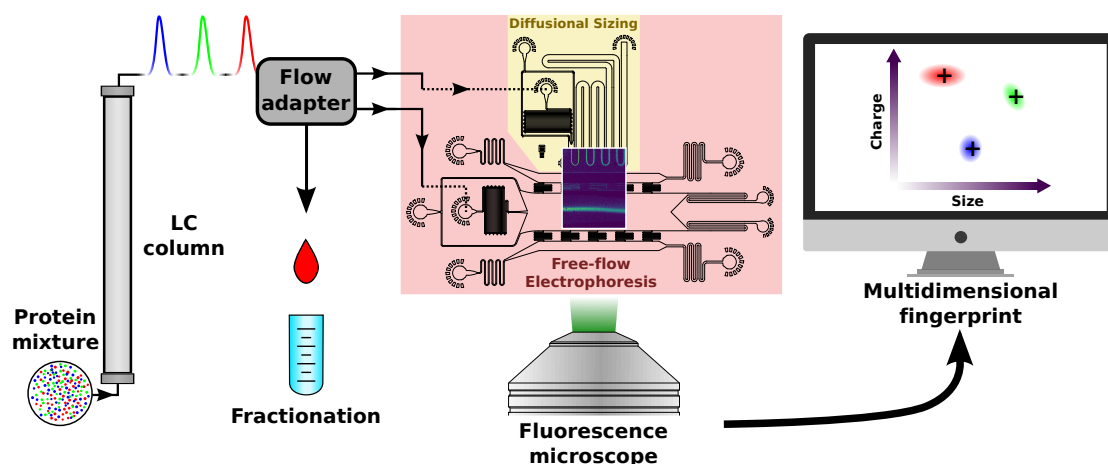


**Figure 4.1:** Scheme of an integrated (in-line) liquid chromatography with analytical microfluidics. Starting with a complex protein mixture, the molecules are separated by their individual properties depending on the column applied. The eluting liquid is divided by a macro- to microfluidic flow adapter. Following this step, the flow-through can be guided to individual microfluidic components or collected separately. In this way, the hydrodynamic radius and electrophoretic mobility of the eluent can be measured continuously on a microfluidic chip. The acquired information is processed and gives multidimensional information of individual species of a complex mixture.

properties under physiological conditions. Simultaneous acquisition of multidimensional characteristics is therefore essential as state and compositions of the sample can change between sequential measurements. Conventional approaches for multidimensional characterisation include e.g. size exclusion chromatography coupled to multi-angle light scattering (SEC-MALS)[222], 2D-gel electrophoresis[170], liquid chromatography-mass

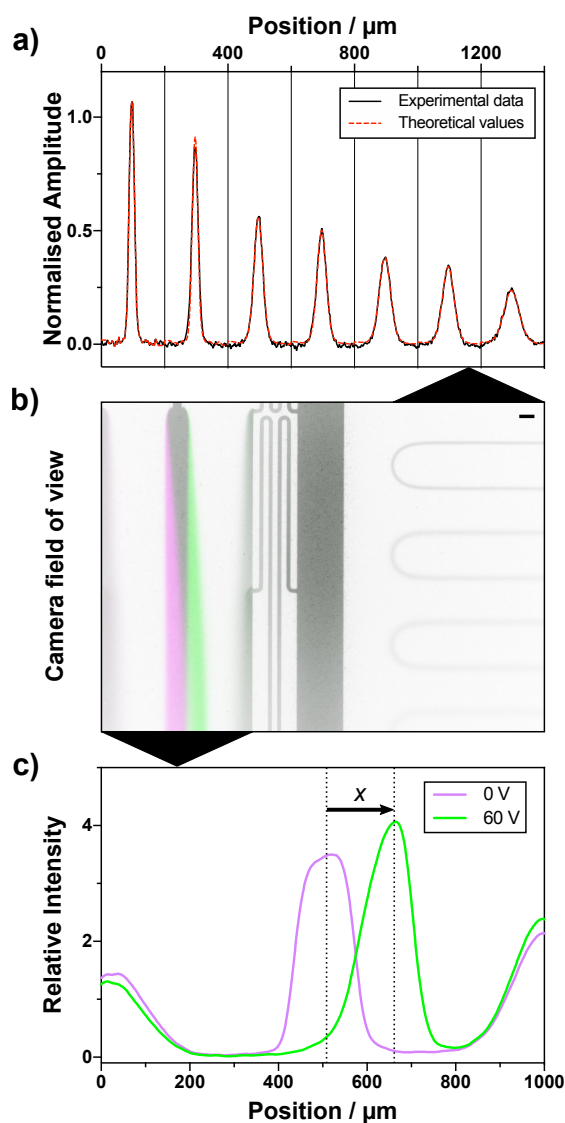


**Figure 4.2:** Microfluidic components in a single camera field of view with subsequent analytical processes. b) Overlay of two images taken at 0 V (magenta) and 60 V (green). The field of view captures the microfluidic electrophoresis device on the left side and the diffusional sizing part on the right side. Scale bar is given in 100  $\mu\text{m}$ . a) Experimental diffusion profiles (black curve) from the diffusional sizing were fitted against theoretical basis functions (red dashed curve) resulting in a hydrodynamic radius prediction. c) The sample gets deflected when an electric field of 60 V (green curve) is applied in the electrophoresis device. From the distance of deflection,  $x$ , the electrophoretic mobility can be deduced.

spectrometry (LC-MS)[47], LC coupled to nuclear magnetic resonance spectroscopy (LC-NMR)[210], high performance anion exchange coupled with pulsed amperometric detection (HPAEC-PAD)[197] and electrochromatography[79, 137]. In many cases, these approaches require special probes, including isotopes, oxidisable functional groups, protein tags or fluorescence labeling[141, 197] or the use non-physiological conditions, such as sample ionisation and high sample concentration[115]. The difficulty in conserving protein conformation and observing non-native complexes, can in principle, be avoided by operating under physiological conditions. Yet, methods with high separation power that work under these conditions have been found challenging to develop and adapt.

In order to overcome current challenges in obtaining high resolution understanding caused by the diversity of molecular species of heterogeneous samples, most of the techniques described above have a chromatographic and/or electrophoretic step as part of the workflow, which requires large sample volumes. The stationary phase used in chromatography can have a major influence on the purification strategy and can consist of biomolecules such as dextran, agarose or cellulose or synthetic substrate such as polyacrylamide, polystyrene or silica-based polymers[213]. By contrast, the selection of the mobile phase controls the interplay between the analyte molecules and the matrix and is usually organic or buffered[65].

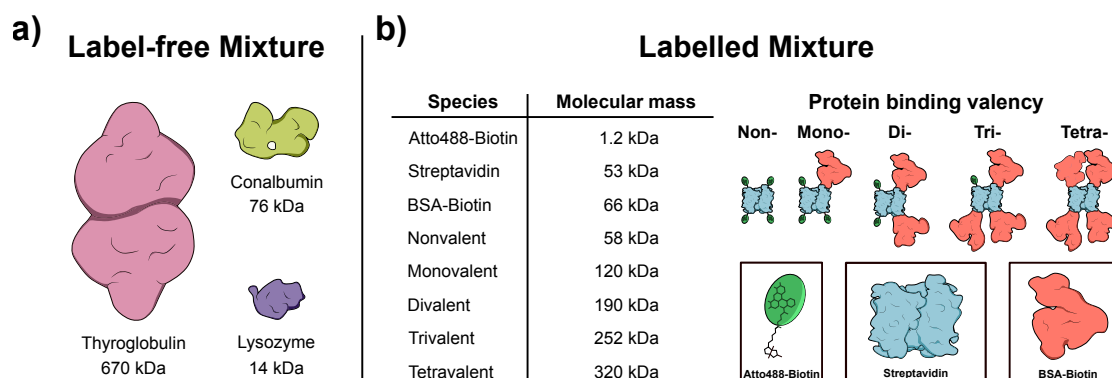


**Figure 4.3:** Composition of molecule mixtures used for label-free and Atto-488 labelled in-line size exclusion chromatography-electrodifffusion measurements a) Proteins used for label-free detection were thyroglobulin (bovine), conalbumin (chicken) and lysozyme (chicken). b) For the labelled mixture, biotinylated Atto-488, streptavidin and biotinylated bovine serum albumin (BSA) were mixed. The three components form various labelled and unlabelled components in different stoichiometry varying in size from 1.2 kDa to 320 kDa.

Microfluidic systems are used to parallelise different assays while allowing small sample volumes being used. Such lab-on-a-chip devices enable manipulation and control over small quantities of fluids, usually in the range of pico- to microliters[238]. Examples of microfluidic analytical tools are diffusional sizing[9, 29, 160, 257], capillary electrophoresis[151], free-flow electrophoresis (FFE)[98, 120, 183, 189, 200] and microscale thermophoresis[239, 249]. Along with the wide range of existing LC methods, e.g. size exclusion, reversed phase, ion-exchange and affinity chromatography[53, 83, 122, 160, 163, 219], microfluidic tools can be used for a resolved characterisation of physiological protein complexes from endogenous samples[96, 237].

In this study, I combined high flow size exclusion chromatography with microfluidic protein analysis. A small fraction of the eluting sample was continuously distributed between two functionally separate fluidic circuits. By measuring the sample composition in the condensed phase, I was able to analyse proteins and their complex formation under native conditions. The microfluidic systems applied here allow for the simultaneous determination of hydrodynamic radius and electrophoretic mobility of molecules in a quantitative manner in complex mixtures[9, 38, 98, 200, 257]. Furthermore, by applying multiple orthogonal downstream analyses approaches, I was able to increase the limited effective resolution of the SEC column. In order to quantify multiple biophysical parameters, the individual microfluidic components were arranged to fit within a single camera field of view (Fig 4.2b), where one part documents the deflection of molecules in an electric field applied on an electrophoretic chamber (Fig 4.2c) and a second part records the molecular diffusion at distinct positions along a channel. The acquired intensity of the diffused molecules is converted into two-dimensional profiles and fitted against theoretical basis functions assuming a range of hydrodynamic radii (Fig 4.2a). Only a small fraction of the solution is used for analysis, whereas the main volume of the sample is collected and can be used for further evaluation.

## 4.2 Results and Discussion

### 4.2.1 Label-free protein characterisation

In order to test whether this combined strategy is capable of detecting and analysing a mixture of unlabelled proteins following SEC, I used a UV-microscope set up, capable of

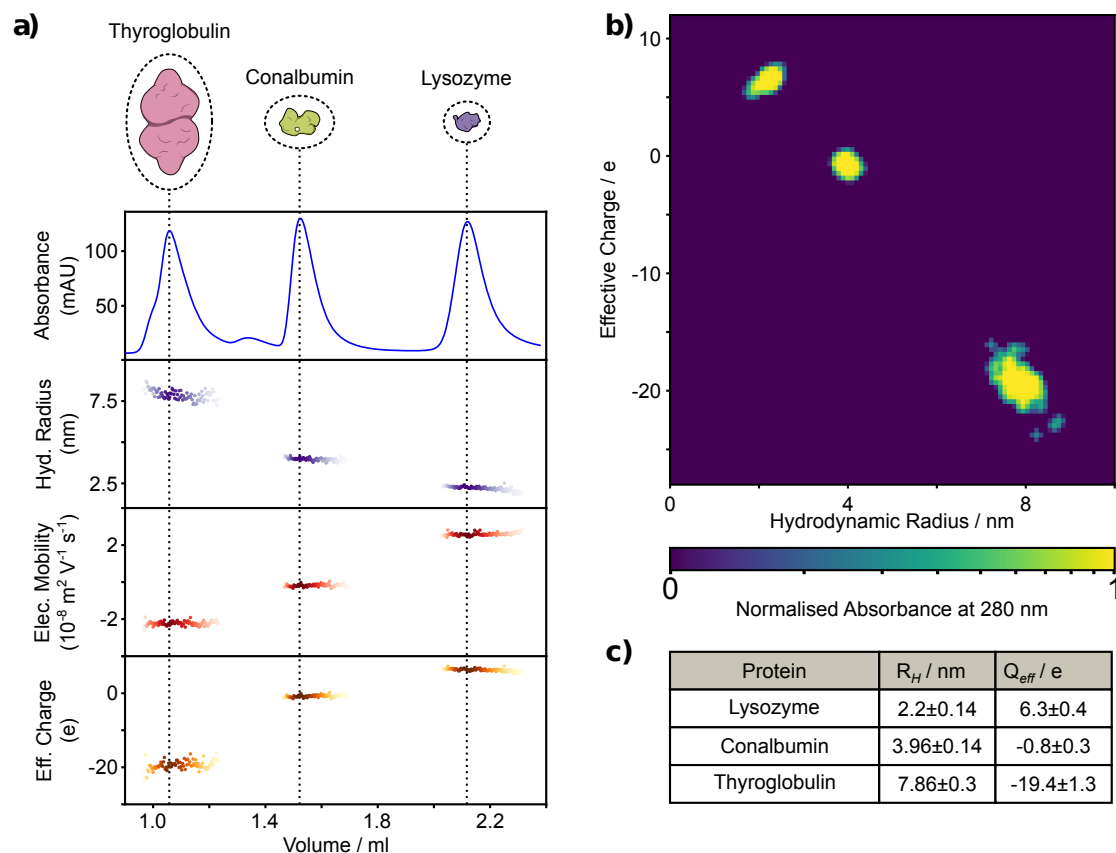


**Figure 4.4:** Label-free multidimensional characterisation of thyroglobulin, conalbumin and lysozyme by in-line SEC Electrodiffusional sizing. a) The mixture was separated into three major peaks and the eluting molecule size, electrophoretic mobility and effective charge were measured continuously. b) Individual measurements conducted every 20 s were analysed based on the molecular absorption at 280 nm revealing 3 major populations in the protein mixture with individual size and charge. c) Hydrodynamic radius and net charge of the three major peaks assigned to the proteins originally being used.

exciting aromatic amino acids and measuring their intrinsic protein fluorescence[38]. The mixture I used consisted of the three unlabelled proteins thyroglobulin dimer (bovine), conalbumin (chicken) and lysozyme (chicken) (see figure 4.3). These proteins vary in size from 14 to 670 kDa and were selected to give adequate separation by size exclusion chromatography. Therefore, all three proteins were completely separated into three major peaks eluting at volumes of 1.06 mL, 1.52 mL and 2.12 mL, respectively, with a minor conalbumin oligomer peak at 1.34 mL (see figure 4.4). Following this, the eluting samples were continuously input into a free-flow electrophoresis and diffusional sizing device (see figure 4.1), devices which have previously been described individually and

are able to measure electrophoretic mobility  $\mu_e$  and hydrodynamic radius  $R_h$  of individual molecules, respectively (see figure 4.4a)[9, 38, 98, 200, 257]. More specifically, one fraction of the sample is loaded into an electrophoresis device between two liquid electrodes with a perpendicularly applied electric field. A second fraction of the sample is loaded into the diffusion device in a simple buffer co-flow geometry along a channel and the diffusion monitored in a time resolved manner. Data from the two devices can be used together to calculate the effective charge  $q$  of individual species (see figure 4.4a-c). To determine the biophysical properties of the separated molecular species more accurately, I have aligned their corresponding elution volume by setting a 10% maximum peak intensity threshold. The measured signals of thyroglobulin, conalbumin and lysozyme correspond to a hydrodynamic radius of  $7.86 \pm 0.30$  nm,  $3.96 \pm 0.14$  nm and  $2.20 \pm 0.14$  nm, respectively (see figure 4.4c). The measurements agree with previously established biophysical values [17, 159, 214]. Furthermore, I have been able to simultaneously acquire the effective charges as  $-19.4 \pm 1.3$  e,  $-0.8 \pm 0.3$  e and  $6.3 \pm 0.4$  e for each protein (see figure 4.4c). The measured net charge at pH 7.4 for the three analysed proteins correlates with reported pIs, which are 4.5 for thyroglobulin, 6.5-6.8 for conalbumin and 10.7-11.3 for lysozyme[194, 230]. The online tools Prot pi/Protein Calculator v3.4 predict a net charge of unfolded lysozyme, conalbumin and thyroglobulin of 6.2/7.3, -5.6/-3.2 and -54.7 -46.8 at pH 7.4, respectively. The overall trend of the predicted values is in good agreement with the experimental results and the absolute difference can be caused by charge screening through protein folding and oligomerisation. Additionally, I combined the measured information in a 3-D plot showing molecular size versus effective charge map with a 280 nm absorption intensity related color-map (see figure 4.4b). The plot shows three species with individual biophysical properties. Thus, I demonstrate an in-line label-free biophysical characterisation tool of a heterogeneous mixture following SEC separation.

#### **4.2.2 Heterogeneous labelled analyte separation and characterisation**

The advantage of fluorescent labels is an increase in sensitivity and specificity such that detection of particular molecules is possible even in highly diverse mixtures and at low concentrations. Thus, fluorescent labelling enables tracking of individual interactions of a probe in complex solutions. In my study, I used a mixture of biotinylated BSA and biotinylated Atto-488 dye, both capable of binding to streptavidin with one of

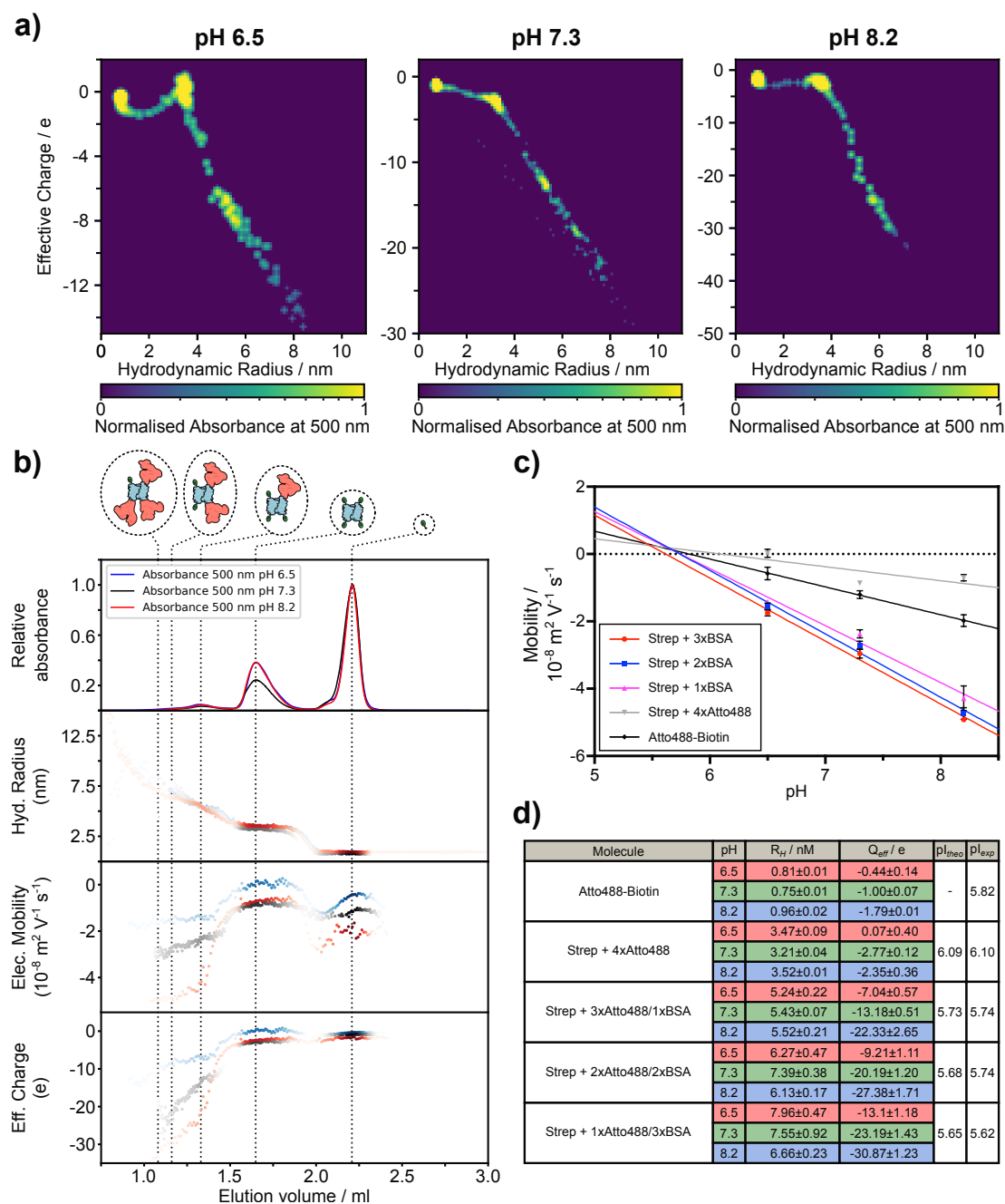


**Figure 4.5:** The labelled streptavidin/BSA/Atto-488 mixture was characterised at three different pH values. a) The five identified labelled molecule complexes were characterised and 3-dimensional charge versus size maps were generated. The points are binned and weighted based on the absorption intensity at 500 nm. b) The labelled mixture was incubated and separated *via* LC at pH 6.5 (blue curve and points), 7.3 (black curve and points) and 8.2 (red curve and points). The hydrodynamic radii, electrophoretic mobilities and effective charges of all elutions were recorded. c) Measured mobilities of the individual identified species were plotted against the different pH conditions and analysed further by linear regression. d) After identifying the molecular elution volume ranges, the molecule biophysical properties as hydrodynamic radius, effective charge, theoretical (ExpASy) and experimental isoelectric point were estimated.

the strongest affinities found in nature ( $K_D = 10^{-15}$  M)[236]. To illustrate the power of this technique and estimate yet another analytical dimension, I have repeated the experiment under three different pH conditions, 6.5, 7.3 and 8.2 and followed changes in molecular charges to investigate individual isoelectric points. The LC separation of the Atto-488 labelled streptavidin-biotin based system resulted in similar sample elution peaks for all three conditions (see figure 4.5b). Simultaneously, I measured the size and electrophoretic mobility of the eluting material *via* fluorescence microscopy (see Experimental Section). Both sets of information were used to calculate the distinct net charge of each molecule (see figure 4.5b). I plot the effective charge versus the molecular size where the intensity of each point is the absorption intensity at 500 nm summarising the biophysical properties of the five Atto-488 labelled molecular complexes abundant in the mixture (see figure 4.5a). By further applying a Savitzky-Golay filter before and after taking the second derivative of the raw absorbance spectrum, four distinct Atto-488 labelled molecules and the free dye itself can be assigned (see Experimental Section). The first major peak with elution volume between 1 ml and 1.5 ml has three subpeaks which could not be separated completely due to the insufficient resolution at the given molecular weight range of my selected column. However, using the second derivative analysis of absorption at 500 nm I estimated the approximate elution volumes for streptavidin with one, two and three BSA molecules to be 1.08 ml, 1.16 ml and 1.33 ml respectively (see Supplementary Fig. F.3b). The second major peak with an elution volume between 1.5 ml and 1.9 ml could be identified to be streptavidin with four Atto-488 dye molecules and, finally, the last well-defined peak with an elution volume between 2 ml and 2.3 ml was the free biotinylated Atto-488 dye. Furthermore, I have used the elution volume ranges to estimate the size and effective charge with the corresponding confidence intervals for each of those five species (see figure 4.5d). All molecules have a negative charge under measured conditions and, more specifically, the charge of a biotinylated Atto-488 dye was measured to be  $-1.00 \pm 0.07$  e at pH 7.3 which agrees with the expected charge of -1 e [11]. Streptavidin with four bound dyes resulted in the size of  $3.21 \pm 0.04$  nm and the effective charge of around  $-2.77 \pm 0.12$  e. The mono-, di-, and trivalent streptavidin-BSA complexes have hydrodynamic radii of  $5.43 \pm 0.07$  nm,  $7.39 \pm 0.38$  nm,  $7.55 \pm 0.92$  nm and effective charges of  $-13.18 \pm 0.51$  e,  $-20.19 \pm 1.20$  e and  $-23.19 \pm 1.43$  e, respectively (see figure 4.5d). The relative charge accumulation between each complex correlates with the relative amino acid contribution

of the individual BSA/streptavidin components. The same characterisation for all five molecules were performed at two further pH conditions (see figure 4.5d).

One way to find the pI of individual molecules is to screen the electrophoretic mobility of those molecules over a range of different pH conditions[136]. Therefore, I analysed my streptavidin/BSA/Atto-488 mixtures described above at pH 6.5, 7.3 and 8.2. By linear regression of mobility values at different pHs of individual species, I extrapolated the condition where the overall net charge is 0 (see figure 4.5c). I determined the theoretical isoelectric point ( $pI_{\text{theo}}$ ) by using the ExPASy platform which predicts the pI based on the amino acid sequence. Comparing the experimental acquired isoelectric points ( $pI_{\text{exp}}$ ) with the ExPASy sequence predicted  $pI_{\text{theo}}$  of all four protein species, a high similarity can be seen, ranging from 6.1 of streptavidin with four dyes to 5.6 and 5.7, respectively, for streptavidin with three BSA. This shows that streptavidin on its own has a significant higher pI than the dye and the pI of BSA is even lower than both of them.

### 4.3 Conclusion

Conventional liquid chromatography, especially size exclusion chromatography, is limited by the effective resolution of protein mixtures. By applying orthogonal multiplex microfluidic downstream analyses, I was able to increase this effective resolution. I established a direct coupling between size exclusion chromatography and multidimensional microfluidic analysis system while diverting only a minor fraction of the sample for analysis with the majority remaining available for preparative purposes. The multidimensional characterisation of distinct complexes yields their size, electrophoretic mobility and effective charge simultaneously. First, I demonstrated the operation principle of my approach by determining the biophysical properties of unlabelled standard proteins within a mixture. I further show the potential of this analytical method with a heterogeneous labelled mixture to analyse multiple partially separated peaks after chromatographic separation and predicting the effective charge and molecular size of complexes within the mixture. By reproducing this separation at different pH conditions I was also able to find the pI of each labelled species of this mixture individually.

The strategy presented here can be further expanded beyond size exclusion and the two microfluidic modules chosen here. Further analytical and separative techniques such as affinity, ion exchange and reversed phase chromatography as well as capillary electrophoresis or isoelectric focusing can be utilised to investigate more complex forms of protein oligomerisation and protein assembly. The study of highly dynamic oligomeric composition and formation, which can either quickly convert to other higher order aggregates or dissociate again, is of vital importance. In particular, the formation of short-lived, on-pathway oligomers represent the major toxic species formed through the aggregation of proteins such as amyloid- $\beta$  and  $\alpha$ -synuclein, resulting in neurodegeneration related to Alzheimer's and Parkinson's diseases, respectively[232, 245]. Recently, however, the aggregation of such amyloidogenic proteins has been found to be inhibited or modulated through the interaction of formed oligomers with chaperones, such as the small heat shock protein family[95]. Therefore, the in-line approach of separation and biophysical characterisation before re-equilibration described here are an ideal approach for investigating protein oligomerisation and their inhibition by a diverse range of chaperones. The proposed approach can further be extended to detect molecular interaction in complex samples, such as serum or cell lysate. The limitations are mainly based on the capabilities of the separation by the liquid chromatography stage. The method can be improved upon by introducing combinations of separation techniques, e.g. size-exclusion and ion-exchange. The use of labelled proteins enables the microfluidic biophysical characterisation of specific proteins even in such complex solutions. However, if multiple molecular species are targeted simultaneously using the presented microfluidic setup, only an average hydrodynamic radius or charge can be determined, when no particular multimodal distribution can be identified[203, 252]. As the duration between the separation following liquid chromatography and microfluidic detection lies in the range of a few minutes, our technique might not be suitable for characterising very transient oligomers and complexes formed of very weak or unspecific interactions. Those complexes conventionally exhibit dissociation constants above hundreds of micromolar or dissociation rate constants above  $k_{\text{off}} = 10^{-4}\text{sec}^{-1}$ [118]. In this particular case, the dissociation rate of the streptavidin complex described above has previously found to be  $5.4 \cdot 10^{-6}\text{s}^{-1}$  and the duration of re-equilibration is in the order of days[58]. Furthermore, the detailed investigation of post-translational modifications of protein mixtures, such as ubiquitination, phosphorylation or carbohydrate moiety, each showing individual changes in either size, charge and hydrophobicity, is another scope my application

can be used for. Therefore, this unique protein analysis approach has great potential to extend the characterisation of heterogeneous protein mixtures in the condensed phase.

# Chapter E

---

## Methods and Analysis

---

### E.1 Analyte mixtures

To demonstrate the functionality of the method I have selected a mixture of three proteins varying in size and isoelectric point (pI): bovine thyroglobulin ( $M_w=670$  kDa, pI=4.5, GE Healthcare, 28-4038-42), chicken conalbumin ( $M_w=76$  kDa, pI=6.7, GE Healthcare, 28-4038-42,) and chicken lysozyme ( $M_w=14.3$  kDa, pI=9.3, Sigma-Aldrich, L6876) (figure 4.3a). The proteins were diluted in a 100 mM sodium HEPES buffer (pH=7.3) at a ratio of 4.6 : 33 : 110  $\mu$ M, respectively; total sample volume was 40  $\mu$ L.

The second system that I used to generate a heterogeneous sample was based on streptavidin-biotin complex formation. I prepared the mixture by incubating streptavidin (Prospec, Israel, PRO-791), biotinylated bovine serum albumin (Generon, UK, 7097-5) and biotinylated Atto-488 (ATTO-TEC GmbH, Germany) dye at a ratio of 1:1:3 (15.7:15.7:47.1  $\mu$ M, total volume was 50  $\mu$ L) for 1 hour at room temperature in 10% Phosphate buffered saline solution (0.1xPBS) at pH 6.5, 7.3 and 8.2, respectively. The mixture is expected to form seven distinct complexes with sizes ranging from 1 kDa to 300 kDa (figure 4.3b). Five of the complexes contain an Atto-488 fluorophore and, therefore, the latter molecules were the focus of detection and analysis.

## E.2 LC separation

Two different buffers were used for the sample elution through the column. First, I used a 100 mM sodium HEPES buffer (pH=7.3) for the label-free sample characterisation. In contrast, the streptavidin-biotin mixture was eluted in a 0.1xPBS buffer with a pH of either 6.5, 7.3 or 8.3. Both buffers also contained 0.01% Sodium azide and 0.1% Tween to reduce sample adhesion to microfluidic channels. A Superdex 200 Increase 3.2/300 column (GE Healthcare, UK) at a flow of 10  $\mu\text{L}/\text{min}$  was operated on an ÄKTA Pure System (GE Healthcare, UK). I was monitoring the eluting sample absorption at 280 nm and 500 nm wavelengths simultaneously with a 10 mm path length absorption monitor U9-M (GE Healthcare, UK). The absorption intensity was used for matching the molecular elution volume with the image sequence on a fluorescence microscope. The flow from the LC separation was connected to the microfluidic flow adapter.

## E.3 Microfluidic flow adapter

A microfluidic junction (P-722, IDEX Health & Science, USA) with carefully pre-cut polyether ether ketone (PEEK) capillaries (IDEX Health & Science, USA) and flow sensors (MF2 7  $\mu\text{L}/\text{min}$ , Elveflow, France) were built, directing only a fraction of the flow coming from chromatographic separation into multiple microfluidic devices (Supplementary Fig. F.1 and F.5). The lengths of the capillaries were as follows: the fractionator output was made of a capillary with  $L_f=10.2$  cm and 125  $\mu\text{m}$  ID and the outputs A and B were made of two capillaries ( $L_1=10$  cm with 125  $\mu\text{m}$  ID and  $L_2=8.1$  cm with 67.8  $\mu\text{m}$  ID). Outputs A and B were connected to microfluidic devices operating at flow rates close to few 100  $\mu\text{L}/\text{h}$  ( $\sim 1.7$   $\mu\text{L}/\text{min}$ ). In general, the flow from the LC protein separation can be in the range of 10  $\mu\text{L}/\text{min}$  - 1 mL/min (600  $\mu\text{L}/\text{h}$  - 60 ml/h) depending on the pressure and column used and, therefore, the capillary resistances have to be fine-tuned for the desired flow splitting ratio. The flow sensors were integrated into ÄKTA Pure system with an I/O-box E9 for real time flow monitoring (GE Healthcare, UK). Stable flow splitting was achieved directing about 10% of the total flow to different parts of the microfluidic chip (Supplementary Fig. F.2). The flow rates at the diffusional sizing and the electrophoresis device sample inlets were measured to be  $40.0\pm 0.7$   $\mu\text{L}/\text{h}$  and  $37.4\pm 0.7$   $\mu\text{L}/\text{h}$  respectively.

## E.4 Flow control

The need for purification or separation techniques of complex mixtures in biomolecular studies is vast. However, most of these bulk techniques cannot directly be transferred to microfluidic scales due to the high pressure flow systems commonly used. In order to match macrofluidic flows used in chromatographic systems with microfluidic flows found in chips with micron sized features, a flow adapter scalable to a wide range of rates had to be designed and implemented (Supplementary Fig. F.2). The incoming flow can be split into numerous outlets, each adjusted for specific applications. Thus, my flow adapter interface enables a standard LC separation, followed by simultaneous multidimensional characterisation. The LC system used was an ÄKTA Pure system which drives two high pressure pumps maintaining a highly stable flow with a 1-5% fluctuation level depending on the buffer and the separation column used (Fig. S3†). In my experiments, the microfluidic flow adapter with carefully adjusted resistances distributed the fluid from the the LC absorption measurement cell between two microfluidic sample inlets and a fractionation outlet. The flow rates at the chip inlets for the free-flow electrophoresis and diffusional sizing were measured to be  $6.7 \pm 0.1\%$  and  $6.2 \pm 0.1\%$ , of the initial flow rate, respectively. The rest of the post LC separation fluid not used for further characterisation ( $\sim 90\%$ ) was collected via the fractionation outlet. The ratios used were adapted to the microfluidic application used or separation procedure applied.

## E.5 Microfluidic chip design and operation

The microfluidic device was designed to fit two distinct analytical parts in one fluorescence microscope field of view. One part contains the diffusional sizing device and consists of a long diffusion channel of a length of  $L_D=43$  mm, a width of  $W_D=300$   $\mu\text{m}$  and a height of  $H_D=55$   $\mu\text{m}$  (figure 4.1). The positions for the diffusion profile acquisition were chosen to allow a high dynamic range for sizing and fixed to distances of 1.4 mm, 2.0 mm, 10.7 mm, 11.3 mm, 19.9 mm, 20.5 mm and 39.2 mm from the sample injection point. I injected a degassed co-flow buffer (same as the LC mobile phase) at a 150  $\mu\text{L}/\text{h}$  flow rate with a neMESYS syringe pump (CETONI GmbH, Germany) into the device. The outlet of the microfluidic flow adapter is connected to the sample inlet on

the diffusional sizing device. I record the injected sample diffusion profile and perform a fit to the numerical diffusion simulations [9, 164].

The second part of the microfluidic chip is a free-flow electrophoresis device with liquid electrodes [200]. It was designed to create up to 60 V/cm transverse electric fields on chip while avoiding bubble formation and electrolysis product build-up on chip. I inject a conductive 3 M KCl electrolyte solution from the sides (figure 4.1) at flow rates of 150  $\mu\text{L}/\text{h}$ . The sample buffer solution is injected as a co-flow of the sample at a flow rate of 150  $\mu\text{L}/\text{h}$  using a neMESYS syringe pump. The second output of my fluidic adapter is connected to the sample inlet of my free-flow electrophoresis device. Hollow stainless steel 1.5 mm ID electrodes are inserted into the liquid electrode channels on the sides of the device and connected to a power supply (EA Elektro-Automatik 6230207, Germany). The power supply is connected to the chip *via* a multimeter (Agilent 34410A, USA) recording a current flowing through the circuit.

The two microfluidic devices were operating continuously and a measurement of the hydrodynamic radius, electrophoretic mobility and charge were obtained for every 3.3  $\mu\text{L}$  of the eluting sample (every 20 s) from the column while still fractionating 90% of the total volume.

## E.6 Microfluidic chip fabrication

The devices were fabricated using a standard polydimethylsiloxane (PDMS) soft-lithography approach [157]. The master for the replica molding of PDMS is fabricated with an SU-8 photolithography process [37]. After mixing PDMS (Sylgard184, Dow Corning, two components 10:1 ratio and degassed) and casting it onto the photolithographically defined structure, it is cured at 65° C for 1 h. A carbon black nanopowder (Sigma-Aldrich) is added to the PDMS before curing to create black devices, thus minimising background noise and the unwanted autofluorescence from PDMS under 280 nm-LED illumination during the measurements. The PDMS replica of each master is then cut, and the connection holes are made with a biopsy punch. The PDMS device is sonicated for 3 min in isopropanol, blow-dried with  $N_2$ , and placed in an oven at 70° C for 10 min. Finally, the replica is activated using  $O_2$  plasma at a 40% power for 10 s (Diener etcher Femto, Germany) and bonded to a clean quartz slide (Alfa Aesar,

76.2 x 25.4 x 1.0 mm) for UV measurements or a simple glass slide for fluorescence measurements.

## E.7 Fluorescence microscope setups

Two different fluorescence microscopes were used for the experiments: an intrinsic fluorescence microscope for a label-free protein detection and a green label epifluorescence measurement setup. First, the autofluorescence measurements of proteins containing aromatic amino acids were measured on a quartz-based intrinsic fluorescence visualisation platform [38]. In short, the proteins were illuminated with a 25 mW 280 nm LED (M280L3, Thorlabs, UK) through an excitation filter (FF01-280/20-25, Semrock, USA) centred at a  $\lambda_{ex}$ =280 nm and a dichroic mirror (FF310-Di01-25x36, Semrock, USA). The fluorescence from the sample was collected through an emission filter (FF01-357/44-25, Semrock, USA) centred at  $\lambda_{em}$ =357 nm, and focused onto a EMCCD camera (Rolera EMC2, QImaging, Canada).

The green epifluorescence microscope, optimised for the Green Fluorescent protein (GFP) / Alexa-488 detection, consisted of a 490 nm LED (M490L4, Thorlabs, UK), an excitation filter at  $482 \pm 9$  nm, a dichroic mirror (350 - 488 nm / 502 - 950 nm) and the emission filter at  $520 \pm 14$  nm (filter set MDF-GFP2, Thorlabs, UK). The microscope had an xyz stage for accurate chip positioning in the field of view of a 2.5x objective, and the pictures were taken with a CCD camera (Retiga R1, QImaging, USA). A raw background corrected fluorescence image of a sample under test is shown in figure 4.1).

## E.8 Time matching

There is a slight delay between the molecule absorption measurement after the LC separation and the detection on chip. The delay volume from the absorption measurement cell to the flow adapter is 70  $\mu L$  and the volume from the flow adapter to the chip detection channel is around 8  $\mu L$  causing 20-30 min delay time depending on the system flow. Both were matched by comparing absorption intensity on the absorbance detector (280 nm and 500 nm) of the LC and the fluorescence intensity of the eluting sample on chip.

## E.9 Electrophoresis device calibration and mobility analysis

I applied a voltage  $V_0$  to the electrodes of the electrophoresis device. First, I performed the mobility measurements while recording the current flowing through the circuit  $I$ . Then, I filled the device electrophoresis chamber with the conductive electrolyte solution and measured the current  $I_0$  while applying the same voltage  $V_0$  (Supplementary Fig. F.4). Then

$$V_0 = I(R_{elec} + R_{ch}), \quad (\text{E.1})$$

$$V_0 = I_0 R_{elec}, \quad (\text{E.2})$$

$$\Rightarrow V = IR_{ch} = R_{elec}(I_0 - I) = V_0(1 - I/I_0). \quad (\text{E.3})$$

Distance along the direction of flow:

$$d_{\parallel} = v_{\parallel}t = \frac{Q}{hw}t \Rightarrow t = \frac{d_{\parallel}hw}{Q} \quad (\text{E.4})$$

The mobility can be expressed as:

$$\mu = \frac{v}{E} = \frac{x}{tE} = \frac{xwQ}{Vdhw} = \frac{Q}{Vdh}x = \frac{Q}{V_0(1 - I/I_0)dh}x \quad (\text{E.5})$$

The total flow to the device  $Q = 146 \mu\text{L/h}$ ,  $V_0 = 60 \text{ V}$ ,  $d = 2880 \mu\text{m}$ ,  $h = 55 \mu\text{m}$ ,  $I = 0.267 \pm 0.002 \text{ mA}$ ,  $I_0 = 0.283 \pm 0.001 \text{ mA}$ .

## E.10 Size and charge calculations

The diffusion profiles were extracted by processing the images and removing the background using image alignment in the Fourier plane. The curve, generated by the non-uniform illumination intensity, was removed by multidimensional polynomial fitting. The channel edge positions and image rotation angle were detected and corrected automatically using an FFT-based technique[190]. The noise was then reduced by spatial

averaging along the channel before extracting the profiles at 7 predefined positions along the diffusion channel. Then, a set of basis functions, predicting the diffusion profiles of predefined sizes (diffusion coefficients), was generated[9, 38, 164, 215]. Finally, a fit deconvolving the measured experimental profiles into a linear combination of the simulated basis functions was computed using a least-squares error algorithm. The fit interpolation yielded the average eluting analyte hydrodynamic radius with the associated error.

The measured hydrodynamic radius  $R_h$  and the electrophoretic mobility  $\mu_e$  can be used to estimate the complex charge using the Nernst-Einstein relation:[111]

$$q = Ze = 6\pi\eta R_h \mu_e, \quad (\text{E.6})$$

with  $Z$  being the charge number and  $e$  the elementary charge, using the corresponding hydrodynamic radius and electrophoretic mobility. The equation is based on the assumption that the electrical force exerted on the analyte molecules balance with the drag force arising from analyte migration through the solution.

## E.11 Isoelectric point and net charge prediction

The isoelectric point of BSA, streptavidin and their various combinations were predicted using the ExPASy online pI/Mw computing tool. Therefore, I used the sequence for BSA (UniProtKB P02769 [25-607]) and streptavidin (MAEAGITGTWYNQLGSTFIVTAGADGALTGTYESAVGNAESRYVLTGRYDSAPATDGSALTGWTVAWKNNYRN AHSATTWSGQYVGGAEARINTQWLLTSGTTEANAWKSTLVGHDTFTKVKPSAAS).

The net charge of lysozyme, conalbumin and thyroglobulin was predicted using the Prot pi and the Protein Calculator v3.4 online tool.

## E.12 Second derivative analysis of chromatograms

An example for separation of the heterogeneous labeled streptavidin/BSA/Atto-488 mixture is shown in Supplementary Fig. F.3a. Taking the second derivative of the absorption

intensity at 500 nm (Supplementary Fig. F.3b) reveals three most significant peaks at 1.08 ml, 1.16 ml and 1.3 ml, respectively. To take the second derivative I have applied Savitzky-Golay filter two times with 251 points: on the original spectrum and on the final second derivative of the spectrum. The three peaks can be identified as streptavidin with one, two and three BSA molecules, respectively.

# Chapter F

---

## Supplementary information

---

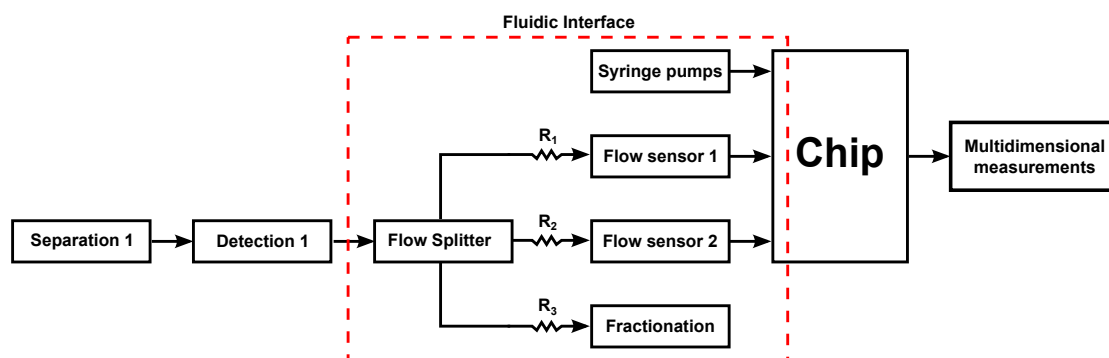


**Figure F.1:** The flow adapter interface contains a 4-way fluidic channel with calibrated PEEK capillaries acting as hydrodynamic resistors. The ratio of the capillary hydrodynamic resistance determines the fluidic adapter flow splitting ratio which can be monitored with flow sensors.

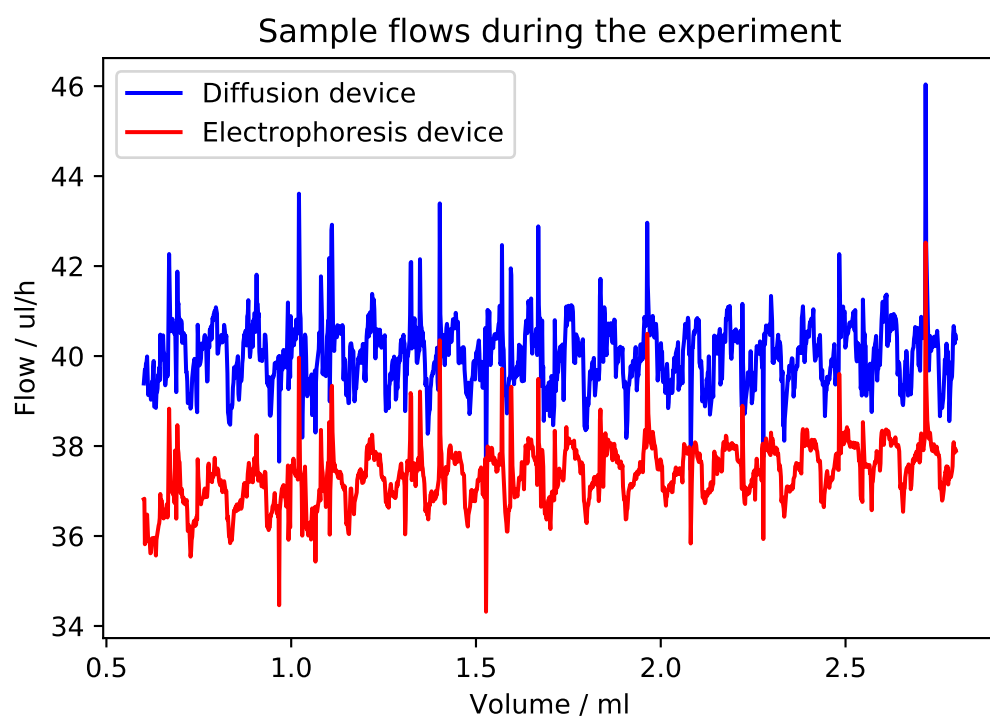


**Figure F.2:** Flow rate measurements recorded at the inlet of the individual devices. The flow at the diffusional size and the electrophoresis devices has been constant to few percent variation.

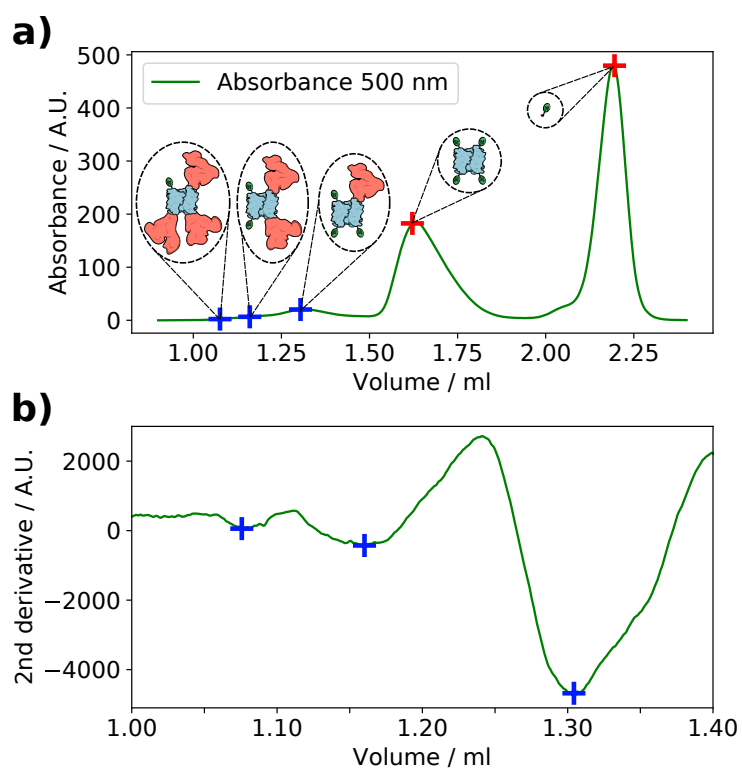


**Figure F.3:** a) Streptavidin, BSA and Atto-488 dye complexes absorbance at 500 nm just after the LC separation at pH 8.2. We can identify three distinct regions in the spectra representing the 5 different labelled molecular complexes. b) second derivative of the spectrum between 1-1.4 ml reveals 3 most significant sub-peaks.

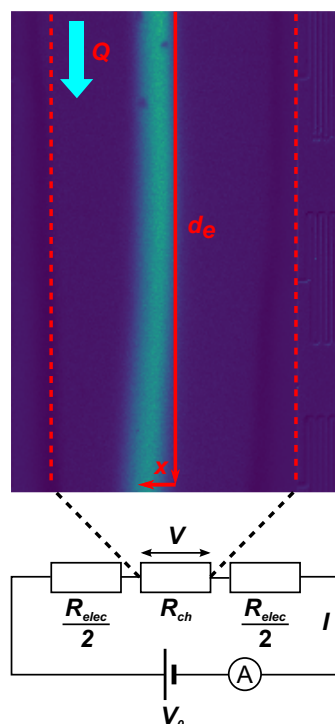


**Figure F.4:** The representation of the electrophoresis device equivalent electronic circuit. During the calibration step, the chamber electric resistance can be neglected, allowing  $R_{elec}$  estimation. Due to a high electrode resistance of  $R_{elec} \sim 250 \text{ k}\Omega$ , the voltage drop was 5% across the main electrophoresis chamber.

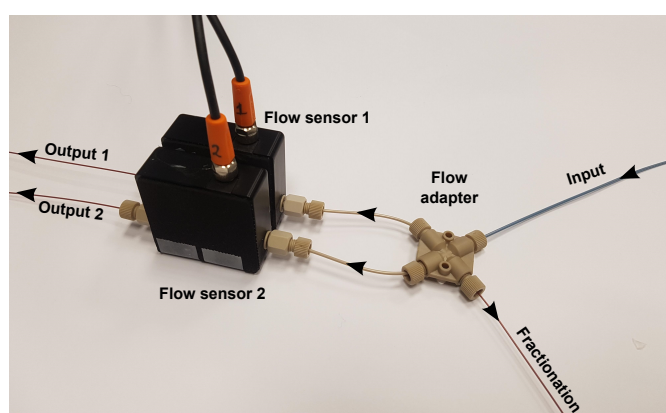


**Figure F.5:** Microfluidic flow adapter matching the flow between liquid chromatography and microfluidic chip over two orders of magnitude. The flow is split between the fractionation outlet and outputs A and B; the flow through the outlets A and B is monitored with flow sensors.

## Chapter 5

---

### Concluding remarks

---

Microfluidic approaches offer an extension of conventional biophysical techniques for the study of the intricate nature of biomolecule recognition. In particular, the microfluidic above described diffusion device on its own or in combination with other techniques such as liquid chromatography or other microfluidic platforms introduce a fundamentally new strategy for the study of molecular interactions in the liquid phase. Thus, this thesis presents a detailed characterisation of molecular chaperone activity in suppressing protein aggregation and the underlying binding mechanisms leading to specific inhibitory phenomena. In particular, I have studied in detail the entropic binding dynamics of the sHsp  $\alpha$ B-c to  $\alpha$ -syn fibrils and have shown that changes in heat capacity are indicating a necessary structural change of the chaperone prior to the binding. For clusterin and Brichos, chaperone systems previously described in the context of A $\beta$ (42) aggregation, binding studies and aggregation kinetics have been conducted and revealed a complex suppression system in which each chaperone specifically inhibits distinct microscopic aggregations steps without overlap. These results together with further binding kinetics of Brichos form a distinct structural picture of elongation sites on fibrillar ends and secondary nucleation sites along the fibrillar surface. However, such secondary nucleation sites found along the fibrils are rather rare events than ordered repetitive structures.

Intuitively, mimicking nature's specific inhibition of aggregation for therapeutic applications in the context of aggregation related diseases seems like an ideal solution. Especially secondary nucleation seems to be the major inhibitory target desired in order to prevent the formation of toxic oligomeric species. However, studies presented here show that potential therapeutic antibodies for Alzheimer's, namely aducanumab, bapineuzumab, gantenerumab and solanezumab, which were or still are under clinical phase 3 trial, are not, on their own, sufficient for inhibiting secondary nucleation. Each antibody shows individual binding properties either to  $A\beta(42)$  monomers, fibrils or both, resulting in a specific inhibition pattern. A full biophysical characterisation of potential therapeutics and all intermolecular interactions involved could thus increase the positive outcome in drug development.

The main challenges of most biophysical techniques in quantifying molecular interactions, are the lack of representation of physiological conditions or inability to deconvolute the composition of complex mixtures. In this work I have demonstrated that the MDS technique applied can overcome both obstacles. A full quantification of serum molecules can be achieved using a fluorescent labelled probe. Thus, the absolute quantification of anti-HLA antibodies and their affinity have been applied, as these have crucial impact on studying and rating the risk for graft rejection. The commercial available MDS instrument, Fluidity One-W from Fluidic Analytics Ltd., have been found to be capable of quantifying target molecules in human serum down to low nanomolar concentrations.

In order to study heterogeneous solutions and measuring multiple molecules simultaneously, I combined the microfluidic diffusion device with liquid chromatography approaches. By coupling a microfluidic electrophoresis device to the system, I have acquired multidimensional biophysical properties such as hydrodynamic radius, electrophoretic mobility, relative amount and isoelectric point of a heterogeneous solution consisting of five different molecular species. This multidimensional characterisation seems well suited for studying oligomerisation and their dynamics seen for sHsps,  $\alpha$ -syn and  $A\beta$ , but can also be extended for protein modification, such as ubiquitination, glycosylation and phosphorylation.

This work focused on studying a range of different intermolecular interactions, obtaining binding parameters and gain insights into molecular processes using microfluidic

---

approaches. However, further microfluidic development has to be done in order to become able to fully quantify and investigate rare transient molecular species such as amyloid precursors. Studying toxic oligomeric species by on-chip separation or single molecule detection is already emerging as a crucial aspect in biophysics and understanding neurodegenerative diseases. In addition, multiplexing binding measurements becomes essential for further clinical application. Fast and sensitive techniques being able to quantify individual composition of body fluids are needed in hospitals for reliable diagnosis and risk assessment.



---

# Bibliography

---

- [1] J. D. Altman, P. a. Moss, P. J. Goulder, D. H. Barouch, M. G. McHeyzer-Williams, J. I. Bell, a. J. McMichael, and M. M. Davis. Phenotypic analysis of antigen-specific T lymphocytes. *Science (New York, N.Y.)*, 274(5284):94–96, 1996.
- [2] M. Andreassen, G. Meisl, J. D. Taylor, T. C. T. Michaels, A. Levin, D. E. Otzen, M. R. Chapman, C. M. Dobson, S. J. Matthews, and T. P. J. Knowles. Physical Determinants of Amyloid Assembly in Biofilm Formation. *mBio*, 10(1), 2019.
- [3] C. B. Anfinsen. Principles that govern folding of protein chains. *SCIENCE*, 181(4096):223–230, 1973.
- [4] F. A. Aprile, P. Arosio, G. Fusco, S. W. Chen, J. R. Kumita, A. Dhulesia, P. Tortora, T. P. J. Knowles, M. Vendruscolo, C. M. Dobson, and N. Cremades. Inhibition of alpha-Synuclein Fibril Elongation by Hsp70 Is Governed by a Kinetic Binding Competition between alpha-Synuclein Species. *Biochemistry*, 56(9):1177–1180, mar 2017.
- [5] F. A. Aprile, P. Sormanni, M. Perni, P. Arosio, S. Linse, T. P. J. Knowles, C. M. Dobson, and M. Vendruscolo. Selective targeting of primary and secondary nucleation pathways in A beta 42 aggregation using a rational antibody scanning method. *Sci. Adv.*, 3(6), jun 2017.
- [6] J. W. Arndt, F. Qian, B. A. Smith, C. Quan, K. P. Kilambi, M. W. Bush, T. Walz, R. B. Pepinsky, T. Bussiere, S. Hamann, T. O. Cameron, and P. H. Weinreb. Structural and kinetic basis for the selectivity of aducanumab for aggregated forms of amyloid-beta. *Sci. Rep.*, 8, apr 2018.
- [7] P. Arosio, R. Cukalevski, B. Frohm, T. P. J. Knowles, and S. Linse. Quantification of the concentration of A beta 42 propagons during the lag phase by an amyloid chain reaction assay. *J. Am. Chem. Soc.*, 136(1):219–225, jan 2014.
- [8] P. Arosio, T. C. T. Michaels, S. Linse, C. Mansson, C. Emanuelsson, J. Presto, J. Johansson, M. Vendruscolo, C. M. Dobson, and T. P. J. Knowles. Kinetic analysis reveals the diversity of

- microscopic mechanisms through which molecular chaperones suppress amyloid formation. *Nat. Commun.*, 7:10948, mar 2016.
- [9] P. Arosio, T. Müller, L. Rajah, E. V. Yates, F. A. Aprile, Y. Zhang, S. I. A. Cohen, D. A. White, T. W. Herling, E. J. De Genst, S. Linse, M. Vendruscolo, C. M. Dobson, and T. P. J. Knowles. Microfluidic diffusion analysis of the sizes and interactions of proteins under native solution conditions. *ACS Nano*, 10(1):333–341, jan 2016.
- [10] P. Arosio, M. Vendruscolo, C. M. Dobson, and T. P. J. Knowles. Chemical kinetics for drug discovery to combat protein aggregation diseases. *Trends Pharmacol. Sci.*, 35(3):127–135, 2014.
- [11] ATTO-TEC GmbH. Properties of ATTO-Dyes.
- [12] R. W. Bailey, A. K. Dunker, C. J. Brown, E. C. Garner, and M. D. Griswold. Clusterin, a binding protein with a molten globule-like region. *Biochemistry*, 40(39):11828–11840, 2001.
- [13] W. E. Balch, R. I. Morimoto, A. Dillin, and J. W. Kelly. Adapting proteostasis for disease intervention. *Science*, 319(5865):916–919, feb 2008.
- [14] A. J. Baldwin, H. Lioe, C. V. Robinson, L. E. Kay, and J. L. P. Benesch. alpha B-Crystallin Polydispersity Is a Consequence of Unbiased Quaternary Dynamics. *J. Mol. Biol.*, 413(2):297–309, oct 2011.
- [15] M. J. Banker, T. H. Clark, and J. A. Williams. Development and validation of a 96-well equilibrium dialysis apparatus for measuring plasma protein binding. *J. Pharm. Sci.*, 92(5):967–974, 2003.
- [16] F. Bard, C. Cannon, R. Barbour, R. L. Burke, D. Games, H. Grajeda, T. Guido, K. Hu, J. P. Huang, K. Johnson-Wood, K. Khan, D. Kholodenko, M. Lee, I. Lieberburg, R. Motter, M. Nguyen, F. Soriano, N. Vasquez, K. Weiss, B. Welch, P. Seubert, D. Schenk, and T. Yednock. Peripherally administered antibodies against amyloid beta-peptide enter the central nervous system and reduce pathology in a mouse model of Alzheimer disease. *Nat. Med.*, 6(8):916–919, aug 2000.
- [17] B. Batas, H. R. Jones, and J. B. Chaudhuri. Studies of the hydrodynamic volume changes that occur during refolding of lysozyme using size-exclusion chromatography. *J. Chromatogr. A*, 766(1-2):109–119, 1997.
- [18] B. A. Becker, K. F. Morris, and C. K. Larive. An improved method for suppressing protein background in PFG NMR experiments to determine ligand diffusion coefficients in the presence of receptor. *J. Magn. Reson.*, 181(2):327–330, aug 2006.
- [19] M. Beeg, M. Stravalaci, M. Romeo, A. D. Carra, A. Cagnotto, A. Rossi, L. Diomedea, M. Salmona, and M. Gobbi. Clusterin binds to A(1-42) oligomers with high affinity and interferes with peptide aggregation by inhibiting primary and secondary nucleation. *J. Biol. Chem.*, 291(13):6958–6966, mar 2016.
- [20] F. Bemporad and F. Chiti. Pathways of Amyloid Formation. In *Amyloid Fibrils and Prefibrillar Aggregates*, pages 151–166. Wiley-VCH Verlag GmbH & Co. KGaA, 2013.

- [21] I. Benilova, E. Karran, and B. De Strooper. The toxic A beta oligomer and Alzheimer's disease: an emperor in need of clothes. *Nat. Neurosci.*, 15(3):349–357, mar 2012.
- [22] T. Berggard, S. Linse, and P. James. Methods for the detection and analysis of protein-protein interactions. *Proteomics*, 7(16):2833–2842, aug 2007.
- [23] J. Bhattacharyya, E. G. P. Udupa, J. Wang, and K. K. Sharma. Mini-alpha B-crystallin: A functional element of alpha B-crystallin with chaperone-like activity. *Biochemistry*, 45(9):3069–3076, mar 2006.
- [24] K. J. Binger, H. Ecroyd, S. Yang, J. A. Carver, G. J. Howlett, and M. D. W. Griffin. Avoiding the oligomeric state: alpha B-crystallin inhibits fragmentation and induces dissociation of apolipoprotein C-II amyloid fibrils. *FASEB J.*, 27(3):1214–1222, mar 2013.
- [25] Biogen. Biogen and Eisai to discontinue phase 3 engage and emerge trials of aducanumab in Alzheimer's disease, 2019.
- [26] Biogen. Biogen plans regulatory filing for aducanumab in Alzheimer's disease based based on new analysis of larger dataset from phase 3 studies, 2019.
- [27] D. L. Bloxam, P. H. Hutson, and G. Curzon. Simple apparatus for ultrafiltration of small volumes - application to measurement of free and albumin-bound tryptophan in plasma. *Anal. Biochem.*, 83(1):130–142, 1977.
- [28] B. Bohrmann, K. Baumann, J. Benz, F. Gerber, W. Huber, F. Knoflach, J. Messer, K. Oroszlan, R. Rauchenberger, W. F. Richter, C. Rothe, M. Urban, M. Bardroff, M. Winter, C. Nordstedt, and H. Loetscher. Gantenerumab: A Novel Human Anti-A beta Antibody Demonstrates Sustained Cerebral Amyloid-beta Binding and Elicits Cell-Mediated Removal of Human Amyloid-beta. *J. Alzheimer's Dis.*, 28(1):49–69, 2012.
- [29] J. P. Brody and P. Yager. Diffusion-based extraction in a microfabricated device. *Sens. Actuator A Phys.*, 58(1):13–18, jan 1997.
- [30] R. Brookmeyer, E. Johnson, K. Ziegler-Graham, and H. M. Arrighi. Forecasting the global burden of Alzheimer's disease. *Alzheimer's & dementia : the journal of the Alzheimer's Association*, 3(3):186–91, jul 2007.
- [31] A. K. Buell, J. R. Blundell, C. M. Dobson, M. E. Welland, E. M. Terentjev, and T. P. J. Knowles. Frequency Factors in a Landscape Model of Filamentous Protein Aggregation. *Phys. Rev. Lett.*, 104(22), jun 2010.
- [32] A. K. Buell, A. Dhulesia, D. A. White, T. P. J. Knowles, C. M. Dobson, and M. E. Welland. Detailed Analysis of the Energy Barriers for Amyloid Fibril Growth. *Angew. Chem. Int. Ed.*, 51(21):5247–5251, 2012.
- [33] A. K. Buell, C. Galvagnion, R. Gaspar, E. Sparr, M. Vendruscolo, T. P. J. Knowles, S. Linse, and C. M. Dobson. Solution conditions determine the relative importance of nucleation and growth processes in alpha-synuclein aggregation. *Proc. Natl. Acad. Sci.*, 111(21):7671–7676, may 2014.

- [34] B. Bukau and A. L. Horwich. The Hsp70 and Hsp60 chaperone machines. *CELL*, 92(3):351–366, feb 1998.
- [35] R. Buttyan, C. A. Olsson, J. Pintar, C. S. Chang, M. Bandyk, P. Y. Ng, and I. S. Sawczuk. Induction of the TRPM-2 gene in cells undergoing programmed death. *Mol. Cell. Biol.*, 9(8):3473–3481, aug 1989.
- [36] B. Caughey and P. T. Lansbury. Protofibrils, pores, fibrils, and neurodegeneration: Separating the responsible protein aggregates from the innocent bystanders. *Annu. Rev. Neurosci.*, 26:267–298, 2003.
- [37] P. K. Challa, T. Kartanas, J. Charmet, and T. P. J. Knowles. Microfluidic devices fabricated using fast wafer-scale LED-lithography patterning. *Biomicrofluidics*, 11(1):14113, 2017.
- [38] P. K. Challa, Q. Peter, M. A. Wright, Y. Zhang, K. L. Saar, J. A. Carozza, J. L. P. Benesch, and T. P. J. Knowles. Real-Time Intrinsic Fluorescence Visualization and Sizing of Proteins and Protein Complexes in Microfluidic Devices. *Anal. Chem.*, 90(6):3849–3855, mar 2018.
- [39] F. Chiti and C. M. Dobson. Protein Misfolding, Amyloid Formation, and Human Disease: A Summary of Progress Over the Last Decade. In R. Kornberg, editor, *Annu. Rev. Biochem.*, volume 86 of *Annual Review of Biochemistry*, pages 27–68. 2017.
- [40] S. M. Clark and L. Konermann. Determination of ligand-protein dissociation constants by electrospray mass spectrometry-based diffusion measurements. *Anal. Chem.*, 76(23):7077–7083, 2004.
- [41] S. I. A. Cohen, P. Arosio, J. Presto, F. R. Kurudenkandy, H. Biverstal, L. Dolfe, C. Dunning, X. Yang, B. Frohm, M. Vendruscolo, J. Johansson, C. M. Dobson, A. Fisahn, T. P. J. Knowles, and S. Linse. A molecular chaperone breaks the catalytic cycle that generates toxic A beta oligomers. *Nat. Struct. Mol. Biol.*, 22(3):207–213, 2015.
- [42] S. I. A. Cohen, S. Linse, L. M. Luheshi, E. Hellstrand, D. A. White, L. Rajah, D. E. Otzen, M. Vendruscolo, C. M. Dobson, and T. P. J. Knowles. Proliferation of amyloid-beta 42 aggregates occurs through a secondary nucleation mechanism. *Proc. Natl. Acad. Sci.*, 110(24):9758–9763, jun 2013.
- [43] S. I. A. Cohen, M. Vendruscolo, C. M. Dobson, and T. P. J. Knowles. Nucleated polymerization with secondary pathways. II. Determination of self-consistent solutions to growth processes described by non-linear master equations. *J. Chem. Phys.*, 135(6):065106, aug 2011.
- [44] S. I. A. Cohen, M. Vendruscolo, C. M. Dobson, and T. P. J. Knowles. From Macroscopic Measurements to Microscopic Mechanisms of Protein Aggregation. *J. Mol. Biol.*, 421(2-3, 1):160–171, aug 2012.
- [45] S. R. Collins, A. Douglass, R. D. Vale, and J. S. Weissman. Mechanism of prion propagation: Amyloid growth occurs by monomer addition. *PLoS Biol.*, 2(10):1582–1590, 2004.

- [46] M. T. Colvin, R. Silvers, Q. Z. Ni, T. V. Can, I. Sergeev, M. Rosay, K. J. Donovan, B. Michael, J. Wall, S. Linse, and R. G. Griffin. Atomic Resolution Structure of Monomorphic A beta(42) Amyloid Fibrils. *J. Am. Chem. Soc.*, 138(30):9663–9674, aug 2016.
- [47] T. R. Covey, E. D. Lee, A. P. Bruins, and J. D. Henion. Liquid chromatography/mass spectrometry. *Anal. Chem.*, 58(14):1451A—1461A, 1986.
- [48] D. Cox, J. A. Carver, and H. Ecroyd. Preventing alpha-synuclein aggregation: The role of the small heat-shock molecular chaperone proteins. *Biochim. Biophys. Acta, Mol. Basis Dis.*, 1842(9):1830–1843, sep 2014.
- [49] D. Cox and H. Ecroyd. The small heat shock proteins alpha B-crystallin (HSPB5) and Hsp27 (HSPB1) inhibit the intracellular aggregation of alpha-synuclein. *Cell Stress Chaperon*, 22(4):589–600, jul 2017.
- [50] D. Cox, E. Selig, M. D. W. Griffin, J. A. Carver, and H. Ecroyd. Small Heat-shock Proteins Prevent -Synuclein Aggregation via Transient Interactions and Their Efficacy Is Affected by the Rate of Aggregation. *J. Biol. Chem.*, 291(43):22618–22629, oct 2016.
- [51] F. H. C. Crick and J. D. Watson. Structure of small viruses. *Nature*, 177(4506):473–475, 1956.
- [52] J. S. Cristovao, S. S. Leal, I. Cardoso, and C. M. Gomes. Small Molecules Present in the Cerebrospinal Fluid Metabolome Influence Superoxide Dismutase 1 Aggregation. *Int J Mol Sci*, 14(9):19128–19145, sep 2013.
- [53] P. Cuatrecasas. Protein purification by affinity chromatography derivatizations of agarose and polyacrylamide beads. *J. Biol. Chem.*, 245(12):3059–3065, 1970.
- [54] R. A. Dabbs and M. R. Wilson. Expression and purification of chaperone-Active recombinant clusterin. *PLoS ONE*, 9(1):e86989, jan 2014.
- [55] J. de la Cruz, K. Karbstein, and J. L. Woolford Jr. Functions of Ribosomal Proteins in Assembly of Eukaryotic Ribosomes In Vivo. In *Annu. Rev. Biochem.*, volume 84, pages 93–129. 2015.
- [56] M. Del Campo, J. J. M. Hoozemans, L.-L. Dekkers, A. J. Rozemuller, C. Korth, A. Mueller-Schiffmann, P. Scheltens, M. A. Blankenstein, C. R. Jimenez, R. Veerhuis, and C. E. Teunissen. BRI2-BRICHOS is increased in human amyloid plaques in early stages of Alzheimer’s disease. *Neurobiol. Aging*, 35(7):1596–1604, jul 2014.
- [57] R. B. DeMattos, M. A. O’dell, M. Parsadanian, J. W. Taylor, J. A. K. Harmony, K. R. Bales, S. M. Paul, B. J. Aronow, and D. M. Holtzman. Clusterin promotes amyloid plaque formation and is critical for neuritic toxicity in a mouse model of Alzheimer’s disease. *Proc. Natl. Acad. Sci.*, 99(16):10843–10848, aug 2002.
- [58] L. Deng, E. N. Kitova, and J. S. Klassen. Dissociation Kinetics of the Streptavidin-Biotin Interaction Measured Using Direct Electrospray Ionization Mass Spectrometry Analysis. *J. Am. Soc. Mass Spectrom.*, 24(1):49–56, jan 2013.

- [59] H. V. Desilva, J. A. K. Harmony, W. D. Stuart, C. M. Gil, and J. Robbuns. Apolipoprotein-J - structure and tissue distribution. *Biochemistry*, 29(22):5380–5389, jun 1990.
- [60] K. A. Dill and H. S. Chan. From Levinthal to pathways to funnels. *NATURE STRUCTURAL BIOLOGY*, 4(1):10–19, jan 1997.
- [61] C. M. Dobson. Protein misfolding, evolution and disease. *Trends Biochem. Sci.*, 24(9):329–332, sep 1999.
- [62] C. M. Dobson. The structural basis of protein folding and its links with human disease. *Philos. Trans. R. Soc. Lond., B, Biol. Sci.*, 356(1406):133–145, feb 2001.
- [63] C. M. Dobson. Protein folding and misfolding. *Nature*, 426(6968):884–890, 2003.
- [64] C. M. Dobson, A. Sali, and M. Karplus. Protein folding: A perspective from theory and experiment. *Angew. Chem.*, 37(7):868–893, apr 1998.
- [65] J. G. Dorsey, W. T. Cooper, B. A. Siles, J. P. Foley, and H. G. Barth. Liquid Chromatography: Theory and Methodology. *Anal. Chem.*, 68(12):515–568, jan 1996.
- [66] P. M. Douglas, S. Treusch, H.-Y. Ren, R. Halfmann, M. L. Duennwald, S. Lindquist, and D. M. Cyr. Chaperone-dependent amyloid assembly protects cells from prion toxicity. *Proc. Natl. Acad. Sci. U.S.A.*, 105(20):7206–11, may 2008.
- [67] A. Drews, S. De, P. Flagmeier, D. C. Wirthensohn, W.-H. Chen, D. R. Whiten, C. Vincke, S. Muyldermans, R. W. Paterson, C. F. Slattey, N. C. Fox, J. M. Schott, H. Zetterberg, C. M. Dobson, S. Gandhi, and D. Klenerman. Inhibiting the Ca<sup>2+</sup> Influx Induced by Human CSF. *Cell Rep.*, 21(11):3310–3316, dec 2017.
- [68] D. Eisenberg and M. Jucker. The amyloid state of proteins in human diseases. *Cell*, 148(6):1188–1203, mar 2012.
- [69] J. Ellis. Proteins as molecular chaperones. *Nature*, 328(6129):378–379, jul 1987.
- [70] R. J. Ellis. The general concept of molecular chaperones. *Philos. Trans. R. Soc. London B Biol. Sci.*, 339(1289):257–261, mar 1993.
- [71] E. B. Erba and R. Zenobi. Mass spectrometric studies of dissociation constants of noncovalent complexes. *Annu. Rep. Prog. Chem.*, {,} Sect. C: Phys. Chem., 107(0):199–228, 2011.
- [72] M. Farias, M. W. Gorman, M. V. Savage, and E. O. Feigl. Plasma ATP during exercise: possible role in regulation of coronary blood flow. *Am. J. Physiol. Heart Circ. Physiol.*, 288(4):H1586–H1590, apr 2005.
- [73] H. Feinberg, J. W. Saldanha, L. Diep, A. Goel, A. Widom, G. M. Veldman, W. I. Weis, D. Schenk, and G. S. Basi. Crystal structure reveals conservation of amyloid-beta conformation recognized by 3D6 following humanization to bapineuzumab. *Alzheimers Res. Ther.*, 6(3), 2014.

- [74] F. Ferrone. Analysis of protein aggregation kinetics. In *Amyloid, Prions, and Other Protein Aggregates*, volume 309 of *Methods Enzymol.*, pages 256–274. Academic press, 1999.
- [75] A. R. Fersht. Transition-state structure as a unifying basis in protein-folding mechanisms: Contact order, chain topology, stability, and the extended nucleus mechanism. *Proc. Natl. Acad. Sci. U.S.A.*, 97(4):1525–1529, feb 2000.
- [76] L. Fielding. NMR methods for the determination of protein-ligand dissociation constants. *Curr. Top. Med. Chem.*, 3(1):39–53, 2003.
- [77] L. Fielding, S. Rutherford, and D. Fletcher. Determination of protein-ligand binding affinity by NMR: observations from serum albumin model systems. *Magn. Reson. Chem.*, 43(6):463–470, jun 2005.
- [78] R. Freilich, M. Betegon, E. Tse, S.-A. Mok, O. Julien, D. A. Agard, D. R. Southworth, K. Takeuchi, and J. E. Gestwicki. Competing protein-protein interactions regulate binding of Hsp27 to its client protein tau. *Nat. Commun.*, 9, nov 2018.
- [79] M. Geiger, N. W. Frost, and M. T. Bowser. Comprehensive multidimensional separations of peptides using nano-liquid chromatography coupled with micro free flow electrophoresis. *Anal. Chem.*, 86(10):5136–5142, 2014.
- [80] K. C. Giese, E. Basha, B. Y. Catague, and E. Vierling. Evidence for an essential function of the N terminus of a small heat shock protein in vivo, independent of in vitro chaperone activity. *Proc. Natl. Acad. Sci.*, 102(52):18896–18901, dec 2005.
- [81] G. Gorbenko and V. Trusova. Protein aggregation in a membrane environment. In R. Donev, editor, *Advances in protein chemistry and structural biology, Vol 84*, volume 84 of *Advances in Protein Chemistry and Structural Biology*, pages 113–142. Academic press, 2011.
- [82] N. J. Greenfield. Using circular dichroism collected as a function of temperature to determine the thermodynamics of protein unfolding and binding interactions. *Nat. Protoc.*, 1(6):2527–2535, 2006.
- [83] B. Guelat, R. Khalaf, M. Lattuada, M. Costioli, and M. Morbidelli. Protein adsorption on ion exchange resins and monoclonal antibody charge variant modulation. *J. Chromatogr. A*, 1447:82–91, may 2016.
- [84] C. Haass and D. J. Selkoe. Soluble protein oligomers in neurodegeneration: lessons from the Alzheimer’s amyloid beta-peptide. *Nat. Rev. Mol. Cell Biol.*, 8(2):101–112, feb 2007.
- [85] J. Habchi, P. Arosio, M. Perni, A. R. Costa, M. Yagi-Utsumi, P. Joshi, S. Chia, S. I. A. Cohen, M. B. D. Mueller, S. Linse, E. A. A. Nollen, C. M. Dobson, T. P. J. Knowles, and M. Vendruscolo. An anticancer drug suppresses the primary nucleation reaction that initiates the production of the toxic A beta 42 aggregates linked with Alzheimer’s disease. *Sci. Adv.*, 2(2), feb 2016.

- [86] S. M. Hammad, S. Ranganathan, E. Loukinova, W. O. Twal, and W. S. Argraves. Interaction of apolipoprotein J-amyloid beta-peptide complex with low density lipoprotein receptor-related protein-2 megalin - A mechanism to prevent pathological accumulation of amyloid beta-peptide. *J. Biol. Chem.*, 272(30):18644–18649, jul 1997.
- [87] T. Hard and C. Lendel. Inhibition of Amyloid Formation. *J. Mol. Biol.*, 421(4-5, 2, SI):441–465, aug 2012.
- [88] B. Hardesty and G. Kramer. Folding of a nascent peptide on the ribosome. In *Progress in nucleic acid research and molecular biology, Vol 66*, volume 66, pages 41–66. Academic Press Inc, 2001.
- [89] J. Hardy. Expression of normal sequence pathogenic proteins for neurodegenerative disease contributes to disease risk: ‘permissive templating’ as a general mechanism underlying neurodegeneration. *Biochem. Soc. Trans.*, 33(4):578–581, aug 2005.
- [90] J. Hardy and D. J. Selkoe. The amyloid hypothesis of Alzheimer’s disease: progress and problems on the road to therapeutics. *Science (New York, N.Y.)*, 297(5580):353–6, jul 2002.
- [91] F. U. Hartl. Molecular chaperones in cellular protein folding. *Nature*, 381(6583):571–580, jun 1996.
- [92] F. U. Hartl, A. Bracher, and M. Hayer-Hartl. Molecular chaperones in protein folding and proteostasis. *Nature*, 475(7356):324–332, jul 2011.
- [93] F. U. Hartl and M. Hayer-Hartl. Protein folding - Molecular chaperones in the cytosol: from nascent chain to folded protein. *Science*, 295(5561):1852–1858, 2002.
- [94] F. U. Hartl and M. Hayer-Hartl. Converging concepts of protein folding in vitro and in vivo. *Nat. Struct. Mol. Biol.*, 16(6):574–581, jun 2009.
- [95] M. Haslbeck, S. Weinkauff, and J. Buchner. Small heat shock proteins: Simplicity meets complexity. *J. Biol. Chem.*, 294(6):2121–2132, feb 2019.
- [96] P. C. Havugimana, G. T. Hart, T. Nepusz, H. Yang, A. L. Turinsky, Z. Li, P. I. Wang, D. R. Boutz, V. Fong, S. Phanse, and Others. A census of human soluble protein complexes. *Cell*, 150(5):1068–1081, 2012.
- [97] J. Hedlund, J. Johansson, and B. Persson. BRICHOS - a superfamily of multidomain proteins with diverse functions. *BMC Res Notes*, 2:180, jan 2009.
- [98] T. W. Herling, P. Arosio, T. Müller, S. Linse, and T. P. J. Knowles. A microfluidic platform for quantitative measurements of effective protein charges and single ion binding in solution. *Phys. Chem. Chem. Phys.*, 17(18):12161–12167, 2015.
- [99] E. Hermansson, S. Schultz, D. Crowther, S. Linse, B. Winblad, G. Westermark, J. Johansson, and J. Presto. The chaperone domain BRICHOS prevents CNS toxicity of amyloid-beta peptide in *Drosophila melanogaster*. *Dis. Model. Mech.*, 7(6):659–665, jun 2014.

- [100] L. Hermo, K. Barin, and R. Oko. Developmental expression of sulfated glycoprotein-2 in the epididymis of the rat. *Anat. Rec.*, 240(3):327–344, nov 1994.
- [101] A. Z. Herskovits, J. J. Locascio, E. R. Peskind, G. Li, and B. T. Hyman. A Luminex Assay Detects Amyloid beta Oligomers in Alzheimer’s Disease Cerebrospinal Fluid. *PLoS ONE*, 8(7):1–11, 2013.
- [102] G. R. Hilton, H. Lioe, F. Stengel, A. J. Baldwin, and J. L. P. Benesch. Small heat-shock proteins: paramedics of the cell. *Top. Curr. Chem.*, 328:69–98, 2013.
- [103] A. Hishiya and S. Takayama. Molecular chaperones as regulators of cell death. *Oncogene*, 27(50):6489–6506, 2008.
- [104] G. K. A. Hochberg and J. L. P. Benesch. Dynamical structure of alpha B-crystallin. *Prog. Biophys. Mol. Biol.*, 115(1):11–20, jul 2014.
- [105] G. K. A. Hochberg, H. Ecroyd, C. Liu, D. Cox, D. Cascio, M. R. Sawaya, M. P. Collier, J. Stroud, J. A. Carver, A. J. Baldwin, C. V. Robinson, D. S. Eisenberg, J. L. P. Benesch, and A. Laganowsky. The structured core domain of alpha B-crystallin can prevent amyloid fibrillation and associated toxicity. *Proc. Natl. Acad. Sci.*, 111(16):E1562–E1570, apr 2014.
- [106] J. Homola, S. S. Yee, and G. Gauglitz. Surface plasmon resonance sensors: review. *Sens. Actuator B Chem.*, 54(1-2):3–15, jan 1999.
- [107] L. S. Honig, B. Vellas, M. Woodward, M. Boada, R. Bullock, M. Borrie, K. Hager, N. Andreasen, E. Scarpini, H. Liu-Seifert, M. Case, R. A. Dean, A. Hake, K. Sundell, V. P. Hoffmann, C. Carlson, R. Khanna, M. Mintun, R. DeMattos, K. J. Selzler, and E. Siemers. Trial of Solanezumab for Mild Dementia Due to Alzheimer’s Disease. *N. Engl. J. Med.*, 378(4):321–330, jan 2018.
- [108] W. Hoyer, T. Antony, D. Cherny, G. Heim, T. M. Jovin, and V. Subramaniam. Dependence of alpha-synuclein aggregate morphology on solution conditions. *J. Mol. Biol.*, 322(2):383–393, sep 2002.
- [109] N. W. Huh, P. Berkowitz, R. G. Hiskey, and L. G. Pedersen. Determination of strontium binding to macromolecules. *Anal. Biochem.*, 198(2):391–393, nov 1991.
- [110] D. T. Humphreys, J. A. Carver, S. B. Easterbrook-Smith, and M. R. Wilson. Clusterin has chaperone-like activity similar to that of small heat shock proteins. *J. Biol. Chem.*, 274(11):6875–6881, 1999.
- [111] R. J. Hunter. *Zeta potential in colloid science: principles and applications*, volume 2. Academic press, 2013.
- [112] R. Inoue, T. Takata, N. Fujii, K. Ishii, S. Uchiyama, N. Sato, Y. Oba, K. Wood, K. Kato, N. Fujii, and M. Sugiyama. New insight into the dynamical system of alpha B-crystallin oligomers. *Sci. Rep.*, 6, jul 2016.
- [113] J. N. Israelachvili. *Intermolecular and Surface Forces Preface to the Third Edition*. Elsevier Academic Press Inc, 2011.

- [114] S. Jackson. *Molecular Chaperones*. Topics in Current Chemistry. Springer Berlin Heidelberg, 2012.
- [115] M. C. Jecklin, S. Schauer, C. E. Dumelin, and R. Zenobi. Label-free determination of protein-ligand binding constants using mass spectrometry and validation using surface plasmon resonance and isothermal titration calorimetry. *J. Mol. Recognit.*, 22(4):319–329, 2009.
- [116] S. Jehle, P. Rajagopal, B. Bardiaux, S. Markovic, R. Kuehne, J. R. Stout, V. A. Higman, R. E. Klevit, B.-J. van Rossum, and H. Oschkinat. Solid-state NMR and SAXS studies provide a structural basis for the activation of alpha B-crystallin oligomers. *Nat. Struct. Mol. Biol.*, 17(9):1037–U1, sep 2010.
- [117] D. E. Jenne and J. Tschopp. Clusterin - The intriguing guises of a widely expressed glycoprotein. *Trends Biochem. Sci.*, 17(4):154–159, apr 1992.
- [118] H. Johansson, M. R. Jensen, H. Gesmar, S. Meier, J. M. Vinther, C. Keeler, M. E. Hodsdon, and J. J. Led. Specific and Nonspecific Interactions in Ultraweak Protein-Protein Associations Revealed by Solvent Paramagnetic Relaxation Enhancements. *J. Am. Chem. Soc.*, 136(29):10277–10286, jul 2014.
- [119] H. Johansson, K. Nordling, T. E. Weaver, and J. Johansson. The Brichos domain-containing C-terminal part of pro-surfactant protein C binds to an unfolded poly-Val transmembrane segment. *J. Biol. Chem.*, 281(30):21032–21039, jul 2006.
- [120] A. C. Johnson and M. T. Bowser. Micro free flow electrophoresis. *Lab Chip*, 18(1):27–40, 2018.
- [121] T. C. Jordan-Starck, D. P. Witte, B. J. Aronow, and J. A. K. Harmony. Apolipoprotein J: a membrane policeman? *Curr. Opin. Lipidol.*, 3(2):75, 1992.
- [122] A. Jungbauer and R. Hahn. Ion-exchange chromatography. In *Methods Enzymol.*, volume 463, pages 349–371. Elsevier, 2009.
- [123] W. Kaar, K. Ahrer, A. Duerauer, S. Greinstetter, W. Sprinzl, P. Wechner, F. Clementschitsch, K. Bayer, C. Achmueller, B. Auer, R. Hahn, and A. Jungbauer. Refolding of N-pro Fusion Proteins. *Biotechnol. Bioeng.*, 104(4):774–784, nov 2009.
- [124] I. G. Kaplan. *Intermolecular Interactions: Physical Picture, Computational Methods and Model Potentials*. John Wiley & Sons, Ltd, 2006.
- [125] E. Karran, M. Mercken, and B. De Strooper. The amyloid cascade hypothesis for Alzheimer’s disease: an appraisal for the development of therapeutics. *Nat. Rev. Drug Discov.*, 10(9):698–U1600, sep 2011.
- [126] E. Kilger, A. Buehler, H. Woelfing, S. Kumar, S. A. Kaeser, A. Nagarathinam, J. Walter, M. Jucker, and J. Coomaraswamy. BRI2 Protein Regulates beta-Amyloid Degradation by Increasing Levels of Secreted Insulin-degrading Enzyme (IDE). *J. Biol. Chem.*, 286(43):37446–37457, oct 2011.

- [127] J. Kim, V. M. Miller, Y. Levites, K. J. West, C. W. Zwizinski, B. D. Moore, F. J. Troendle, M. Bann, C. Verbeeck, R. W. Price, L. Smithson, L. Sonoda, K. Wagg, V. Rangachari, F. Zou, S. G. Younkin, N. Graff-Radford, D. Dickson, T. Rosenberry, and T. E. Golde. BRI2 (ITM2b) inhibits A beta deposition in vivo. *J. Neurosci.*, 28(23):6030–6036, jun 2008.
- [128] S. D. Knight, J. Presto, S. Linse, and J. Johansson. The BRICHOS domain, amyloid fibril formation, and their relationship. *Biochemistry*, 52(43):7523–31, oct 2013.
- [129] T. P. J. Knowles, M. Vendruscolo, and C. M. Dobson. The amyloid state and its association with protein misfolding diseases. *Nat. Rev. Mol. Cell Bio.*, 15(6):384–396, jun 2014.
- [130] T. P. J. Knowles, C. A. Waudby, G. L. Devlin, S. I. A. Cohen, A. Aguzzi, M. Vendruscolo, E. M. Terentjev, M. E. Welland, and C. M. Dobson. An analytical solution to the kinetics of breakable filament assembly. *Science*, 326(5959):1533–1537, dec 2009.
- [131] F. D. L. Kondrat, W. B. Struwe, and J. L. P. Benesch. Native mass spectrometry: towards high-throughput structural proteomics. *Methods Mol. Biol.*, 1261:349–371, 2015.
- [132] R. Koradi, M. Billeter, and K. Wuthrich. MOLMOL: A program for display and analysis of macromolecular structures. *J. Mol. Graph.*, 14(1):51–&, feb 1996.
- [133] J. R. Kumita, S. Poon, G. L. Caddy, C. L. Hagan, M. Dumoulin, J. J. Yerbury, E. M. Stewart, C. V. Robinson, M. R. Wilson, and C. M. Dobson. The extracellular chaperone clusterin potentially inhibits human lysozyme amyloid formation by interacting with prefibrillar species. *J. Mol. Biol.*, 369(1):157–167, may 2007.
- [134] N. Lachmann, K. Todorova, H. Schulze, and C. Schönemann. Luminex® and its applications for solid organ transplantation, hematopoietic stem cell transplantation, and transfusion. *Transfus Med Hemother*, 40(3):182–189, 2013.
- [135] M. P. Lambert, A. K. Barlow, B. A. Chromy, C. Edwards, R. Freed, M. Liosatos, T. E. Morgan, I. Rozovsky, B. Trommer, K. L. Viola, P. Wals, C. Zhang, C. E. Finch, G. A. Krafft, and W. L. Klein. Diffusible, nonfibrillar ligands derived from A beta(1-42) are potent central nervous system neurotoxins. *Proc. Natl. Acad. Sci.*, 95(11):6448–6453, 1998.
- [136] U. Lapinska, K. L. Saar, E. V. Yates, T. W. Herling, T. Müller, P. K. Challa, C. M. Dobson, and T. P. J. Knowles. Gradient-free determination of isoelectric points of proteins on chip. *Phys. Chem. Chem. Phys.*, 19(34):23060–23067, sep 2017.
- [137] J. P. Larmann Jr, A. V. Lemmo, A. W. Moore Jr, and J. W. Jorgenson. Two-dimensional separations of peptides and proteins by comprehensive liquid chromatography-capillary electrophoresis. *Electrophoresis*, 14(1):439–447, 1993.
- [138] R. A. Laskey, B. M. Honda, A. D. Mills, and J. T. Finch. Nucleosomes are assembled by an acidic protein which binds histones and transfers them to DNA. *Nature*, 275(5679):416–420, 1978.
- [139] S. H. Lee and R. Dominguez. Regulation of actin cytoskeleton dynamics in cells. *Mol. Cells*, 29(4):311–325, apr 2010.

- [140] Y. C. Lee. Fluorescence spectrometry in studies of carbohydrate-protein interactions. *J. Biochem.*, 121(5):818–825, 1997.
- [141] C. A. Lepre, J. M. Moore, and J. W. Peng. Theory and applications of NMR-based screening in pharmaceutical research. *Chem. Rev.*, 104(8):3641–3675, aug 2004.
- [142] G. J. Lesser and G. D. Rose. Hydrophobicity of amino-acid subgroups in proteins. *Proteins*, 8(1):6–13, 1990.
- [143] Lilly. Lilly Announces Top-Line Results of Solanezumab Phase 3 Clinical Trial. *Press Release*, 2016.
- [144] D. H. Lin, T. Stuwe, S. Schilbach, E. J. Rundlet, T. Perriches, G. Mobbs, Y. Fan, K. Thierbach, F. M. Huber, L. N. Collins, A. M. Davenport, Y. E. Jeon, and A. Hoelz. Architecture of the symmetric core of the nuclear pore. *Science*, 352(6283), apr 2016.
- [145] A. Lipas, M. Vandyke, and J. Stock. PREDICTING COILED COILS FROM PROTEIN SEQUENCES. *Science*, 252(5009):1162–1164, 1991.
- [146] L. Lo Conte, C. Chothia, and J. Janin. The atomic structure of protein-protein recognition sites. *J. Mol. Biol.*, 285(5):2177–2198, feb 1999.
- [147] L.-F. Lue, Y.-M. Kuo, A. E. Roher, L. Brachova, Y. Shen, L. Sue, T. Beach, J. H. Kurth, R. E. Rydel, and J. Rogers. Soluble Amyloid  $\beta$  Peptide Concentration as a Predictor of Synaptic Change in Alzheimer’s Disease. *Am. J. Pathol.*, 155(3):853–862, sep 1999.
- [148] D. Magen, C. Georgopoulos, P. Bross, D. Ang, Y. Segev, D. Goldsher, A. Nemirovski, E. Shahar, S. Ravid, A. Luder, B. Heno, R. Gershoni-Baruch, K. Skorecki, and H. Mandel. Mitochondrial Hsp60 chaperonopathy causes an autosomal-recessive neurodegenerative disorder linked to brain hypomyelination and leukodystrophy. *Am. J. Hum. Genet.*, 83(1):30–42, jul 2008.
- [149] A. Mainz, J. Peschek, M. Stavropoulou, K. C. Back, B. Bardiaux, S. Asami, E. Prade, C. Peters, S. Weinkauff, J. Buchner, and B. Reif. The chaperone alpha B-crystallin uses different interfaces to capture an amorphous and an amyloid client. *Nat. Struct. Mol. Biol.*, 22(11):898–905, nov 2015.
- [150] C. Mansson, P. Arosio, R. Hussein, H. H. Kampinga, R. M. Hashem, W. C. Boelens, C. M. Dobson, T. P. J. Knowles, S. Linse, and C. Emanuelsson. Interaction of the Molecular Chaperone DNAJB6 with Growing Arnyloid-beta 42 (A beta 42) Aggregates Leads to Sub-stoichiometric Inhibition of Amyloid Formation. *J. Biol. Chem.*, 289(45):31066–31076, nov 2014.
- [151] A. Manz, D. J. Harrison, E. M. J. Verpoorte, J. C. Fettingner, A. Paulus, H. Ludi, and H. M. Widmer. Planar chips technology for miniturization and integration of separation techniques into monitoring systems - capillary electrophoresis on a chip. *J. Chromatogr. A*, 593(1-2):253–258, feb 1992.
- [152] J. A. Marsh and S. A. Teichmann. Structure, Dynamics, Assembly, and Evolution of Protein Complexes. In *Annu. Rev. Biochem.*, volume 84, pages 551–575. 2015.

- [153] L. Martin, R. Fluhrer, K. Reiss, E. Kremmer, P. Saftig, and C. Haass. Regulated intramembrane proteolysis of Bri2 (Itm2b) by ADAM10 and SPPL2a/SPPL2b. *J. Biol. Chem.*, 283(3):1644–52, jan 2008.
- [154] M. T. Marty, A. J. Baldwin, E. G. Marklund, G. K. A. Hochberg, J. L. P. Benesch, and C. V. Robinson. Bayesian Deconvolution of Mass and Ion Mobility Spectra: From Binary Interactions to Polydisperse Ensembles. *Anal. Chem.*, 87(8):4370–4376, apr 2015.
- [155] V. Masilamani, K. Al-Zhrani, M. Al-Salhi, A. Al-Diab, and M. Al-Ageily. Cancer diagnosis by autofluorescence of blood components. *J. Lumin.*, 109(3-4):143–154, sep 2004.
- [156] S. Matsuda, L. Giliberto, Y. Matsuda, E. M. McGowan, and L. D’Adamio. BRI2 inhibits amyloid beta-peptide precursor protein processing by interfering with the docking of secretases to the substrate. *J. Neurosci.*, 28(35):8668–8676, aug 2008.
- [157] J. C. McDonald and G. M. Whitesides. Poly (dimethylsiloxane) as a material for fabricating microfluidic devices. *Acc. Chem. Res.*, 35(7):491–499, 2002.
- [158] G. Meisl, X. Yang, E. Hellstrand, B. Frohm, J. B. Kirkegaard, S. I. A. Cohen, C. M. Dobson, S. Linse, and T. P. J. Knowles. Differences in nucleation behavior underlie the contrasting aggregation kinetics of the A beta 40 and A beta 42 peptides. *Proc. Natl. Acad. Sci. U.S.A.*, 111(26):9384–9389, jul 2014.
- [159] F. A. Meyer. Macromolecular basis of globular protein exclusion and of swelling pressure in loose connective-tissue (umbilical-cord). *Biochim. Biophys. Acta*, 755(3):388–399, 1983.
- [160] N. N. Mhurchu, L. Zoubak, G. McGauran, S. Linse, A. Yeliseev, and D. J. O’Connell. Simplifying G Protein-Coupled Receptor Isolation with a Calcium-Dependent Fragment Complementation Affinity System. *Biochemistry*, 57(30):4383–4390, jul 2018.
- [161] L. Michaelis. *Die Wasserstoffionenkonzentration*. Springer, Berlin, Heidelberg, 1914.
- [162] M. Milan, C. R. Jimenez, and C. E. Teunissen. Bri2 as a novel biomarker for alzheimer’s disease, 2014.
- [163] S. Mori and H. G. Barth. *Size exclusion chromatography*. Springer Science & Business Media, 2013.
- [164] T. Müller, P. Arosio, L. Rajah, S. I. A. Cohen, E. V. Yates, M. Vendruscolo, C. M. Dobson, and T. P. J. Knowles. Particle-based Monte-Carlo simulations of steady-state mass transport at intermediate Peclet numbers. *Int. J. Nonlin. Sci. Num.*, 17(3-4):175–183, jun 2016.
- [165] A. Munke, J. Persson, T. Weiffert, E. De Genst, G. Meisl, P. Arosio, A. Carnerup, C. M. Dobson, M. Vendruscolo, T. P. J. Knowles, and S. Linse. Phage display and kinetic selection of antibodies that specifically inhibit amyloid self-replication. *Proc. Natl. Acad. Sci.*, 114(25):6444–6449, jun 2017.

- [166] P. Narayan, A. Orte, R. W. Clarke, B. Bolognesi, S. Hook, K. A. Ganzinger, S. Meehan, M. R. Wilson, C. M. Dobson, and D. Klenerman. The extracellular chaperone clusterin sequesters oligomeric forms of the amyloid-beta(1-40) peptide. *Nat. Struct. Mol. Biol.*, 19(1):79–U97, jan 2012.
- [167] I. Navratilova, G. A. Papalia, R. L. Rich, D. Bedinger, S. Brophy, B. Condon, T. Deng, A. W. Emerick, H.-W. Guan, T. Hayden, T. Heutmekers, B. Hoorelbeke, M. C. McCroskey, M. M. Murphy, T. Nakagawa, F. Parmeggiani, X. Qin, S. Rebe, N. Tomasevic, T. Tsang, M. B. Waddell, F. F. Zhang, S. Leavitt, and D. G. Myszka. Thermodynamic benchmark study using Biacore technology. *Anal. Biochem.*, 364(1):67–77, 2007.
- [168] M. Nilsson, V. Harang, M. Bergstrom, S. Ohlson, R. Isaksson, and G. Johansson. Determination of protein-ligand affinity constants from direct migration time in capillary electrophoresis. *Electrophoresis*, 25(12):1829–1836, jun 2004.
- [169] S. Nim, J. Jeon, C. Corbi-Verge, M.-H. Seo, Y. Ivarsson, J. Moffat, N. Tarasova, and P. M. Kim. Pooled screening for antiproliferative inhibitors of protein-protein interactions. *Nat. Chem. Biol.*, 12(4):275–281, 2016.
- [170] P. O’Farrell. High Resolution of Proteins \* Electrophoresis. *J. Biol. Chem.*, 250(10):4007–4021, 1975.
- [171] I. R. Olmsted, A. Kussrow, and D. J. Bornhop. Comparison of Free-Solution and Surface-Immobilized Molecular Interactions Using a Single Platform. *Anal. Chem.*, 84(24):10817–10822, 2012.
- [172] H. Olzscha, S. M. Schermann, A. C. Woerner, S. Pinkert, M. H. Hecht, G. G. Tartaglia, M. Vendruscolo, M. Hayer-Hartl, F. U. Hartl, and R. M. Vabulas. Amyloid-like Aggregates Sequester Numerous Metastable Proteins with Essential Cellular Functions. *Cell*, 144(1):67–78, jan 2011.
- [173] S. Ostrowitzki, R. A. Lasser, E. Dorflinger, P. Scheltens, F. Barkhof, T. Nikolcheva, E. Ashford, S. Retout, C. Hofmann, P. Delmar, G. Klein, M. Andjelkovic, B. Dubois, M. Boada, K. Blennow, L. Santarelli, P. Fontoura, and S. R. Investigators. A phase III randomized trial of gantenerumab in prodromal Alzheimer’s disease. *Alzheimers Res. Ther.*, 9, dec 2017.
- [174] D. Otzen and R. Riek. Functional Amyloids. *Cold Spring Harb Perspect Biol*, page a033860, 2019.
- [175] T. F. Outeiro, J. Klucken, K. E. Strathearn, F. Liu, P. Nguyen, J.-C. Rochet, B. T. Hyman, and P. J. McLean. Small heat shock proteins protect against alpha-synuclein-induced toxicity and aggregation. *Biochem. Biophys. Res. Commun.*, 351(3):631–638, dec 2006.
- [176] F. Panza, V. Frisardi, B. P. Imbimbo, G. D’Onofrio, G. Pietrarossa, D. Seripa, A. Pilotto, and V. Solfrizzi. Bapineuzumab: anti-beta-amyloid monoclonal antibodies for the treatment of Alzheimer’s disease. *Immunotherapy*, 2(6):767–782, nov 2010.
- [177] L. Partridge, J. Thornton, and G. Bates. The new science of ageing Introduction. *Philos. Trans. Royal Soc. B*, 366(1561):6–8, jan 2011.

- [178] H. R. B. Pelham. Speculations on the functions of the major heat-shock and glucose-regulated proteins. *Cell*, 46(7):959–961, sep 1986.
- [179] R. Pender. World Alzheimer Report 2014 Dementia and Risk Reduction. 2014.
- [180] S. Peng, M. Fitzen, H. Jornvall, and J. Johansson. The extracellular domain of Bri2 (ITM2B) binds the ABri peptide (1-23) and amyloid beta-peptide (A beta 1-40): Implications for Bri2 effects on processing of amyloid precursor protein and A beta aggregation. *Biochem. Biophys. Res. Commun.*, 393(3):356–361, mar 2010.
- [181] J. R. Perkins, I. Diboun, B. H. Dessailly, J. G. Lees, and C. Orengo. Transient Protein-Protein Interactions: Structural, Functional, and Network Properties. *Structure*, 18(10):1233–1243, oct 2010.
- [182] J. Peschek, N. Braun, T. M. Franzmann, Y. Georgalis, M. Haslbeck, S. Weinkauff, and J. Buchner. The eye lens chaperone alpha-crystallin forms defined globular assemblies. *Proc. Natl. Acad. Sci.*, 106(32):13272–13277, aug 2009.
- [183] S. A. Pfeiffer, B. M. Rudisch, P. Glaeser, M. Spanka, F. Nitschke, A. A. Robitzki, C. Schneider, S. Nagl, and D. Belder. Continuous purification of reaction products by micro free-flow electrophoresis enabled by large area deep-UV fluorescence imaging. *Anal. Bioanal. Chem.*, 410(3):853–862, 2018.
- [184] Pfizer. Pfizer announces co-primary clinical endpoints not met in second phase 3 bapineuzumab study in mild-to-moderate Alzheimer’s disease patients who do not carry the ApoE4 genotype. *Press Release*, 2012.
- [185] M. M. Pierce, C. S. Raman, and B. T. Nall. Isothermal titration calorimetry of protein-protein interactions. *Methods*, 19(2):213–221, 1999.
- [186] S. Poon, S. B. Easterbrook-Smith, M. S. Rybchyn, J. A. Carver, and M. R. Wilson. Clusterin is an ATP-independent chaperone with very broad substrate specificity that stabilizes stressed proteins in a folding-competent state. *Biochemistry*, 39(51):15953–15960, dec 2000.
- [187] K. D. Powell, S. Ghaemmaghami, M. Z. Wang, L. Y. Ma, T. G. Oas, and M. C. Fitzgerald. A general mass spectrometry-based assay for the quantitation of protein-ligand binding interactions in solution. *J. Am. Chem. Soc.*, 124(35):10256–10257, sep 2002.
- [188] V. Ramachandiran, V. Grigoriev, L. Lan, E. Ravkov, S. A. Mertens, and J. D. Altman. A robust method for production of MHC tetramers with small molecule fluorophores. *J. Immunol. Methods*, 319(1-2):13–20, jan 2007.
- [189] D. E. Raymond, A. Manz, and H. M. Widmer. Continuous sample pretreatment using a free-flow electrophoresis device integrated onto a silicon chip. *Anal. Chem.*, 66(18):2858–2865, 1994.
- [190] B. S. Reddy and B. N. Chatterji. An FFT-based technique for translation, rotation, and scale-invariant image registration. *IEEE Trans Image Process*, 5(8):1266–1271, 1996.

- [191] D. Reichmann, Y. Xu, C. M. Cremers, M. Ilbert, R. Mittelman, M. C. Fitzgerald, and U. Jakob. Order out of Disorder: Working Cycle of an Intrinsically Unfolded Chaperone. *Cell*, 148(5):947–957, mar 2012.
- [192] A. Rekas, C. G. Adda, J. A. Aquilina, K. J. Barnham, M. Sunde, D. Galatis, N. A. Williamson, C. L. Masters, R. F. Anders, C. V. Robinson, R. Cappai, and J. A. Carver. Interaction of the molecular chaperone alpha B-crystallin with alpha-synuclein: Effects on amyloid fibril formation and chaperone activity. *J. Mol. Biol.*, 340(5):1167–1183, jul 2004.
- [193] A. Rekas, L. Jankova, D. C. Thorn, R. Cappai, and J. A. Carver. Monitoring the prevention of amyloid fibril formation by alpha-crystallin. *FEBS J.*, 274(24):6290–6305, dec 2007.
- [194] M. B. Rhodes, P. R. Azari, and R. E. Feeney. Analysis, fractionation, and purification of egg white proteins with cellulosecation exchanger. *J. Biol. Chem.*, 230(1):399–408, 1958.
- [195] P. H. Richter. Estimating Errors in Least-Squares Fitting. *TDA Progress Report*, 122:107–137, apr 1995.
- [196] Roch. Roche to discontinue Phase III CREAD 1 and 2 clinical studies of crenezumab in early Alzheimer’s disease (AD) - other company programmes in AD continue. *Press Release*, 2019.
- [197] J. S. Rohrer, L. Basumallick, and D. Hurum. High-performance anion-exchange chromatography with pulsed amperometric detection for carbohydrate analysis of glycoproteins. *Biochemistry (Moscow, Russ. Fed.)*, 78(7):697–709, jul 2013.
- [198] R. Roychaudhuri, M. Yang, M. M. Hoshi, and D. B. Teplow. Amyloid beta-protein assembly and Alzheimer disease. *J. Biol. Chem.*, 284(8):4749–53, feb 2009.
- [199] K. L. Rundlett and D. W. Armstrong. Methods for the determination of binding constants by capillary electrophoresis. *Electrophoresis*, 22(7):1419–1427, apr 2001.
- [200] K. L. Saar, Y. Zhang, T. Müller, C. P. Kumar, S. Devenish, A. Lynn, U. Lapinska, X. Yang, S. Linse, and T. P. J. Knowles. On-chip label-free protein analysis with downstream electrodes for direct removal of electrolysis products. *Lab Chip*, 18(1):162–170, jan 2018.
- [201] C. A. Sacks, J. Avorn, and A. S. Kesselheim. The Failure of Solanezumab - How the FDA Saved Taxpayers Billions. *N. Engl. J. Med.*, 376(18):1706–1708, may 2017.
- [202] L. Sánchez-Pulido, D. Devos, and A. Valencia. BRICHOS: a conserved domain in proteins associated with dementia, respiratory distress and cancer. *Trends Biochem. Sci.*, 0004(02):5–8, 2002.
- [203] T. Scheidt, U. Łapińska, J. R. Kumita, D. R. Whiten, D. Klenerman, M. R. Wilson, S. I. A. Cohen, S. Linse, M. Vendruscolo, C. M. Dobson, T. P. J. Knowles, and P. Arosio. Secondary nucleation and elongation occur at different sites on Alzheimer’s amyloid- $\beta$  aggregates. *Sci. Adv.*, 5(4), 2019.
- [204] G. Schreiber, G. Haran, and H.-X. Zhou. Fundamental Aspects of Protein-Protein Association Kinetics. *Chem. Rev.*, 109(3):839–860, mar 2009.

- [205] S. L. Seager and M. R. Slabaugh. *Chemistry for today*. Brooks Cole Thomson Learning, 2008.
- [206] J. Sevigny, P. Chiao, T. Bussiere, P. H. Weinreb, L. Williams, M. Maier, R. Dunstan, S. Saloway, T. Chen, Y. Ling, J. O’Gorman, F. Qian, M. Arastu, M. Li, S. Chollate, M. S. Brennan, O. Quintero-Monzon, R. H. Scannevin, H. M. Arnold, T. Engber, K. Rhodes, J. Ferrero, Y. Hang, A. Mikulskis, J. Grimm, C. Hock, R. M. Nitsch, and A. Sandrock. The antibody aducanumab reduces A beta plaques in Alzheimer’s disease. *Nature*, 537(7618):50–56, sep 2016.
- [207] S. L. Shammass, C. A. Waudby, S. Wang, A. K. Buell, T. P. J. Knowles, H. Ecroyd, M. E. Welland, J. A. Carver, C. M. Dobson, and S. Meehan. Binding of the Molecular Chaperone alpha B-Crystallin to A beta Amyloid Fibrils Inhibits Fibril Elongation. *Biophys. J.*, 101(7):1681–1689, 2011.
- [208] A. G. Shanbhag. UTILIZATION OF INFORMATION MEASURE AS A MEANS OF IMAGE THRESHOLDING. *Graphical Models*, 56(5):414–419, sep 1994.
- [209] F. B. Sheinerman, R. Norel, and B. Honig. Electrostatic aspects of protein-protein interactions. *Curr Opin Struct Biol*, 10(2):153–159, apr 2000.
- [210] J. P. Shockcor, S. E. Unger, I. D. Wilson, P. J. D. Foxall, J. K. Nicholson, and J. C. Lindon. Combined HPLC, NMR spectroscopy, and ion-trap mass spectrometry with application to the detection and characterization of xenobiotic and endogenous metabolites in human urine. *Anal. Chem.*, 68(24):4431–4435, 1996.
- [211] J. D. Sipe, M. D. Benson, J. N. Buxbaum, S.-i. Ikeda, G. Merlini, M. J. M. Saraiva, and P. Westermark. Amyloid fibril protein nomenclature: 2012 recommendations from the Nomenclature Committee of the International Society of Amyloidosis. *Amyloid*, 19(4):167–170, 2012.
- [212] R. Sitia and I. Braakman. Quality control in the endoplasmic reticulum protein factory. *NATURE*, 426(6968):891–894, 2003.
- [213] L. R. Snyder, J. J. Kirkland, and J. W. Dolan. *Introduction to modern liquid chromatography*. John Wiley & Sons, 2011.
- [214] W. M. Southerland, D. R. Winge, and K. V. Rajagopalan. Domains of rat-liver sulfite oxidase - proteolytic separation and characterization. *J. Biol. Chem.*, 253(24):8747–8752, 1978.
- [215] M. Spiga and G. L. Morino. A symmetric solution for velocity profile in laminar flow through rectangular ducts. *Int J Heat Mass Transf*, 21(4):469–475, 1994.
- [216] F. Stengel, A. J. Baldwin, A. J. Painter, N. Jaya, E. Basha, L. E. Kay, E. Vierling, C. V. Robinson, and J. L. P. Benesch. Quaternary dynamics and plasticity underlie small heat shock protein chaperone function. *Proc. Natl. Acad. Sci.*, 107(5):2007–2012, feb 2010.
- [217] M. Sunde and C. Blake. The structure of amyloid fibrils by electron microscopy and X-ray diffraction. In *Advances in protein chemistry, Vol 50: Protein misassembly*, volume 50, pages 123–159. Academic press, 1997.

- [218] S. L. Swann, D. Song, C. Sun, P. J. Hajduk, and A. M. Petros. Labeled Ligand Displacement: Extending NMR-Based Screening of Protein Targets. *ACS Med. Chem. Lett.*, 1(6):295–299, sep 2010.
- [219] J. Tamaoka and K. Komagata. Determination of DNA base composition by reversed-phase high-performance liquid chromatography. *FEMS Microbiol. Lett.*, 25(1):125–128, 1984.
- [220] L. Tan, H.-F. Wang, M.-S. Tan, C.-C. Tan, X.-C. Zhu, D. Miao, W.-J. Yu, T. Jiang, L. Tan, J.-T. Yu, and A. D. Neuroimaging. Effect of CLU genetic variants on cerebrospinal fluid and neuroimaging markers in healthy, mild cognitive impairment and Alzheimer’s disease cohorts. *Sci. Rep.*, 6:26027, may 2016.
- [221] M. Tanaka, S. R. Collins, B. H. Toyama, and J. S. Weissman. The physical basis of how prion conformations determine strain phenotypes. *Nature*, 442(7102):585–589, aug 2006.
- [222] M. P. Tarazona and E. Saiz. Combination of SEC/MALS experimental procedures and theoretical analysis for studying the solution properties of macromolecules. *J. Biochem. Biophys. Methods*, 56(1-3):95–116, jun 2003.
- [223] E. Thorsby. A short history of HLA. *Tissue Antigens*, 74(2):101–116, 2009.
- [224] A. O. Tiroli-Cepeda and C. H. I. Ramos. Heat causes oligomeric disassembly and increases the chaperone activity of small heat shock proteins from sugarcane. *Plant Physiol. Biochem.*, 48(2-3):108–116, 2010.
- [225] J. L. Tiwari and P. I. Terasaki. *HLA and Disease Associations*. Springer New York, 1985.
- [226] P. Tompa and P. Csermely. The role of structural disorder in the function of RNA and protein chaperones. *FASEB J.*, 18(11):1169–1175, aug 2004.
- [227] M. Törnquist, T. C. T. Michaels, K. Sanagavarapu, X. Yang, G. Meisl, S. I. A. Cohen, T. P. J. Knowles, and S. Linse. Secondary nucleation in amyloid formation. *ChemComm*, 2018.
- [228] T. M. Treweek, S. Meehan, H. Ecroyd, and J. A. Carver. Small heat-shock proteins: important players in regulating cellular proteostasis. *Cell. Mol. Life Sci.*, 72(3):429–451, feb 2015.
- [229] C. J. Tsai, S. L. Lin, H. J. Wolfson, and R. Nussinov. Studies of protein-protein interfaces: A statistical analysis of the hydrophobic effect. *Protein Sci.*, 6(1):53–64, jan 1997.
- [230] N. Ui. Electrophoretic mobility and isoelectric point of hog thyroglobulin. *Biochim. Biophys. Acta*, 257(2):350–364, 1972.
- [231] A. Velazquez-Campoy and E. Freire. Isothermal titration calorimetry to determine association constants for high-affinity ligands. *Nat. Protoc.*, 1(1):186–191, 2006.
- [232] D. M. Walsh, I. Klyubin, J. V. Fadeeva, W. K. Cullen, R. Anwyl, M. S. Wolfe, M. J. Rowan, and D. J. Selkoe. Naturally secreted oligomers of amyloid beta protein potently inhibit hippocampal long-term potentiation in vivo. *Nature*, 416(6880):535–9, apr 2002.

- [233] D. M. Walsh, E. Thulin, A. M. Minogue, N. Gustavsson, E. Pang, D. B. Teplow, and S. Linse. A facile method for expression and purification of the Alzheimer's disease-associated amyloid beta-peptide. *FASEB J.*, 276(5):1266–1281, mar 2009.
- [234] M. A. Walti, F. Ravotti, H. Arai, C. G. Glabe, J. S. Wall, A. Bockmann, P. Guentert, B. H. Meier, and R. Riek. Atomic-resolution structure of a disease-relevant A beta(1-42) amyloid fibril. *Proc. Natl. Acad. Sci. U.S.A.*, 113(34):E4976–E4984, aug 2016.
- [235] C. A. Waudby, T. P. J. Knowles, G. L. Devlin, J. N. Skepper, H. Ecroyd, J. A. Carver, M. E. Welland, J. Christodoulou, C. M. Dobson, and S. Meehan. The Interaction of alpha B-Crystallin with Mature alpha-Synuclein Amyloid Fibrils Inhibits Their Elongation. *Biophys. J.*, 98(5):843–851, mar 2010.
- [236] P. C. Weber, D. H. Ohlendorf, J. J. Wendoloski, and F. R. Salemme. Structural origins of high-affinity biotin binding to streptavidin. *Science*, 243(4887):85–88, jan 1989.
- [237] H. J. C. T. Wessels, R. O. Vogel, R. N. Lightowers, J. N. Spelbrink, R. J. Rodenburg, L. P. van den Heuvel, A. J. van Gool, J. Gloerich, J. A. M. Smeitink, and L. G. Nijtmans. Analysis of 953 human proteins from a mitochondrial HEK293 fraction by complexome profiling. *PLoS One*, 8(7):e68340, 2013.
- [238] G. M. Whitesides. The origins and the future of microfluidics. *Nature*, 442(7101):368–373, 2006.
- [239] C. J. Wienken, P. Baaske, U. Rothbauer, D. Braun, and S. Duhr. Protein-binding assays in biological liquids using microscale thermophoresis. *Nat. Commun.*, 1, 2010.
- [240] K. Wilkinson. Quantitative Analysis of Protein-Protein Interactions. *Methods Mol. Biol.*, 261:15–31, 2004.
- [241] H. Willander, G. Askarieh, M. Landreh, P. Westermark, K. Nordling, H. Keranen, E. Hermansson, A. Hamvas, L. M. Noguee, T. Bergman, A. Saenz, C. Casals, J. Aqvist, H. Jornvall, H. Berglund, J. Presto, S. D. Knight, and J. Johansson. High-resolution structure of a BRICHOS domain and its implications for anti-amyloid chaperone activity on lung surfactant protein C. *Proc. Natl. Acad. Sci. U.S.A.*, 109(7):2325–2329, feb 2012.
- [242] H. Willander, J. Presto, G. Askarieh, H. Biverstal, B. Frohm, S. D. Knight, J. Johansson, and S. Linse. BRICHOS domains efficiently delay fibrillation of amyloid beta-peptide. *J. Biol. Chem.*, 287(37):31608–31617, sep 2012.
- [243] M. R. Wilson, J. J. Yerbury, and S. Poon. Heat Shock Proteins and the Brain: Implications for Neurodegenerative Diseases and Neuroprotection. volume 3, pages 283–315. Springer Science & Business Media, 2008.
- [244] M. R. Wilson, J. J. Yerbury, and S. Poon. Potential roles of abundant extracellular chaperones in the control of amyloid formation and toxicity. *Mol Biosyst*, 4(1):42–52, jan 2008.

- [245] B. Winner, R. Jappelli, S. K. Maji, P. A. Desplats, L. Boyer, S. Aigner, C. Hetzer, T. Loher, M. Vilar, S. Campioni, C. Tzitzilonis, A. Soragni, S. Jessberger, H. Mira, A. Consiglio, E. Pham, E. Masliah, F. H. Gage, and R. Riek. In vivo demonstration that alpha-synuclein oligomers are toxic. *Proc. Natl. Acad. Sci. U.S.A.*, 108(10):4194–4199, mar 2011.
- [246] D. J. Winzor. Determination of binding constants by affinity chromatography. *J. Chromatogr. A*, 1037(1-2):351–367, 2004.
- [247] A. M. Wojtas, S. S. Kang, B. M. Olley, M. Gatherer, M. Shinohara, P. A. Lozano, C.-C. Liu, A. Kurti, K. E. Baker, D. W. Dickson, M. Yue, L. Petrucelli, G. Bu, R. O. Carare, and J. D. Fryer. Loss of clusterin shifts amyloid deposition to the cerebrovasculature via disruption of perivascular drainage pathways. *Proc. Natl. Acad. Sci.*, 114(33):E6962–E6971, aug 2017.
- [248] K. J. Wolfe and D. M. Cyr. Amyloid in neurodegenerative diseases: Friend or foe? *Semin. Cell Dev. Biol.*, 22(5):476–481, jul 2011.
- [249] M. Wolff, J. J. Mittag, T. W. Herling, E. De Genst, C. M. Dobson, T. P. J. Knowles, D. Braun, and A. K. Buell. Quantitative thermophoretic study of disease-related protein aggregates. *Sci. Rep.*, 6, mar 2016.
- [250] P. G. Wolynes, J. N. Onuchic, and D. Thirumalai. NAVIGATING THE FOLDING ROUTES. *Science*, 267(5204):1619–1620, 1995.
- [251] M. A. Wright, F. A. Aprile, P. Arosio, M. Vendruscolo, C. M. Dobson, and T. P. J. Knowles. Biophysical approaches for the study of interactions between molecular chaperones and protein aggregates. *Chem. Commun.*, 51(77):14425–14434, 2015.
- [252] M. A. Wright, F. S. Ruggeri, K. L. Saar, P. K. Challa, J. L. P. Benesch, and T. P. J. Knowles. Analysis of alpha B-crystallin polydispersity in solution through native microfluidic electrophoresis. *The Analyst*, 144(14):4413–4424, jul 2019.
- [253] A. R. Wyatt, J. J. Yerbury, H. Ecroyd, and M. R. Wilson. Extracellular chaperones and proteostasis. In R. Kornberg, editor, *Annu. Rev. Biochem.*, volume 82 of *Annual Review of Biochemistry*, pages 295–322. 2013.
- [254] Y. Xie, D. Zhang, and D. Ben-Arnotz. Protein-ligand binding detected using ultrafiltration Raman difference spectroscopy. *Anal. Biochem.*, 373(1):154–160, feb 2008.
- [255] D. Xu, S. L. Lin, and R. Nussinov. Protein binding versus protein folding: The role of hydrophilic bridges in protein associations. *J. Mol. Biol.*, 265(1):68–84, jan 1997.
- [256] Y. L. Yan and G. Marriott. Analysis of protein interactions using fluorescence technologies. *Curr. Opin. Chem. Biol.*, 7(5):635–640, 2003.
- [257] E. V. Yates, T. Müller, L. Rajah, E. J. De Genst, P. Arosio, S. Linse, M. Vendruscolo, C. M. Dobson, and T. P. J. Knowles. Latent analysis of unmodified biomolecules and their complexes in solution with attomole detection sensitivity. *Nat. Chem.*, 7(10):802–809, oct 2015.

- [258] J. J. Yerbury, J. R. Kumita, S. Meehan, C. M. Dobson, and M. R. Wilson. alpha(2)-Macroglobulin and Haptoglobin suppress amyloid formation by interacting with prefibrillar protein species. *J. Biol. Chem.*, 284(7):4246–4254, feb 2009.
- [259] J. J. Yerbury, S. Poon, S. Meehan, B. Thompson, J. R. Kumita, C. M. Dobson, and M. R. Wilson. The extracellular chaperone clusterin influences amyloid formation and toxicity by interacting with prefibrillar structures. *FASEB J.*, 21(10):2312–2322, aug 2007.
- [260] J. J. Yerbury, E. M. Stewart, A. R. Wyatt, and M. R. Wilson. Quality control of protein folding in extracellular space. *EMBO Rep.*, 6(12):1131–6, dec 2005.
- [261] J. J. Yerbury and M. R. Wilson. Extracellular chaperones modulate the effects of Alzheimer’s patient cerebrospinal fluid on A beta(1-42) toxicity and uptake. *Cell Stress Chaperones*, 15(1):115–121, jan 2010.
- [262] L. Young, R. L. Jernigan, and D. G. Covell. A role for surface hydrophobicity in protein-protein recognition. *Protein Sci.*, 3(5):717–729, may 1994.
- [263] K. Ziolkowska, R. Kwapiszewski, and Z. Brzozka. Microfluidic devices as tools for mimicking the in vivo environment. *New J. Chem.*, 35(5):979–990, 2011.